University of Nottingham
UK | CHINA | MALAYSIA

CHEMICAL TRANSFORMATIONS IN THE TRANSMISSION ELECTRON MICROSCOPE

Kayleigh L. Y. Fung, MSci

Thesis submitted to the University of Nottingham

for the degree of Doctor of Philosophy

2020

For Mum, Sis, and Kiki.

Abstract

"At least I know I'm bewildered about the really fundamental and important facts of the universe." - Terry Pratchett, Equal Rites (1987)

The transmission electron microscope (TEM) is routinely used to study the nanoscale structure of many types of materials. The high energy electron beam can impart some or all of its energy to the sample which can be useful for analysis (for example in electron energy loss spectroscopy) or not (when unwanted beam damage occurs). Throughout this thesis, the electron beam was used to initiate chemical transformations which was followed *in-situ* using imaging, diffraction, and spectroscopy. Electron-transparent, nanometre-thick materials are the ideal samples for studying beam-induced chemical transformations because heating and charging effects are minimised. Individual molecules of perchlorocoronene (PCC), a polycyclic aromatic hydrocarbon (PAH), were imaged over time by encapsulating them inside single-walled carbon nanotubes (SWNTs). These image series were used to study the kinetics of the beam-induced polymerisation of PCC inside SWNTs. *In-situ* heating and cryogenic experiments allowed us to study the effects of temperature on these PCC polymerisations. Nanoscale crystals of hexaazatrinaphthylenes (HATs), another type of PAH, were irradiated under constant electron flux (electrons nm^{-2} s^{-1}) in order to understand their stabilities and reactivities. HATs can be building blocks for organic frameworks and the electron beam can be used to crosslink aromatic molecules in electron beam lithography (EBL). Understanding HAT reactivity under the electron beam and combining this with EBL could

lead to a straightforward method of synthesising HAT-derived organic frameworks in bulk. The product of irradiating the endohedral fullerene HF@C_{60} was investigated using imaging, diffraction, and spectroscopy in the TEM. It is likely that a trapped radical, F@C_{60}, is generated under irradiation. Developing a new method of processing the TEM sample allowed us to analyse the specific irradiated area using another technique: optically detected magnetic resonance (ODMR). This technique can be used to detect radicals using fluorescence and is capable of nanoscale resolution through use of nitrogen vacancies in nanodiamonds (which exhibit ODMR behaviour). TEM and ODMR together may be useful for characterisation and analysis of many different materials.

Acknowledgements

"Don't Panic." - Douglas Adams, The Hitchhiker's Guide to the Galaxy (1978)

I am eternally grateful to my mum for her unconditional love and support (as well as her stubborn refusal to conform to cultural expectations of women). When I stumbled upon the path towards electron microscopy (the terrible eyesight came before the PhD), my supervisor Andrei Khlobystov patiently guided me throughout my research and gave me many opportunities to expand my experiences. Mike Fay taught me everything I know about electron microscopy and suffered my incessant bothering with grace for which I am thankful for. Steve Skowron gave me so much advice and feedback on the kinetics studies in this thesis, as well as general comments on many other topics. Much of the work in this thesis was carried out with the two MSci students I supervised: Ruth Hayter and Ben Weare, both of whom are extremely talented and hardworking humans. The microscopy data was obtained at various facilities: the Nanoscale and Microscale Research Centre at the University of Nottingham (nmRC), the electron Physical Science Imaging Centre at Diamond Light Source (ePSIC), and SuperSTEM at the SciTech Daresbury Science and Innovation Campus. The staff at these facilities were instrumental in assisting data collection and their experience and knowledge proved invaluable to me. Finally, the Nottingham Nanocarbon Group has been a wonderful part of my life. Every time I needed help during my PhD, someone from the group was there for me. Thank you.

Table of Abbreviations and Symbols

@	[...] encapsulated within [...]
AC-HRTEM	Abberation corrected high resolution transmission electron microscropy/microscope
C_s	Spherical abberation correction
C_c	Chromatic abberation correction
CNM	Carbon nanomembrane
COF	Covalent organic framework
CTF	Contrast transfer function
CuPc	Copper(II) phthalocyanine
Cl_{16}-CuPc	Hexadecachloro-copper(II) phthalocyanine
DWNTs	Double-walled carbon nanotubes
EBL	Electron beam lithography
EDXS	Energy dispersive X-ray spectroscopy
EELS	Electron energy loss spectroscopy
EPR	Electron paramagnetic resonance (spectroscopy)
FEG	Field-emission gun
FT	Fourier transform
FWHM	Full-width half-maximum
GNR	Graphene nanoribbon

HAADF-STEM	High-angle annular-dark field scanning transmission electron microscropy/microscope
HAT	Hexaazatrinaphthylene
HOMO	Highest occupied molecular orbital
HRTEM	High resolution transmission electron microscropy/microscope
LUMO	Lowest occupied molecular orbital
MALDI-ToF MS	Matrix-assisted laser desorption/ionisation – time of flight mass spectrometry
MOF	Metal organic framework
ND	Nanodiamond
NMR	Nuclear magnetic resonance (spectroscopy)
NV	Nitrogen vacancy
ODMR	Optically detected magnetic resonance
OTC	Octathio[8]circulene
PAH	Polycyclic aromatic hydrocarbons
PCC	Perchlorocoronene
PL	Photoluminescence
SAD	Selected area diffraction
SAM	Self-assembled monolayer
SCXRD	Single crystal X-ray diffraction
STEM	Scanning transmission electron microscropy/microscope
SWNTs	Single-walled carbon nanotubes
TEM	Transmission electron microscopy/microscope
TTC	Tetrathiotetraseleno[8]circulene
UV	Ultraviolet

Vib-EELS	Vibrational electron energy loss spectroscopy
XRD	X-ray diffraction
ZLP	Zero loss peak

Contents

CHAPTER 1

Chemical transformations in the TEM

1.1 The transmission electron microscope

The first transmission electron microscope (TEM) was built by Knoll and Ruska in the early 1930s[1] in order to overcome the diffraction limit of optical microscopes. The relativistic wavelength of an electron λ in nm is related to its kinetic energy eV in electron volts as shown in Eq. 1.1.

$$\lambda = \frac{h}{[2m_0eV(1+\frac{eV}{2m_0c^2})]^{1/2}}$$

Equation 1.1. An electron's wavelength λ is related to its kinetic energy eV where h is the Planck constant (6.6×10^{-34} J.s), m_0 is the mass of the electron (9.109×10^{-31} kg), e is the elementary charge (1.602×10^{-19} C), V is the electric potential that the electrons are accelerated to, and c is the speed of light (2.998×10^{8} m/s).

The higher the energy of the electron, the shorter the wavelength. For example, an 80 keV electron has a wavelength of ~0.0043 nm. Theoretically, it should be possible to resolve detail much smaller than an atom using a TEM. However, this theoretical limit[2] has not yet been reached because we cannot make perfect electron lenses and as a result, aberrations are present in the resulting image.

1.1.1 The instrument

The TEM is routinely used for structural characterisation and, in more recent decades, as a laboratory with a finely controlled internal environment. We shall see in later discussions of the literature that researchers across the world have employed the electron beam of a TEM to study dynamic processes in real time. The electron beam can not only resolve nanoscopic details, it can also be used as a source of energy to initiate transformations. The TEM was the main instrument used throughout this thesis and so we shall first discuss how the microscope operates (Fig. 1.1) in order to explain why the TEM is crucial in all of our studies. Almost all of the information in this section has been drawn from the excellent book "Transmission Electron Microscopy" by Williams and Carter.[3]

There are two main electron sources or guns in use; thermionic and field-emission. A thermionic source produces electrons when heated while a field-emission source produces electrons when a strong electric field is applied across it. When a material is heated to a temperature where the thermal energy is above the work function of electron emission, an electron beam can be formed from the thermionic source. Field-emission sources work based on the principle that the electric field is much higher at sharp points. A strong electric field lowers the work function barrier to the point where electrons can tunnel out, producing an electron beam. When used at ambient temperatures, this is known as "cold field emission". If the source is heated, the work function is lowered further and electrons no longer need to tunnel out. This is known as "thermal field emission".

The brightness, or the emitted current density, is defined by Eq. 1.2 and shows that brightness β is related to the diameter d_0 of the electron source that gives off a cathode emission current i_e. There is an angular distribution of electrons where they diverge from the source with a semiangle α_0 which also affects the brightness.

$$\beta = \frac{i_e}{\pi(\frac{d_0}{2})^2 \pi(\alpha_0)^2} = \frac{4i_e}{(\pi d_0 \alpha_0)^2}$$

Equation 1.2. The brightness β of an electron source is related to its cathode emission current i_e and its diameter d_0. α_0 is the divergence semiangle of electrons emitted from the source.

The temporal coherence of an electron gun arises from the wavelength distribution of the beam of electrons. The coherence length λ_c is defined by Eq. 1.3 and is related to the electron velocity ν and the energy spread of the beam ΔE (typically in the range of 0.1 to 3 eV). To achieve as monochromatic a beam as possible, the high-voltage supply (or high tension as it is otherwise known) must be stable in order to give a small ΔE. Thermionic sources have a slightly larger energy spread than field-emission sources.

$$\lambda_c = \frac{\nu h}{\Delta E}$$

Equation 1.3. The coherence length λ_c is related to the electron velocity ν and the energy spread of the beam ΔE. h is Planck's constant.

The spatial coherence of an electron gun is related to the size of the electron source. Because electron sources are at least a few nanometres in size, electrons emitted from the source do not all come from the same point. Smaller source sizes give better spatial coherence and therefore spatial resolution which is important for high resolution imaging and high contrast diffraction. The effective source size d_c for coherent illumination is much smaller than the electron wavelength λ divided by the angle subtended by the source at the sample α (Eq. 1.4). Field-emission sources have higher spatial coherence than thermionic sources.

Finally, the stability of the electron current emitted by the source is also an important characteristic. Thermionic sources tend to be very stable while cold field-emission sources require electrical feedback circuits to maintain stability. The take-home message is that the smaller the source size, the better the brightness and spatial coherency, but the lower the stability. Therefore, all types of electron sources

$$d_c << \frac{\lambda}{2\alpha}$$

Equation 1.4. The effective source size d_c for coherent illumination is much smaller than the electron wavelength λ divided by the angle subtended by the source at the sample α. This angle can be decreased by inserting a limiting aperture; otherwise the smaller the source size, the smaller the angle α. Spatial coherence can also be increased by reducing the accelerating voltage, thus increasing λ.

are useful in some way or another. Both types of electron sources were used for the studies in this thesis.

1.1.2 Imaging in the TEM

Beam formation comes about through the use of multiple magnetic lenses. Imperfections in these lenses create a number of abberations which can reduce the practical resolution. Axial abberations such as astigmatism and spherical abberations are series of aberrations increasing in radial and azimuthal degrees of symmetry. Principally, axial abberations are caused by a non-uniform magnetic field due to asymmetry of the cylindrical hole or bore through the magnetic lens. Spherical aberration is caused by the magnetic field acting more strongly on electrons that are further off axis i.e. electrons that deviate significantly from the center of the lens. This causes those electrons to be bent more strongly back towards the axis which gives rise to a spherical aberration disk. Chromatic aberration comes from non-monochromatic electrons which are likely to occur after the electrons have passed through a sample, resulting in a range of different energies. The objective lens below the sample (see Fig. 1.1) will bend lower energy electrons more strongly, again creating an aberration disk. A thinner sample reduces the effect of chromatic aberration. Two-fold astigmatism is a significant contribution to abberations in images and is commonly corrected for during the microscope alignment procedure. Both spherical and chromatic aberrations (C_s and C_c respectively) can be corrected for using additional sets of lenses. C_s correctors also affect axial abberations.

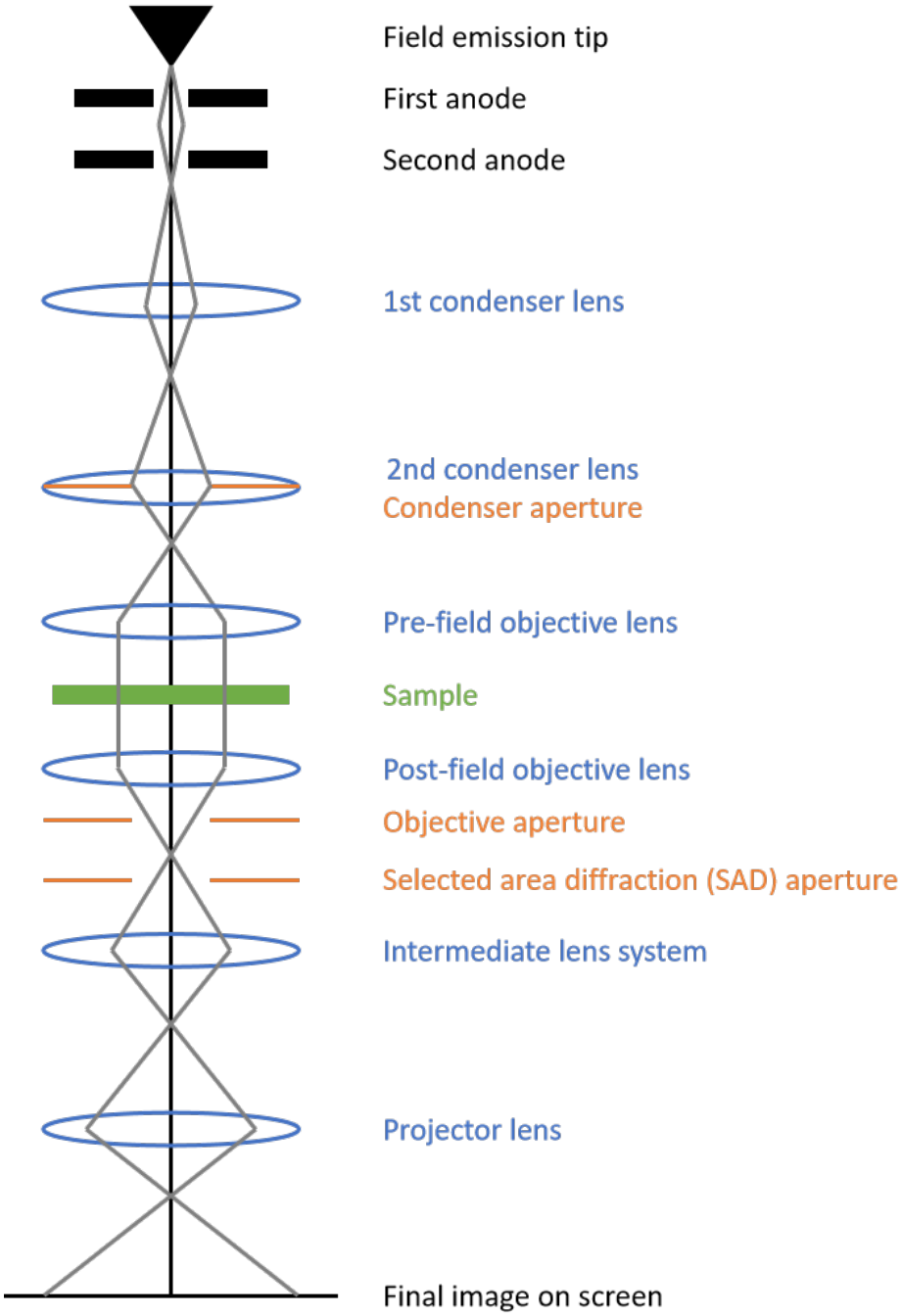

Figure 1.1. A ray diagram of a field-emission gun (FEG) TEM. An initial anode applies the electric field to extract electrons out from the source which is then accelerated by a second anode. A series of magnetic lenses illuminate the sample and form the final image on the viewing screen or camera.

A modern aberration-corrected TEM[3–6] is capable of sub-Ångström resolution and when the "stars" are aligned (the "stars" being the magnetic lenses, the environment of the microscopy room, the quality of the sample, the mental state of the microscopist, the amount of caffeine available...) it becomes possible to resolve individual atoms. When molecules are supported by atomically-thin, electron-transparent substrates such as graphene or single-walled carbon nanotubes (SWNTs), each molecule can be observed separately with atomic resolution which allows us to follow the dynamics of that system on the single-molecule level. Such dynamics can be induced thermally as well as through energy transfer from the high energy electron beam and provides the opportunity to study fundamental aspects of chemistry in direct-space and real-time.

This leads us onto the images themselves which form due to electron scattering. At this point, we should explain how we have defined the types of electron scattering: elastic and inelastic. These definitions are from Williams and Carter.[3] Use of terminology within the field of TEM can vary and it is important to be precise with what a word means in context. Both types of scattering can occur from interactions between the incident electron beam and the nuclei or electron cloud of the sample. The difference between the two types of scattering is that *elastically* scattered electrons lose negligible kinetic energy (and are often treated mathematically as waves) while *inelastically* scattered electrons lose a significant amount of their kinetic energy (and are often treated mathematically as particles). Images have contrast which is defined here as the difference in intensity between two adjacent areas. Contrast comes from the *elastic* scattering of the incident electron wave by the sample which can change both the wave's amplitude and phase. There are two kinds of amplitude contrast in conventional TEM imaging: mass-thickness contrast and diffraction contrast. Mass-thickness contrast arises from the sample material and its thickness. Any variation in atomic number Z or sample thickness

will produce a variation in contrast. Thicker or higher-Z areas of the sample will scatter more electrons off axis than thinner or lower-Z areas. Use of an aperture to exclude highly scattered electrons results in greater contrast in the image where fewer electrons from thicker or higher-Z areas fall on the image plane and therefore appear darker (Fig. 1.2). Diffraction contrast occurs when an incident beam is scattered at specific Bragg angles in a crystalline sample. The sample is tilted, often multiple times, to select for one strongly diffracted beam. The set of images can then be used to give complementary information on the sample.

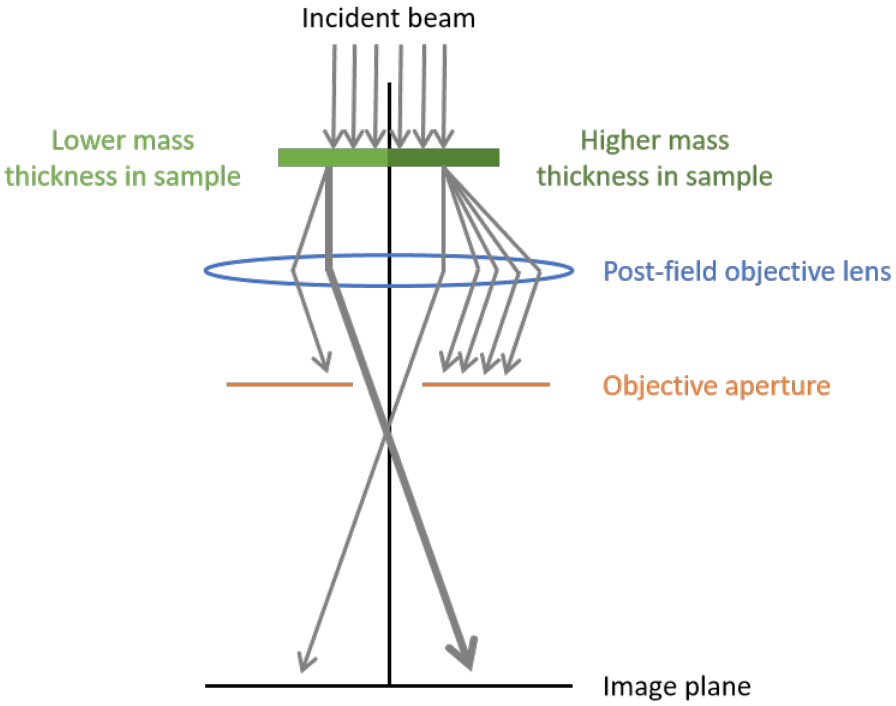

Figure 1.2. Ray diagram showing how mass-thickness contrast arises. Areas of the sample that are thicker or contain heavier elements will scatter electrons more off axis than areas that are thinner or contain lighter elements. Inserting a post-field objective lens excludes highly scattered electrons which results in a greater image contrast. Reprinted (adapted) with permission from D. B. Williams and C. B. Carter, *Transmission Electron Microscopy, A Textbook for Materials Science*, Springer US, 2nd Edition, 2009, ch. 22, p. 374. Copyright (2009) Springer Nature.[3]

Phase contrast is a result of changes in phase as electron waves are scattered through a sample. This type of contrast can give atomic resolution in high resolution TEM (HRTEM) images. The purpose of HRTEM is to increase the useful detail in the resultant image, thus giving more information on the structural characteristics of the sample. Due to imperfect magnetic lenses, when we illuminate a sample with an electron beam a point in the sample becomes transformed into a disk in the image. This transformation is known as the point-spread function. Using an audio track as an analogy (an extremely useful explanation from Williams and Carter[3]), if we want to hear the high frequencies (i.e. high notes) at various amplitudes (i.e. various volumes) in a song, we need high frequency which is related to $1/t$ where t is time. Likewise, if we wish to resolve small distances x in our sample, we need high spatial frequency which is related to $1/x$. Transferring information (or contrast) in the sample from reciprocal space to real space in the image is known as the contrast transfer function (CTF). A very thin sample can be simplified and thought of as a 'phase object' where the amplitude of an electron wave function transmitted through is linearly related to the projected potential of the sample (the potential that the electron wave 'sees' when it passes through the sample). This is the CTF; if negative, this results in positive phase contrast giving dark atoms against a bright background. A positive contrast transfer function results in the opposite; bright atoms against a dark background. The maths describing all this is beyond the scope of this thesis but the brief description above is important to bear in mind when carrying out HRTEM.[7–9]

1.1.3 Diffraction in the TEM

Electron diffraction is often used to study crystal morphology, boundaries, and defects on the nanoscale. A beam of electrons passing through a crystalline sample may diffract, often multiple times, through the sample. Electron beam diffraction has many of the same principles as X-ray diffraction (XRD) with some key differences. Electrons are able to interact with both the nucleus as well as the electrons of the scattering atoms. Electron beams also have much shorter wavelengths than X-rays so diffraction of crystals too small for XRD is possible. For the equivalent amount of radiation damage, much more information is gained using electrons than X-rays.[10]

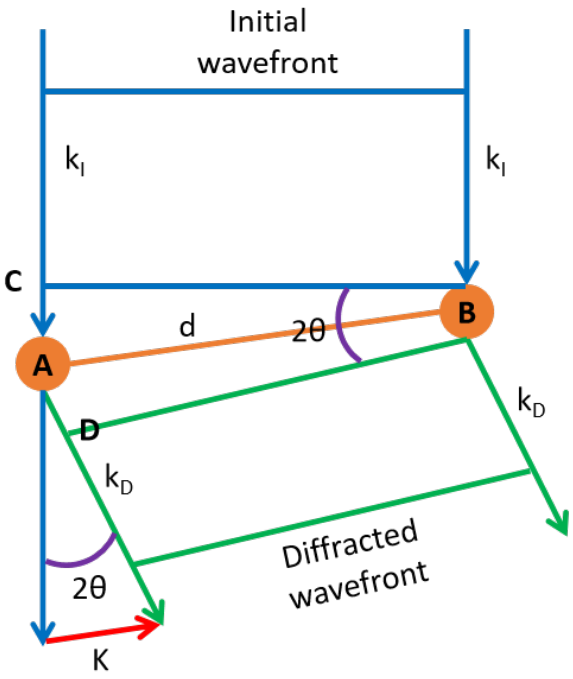

Figure 1.3. A simplified diagram describing the scattering from two atoms. An initial wavefront consisting of two rays scatter off two points, A and B, to give the diffracted wavefront. At Bragg angles of θ_B, the path difference of $CA + AD$ is $n\lambda$ where n is any integer. Since $CA + AD = 2dsin\theta$, $n\lambda = 2dsin\theta_B$, which is Bragg's law. Reprinted (adapted) with permission from D. B. Williams and C. B. Carter, *Transmission Electron Microscopy, A Textbook for Materials Science*, Springer US, 2nd Edition, 2009, ch. 11, p. 200. Copyright (2009) Springer Nature.[3]

If we consider an incident wavefront scattering off two planes of atoms indicated by the circles labelled A and B in Fig. 1.3, the waves have wave-vectors k_I and k_D for the incident and diffracted wavefronts respectively. The angle between k_I and k_D is 2θ and the difference vector is K. This difference vector is the change in the k-vector due to diffraction. $sin\theta$ is therefore $K/2k_I$ or $|K| = 2sin\theta/\lambda$ since the k-vectors are reciprocal-lattice vectors with units of nm^{-1} and therefore $|k| = 1/\lambda$. The ray on the left in Fig. 1.3 travels further from point C to point D; this extra path distance is $CA + AD$ and therefore $CA + AD = 2dsin\theta$. The angle θ does not necessarily have to be a Bragg angle. When θ is a Bragg angle i.e. θ_B, the path difference of $CA + AD$ is $n\lambda$ where n is any integer. Therefore $n\lambda = 2dsin\theta_B$ which is a familiar equation to many researchers. At Bragg angles, the difference vector of K is given a special value of g, also known as the diffraction vector. In reality, a crystal will have a set of planes with a distance of d/n which the electron beam will diffract from both constructively and destructively.

Using a spread beam of nearly parallel electrons to form a diffraction pattern is known as selected area diffraction (SAD) and was the diffraction mode used throughout this thesis. The intermediate lens system (see Fig. 1.1) can select for either the image plane (resulting in imaging mode; see Fig. 1.4a) or the back focal plane (resulting in diffraction mode; see Fig. 1.4b). A SAD pattern contains sharp spots which can be associated with the diffraction vectors g where g is the difference vector between the incident beam and the diffracted beam. Most diffraction in a TEM is of small volumes e.g. nanoparticles so the diffraction spots will not be mathematical points since the samples are not perfect and infinite in all directions. Indeed, many samples are studied using a TEM in order to understand any defects and imperfections (which may be important for the overall function of the material).

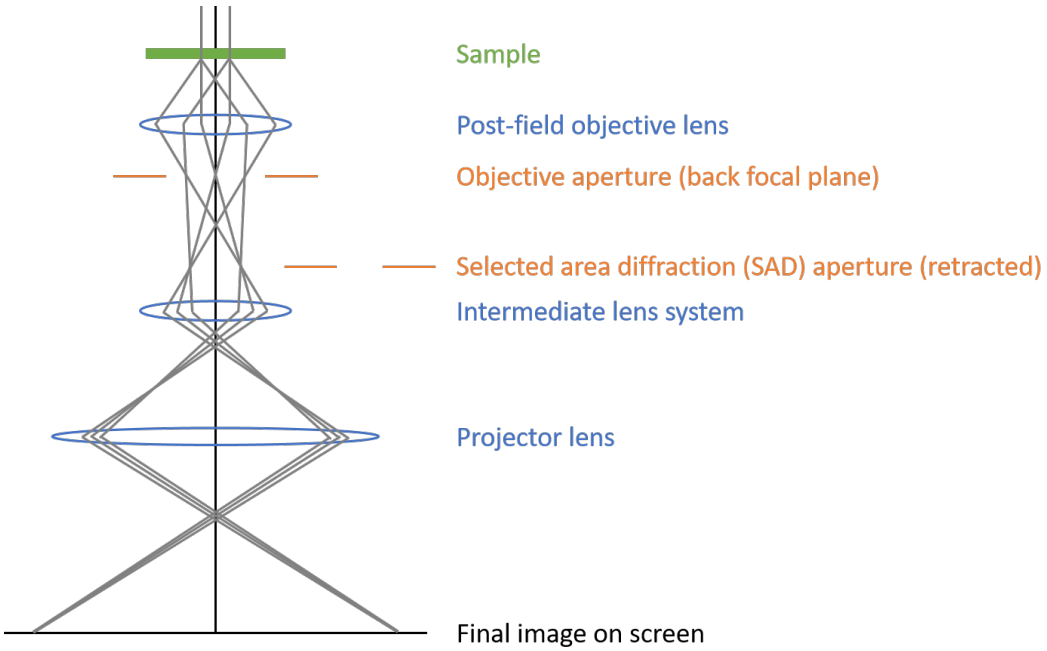

(a)

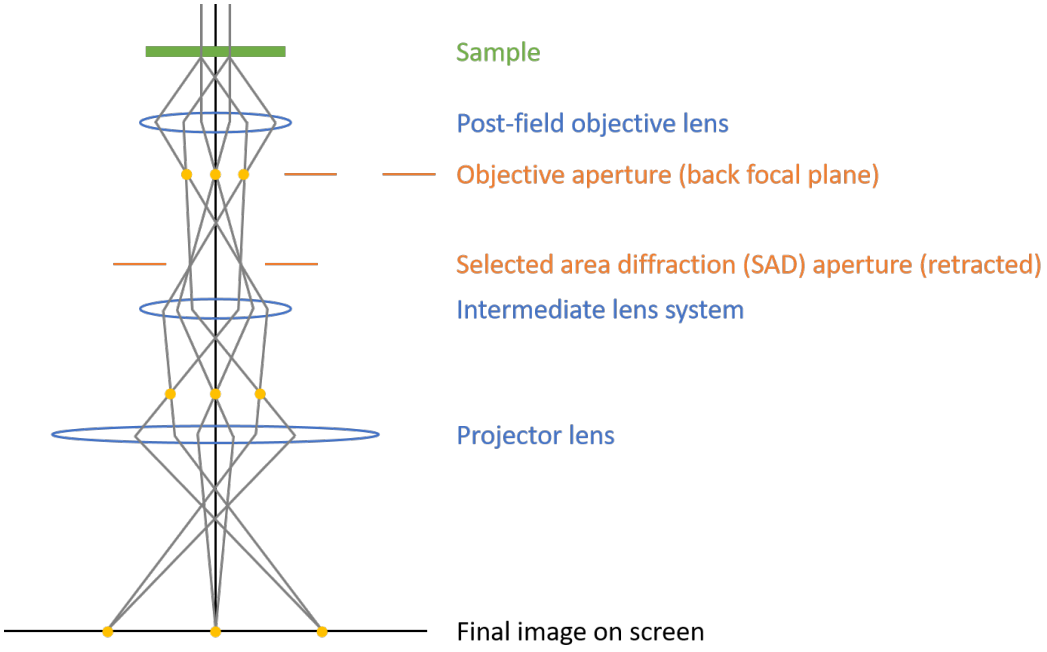

(b)

Figure 1.4. Ray diagrams showing (a) the imaging mode of a TEM where the image is projected onto the screen and (b) the diffraction mode of a TEM where the diffraction pattern is projected onto the screen. Reprinted (adapted) with permission from D. B. Williams and C. B. Carter, *Transmission Electron Microscopy, A Textbook for Materials Science*, Springer US, 2nd Edition, 2009, ch. 9, p. 153. Copyright (2009) Springer Nature.[3]

Both imaging and diffraction use *elastically* scattered electrons, whether with the nucleus or the electron cloud through Coulomb forces, to give contrast. Describing electron scattering accurately requires consideration of the wave-particle duality of electrons. However, that requires diving deep into wave mechanics and relativity which we will not be doing here. In terms of interpreting images, we need to understand, at least simplistically, how an electron might be scattered. Rutherford derived the differential electron cross section for scattering from the nucleus (Eq. 1.5) following the famous experiment involving the backscattering of α particles from a thin metal foil.

$$\sigma_R(\theta) = \frac{e^4 Z^2}{16(4\pi\eta_0 E_0)^2} \frac{d\Omega}{sin^4 \frac{\Omega}{2}}$$

Equation 1.5. The Rutherford electron scattering cross section equation where $\sigma_R(\theta)$ is the scattering cross section with angle θ, Z is the atomic number, η_0 is the permittivity of free space (the dielectric constant), E_0 is the electron energy in eV, and Ω is the total solid angle of scattering.

$$|f(\theta)|^2 = \frac{d\sigma(\theta)}{d\Omega}$$

Equation 1.6. The amplitude of a scattered electron wave $f(\theta)$ from an isolated atom is inversely related to the scattering angle θ. This amplitude is related to the scattering cross section $\sigma(\theta)$ as well as the differential scattering cross section $\frac{d\sigma(\theta)}{d\Omega}$.

However, in order to calculate the scattering cross section, the wave nature of the electrons must be accounted for. The atomic scattering factor $f(\theta)$ is part of the wave approach to cross sections and is related to the differential cross section in Eq. 1.6. When an electron is scattered through an angle of θ (Fig. 1.5), $f(\theta)$ is the amplitude of that scattered electron wave which varies inversely with θ. This becomes important when understanding the origin of contrast and subsequent interpretation of images and diffraction patterns for structural analysis.

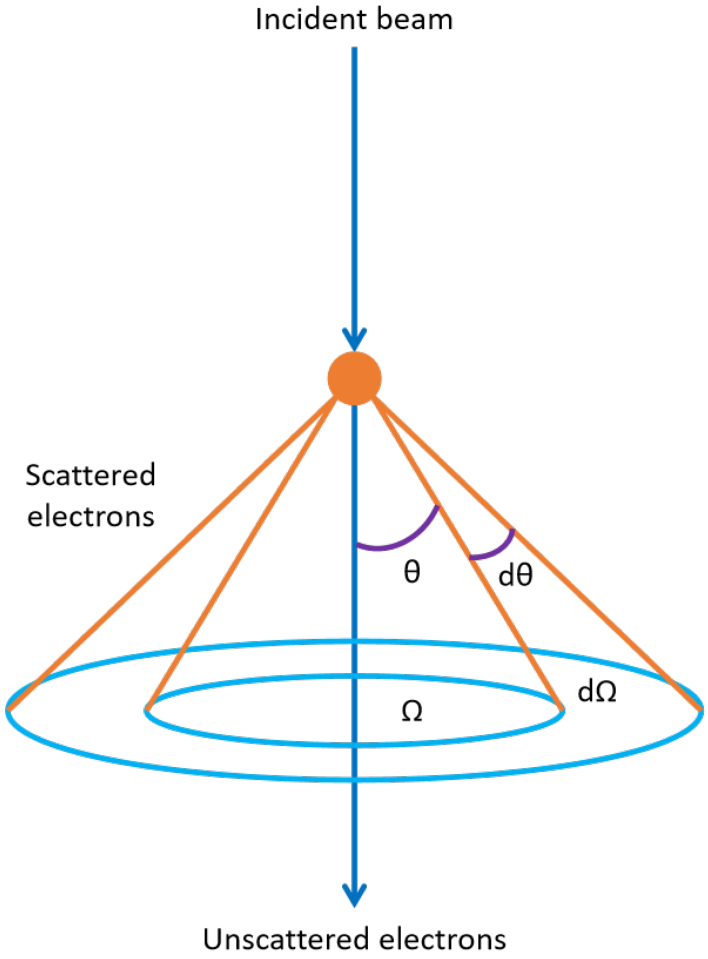

Figure 1.5. When an electron is scattered from an isolated atom through an angle of θ and a total solid angle of Ω, an increase in the scattering angle $d\theta$ gives an increase in the solid angle $d\Omega$. This allows us to calculate the differential scattering cross section which is related to the amplitude of the scattered electron wave (see Eq. 1.6). Reprinted (adapted) with permission from D. B. Williams and C. B. Carter, *Transmission Electron Microscopy, A Textbook for Materials Science*, Springer US, 2nd Edition, 2009, ch. 2, p. 27. Copyright (2009) Springer Nature.[3]

1.1.4 Spectroscopy in the TEM

A TEM is not only an instrument for imaging and diffraction. Electrons are a form of ionising radiation and therefore can interact with a sample *inelastically* to produce a multitude of secondary signals, many of which are used routinely during sample analysis to give information on characteristics such as chemical composition. We shall discuss briefly the signals that have been studied in this thesis since there are enough beam-sample interactions to (quite literally) fill a textbook.[3] Inelastic scattering may occur with both the nuclei and the electrons of the sample and lose significant amounts of energy. For these types of scattering, the beam electrons are often treated as particles. If the energy transferred from the electron beam to an inner-shell electron is greater than the critical ionization energy, a beam electron may knock out a core electron of an atom. A higher energy electron can drop down to that 'electron hole', releasing a characteristic X-ray in the process which has a specific energy unique to the atom, corresponding to the energy difference between the two electron shells involved. This is the signal collected in energy dispersive X-ray spectroscopy (EDXS). Similarly, after a beam electron has lost energy from knocking out a core electron, this energy loss is measured in electron energy loss spectroscopy (EELS) where the onset of peaks in spectra as well as peak shapes are characteristic of the elements and their environments in the sample.[3] Both of these processes are illustrated in the cartoon in Fig. 1.6.

Transfer of significant amounts of energy from the electron beam to the sample eventually causes damage which can complicate analysis.[11,12] The sample can be heated by phonons (oscillations of atoms in the sample caused by collisions from beam electrons) which are a major source of damage for biological specimens and polymers. There may also be radiolysis where inelastic scattering such as ionization breaks bonds, creating reactive species which can cause further damage. Finally, knock-on damage can occur where incident beam electrons eject atoms

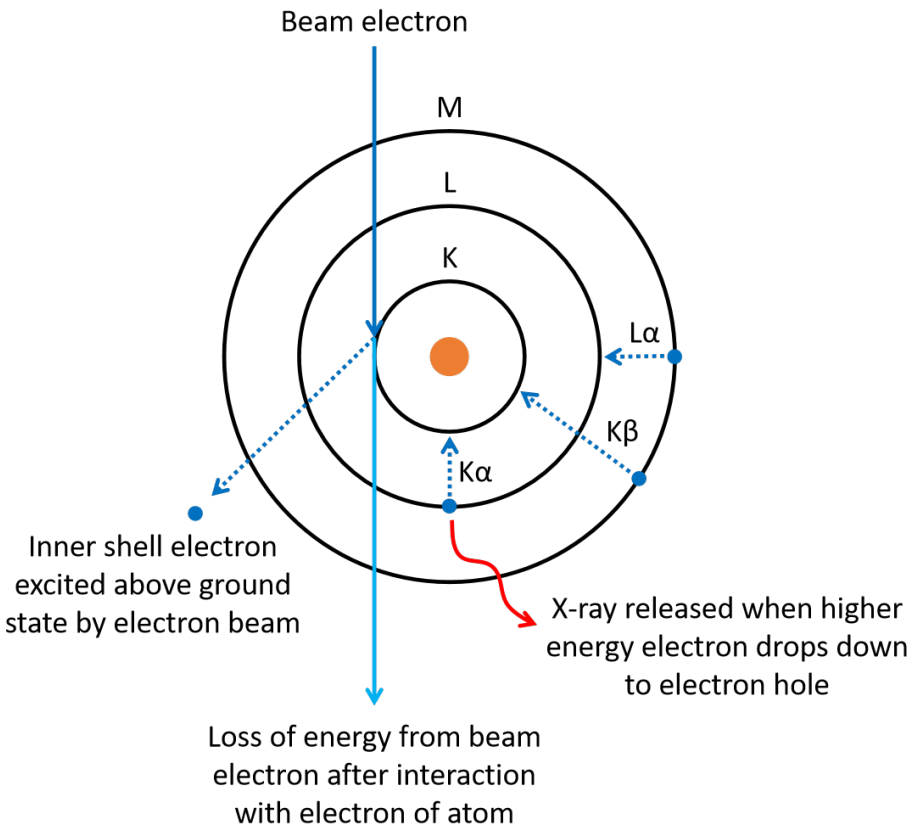

Figure 1.6. Beam electrons may knock out core electrons of atoms from their ground state in the sample, producing an 'electron hole'. Higher energy electrons can lose energy to occupy that electron hole, emitting an X-ray in the process. These X-rays are collected in energy dispersive X-ray spectroscopy (EDXS) and are characteristic of the elements they are emitted from. Peaks in EDXS are assigned to the K, L, M shells and α, β etc. depending on which orbital the higher energy electron originated from. The beam electrons passing through the sample can be collected in electron energy loss spectroscopy (EELS) and the electrons that have lost energy have peak onsets and shapes that give information on the elemental composition of the sample as well as the chemical environments of those elements.

from the sample, again creating defects and reactive species. Cooling the sample or coating it with a conducting metal film may mitigate damage from heating and radiolysis.[13] Knock-on damage is not controlled by any heat transfer so cooling the sample does not stop this type of beam damage. Reducing the accelerating voltage to below the threshold energy for atom ejection can reduce knock-on damage. Alternatively, increasing the accelerating voltage can lower the cross section

for electron-electron interactions, reducing the rate of radiolysis. The predominant type of damage depends on the material and generally speaking, knock-on damage dominates in conducting samples since ionisation damage (radiolysis) is quenched by the high electron density. In insulating samples, ionisation cannot be mitigated, leading to radiolysis damage.[13] Heating and charging are also bigger issues for insulating samples. In practice, beam damage can occur at any set of conditions and many microscopists use low electron flux (total number of electrons hitting an area per unit time) imaging conditions to reduce damage.

1.1.5 Calculating the electron flux

Electron flux in units of number of electrons nm^{-2} s^{-1} can be calculated in one of two ways. A Faraday cup can be inserted into the TEM to measure the current per area which can be converted into the number of electrons hitting that area per unit time. This is then correlated to the pixel count of a TEM micrograph of vacuum i.e. the counts per primary electron (or conversion efficiency) when the electron beam hits the camera without passing through the sample. Alternatively, if a Faraday cup is unavailable, the conversion efficiency can be found in the camera datasheet provided by the manufacturers. Measuring the current per area with a Faraday cup can be more accurate on a day-to-day basis but the information in a datasheet will be a reasonable average for the camera.

Once the conversion efficiency for a specific camera has been found, the electron flux during experiments can then be calculated using the counts from an area of vacuum in micrographs. For samples of carbon nanotubes, this is a straightforward task. Areas of interest will be single nanotubes suspended in vacuum that have little to no overlap with other nanotubes. As a result, there will often be vacuum in micrograph series. The pixel counts of vacuum can be found using software such as Gatan Microscopy Suite 3 (GMS 3; see Fig. 1.7).

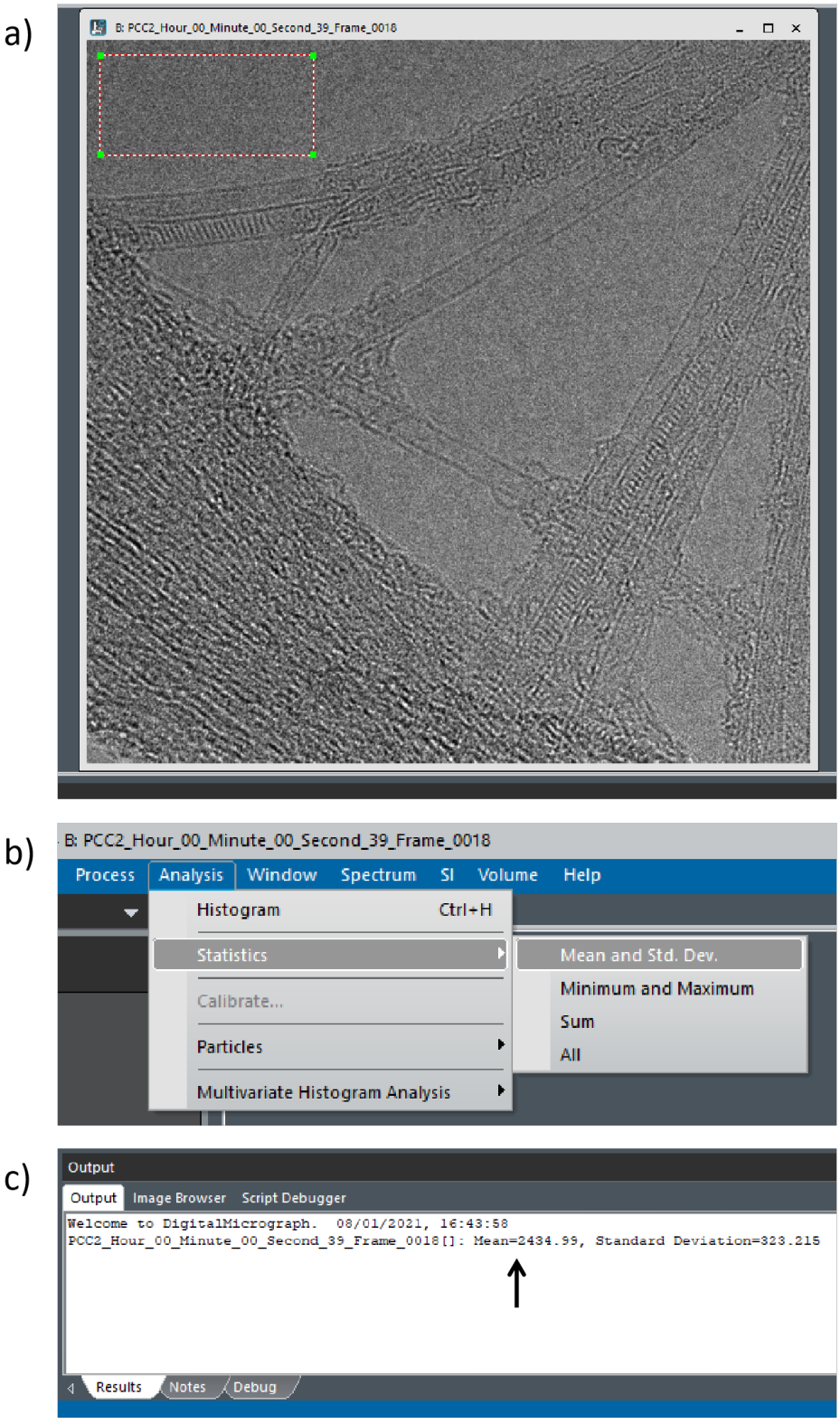

Figure 1.7. Using Gatan Microscopy Suite 3 to find the pixel counts of vacuum in micrographs. a) An area of interest is drawn on vacuum (red box). b) The mean and standard deviation can be found in the menu Analysis > Statistics > Mean and Std Dev. c) The statistics are then displayed in the Output window at the bottom of the screen (the black arrow indicates the mean pixel count).

The pixel count is then used to calculate the incident electron flux on the sample as well as the total electron dose (in e^- nm^{-2}) deposited on the sample over the duration of the experiment. An example calculation is shown in Fig. 1.8. Calculating the average electron flux of the experiment as well as correlating total dose with each micrograph in the image series is important for understanding the progress of the reaction(s). It may also be useful to the user to include columns in the spreadsheet for values such as "number of molecules present in the nanotube" to track the reaction or "comments on each micrograph" to make notes for future reference.

	A	B	C	D	E	F	G
1	Frame (m.s.ms)	Mean bkg count	Electrons per pixel	Electrons per area (e^- nm^{-2})	Capture time (s)	Total time after each image (s)	Electrons per area per second (e^- nm^{-2} s^{-1})
2	00.00.20.00	2688.070	Pixel count/conversion efficiency	Electrons per pixel/area of pixel	Capture time of the micrograph	20	Electrons per area/capture time
3					Electron flux (e^- nm^{-2} s^{-1})		Average of all calculations of e^- nm^{-2} s^{-1}
4					Δt (s)		Total time of experiment
5					Total electron dose (e^- nm^{-2})		Electron flux/total time

Figure 1.8. An example spreadsheet for calculating electron flux and dose. The cells shaded green indicate values that should be inputted by the user. These include the time of the frame (A2) in minutes.seconds.milliseconds or whatever unit of time is appropriate; the mean background count (B2) that was found using software such as GMS 3 (see Fig. 1.7); the capture time of each frame (E2) which is related to the frames per second of the camera; and the total time after each image (F2) which is necessary for tracking the experiment progress. Non-shaded cells can have formulas to calculate the electron flux per frame (G2), the average electron flux over the duration of the experiment (G3), and the total electron dose experienced by the sample during the experiment (G5).

1.1.6 Beam-induced transformations

Beam damage in the TEM can be thought of in a different way; as in-situ transformations which we can study. If the sample is a layer of molecules supported by a conductive substrate such as graphene or carbon nanotube, damage via heating and charging can be reduced. A thin, conductive sample may also have reduced incidences of radiolysis since the scattering cross section for electron-electron interactions is reduced. Radiolysis, as we have seen earlier, may be mitigated by the high electron density in a conducting sample. Therefore, transformations in these samples can be dominated by direct knock-on from an incident electron colliding with the nuclei of atoms in the sample. We can think of these reactions initiated by the electron beam in analogy to those initiated by temperature.

When modelling electron collisions with atoms, the differential scattering cross section is calculated according to the McKinley-Feshbach formula in Eq. 1.7.

$$\sigma(\theta) = \sigma_R[1 - \beta^2 sin^2\frac{\theta}{2} + \pi\frac{Ze^2}{hc}\beta sin\frac{\theta}{2}(1 - sin\frac{\theta}{2})]$$

Equation 1.7. σ_R is the classical Rutherford scattering cross section, $\beta = V_e/c$ is the ratio of electron velocity V_e to the speed of light c, Z is the nuclear charge, e is the electron charge, h is the Planck constant, and θ is the electron scattering angle.

The maximum transferred energy T_{max} for elastic collisions is shown in Eq. 1.8 where the angular dependence of the transferred energy in Eq. 1.9 shows that T_{max} corresponds to a scattering angle $\theta = \pi$.

$$T_{max} = \frac{2ME(E+2m_ec^2)}{(M+m_e)^2c^2+2ME}$$

Equation 1.8. The maximum transferred energy T_{max} via knock-on damage from an incident electron to a nucleus of an atom is inversely proportional to the atomic weight M. E is the energy of the incident electron, m_e is the mass of the electron, and c is the speed of light.

For electron beam-induced transformations to take place, the energy transfer E_T must exceed some threshold energy E_d for the transformation i.e. $E_T > E_d$. A

$$T(\theta) = T_{max} sin^2(\frac{\theta}{2})$$

Equation 1.9. The angular dependence of the transferred energy from a beam electron to a static atom.

simple situation would be atom emission where the displacement threshold energy is the minimum kinetic energy required to knock out the atom so that it does not immediately recombine. Integrating Eq.1.7 where $E_T > E_d$ gives Eq. 1.10 which describes the cross section of atom ejection σ_d.

$$\sigma_d = 4\pi(\frac{Ze^2}{2m_e c^2})^2 \frac{1-\beta^2}{\beta^4}\{\frac{T_{max}}{E_d} - 1 - \beta^2 ln(\frac{T_{max}}{E_d}) + \pi\frac{Ze^2}{hc}\beta[2(\frac{T_{max}}{E_d})^{1/2} - ln(\frac{T_{max}}{E_d}) - 2]\}$$

Equation 1.10. The cross section of atom ejection σ_d.

As can be seen in Eq. 1.10, σ_d depends on the kinetic energy of the incident electrons. The optimum accelerating voltage for imaging graphitic materials is 80 kV as this is where σ_d for carbon approaches zero but at and below 80 kV, lighter elements such as hydrogen are removed rapidly due to the significantly higher σ_d. The origin for this large σ_d for hydrogen is because the maximum transferred energy T_{max} (Eq. 1.8) from an incident electron to the atom is dependent upon both the nuclear charge and the mass of the element. T_{max} is inversely proportional to atomic weight M and therefore significantly more kinetic energy is transferred to lighter elements at all TEM operating voltages.[14]

Chamberlain *et al.* illustrated the beam stability dependence on atomic weight M experimentally by substituting the protium isotope for deuterium in the model molecule coronene ($C_{24}H_{12}$; a polycyclic aromatic hydrocarbon). This substitution doubles the atomic weight of the terminating atoms of coronene without significantly changing the structure or chemistry of the molecule and resulted in an approximately two-fold increase in the stability of the molecule to the electron beam when encapsulated inside single walled carbon nanotubes, SWNTs (Fig. 1.9).[14]

Meyer *et al.* have also used different isotopes, ^{12}C and ^{13}C in single-layer graphene, to carry out quantitative analyses on a "tremendous data set" of electron beam-induced atom ejection. Graphene is a useful model system for studying electron beam damage mechanisms quantitatively. They directly measured the ejection cross-section of carbon by counting the lost atoms as a function of the electron beam energy and applied electron dose. The authors were able to separate knock-on damage from other radiation damage mechanisms such as ionisation by comparing graphene made from those two isotopes of carbon.[15] So far, we have focused on systems containing carbon or organic molecules because these were the systems studied in this thesis. However, it is worth mentioning the work by Algara-Siller *et al.*[16] where graphene was used as a protective coating to reduce the beam sensitivity of monolayer MoS_2. The authors measured the experimental cross-sections and were able to separate the contributions of direct knock-on and electronic excitations from the total damage cross-section.

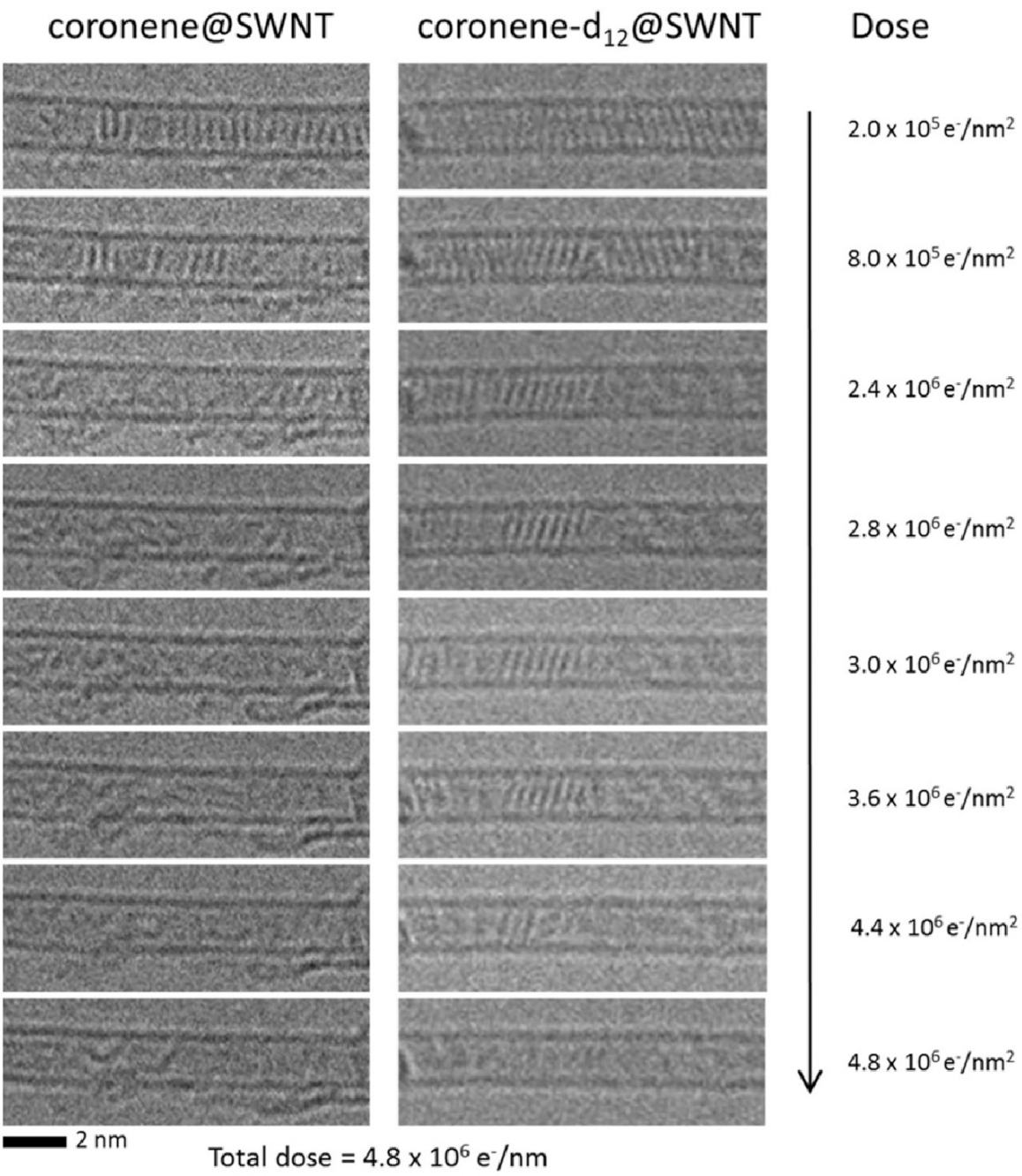

Figure 1.9. Aberration corrected high resolution TEM time series of the decomposition of coronene@SWNT (left) and coronene-d_{12}@SWNT (right) at 80 kV. The total electron dose required to decompose all coronene molecules was 2.8×10^6 e^- nm^{-2} while for coronene-d_{12}, the total dose was 4.8×10^6 e^- nm^{-2}. Reproduced from T. W. Chamberlain *et al.*, *Small*, 2015, **11**, 622-629. Licensed under CC by 4.0.[14]

Skowron *et al.* also studied reactions in graphene, in this case the reaction kinetics of the reversible Stone-Wales bond rotation (Fig. 1.10).[17] The rates and mechanisms of this rotation of a carbon-carbon bond were quantitatively analysed by imaging at the atomic scale under different conditions such as accelerating voltage and electron dose rate, obtaining over 10,000 micrographs. The authors carried out their analysis of irradiation-induced reactions in analogy to thermally-induced reactions and developed a statistical method for measuring and describing the kinetics of irradiation-dependent reactions. Their method is mechanism-agnostic i.e. the maths describing the kinetics does not depend on the electron-atom collision process.

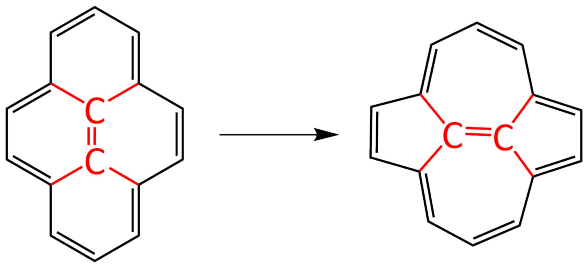

Figure 1.10. A scheme of a Stone-Wales transformation in graphene.[18] The C=C bond between four adjacent six-membered rings rotates by 90° to form two five-membered and two seven-membered rings. This involves breaking of two sigma bonds and formation of new bonds.

For a unimolecular reaction where species A reacts to form one or more products, the rate constant k is described in Eq. 1.11, where $-\frac{d[A]}{dt}$ is the change in the concentration of species A over time t.

$$-\frac{d[A]}{dt} = k[A]$$

Equation 1.11

The reaction rate constant for a thermally-induced reaction k^t can be described using the Arrhenius equation in Eq. 1.12, where P is the pre-exponential factor; the rate of collisions between particles in a gas or liquid, or the rate of bond vibrations in a solid. The exponent is the probability factor; the rate of successful

transformations which can be described as the proportion of particles at temperature T with energy greater than the activation energy E_a.

$$k^t = P.exp(\frac{-E_a}{k_B T})$$

Equation 1.12

For an irradiation-induced reaction, the rate can correspondingly be described in Eq. 1.13, where j is the electron dose rate in nm^{-2} s^{-1} and σ is the reaction cross-section in barn (equivalent to 10^{-10} nm^2).

$$-\frac{d[A]}{dt} = j\sigma[A]$$

Equation 1.13

Therefore, the reaction rate constant for an irradiation-induced reaction k^i can be described in Eq. 1.14, where j is the pre-exponential factor; the rate of collisions between electrons and atoms, and σ is the probability factor; the reaction cross-section which is a measure of a reactive collision between incident electrons and the atomic nuclei.

$$k^i = j\sigma$$

Equation 1.14

Skowron *et al.* were able to determine the experimental σ of the Stone-Wales bond rotation, giving insight into the underlying electron beam-induced mechanism.

1.2 A (very) brief history on the use of TEM to image molecules

1.2.1 Molecules in crystalline forms

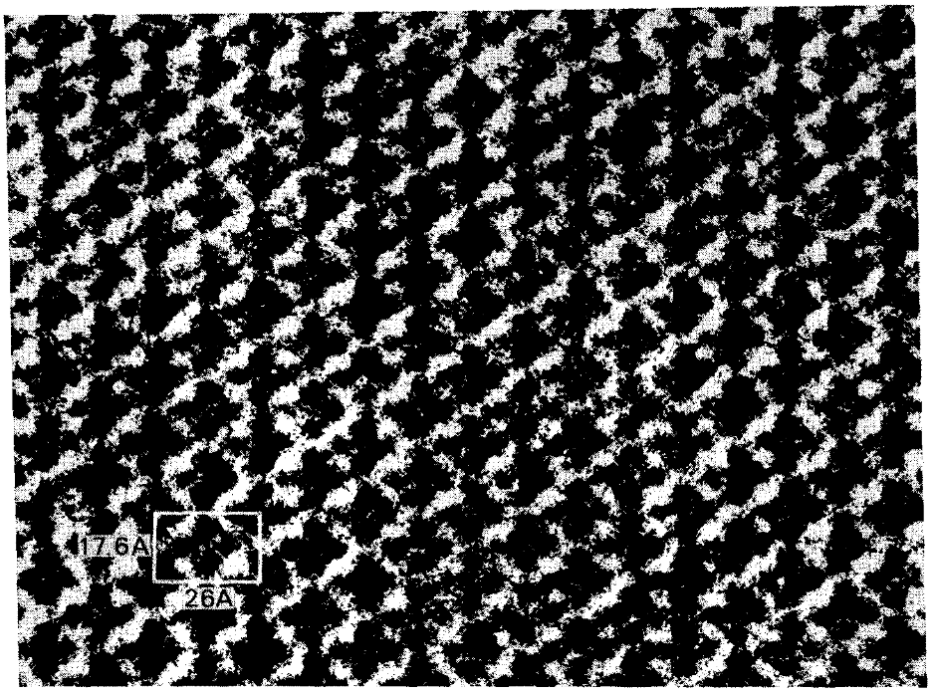

Figure 1.11. A HRTEM image of copper hexadecachloro-phthalocyanine in an epitaxial crystallite with molecular resolution - the first of its kind. The clover-shaped leaf with dimensions of 17.6 Å by 26 Å corresponds to a chlorinated isoindole ring. Reprinted (adapted) with permission from N. Uyeda *et al.*, *J. Appl. Phys.*, 1972, **43**, 5181-5189. Copyright (1972) AIP Publishing.[19]

Having introduced the instrument and the various ways in which the electron beam can interact with the sample, we can now discuss some of the history of imaging molecules using TEM. This huge volume of literature led to the development of equipment and techniques which made the work in this thesis possible. The lattice of copper phthalocyanine was resolved in 1956[20] and only a few decades later in 1972, Uyeda *et al.* achieved molecular resolution of columns of copper hexadecachloro-phthalocyanine molecules (Fig. 1.12) in microcrystals using a TEM (Fig. 1.11).[19]

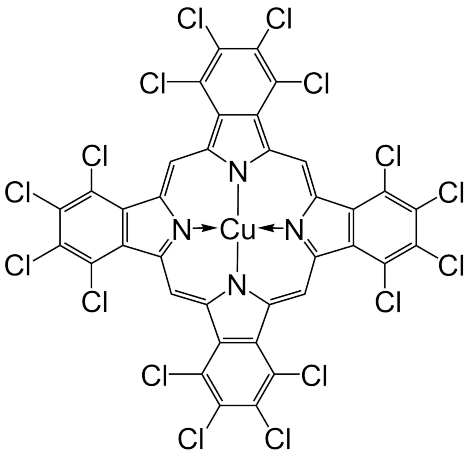

Figure 1.12. The chemical structure of copper hexadecachloro-phthalocyanine.

This molecule was chosen because aromatic species were found to be more stable than their aliphatic counterparts. The substitution of all sixteen hydrogens in copper phthalocyanine with chlorines further improved beam stability of the organic crystals and enhanced image contrast through a larger scattering amplitude of electron waves. The hitherto unknown crystal structure of copper hexadecachloro-phthalocyanine could even be derived from information in the selected area diffraction (SAD) patterns of single microcrystals. While the atomic positions were not resolved, the authors suggested several ways of improving image resolution such as making thinner crystals, increasing the TEM operating voltage, and cooling the sample to suppress thermal vibrations.

Murata *et al.* subsequently carried out a study in 1977 into the kinetics of electron beam damage of copper hexadecachloro-phthalocyanine crystals.[21] There are two main ways of investigating the stability of molecules under the electron beam: with direct-space imaging or diffraction. Using both methods, Murata *et al.* found that these crystals of copper hexadecachloro-phthalocyanine degraded preferentially along certain crystallographic planes, suggesting crystal damage was related to its crystal structure. Loss of Cl atoms is a likely degradation mechanism because the image contrast decreased as the crystal was irradiated. This would produce re-

active species which could cross-link with adjacent molecules, causing further damage and distortion to the lattice along those planes. In 1984, Fryer *et al.* used high resolution TEM imaging to show that addition of encapsulating layers of amorphous carbon reduced the rate of damage of organic crystals. They found that the mechanism of radiation damage seemed similar for many types of organic molecules, ranging from derivatives of the aforementioned copper phthlalocyanine to aromatic and aliphatic hydrocarbons.[22] Fryer *et al.* suggested that peripheral bonds were broken by the electron beam, forming activated species which have a probability of recombining. The rates of bond scission and recombination determined the lifetimes of the organic crystals under electron irradiation. Adding encapsulating layers encouraged bond recombination by limiting diffusion of the emitted fragments in all the organic crystals studied and therefore increased the crystal lifetimes.

Crystals of pharmaceutical molecules in particular have been extensively studied using TEM because there is the potential for much higher resolution of biological samples in an electron microscope than in a light microscope. Localised information at the nanoscale from TEM analysis can also be complementary to bulk techniques such as X-ray diffraction (XRD).[23] However, organic and biological molecules are incredibly beam sensitive and suffer much damage during imaging. As a result, the sample can change drastically, making structural and chemical characterisation challenging. Therefore, if the beam stabilities of these molecules are studied, beam damage can be controlled and minimised. For example, in 2015, crystals of theophylline (a xanthine derivative similar to caffeine) were imaged under conditions where electron dose rate was kept constant and the accelerating voltage, sample temperature, and support film type were varied to see their effects on the electron beam-induced damage.[24] Crystal beam stabilities were compared using the critical dose, the total dose required for the diffraction spots to fade away to e^{-1} of the highest intensity diffraction spot.[25] Cattle *et al.* found that use of graphene film supports

led to an increase in critical dose compared to use of holey carbon (an amorphous type of carbon film), suggesting graphene offered some protection from electron beam damage. Graphene is highly thermally and electrically conductive which prevents heat and charge build up. This likely prolongs the lifetime of the crystals under the electron beam. Cooling the sample as well as using a higher accelerating voltage also increased the critical dose. Cooling the sample again reduces heat build up and thermal motion, both of which contribute to bond breaking, while using a higher accelerating voltage reduces the ionisation cross-section and therefore reduces damage due to radiolysis. This study showed that the major beam damage mechanism for theophylline crystals was radiolysis and provided quantitative information on the best imaging conditions for characterisation of such crystals.

In a similar vein, S'ari *et al.* studied the critical doses of ten different crystalline pharmaceutical compounds to determine whether a particular chemical moiety increased beam sensitivity.[23] They found no discernable trends that could describe the differences in stabilities, including any aromatic rings or halogen groups which can improve beam stability of organic molecules. The authors suggested other factors that might contribute, such as lattice enthalpy, which may improve stability of the overall crystal, and enthalpy of sublimation, which is related to interactions between the molecules in the crystal. This method was improved further in 2018 towards an approach to predict the beam stabilities of pharmaceutical ingredients.[26] The authors developed a model to predict the stabilities of the twenty molecules used in their study with an accuracy of ± 2 e^- $Å^{-2}$. The degree of conjugation, the number of hydrogen bond donors and acceptors, and the number of rotatable bonds were all found to be important for determining beam stability.

1.2.2 Molecules in carbon nanotubes

Similar to the idea of using layers of carbon to protect crystals from beam damage, single walled carbon nanotubes (SWNTs) have been used extensively for their incredible mechanical strength, thermal and electrical conductivity, as well their capacity to hold material in their cavities to form composites.[27] SWNTs are atomically-thin and electron transparent so encapsulated species can be directly observed with high resolution. Molecules encapsulated within SWNTs have a number of unique features that differentiate them from the crystalline forms: i) the confinement limits the degrees of freedom; ii) the electrically and thermally conducting lattice of carbon envelopes each molecule; and iii) the number of nearest neighbours are reduced for each molecule, for example there are twelve neighbours to a molecule in a C_{60} buckminsterfullerene crystal and only two when the fullerenes are encapsulated inside a nanotube.

The first example of a material encapsulated inside SWNTs was achieved by Sloan *et al.* in 1998.[29] The authors filled ruthenium trichloride into SWNTs and heated the sample to form encapsulated ruthenium crystallites inside the SWNTs.[29] Many other encapsulated crystallites have been imaged with atomic resolution since then such as potassium iodide[30,31] and lanthanide halides.[32] In 2001, Brown *et al.* imaged zirconium tetrachloride encapsulated inside SWNTs and discovered a chemical transformation induced by the electron beam (Fig. 1.13).[28] The authors suggested the electron beam knocked out chlorine and formed $ZrCl_x$ of progressively lower stoichiometry, possibly finally forming metallic zirconium clusters. In all of these examples, the researchers discovered unusual crystal structures formed from extreme confinement inside SWNTs.

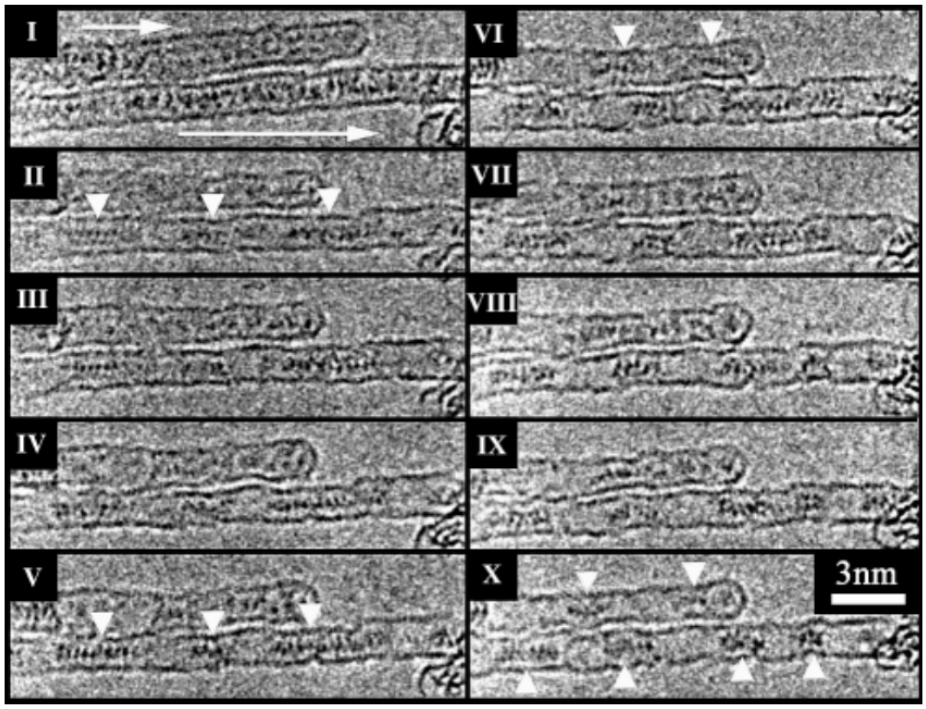

Figure 1.13. TEM imaging showing the *in-situ* clusterisation of zirconium tetrachloride within SWNTs, induced by the electron beam. The large arrows in image I show two continuously filled SWNTs while the small arrows in subsquent images indicate distinct separated clusters. After prolonged imaging, visible damage had occurred to the SWNTs. Reproduced from G. Brown *et al.*, *Chem. Commun.*, 2001, 845-846 with permission from The Royal Society of Chemistry.[28]

Molecules such as C_{60} buckminsterfullerene have also been encapsulated inside carbon nanotubes from 1998 onwards, forming so-called one-dimensional crystals. C_{60}, first synthesised and described by Kroto *et al.* in 1985, was found to spontaneously form during the synthetic and purification steps to make SWNTs.[33–35] These fullerenes self-assembled into chains known as "peapods" within the SWNTs. The authors observed the translation of fullerenes along the nanotube axes as well as the dimerisation and coalescence of these fullerenes into coaxial nanotubes within the original SWNTs.[33,36,37] They suggested such occurrences were due to beam-sample interactions (Fig. 1.14). Smith *et al.* subsequently developed a quantitative nanotube-filling method for fullerenes in 2000 producing C_{60} inside SWNTs (C_{60}@SWNTs).[38]

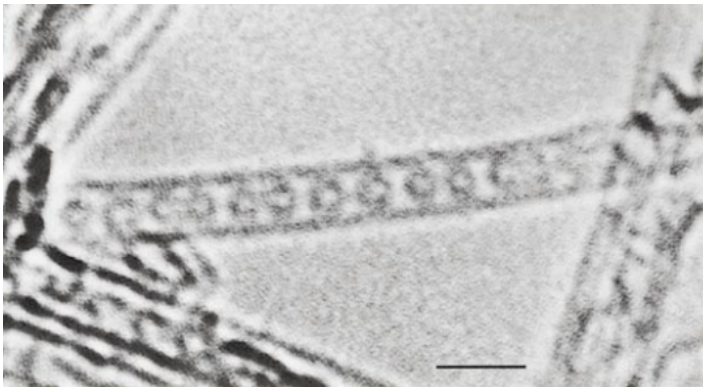

Figure 1.14. A chain of C_{60} fullerenes known as "peapods" encapsulated inside a SWNT. These peapods spontaneously formed during SWNT synthesis and purification. Electron beam-induced fullerene dimerisation can be seen where the circular fullerenes have reacted to form "peanuts". The scale bar is 2 nm. Reprinted (adapted) with permission from B. W. Smith *et al.*, *Nature*, 1998, **396**, 323-324. Copyright (1998) Springer Nature.[33]

Soon after, fullerenes containing metal atoms (endohedral metallofullerenes) such as $[La_2@C_{80}]$[39] and $[Gd@C_{82}]$[40,41] were inserted into SWNTs and individual endohedral atoms could even be directly imaged. Smith *et al.* observed discontinuous tumbling of La atoms and suggested this was due to an electrostatic interaction between the SWNT and the La atoms which would increase the energy barrier for occupying certain endohedral sites, leading to discrete jumps rather than randomised motion (Fig. 1.15).

In 2002, the boron-containing cluster molecule *ortho*-carborane ($C_2H_{12}B_{10}$) was found to pack into peapod-type arrangements inside SWNTs similar to fullerenes.[42] Unusual ordering of molecules due to confinement inside SWNTs was also discovered for a perylene derivative[43] in 2005. The perylene-like molecules arranged themselves one-dimensionally along the SWNTs and upon heat treatment, smaller internal nanotubes templated by the host SWNT were formed. In the same year, cobaltocenes[44] were discovered to only fill into SWNTs with a certain diameter suggesting that the van der Waals interactions between host and guest were important in driving encapsulation. However, not all molecules pack neatly inside SWNTs;

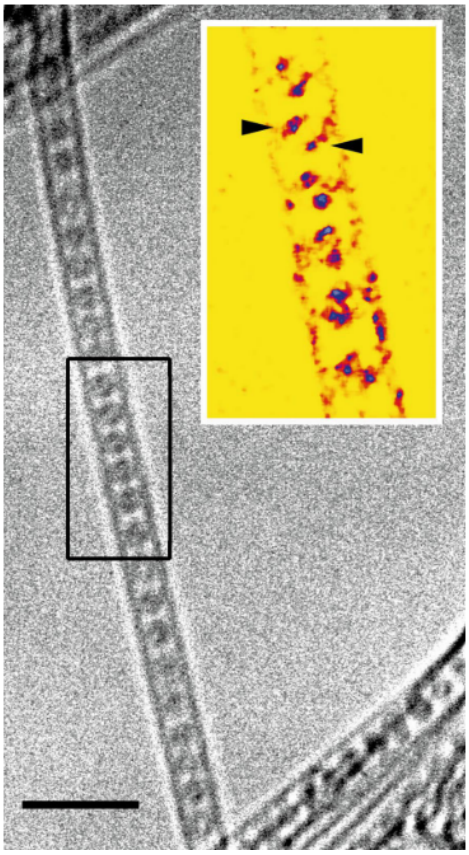

Figure 1.15. A chain of [$La_2@C_{80}$] endohedral fullerenes encapsulated inside a SWNT. The false-colour inset enhances the position of the La atoms. The arrows indicate two opposing La atoms inside a single C_{80} cage. The scale bar is 4 nm. Figure adapted from Smith *et al.* Reprinted (adapted) with permission from B. W. Smith *et al.*, *Chem. Phys. Lett.*, 2000, **331**, 137-142. Copyright (2000) Elsevier.[39]

the cube-shaped octasilasesquioxane ($H_8Si_8O_{12}$) exhibited disordered packing inside nanotubes.[45]

Khlobystov *et al.* discovered that the diameter of the host nanotube directly influenced the packing arrangement of guest fullerenes simply due to geometry effects. C_{60} self-assembled into a zigzag phase (Fig. 1.16 a), a chiral phase (Fig. 1.16 c), or two-molecule layer phases (Fig. 1.16 e) depending on the diameter of nanotube.[46] Likewise, the ellipsoidal fullerene C_{70} self-assembled into two different alignment orientations of packing: transverse (Fig. 1.17, a) or longitudinal (Fig. 1.17, c).[47] To this day, both examples are still used at university open days in order to explain nanoscale architecture to prospective students.

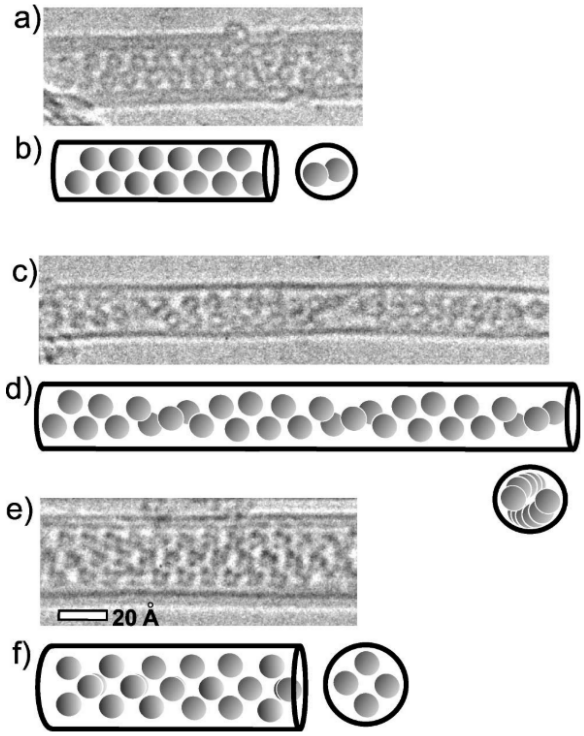

Figure 1.16. a) C_{60} in a zigzag phase inside a double-walled carbon nanotube (DWNT); c) C_{60} in a chiral phase inside a single-walled carbon nanotube (SWNT); and e) two-molecule layer phases in a DWNT. The schematic representations are shown in b), d), and f) respectively. Reprinted (adapted) with permission from A. N. Khlobystov *et al.*, *Phys. Rev. Lett.*, 2004, **92**, 245507. Copyright (2004) American Physical Society.[46]

C_{60} has been modified with sterically bulky alkyl chains in order to control the intermolecular spacing. In 2007, Chamberlain *et al.* found that the alkyl groups acted as physical barriers between molecules and increased the range of intermolecular spacings in SWNTs.[48] This resulted in a lack of long-range order compared to the periodic peapod structures of C_{60}@SWNTs. The larger the alkyl group, the larger the interfullerene spaces. This lack of periodicity was attributed to the conformational flexibility of the alkyl groups which can adopt many different folding arrangements inside the SWNTs. Leading on from the alkyl-chain modified fullerenes, Chamberlain *et al.* fine-tuned the intermolecular spacing of ordered arrays of fullerenes inside SWNTs by using more conformationally rigid polyaromatic groups of different sizes. The modified fullerenes formed π-π interactions

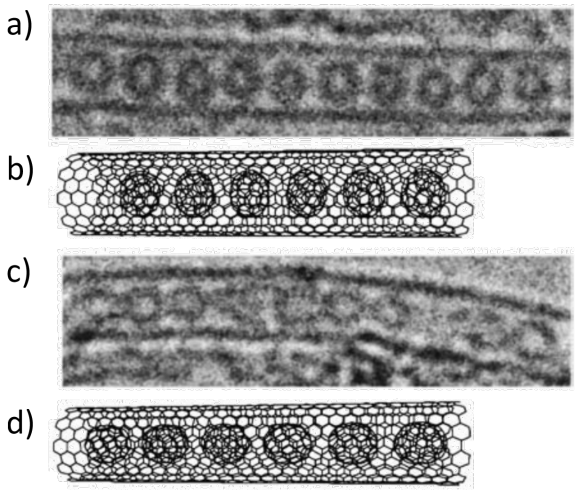

Figure 1.17. C_{70} in single-walled carbon nanotubes (SWNTs) with a) transverse and c) longitudinal orientations. Models of each type of orientation are shown in b) and d) respectively. Reprinted (adapted) with permission from A. N. Khlobystov *et al.*, *Appl. Phys. Lett.*, 2004, **84**, 792-794.[47]

which resulted in a certain degree of periodicity compared to the alkyl chain modified fullerenes.[49] Functionalised *endohedral* fullerenes also form ordered arrays in SWNTs where the majority of the fullerenes had the same cage-to-tail orientation. Gimenez-Lopez *et al.* directly observed endohedral atoms as well as the exohedral function groups which gave insight into the orientational selectivity for encapsulation of functionalised fullerenes.[50]

Translational and conformational movement of molecules in SWNTs have also been studied in the TEM. Molecules such as functionalised C_{60} fullerenes,[51–53] functionalised endohedral fullerenes,[50] *ortho*-carborane with covalently attached hydrocarbon chains,[54] tungsten polyoxometalate Linqvist ions $[W_6O_{19}]^{2-}$,[55] and tris(η^5-cyclopentadienyl)erbium or $ErCp_3$[56] have been observed in SWNTs in real time. Detailed studies of conformational behaviour have been carried out by Nakamura *et al.* on molecules such as an aromatic amide compound covalently attached to the end of a carbon nanotube,[57] single perfluoroalkyl chains,[58] as well as biotin derivatives (otherwise known as vitamin B7).[59] These researchers have imaged the transport of a single long hydrocarbon chain attached to a fullerene through nanoscale

pores in a SWNT[60] and suggested such detailed image series could be used to understand the kinetics and interactions of transportation processes observed in the bulk with molecular level information.

TEM *in-situ* studies by Khlobystov *et al.* of molecular motion in nanotubes at the single-molecule level revealed differences in motion of endohedral fullerenes depending on the filling rate of nanotubes. Fullerenes in sparsely-filled SWNTs had sporadic motions and moved more often than fullerenes in highly-filled SWNTs which had slower and more continuous motions as a long chain of molecules. The authors suggested that because endohedral fullerenes were mobile within the nanotube cavity, the orientations may be tuned by external electrostatic fields. Studies of molecular motion provided insight into the interactions between the encapsulated molecules and the SWNT; the alignment and rotational mode of (Ce@C_{82})@SWNTs in the nanotube suggested that electrostatic dipole interactions influenced the orientation of Ce@C_{82} in the nanotube.[61] The same group of researchers found that hydrogen-bonding between fullerenes functionalised with carboxylic groups prevented successful encapsulation of the molecules because they preferentially aggregated on the surface of the nanotube. Khlobystov *et al.* suggested that use of TEM to understand interactions at the molecular level would allow further development of novel, functional nano-architectures and this is especially true for self-assembled molecular materials.[62]

1.2.3 Thermally-induced reactions in carbon nanotubes

A rather interesting and thought-provoking read was the work carried out by Britz *et al.* on heat-induced polymerisation of $C_{60}O$ inside SWNTs. The SWNTs acted as a template during heat treatment, confining polymerisation of $C_{60}O$ to one-dimension to form linear covalent polymeric chains of $C_{60}O$ (Fig. 1.18). The authors went on to synthesise a 65:35 mixture of $C_{60}O$ and C_{60}, with the expectation that C_{60} would terminate the oligomer since there was no epoxide that would ring-open to form a furan-type bridge linking the fullerenes. This would result in shorter chains three units long. A time series of TEM images (Fig. 1.19) was used to determine whether the products were chains, which would remain together under electron beam irradiation, or peapods, in which individual molecules would translate along the nanotube over time. Their predictions were correct and the chains were indeed shorter.[63]

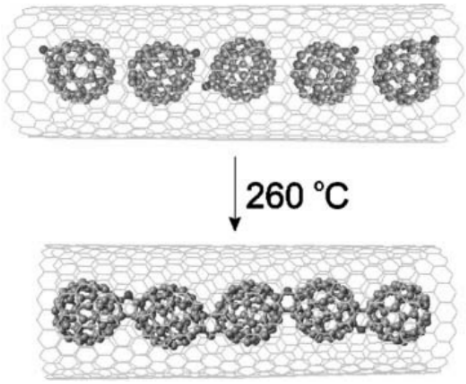

Figure 1.18. A scheme of the linear polymerisation of $C_{60}O$ inside a SWNT to form covalent polymeric chains of $C_{60}O$. Reproduced from D. A. Britz *et al.*, *Chem. Commun.*, 2005, 37-39 with permission from The Royal Society of Chemistry.[63]

A different type of linear polymer was studied using TEM by a number of researchers in the early 2010s. Tetrathiafulvalene, a small sulfur-containing molecule, can be heat treated inside carbon nanotubes to spontaneously form sulfur-terminated graphene nanoribbons (S-GNRs). This process is templated by

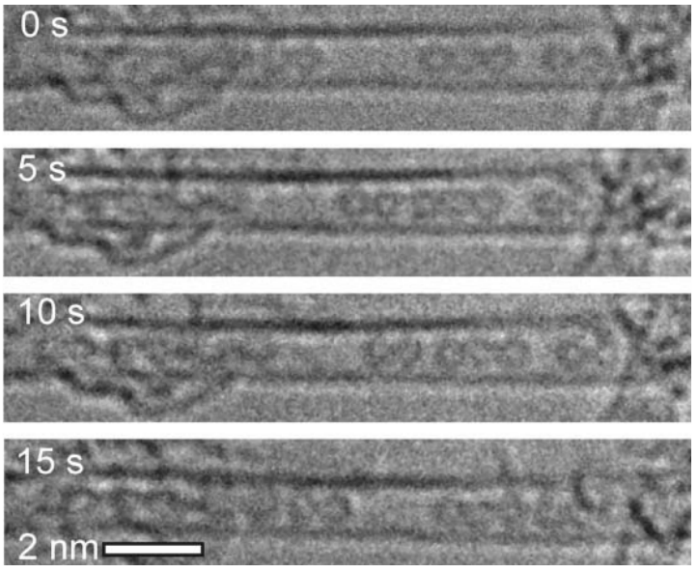

Figure 1.19. A time series of TEM images showing the 65:35 mixture of $C_{60}O$ and C_{60} translating inside a single-walled carbon nanotube. Reproduced from D. A. Britz *et al.*, *Chem. Commun.*, 2005, 37-39 with permission from The Royal Society of Chemistry.[63]

the host nanotube and can also occur under electron beam irradiation. Chamberlain *et al.* determined the optimum range of internal diameters of host nanotubes to be between 1 and 2 nm which consistently led to the formation of S-GNRs with widths of 0.5-1.4 nm. Outside of this range, GNRs did not form because the nanotube was either too wide or too thin to efficiently template nanoribbon formation and resulted in poorly defined, semi-amorphous structures without helical twists. The formation of S-GNRs under the electron beam was a complex and highly dynamic process which made it difficult to capture using TEM so energy-dispersive X-ray spectroscopy (EDXS) was used to monitor the elemental composition of structures generated inside the nanotubes. The authors found that the sulfur content halved during S-GNR formation from the tetrathiafulvalene precursor which suggested that expulsion of sulfur led to formation of a nanoribbon. Rotational and translational motions of these S-GNRs were observed using TEM.[64]

1.2.4 Electron beam-induced reactions in carbon nanotubes

This leads us onto electron beam-induced transformations in the TEM. There has been much interest in using the electron beam as a source of energy to initiate reactions while imaging the process. Chuvilin *et al.* studied the *in-situ* formation of S-GNRs from functionalised fullerenes with organic groups containing sulfur atoms. These molecules decomposed under prolonged exposure to the electron beam and self-assembled into an S-GNR inside the SWNT (Fig.1.20).[65] The size, structure, and helical twist (the characteristic structural fingerprint of GNRs) of S-GNRs could be controlled through confinement in nanotubes.

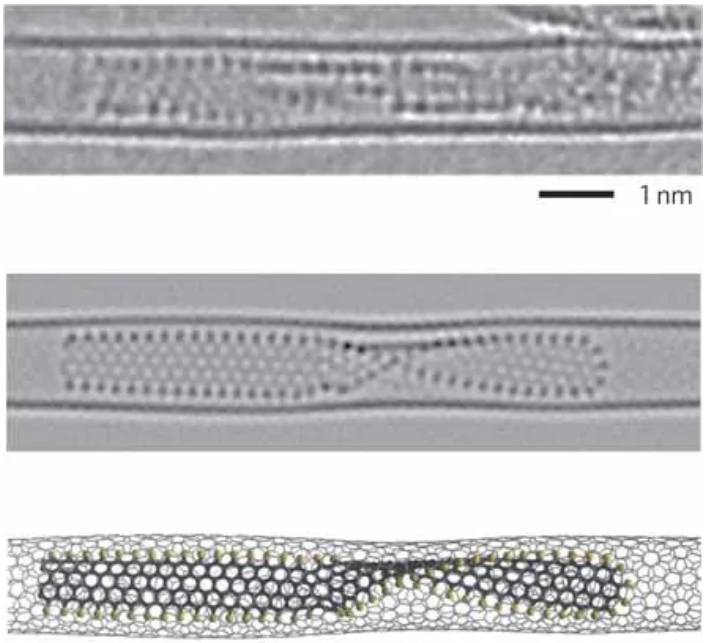

Figure 1.20. Sulfur-containing precursors react under heat or the electron beam to form graphene nanoribbons templated by the host SWNT. The heavier sulfur atoms terminate the edges and can be seen as a chain of dark atoms in the AC-HRTEM image (top). A simulated image (middle) from the model of S-GNR@SWNT (bottom) is also shown for comparison. Reprinted (adapted) with permission from A. Chuvilin *et al.*, *Nature Mater.*, 2011, **10**, 687-692. Copyright (2011) Springer Nature.[65]

Studies of fullerene and fullerene derivatives under the electron beam have been particularly fruitful for many groups of researchers. For example, Koshino *et al.* carried out a large-scale analysis on electron beam-induced fullerene dimerisation reactions in SWNTs under different reaction conditions such as varied voltages and temperatures in order to understand the process of dimerisation as well as how reaction conditions affect dimerisation.[66] Warner *et al.* have used the electron beam to both synthesise novel fullerene structures by irradiating fullerene chains in peapods and observe the molecular dynamics of these polymerised C_{60} chains. A C_{300} fullerene structure formed from the fusion of five fullerenes translated along the nanotube and exhibited a unique corkscrew-like rotational motion parallel to the axis of the SWNT (Fig. 1.21).[67]

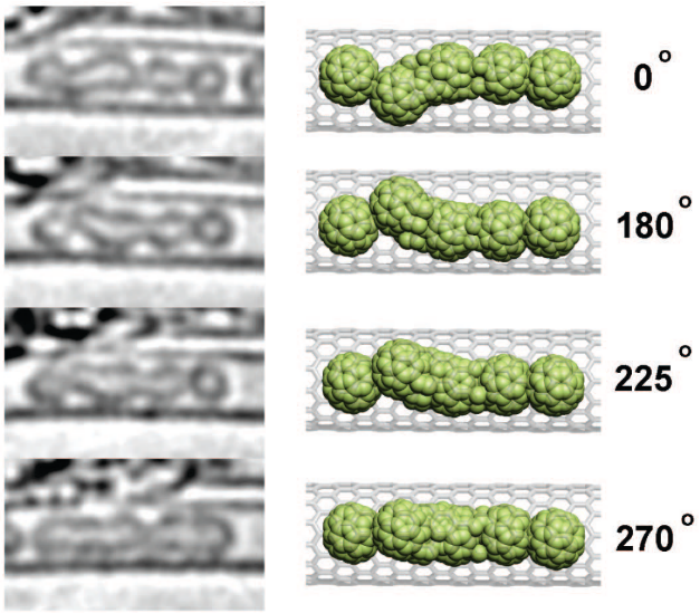

Figure 1.21. A time series of the rotation of a C_{300} fullerene structure inside a SWNT, with 10 s between each image. Schematic representations with the relative orientations are shown on the right of each image. Reprinted (adapted) with permission from J. H. Warner *et al.*, *Nano Lett.*, 2008, **8**, 2328-2335. Copyright (2008) American Chemical Society.[67]

Chamberlain *et al.* imaged functionalised metallofullerenes of osmium complexes attached to C_{60} encapsulated in SWNTs under conditions that would not damage the C_{60} cage but would initiate decomposition and polymerisation catalysed by the Os atoms. The authors suggested this high catalytic activity of the metallofullerenes could be implemented in chemical reactions confined within the carbon nanotube.[68] *In-situ* TEM coupled with electron energy loss spectroscopy (EELS) was used by Liu *et al.* to image and identify the reactivity of functional groups on fullerene-derivatives. The authors observed fusion of these metallofullerenes, not from the functional groups, but through the fullerene cages themselves. They suggested that under electron beam irradiation, the hydrogen-containing functional groups fell off readily and allowed the metallofullerenes to form bonds with the internal wall of the SWNTs.[69] Nakamura *et al.* have imaged a single group 8 metal in bucky-ferrocene and -ruthenocene molecules catalysing the C-C bond reorganisation of fullerenes.[70]

Warner *et al.* have also studied the electron beam-induced reactions of La@C_{82} metallofullerenes encapsulated within SWNTs. These metallofullerenes readily reacted to form internal SWNTs when other fullerenes were in close proximity.[71] They observed, through their detailed kinematics studies, transformation of the metallofullerenes into metal clusters and the "piston-like" movement of this LaC_2 metal cluster along the host nanotube axis well as a reaction where the metal cluster opened up the nanotube sidewall, exited, and sealed the hole back up with carbon from surrounding region.[72] Such "cutting" of nanotubes has also been catalysed by nickel under the electron beam. This was imaged with *in-situ* TEM and analysed in detail using molecular dynamics simulations by Lebedeva *et al.* to reveal the atomistic mechanism for the electron beam-induced reactions of bond reorganisation and atom ejection in the vicinity of the nickel cluster. The authors found that a combination of both electron beam irradiation and the nickel catalyst was crucial

for the cutting process to take place and the atom ejection rate varied significantly depending on the process stage and nanotube diameter.[73]

The reactivity of metals encapsulated in SWNTs under the electron beam has also been of great interest to researchers. The relative reactivities can be compared to understand fundamental properties and differences between metals. Zoberbier *et al.* analysed the interactions and bonding between carbon and the group VIII metals iron, ruthenium, and osmium at the atomic-level using TEM. Each type of metal cluster catalysed a wide variety of different transformations under the electron beam. These transformations were initiated when the electron beam knocked out a carbon atom from the SWNT sidewall in the vicinity of the metal cluster which then adhered to the metal cluster and formed a metal carbide (in the case of iron), a carbon shell (when the metal was ruthenium), or was completely removed, causing degradation and breakage of the nanotube (when osmium clusters were used). The authors found that this variation in chemical reactions was a result of a balance between the cohesive energy of the metal cluster and the strength of the metal-carbon σ- or π-bonds. Both iron and ruthenium quickly become deactivated by carbon while osmium remained in its pure metalic form throughout the reaction and was therefore able to completely cleave the nanotube. Additionally, the types of transformations could be changed by using different accelerating voltages of the electron beam. Reducing the electron beam energy from 80 to 40 keV resulted in formation of carbon structures with osmium rather than cutting of the nanotube.[74]

1.2.5 Molecules on graphene

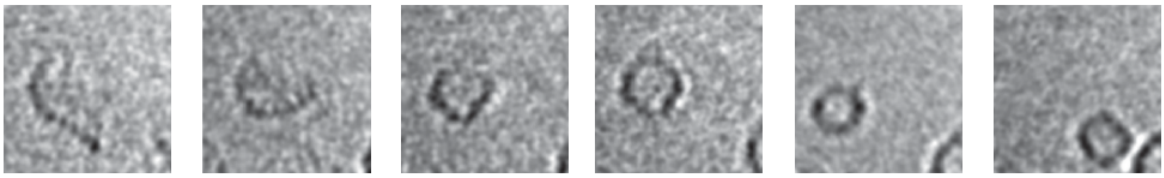

Figure 1.22. A series of images showing the transformation of a small graphene flake into the fullerene molecule. Reprinted (adapted) with permission from A. Chuvilin *et al.*, *Nature Chem.*, 2010, **2**, 450-453. Copyright (2010) Springer Nature.[75]

Another significant field of research involved using graphene as the support rather than SWNTs. A graphene flake on the surface of a graphene sheet was observed in real-time tranforming into a fullerene molecule (Fig. 1.22). This was the first example of direct visualisation of a process of fullerene formation,[75] the mechanism of which was supported by the atomistic modelling of this irradiation-induced process.[76] Single molecules of C_{60} have been imaged in a novel two-dimensional material where the fullerenes were sandwiched between two graphene layers in what is known as a "buckyball sandwich" structure. Mirzayev *et al.* observed the diffusion and rotation of individual C_{60}. Some C_{60} reacted under the e-beam to form dimers and then fused into peanut-like structures which continued to rotate around the joint axis, and this rotation was only hindered for structures involving three or more molecules. The authors demonstrated that a graphene sandwich could also be used as a nanoscale reaction chamber, much like SWNTs, and individual molecules encapsulated between the layers can be imaged with atomic resolution (although in this case the sample was imaged with scanning TEM or STEM where the beam is focused to a fine point and rastered across the sample, see Fig. 1.23).[77]

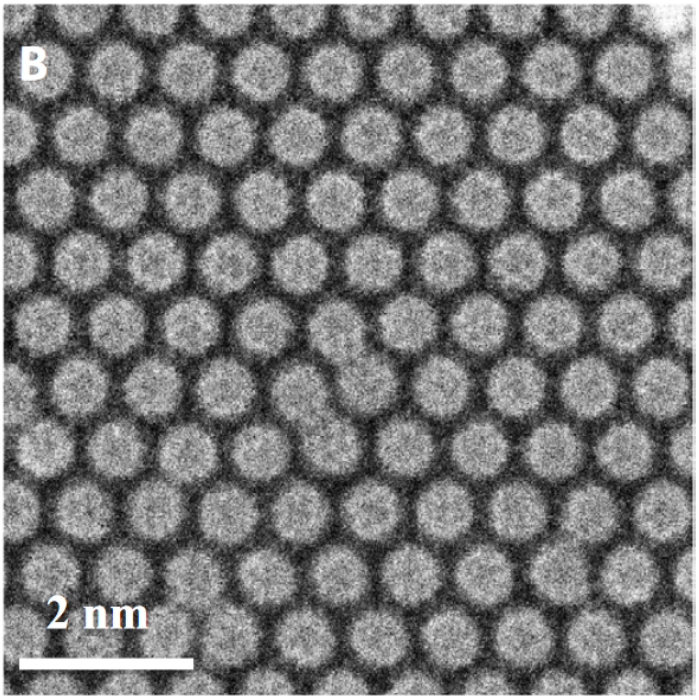

Figure 1.23. A monolayer of C_{60} sandwiched between two graphene layers: a buckyball sandwich. Reproduced from R. Mirazayev *et al.*, *Sci. Adv.*, 2017, **3**, e170017. Licensed under CC by-NC 4.0.[77]

Pitto-Barry and Barry *et al.* have carried out several investigations into metal atoms and nanoclusters on carbon supports with a focus on the fabrication of such materials using the electron beam. They have created nm-sized osmium nanocrystals by reduction of Os(II) precursors in polymer micelles *in situ* via irradiation with the electron beam.[78] Not only did they produce osmium nanocrystals with a narrow size distribution (1.5 ± 1 nm), they were able to do so at a relatively large scale (the entire 3×3 mm^2 TEM grid was irradiated) using their straightforward methodology. This would otherwise be extremely synthetically challenging. While the authors did not fully understand how the electron beam interacted with their Os(II) precursors to create the Os nanocrystals, they hypothesised that the formation of nanocrystals was initiated by the kinetic energy imparted by the incident electron beam. Understanding the fundamental processes behind the electron beam-driven transformations would be incredibly valuable for synthesis at the atomic scale.

The authors suggested that their methodology could be easily applied to synthesis of other metal nanocrystals and subsequently demonstrated this by synthesising ruthenium, iridium, and gold nanocrystals using similar metal precursors encapsulated in polymer micelles.[79] They were able to image the process of nanocrystallisation during irradiation where, after the micelles formed a graphitic surface, individual metal atoms were able to migrate and aggregate into nanocrystals. The metal precursors varied in chemical composition; the authors used an organometallic Ru(II) arene complex, an Ir(III) complex with a cyclopentadienyl ligand, and a Au(III) complex that was not an organometallic compound at all. In doing so, the authors showed that the formation of metal nanocrystals did not depend strictly on the nature of the metal precursors and therefore their methodology is likely incredibly easy to adapt. Image series of the early steps in the nanocrystallisation process showed no change in metal-metal distances, with examples for Ru and Au shown in Fig. 1.24. There was also an approximately linear relationship between the length of the metal aggregates with irradiation time for all metals studied, suggesting that the size of nanocrystals could be controlled by adjusting the irradiation time. Such an unusual use of the electron beam as a synthetic tool could have interesting applications in fields such as biotechnology and materials sciences.

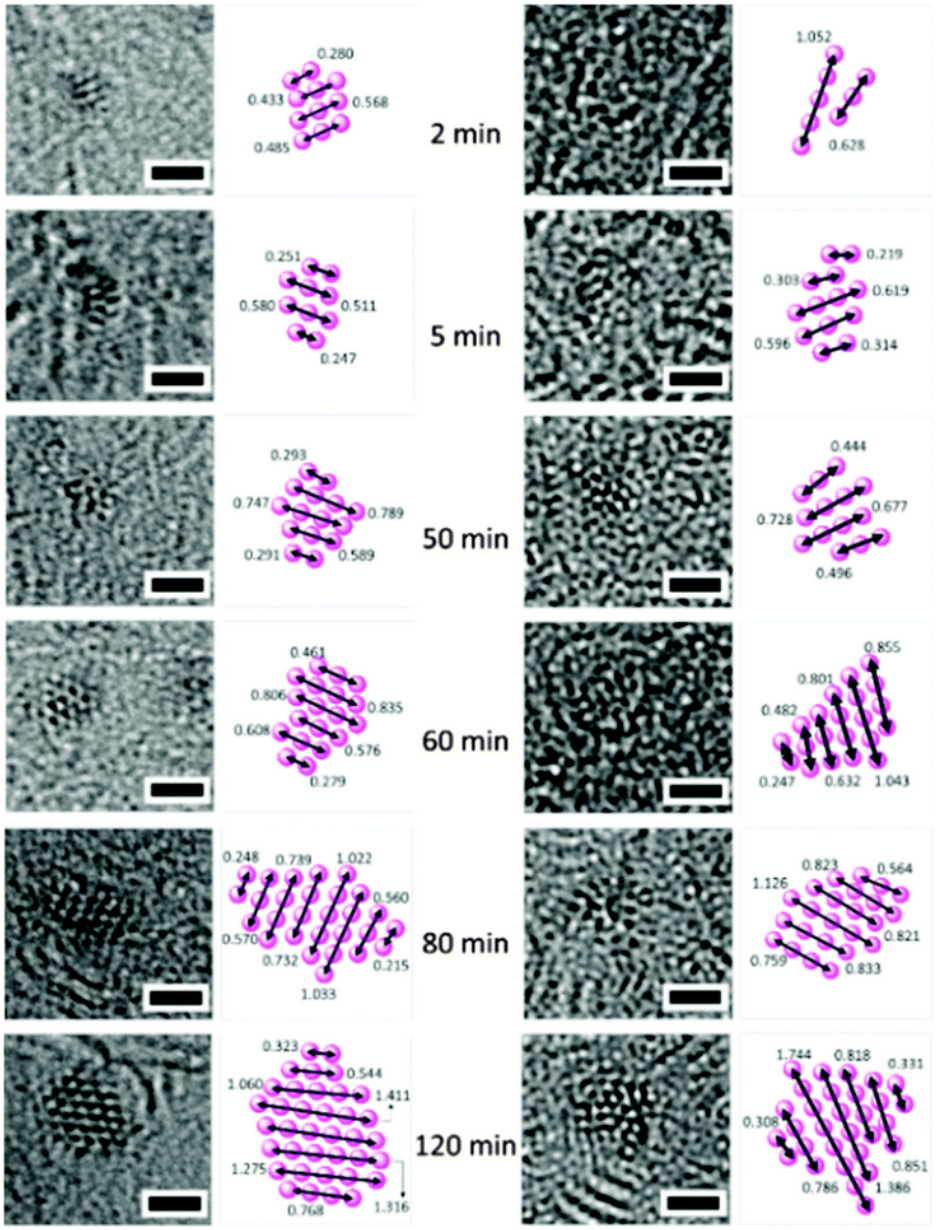

Figure 1.24. The early steps in the nanocrystallisation process for Ru (left) and Au (right) nanocrystals. Models of the atoms with interatomic distances are shown. The scale bar is 1 nm. Reproduced from A. Pitto-Barry *et al.*, *Chem. Commun.*, 2016, **52**, 3895-3898. Licensed under CC by 3.0.[79]

Pitto-Barry and Barry *et al.* have also investigated the effects of dopants such as sulfur and boron in the graphitic matrix on the dynamics of formation of osmium metal nanocrystals.[80,81] The rate of migration and aggregation varied between doped and non-doped graphitic surfaces, suggesting interactions between osmium and the dopant atoms. Temperature also had an effect on the growth of nanocrystals.[82] The rate of nanocrystallisation seemed to be linearly related to the temperature. However, the different temperatures did not seem to affect the atomic arrangement within the nanocrystals. showing that increasing the temperature did not reduce the quality of the fabricated nanocrystals.

This approach by Pitto-Barry and Barry *et al.* is similar to the chemTEM framework developed by Chamberlain *et al.*,[83] a technique that uses the electron beam of TEM as both the imaging probe and the source of energy. The work in this thesis was also based on the chemTEM framework which will be discussed in more detail in the introduction of the second chapter. Understanding and controlling what happens at the atomic-level has always been the rationale behind designing any synthetic procedure. Now, after the development of aberration corrected TEM, we and many others can explore the "plenty of room at the bottom", directly manipulating atoms while at the same time recording the entire process. This concept has advanced further in two-dimensional materials, leading to some incredible developments in material fabrication with atomic precision.[84,85]

1.3 Aim and Objectives

Having gone at breakneck-speed through a description of the TEM and a history of using the TEM to image molecules (both in crystals and as individual species), we can see that TEM is routinely used to study the nanoscale structure of a material and more recently, is being considered as a lab environment to probe interactions at the single-molecule level. Although there is much interest in using the TEM for studying and manipulating samples at the atomic level, the electron beam is a powerful irradiation source that can be difficult to control when attempting to image a sample without beam damage. There can also be difficulties with understanding the nature of beam damage. The aim of this thesis is to use a selection of candidate materials to gain an understanding of the current and potential capabilities of TEM *in-situ* for use in studying beam-induced reactions and to establish protocols for such experiments. It is intended that this thesis will build upon the ChemTEM methodology developed by Chamberlain *et al.* and incorporate kinetics studies into these TEM experiments. Kinetic experiments of bulk reactions typically involve many tightly controlled parameters such as concentration, temperature, and time. Likewise, for kinetic experiments at the nanoscale, we must also take into account any factors which may affect the reaction and keep certain factors constant throughout a particular study, such as the electron flux.

Firstly, we will expand upon the work of Chamberlain *et al.* on the familiar molecule perchlorocoronene (PCC; $C_{24}Cl_{12}$) inside SWNTs by carrying out kinetic studies of the polymerisation at the single-molecule level in order to calculate the experimental cross section. To this aim, a number of parameters need to be further investigated. The SWNT acts as a nano-test tube and under the influence of the electron beam, PCC molecules can polymerise inside the nanotube to form a chlorine-terminated graphene nanoribbon. Many of the intermediates of the polymerisation have been revealed by TEM. However, the nanotubes in a sample of

PCC@SWNTs may be quite different from one another. For example, the nanotube width varies in a sample and as a result, the packing of PCC inside these nanotubes may vary, which could influence the reaction. To address this issue, we will image multiple areas to understand how the reaction varies from area to area. In order to understand the contributions of both the electron beam and heat on PCC polymerisation we will apply heating conditions *in-situ* to a PCC@SWNTs sample. We will also carry out a second kinetics study into the thermally activated polymerisation to find the activation energy of heat-induced PCC polymerisation inside SWNTs. On the other end of the temperature scale, cryogenic conditions can allow us to understand how removing thermal energy from PCC@SWNTs affects the system. We can also compare and contrast PCC polymerisation to the electron beam-induced reactions of other large polycyclic aromatic hydrocarbons such as the parent molecule coronene. In addition to these experiments, an efficient methodology will be required for analysis and processing of this huge amount of data.

Secondly, we will investigate the use of the electron beam as the source of energy for cross-linking of molecules by studying the electron beam-induced transformations of hexaazatrinaphthylenes (HATs), heterocyclic aromatic hydrocarbons. These molecules are related to PCC and coronene as well as precursors used to synthesise metal and covalent organic frameworks (MOFs and COFs respectively). We shall see in chapter three that a major challenge when making extended frameworks is controlling the reaction to give an orderly structure. There may be many kinds of side-products and consequently a low yield of the desired product. MOF and COF synthesis may require an impractically long time and can be difficult to scale up. An alternative to bulk synthesis in solution is use of the electron beam as the source of energy for cross-linking of molecules. This is widely used in electron beam lithography (EBL) and was the inspiration for studying the behaviour of

nanocrystals of HATs in the TEM. We can use diffraction to follow the crystallinity of each type of HAT crystal and measure the total electron dose required for the set of diffraction spots to fade into noise. This can be used to define the critical dose for each molecule, as covered in more detail in chapter three. By comparing the critical doses of the HAT molecules to well-studied molecules such as PCC and copper(II) phthalocyanine, we can place the critical doses of HATs in context with other similar molecules. These TEM irradiation studies will be useful for any future experiments involving EBL.

Finally, we will investigate the interaction of the electron beam with an individual molecule, using the molecule HF@C_{60}. This molecule is an endohedral fullerene which contains, imprisoned inside the carbon cage, the incredibly reactive molecule HF. This provided the opportunity to investigate individual molecules of HF without any external influence. The electron beam of a TEM can be focused to a sub-atomic point, allowing the input of energy and therefore excitation of single molecules of HF@C_{60}. Although the signals from any one molecule are too weak for current detectors, analysis can be performed on nanoscopic quantities of HF@C_{60} in crystal form as well as encapsulated in SWNTs. High resolution TEM and STEM combined with several spectroscopic techniques can be used to probe HF@C_{60} during and after electron irradiation. This analysis can also be subsequently combined with the non-TEM spectroscopic technique of optically detected magnetic resonance (ODMR) which is capable of detecting unpaired electron spins in nanoscopic quantities of a material. This study will also involve developing a methodology for analysis of electron beam irradiated material on a TEM grid in multiple laboratories, the so-called “lab on a grid”. This methodology of combining high spatial resolution of TEM with analytical techniques both inside and outside the microscope may prove useful for studying many types of materials at the nanoscale.

Underscoring each study in this thesis is the idea that the electron beam is both a useful source of energy and an analytical probe. This has been used throughout the literature described in this chapter. We hope to contribute to this wealth of knowledge by developing general methodologies that apply rigorous kinetic analyses to nanoscale reactions as well as combining bulk techniques such as EBL and ODMR with the high spatiotemporal resolution available in a TEM. Studying a sample from many different angles is key to understanding fundamental properties and it is from this viewpoint where we approached each study.

1.4 References

1. M. Knoll and E. Ruska, *Z. Phys.*, 1932, **78**, 318–339.
2. O. Scherzer, *J. Appl. Phys.*, 1949, **20**, 20–29.
3. D. B. Williams and C. B. Carter, *Transmission Electron Microscopy, A Textbook for Materials Science*, Springer US, 2nd edn., 2009, LXII, 775.
4. M. Haider, S. Uhlemann, E. Schwan, H. Rose, B. Kabius and K. Urban, *Nature*, 1998, **392**, 768–769.
5. O. Krivanek, N. Dellby and A. Lupini, *Ultramicroscopy*, 1999, **78**, 1–11.
6. H. Rose, *Optik*, 1990, **85**, 19–24.
7. P. R. Buseck, J. M. Cowley and L. Eyring, *High-Resolution Electron Microscopy and Associated Techniques*, Oxford University Press New York, 1988.
8. S. Horiuchi, *High-Resolution Transmission Electron Microscopy*, North-Holland Amsterdam, 1994.
9. J. C. H. Spence, *High-Resolution Electron Microscopy*, Oxford University Press New York, 3rd edn., 2003.
10. R. Henderson, *Q. Rev. Biosphys.*, 1995, **28**, 171–193.
11. R. F. Egerton, *Ultramicroscopy*, 2013, **127**, 100–108.
12. R. F. Egerton, *Micron*, 2019, **119**, 72–87.
13. R. F. Egerton, *Microsc. Res. Tech.*, 2012, **75**, 1550–1556.
14. T. W. Chamberlain, J. Biskupek, S. T. Skowron, P. A. Bayliss, E. Bichoutskaia, U. Kaiser and A. N. Khlobystov, *Small*, 2015, **11**, 622–629.
15. J. C. Meyer, F. Eder, S. Kurasch, V. Skakalova, J. Kotakoski, H. J. Park, S. Roth, A. Chuvilin, S. Eyhusen, G. Benner, A. V. Krasheninnikov and U. Kaiser, *Phys. Rev. Lett.*, 2012, **108**, 196102.
16. G. Algara-Siller, S. Kurasch, M. Sedighi, O. Lehtinen and U. Kaiser, *Appl. Phys. Lett.*, 2013, **103**, 203107.
17. S. T. Skowron, V. O. Koroteev, M. Baldoni, S. Lopatin, A. Zurutuza, A. Chuvilin and E. Besley, *Carbon*, 2016, **105**, 176–182.
18. A. Stone and D. Wales, *Chem. Phys. Lett.*, 1986, **128**, 501–503.
19. N. Uyeda, T. Kobayashi and E. Suito, *J. Appl. Phys.*, 1972, **43**, 5181–5188.

20. J. Menter, *Proc. Royal Soc. A*, 1956, **236**, 119–135.

21. Y. Murata, J. R. Fryer, T. Baird and H. Murata, *Acta Cryst.*, 1977, **A 33**, 198–200.

22. J. R. Fryer, *Ultramicroscopy*, 1984, **14**, 227–236.

23. M. S'ari, J. Cattle, N. Hondow, H. Blade, S. Cosgrove, R. M. D. Brydson and A. P. Brown, *J. Phys.: Conf. Ser.*, 2015, **644**, 012038.

24. J. Cattle, M. S'ari, N. Hondow, P. Abellán, A. P. Brown and R. M. D. Brydson, *J. Phys.: Conf. Ser.*, 2015, **644**, 012030.

25. R. Henderson and R. Glaeser, *Ultramicroscopy*, 1985, **16**, 139–150.

26. M. S'ari, H. Blade, R. Brydson, S. D. Cosgrove, N. Hondow, L. P. Hughes and A. Brown, *Mol. Pharmaceutics*, 2018, **15**, 5114–5123.

27. M. Monthioux, *Carbon*, 2002, **40**, 1809–1823.

28. G. Brown, S. R. Bailey, J. Sloan, C. Xu, S. Friedrichs, E. Flahaut, K. S. Colman, J. L. Hutchison, R. E. Dunin-Borkowski and M. L. H. Green, *Chem. Commun.*, 2001, 845–846.

29. J. Sloan, J. Hammer, M. Zwiefka-Sibley and M. L. H. Green, *Chem. Commun.*, 1998, 347–348.

30. J. Sloan, M. C. Novotny, S. R. Bailey, G. Brown, C. Xu, V. C. Williams, S. Friedrichs, E. Flahaut, R. L. Callender, A. P. E. York, K. S. Coleman, M. L. H. Green, R. E. Dunin-Borkowski and J. L. Hutchison, *Chem. Phys. Lett.*, 2000, **329**, 61–65.

31. R. R. Meyer, J. Sloan, R. E. Dunin-Borkowski, A. I. Kirkland, M. C. Novotny, S. R. Bailey, J. L. Hutchison and M. L. H. Green, *Science*, 2000, **289**, 1324–1326.

32. C. Xu, J. Sloan, G. Brown, S. Bailey, V. C. Williams, S. Friedrichs, K. S. Coleman, E. Flahaut, J. L. Hutchison, R. E. Dunin-Borkowski and M. L. H. Green, *Chem. Commun.*, 2000, 2427–2428.

33. B. W. Smith, M. Monthioux and D. E. Luzzi, *Nature*, 1998, **396**, 323–324.

34. Y. Zhang, S. Iijima, Z. Shi and Z. Gu, *Phil. Mag. Lett.*, 1999, **79**, 473–479.

35. J. Sloan, R. E. Dunin-Borkowski, J. L. Hutchison, K. S. Coleman, V. C. Williams, J. B. Claridge, A. P. E. York, C. Xu, S. R. Bailey, G. Brown, S. Friedrichs and M. L. Green, *Chem. Phys. Lett.*, 2000, **329**, 61–65.

36. B. W. Smith, M. Monthioux and D. E. Luzzi, *Chem. Phys. Lett.*, 1999, **315**, 31–36.

37. D. E. Luzzi and B. W. Smith, *Carbon*, 2000, **38**, 1751–1756.

38. B. W. Smith and D. E. Luzzi, *Chem. Phys. Lett.*, 2000, **321**, 169–174.

39. B. W. Smith, D. E. Luzzi and Y. Achiba, *Chem. Phys. Lett.*, 2000, **331**, 137–142.

40. K. Suenaga, M. Tencé, C. Mory, C. Colliex, H. Kato, T. Okazaki, H. Shinohara, K. Hirahara, S. Bandow and S. Iijima, *Science*, 2000, **290**, 2280–2282.

41. K. Hirahara, K. Suenaga, S. Bandow, H. Kato, T. Okazaki, H. Shinohara and S. Iijima, *Phys. Rev. Lett.*, 2000, **85**, 5384–5387.

42. D. A. Morgan, J. Sloan and M. L. H. Green, *Chem. Commun.*, 2002, 2442–2443.

43. Y. Fujita, S. Bandow and S. Iijima, *Chem. Phys. Lett.*, 2005, **413**, 410–414.

44. L. Li, A. N. Khlobystov, J. G. Wiltshire, G. A. D. Briggs and R. J. Nicholas, *Nature Mater.*, 2005, **4**, 481–485.

45. J. Wang, M. K. Kuimova, M. Poliakoff, G. A. D. Briggs and A. N. Khlobystov, *Angew. Chem. Int. Ed.*, 2006, **45**, 5188–5191.

46. A. N. Khlobystov, D. A. Britz, A. Ardavan and G. A. D. Briggs, *Phys. Rev. Lett.*, 2004, **92**, 245507.

47. A. N. Khlobystov, R. Scipioni, D. Nguyen-Manh, D. A. Britz, D. G. Pettifor and G. A. D. Briggs, *Appl. Phys. Lett.*, 2004, **84**, 792–794.

48. T. W. Chamberlain, A. Camenisch, N. R. Champness, G. A. D. Briggs, S. C. Benjamin, A. Ardavan and A. N. Khlobystov, *J. Am. Chem. Soc.*, 2007, **129**, 8609–8614.

49. T. W. Chamberlain, R. Pfeiffer, H. Peterlik, H. Kuzmany, F. Zerbetto, M. Melle-Franco, L. Staddon, N. R. Champness, G. A. D. Briggs and A. N. Khlobystov, *Small*, 2008, **4**, 2262–2270.

50. M. C. Giménez-López, A. Chuvilin, U. Kaiser and A. N. Khlobystov, *Chem. Commun.*, 2011, **47**, 2116–2118.

51. N. Solin, M. Koshino, T. Tanaka, S. Takenaga, H. Kataura, H. Isobe and E. Nakamura, *Chem. Lett.*, 2007, **36**, 1208–1209.

52. J. Fan, T. W. Chamberlain, Y. Wang, S. Yang, A. J. Blake, M. Schröder and A. N. Khlobystov, *Chem. Commun.*, 2011, **47**, 5696–5698.

53. T. W. Chamberlain, R. Pfeiffer, J. Howells, H. Peterlik, H. Kuzmany, B. Kraütler, T. D. Ros, M. Melle-Franco, F. Zerbetto, D. Milić and A. N. Khlobystov, *Nanoscale*, 2012, **4**, 7540–7548.

54. M. Koshino, T. Tanaka, N. Solin, K. Suenaga, H. Isobe and E. Nakamura, *Science*, 2007, **316**, 853.

55. J. Sloan, G. Matthewman, C. Dyer-Smith, A.-Y. Sung, Z. Liu, K. Suenaga, A. I. Kirkland and E. Flahaut, *ACS Nano*, 2008, **2**, 966–976.

56. D. Ogawa, R. Kitaura, T. Saito, S. Aoyagi, E. Nishibori, M. Sakata, T. Nakamura and H. Shinohara, *J. Nanomater.*, 2014, 539295.

57. E. Nakamura, M. Koshino, T. Tanaka, Y. Niimi, K. Harano, Y. Nakamura and H. Isobe, *J. Am. Chem. Soc.*, 2008, **130**, 7808–7809.

58. K. Harano, S. Takenaga, S. Okada, Y. Niimi, N. Yoshikai, H. Isobe, K. Suenaga, H. Kataura, M. Koshino and E. Nakamura, *J. Am. Chem. Soc.*, 2014, **136**, 466–473.

59. R. M. Gorgoll, E. Yücelen, A. Kumamoto, N. Shibata, K. Harano and E. Nakamura, *J. Am. Chem. Soc.*, 2015, **137**, 3474–3477.

60. M. Koshino, N. Solin, T. Tanaka, H. Isobe and E. Nakamura, *Nature Nanotech.*, 2008, **3**, 595–597.

61. A. N. Khlobystov, K. Porfyrakis, M. Kanai, D. A. Britz, A. Ardavan, H. Shinohara, T. J. S. Dennis and G. A. D. Briggs, *Angew. Chem. Int. Ed.*, 2004, **43**, 1386–1389.

62. A. N. Khlobystov, K. Porfyrakis, D. A. Britz, M. Kanai, R. Scipioni, S. G. Lyapin, J. G. Wiltshire, A. Ardavan, D. Nguyen-Manh, R. J. Nicholas, D. G. Pettifor, T. J. S. Dennis and G. A. D. Briggs, *Mater. Sci. Technol.*, 2004, **20**, 969–974.

63. D. A. Britz, A. N. Khlobystov, K. Porfyrakis, A. Ardavan and G. A. D. Briggs, *Chem. Commun.*, 2005, 37–39.

64. T. W. Chamberlain, J. Biskupek, G. A. Rance, A. Chuvilin, T. J. Alexander, E. Bichoutskaia, U. Kaiser and A. N. Khlobystov, *ACS Nano*, 2012, **6**, 3943–3953.

65. A. Chuvilin, E. Bichoutskaia, M. C. Giménez-López, T. W. Chamberlain, G. A. Rance, N. Kuganathan, J. Biskupek, U. Kaiser and A. N. Khlobystov, *Nat. Mater.*, 2011, **10**, 687–692.

66. M. Koshino, Y. Niimi, E. Nakamura, H. Kataura, T. Okazaki, K. Suenaga and S. Iijima, *Nat. Chem.*, 2010, **2**, 117–124.

67. J. H. Warner, Y. Ito, M. Zaka, L. Ge, T. Akachi, H. Okimoto, K. Porfyrakis, A. A. R. Watt, H. Shinohara and G. A. D. Briggs, *Nano Lett.*, 2008, **8**, 2328–2335.

68. T. W. Chamberlain, N. R. Champness, M. Schröder and A. N. Khlobystov, *Chem. Eur. J.*, 2011, **17**, 668–674.

69. Z. Liu, M. Koshino, K. Suenaga, A. Mrzel, H. Kataura and S. Iijima, *Phys. Rev. Lett.*, 2006, **96**, 088304.

70. E. Nakamura, M. Koshino, T. Saito, Y. Niimi, K. Suenaga and Y. Matsuo, *J. Am. Chem. Soc.*, 2011, **133**, 14151–14153.

71. J. H. Warner, Y. Ito, M. H. Rümmeli, T. Gemming, B. Büchner, H. Shinohara and G. A. D. Briggs, *Phys. Rev. Lett.*, 2009, **102**, 195504.

72. J. H. Warner, Y. Ito, M. H. Rümmeli, B. Büchner, H. Shinohara and G. A. D. Briggs, *ACS Nano*, 2009, **3**, 3037–3044.

73. I. V. Lebedeva, T. W. Chamberlain, A. M. Popov, A. A. Knizhnik, T. Zorberbier, J. Biskupek, U. Kaiser and A. N. Khlobystov, *Nanoscale*, 2014, **6**, 14877–14890.

74. T. Zoberbier, T. W. Chamberlain, J. Biskupek, M. Suyetin, A. G. Majouga, E. Besley, U. Kaiser and A. N. Khlobystov, *Small*, 2016, **12**, 1649–1657.

75. A. Chuvilin, U. Kaiser, E. Bichoutskaia, N. A. Besley and A. N. Khlobystov, *Nat. Chem.*, 2010, **2**, 450–453.

76. S. T. Skowron, I. V. Lebedeva, A. M. Popov and E. Bichoutskaia, *Nanoscale*, 2013, **5**, 6677–6692.

77. R. Mirzayev, K. Mustonen, M. R. A. Monazam, A. Mittelberger, T. J. Pennycook, C. Mangler, T. Susi, J. Kotakoski and J. C. Meyer, *Sci. Adv.*, 2017, **3**, e1700176.

78. A. Pitto-Barry, L. M. A. Perdigao, M. Walker, J. Lawrence, G. Costantini, P. J. Sadler and N. P. E. Barry, *Dalton Trans.*, 2015, **44**, 20308.

79. A. Pitto-Barry, P. J. Sadler and N. P. E. Barry, *Chem. Commun.*, 2016, **52**, 3895–3898.

80. N. P. E. Barry, A. Pitto-Barry, J. Tran, S. E. F. Spencer, A. M. Johansen, A. M. Sanchez, A. P. Dove, R. K. O'Reilly, R. J. Deeth, R. Beanland and P. J. Sadler, *Chem. Mater.*, 2015, **27**, 5100–5105.

81. A. Pitto-Barry and N. P. E. Barry, *Chem. Commun.*, 2019, **55**, 6038–6041.

82. A. Pitto-Barry and N. P. E. Barry, *Angew. Chem. Int. Ed.*, 2019, **58**, 18482–18486.

83. T. W. Chamberlain, J. Biskupek, S. T. Skowron, A. V. Markevich, S. Kurasch, O. Reimer, K. E. Walker, G. A. Rance, X. Feng, K. Müllen, A. Turchanin, M. A. Lebedeva, A. G. Majouga, V. G. Nenajdenko, U. Kaiser, E. Besley and A. N. Khlobystov, *ACS Nano*, 2017, **11**, 2509–2520.

84. T. Susi, J. C. Meyer and J. Kotakoski, *Ultramicroscopy*, 2017, **180**, 163–172.

85. O. Dyck, M. Ziatdinov, D. B. Lingerfelt, R. R. Unocic, B. M. Hudak, A. R. Lupini, S. Jesse and S. V. Kalinin, *Nat. Rev. Mater.*, 2019, **4**, 497–507.

CHAPTER 2

Reactions of polycyclic aromatic hydrocarbons

2.1 Introduction

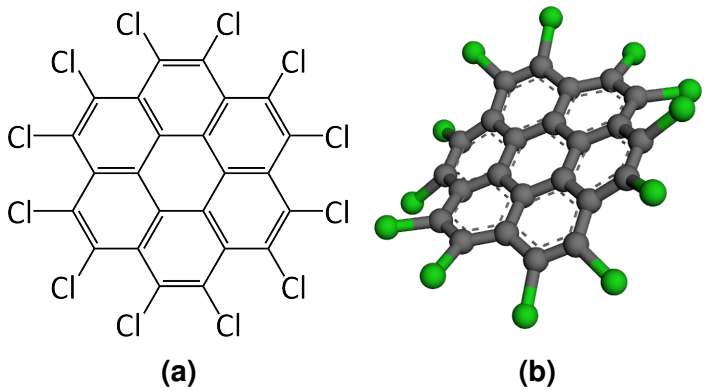

Figure 2.1. (a) Chemical structure and (b) three-dimensional model of $C_{24}Cl_{12}$ perchlorocoronene (PCC) determined using single crystal X-ray diffraction by Baird *et al.*[1] The polycyclic aromatic hydrocarbon (PAH) is not planar due to the bulky adjacent chlorine substituents.

A particularly well-studied molecule by transmission electron microscopy (TEM) is perchlorocoronene (PCC), the fully chlorinated derivative of coronene (Fig. 2.1). As discussed previously, the substitution of hydrogen for heavier elements improves electron beam stabilty of molecules encapsulated in SWNTs by reducing the atom ejection cross-section.[2] PCC has been studied in crystal form,[3–5] supported

on a graphene substrate as single molecules (Fig. 2.2),[6] and encapsulated as a one dimensional 'molecular stack' inside single-walled carbon nanotubes (SWNTs; Fig. 2.6).[7] The remarkable beam stability of PCC enabled the systematic study of structural damage to microcrystals with single molecule resolution, including imaging of defects and edge structures.[8]

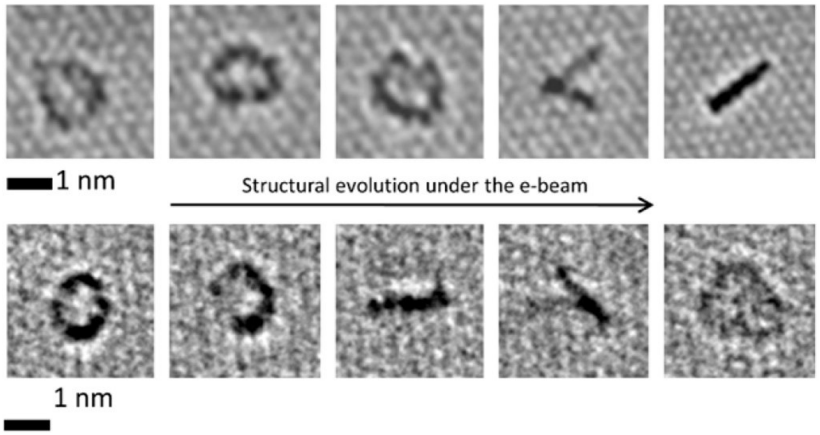

(a)

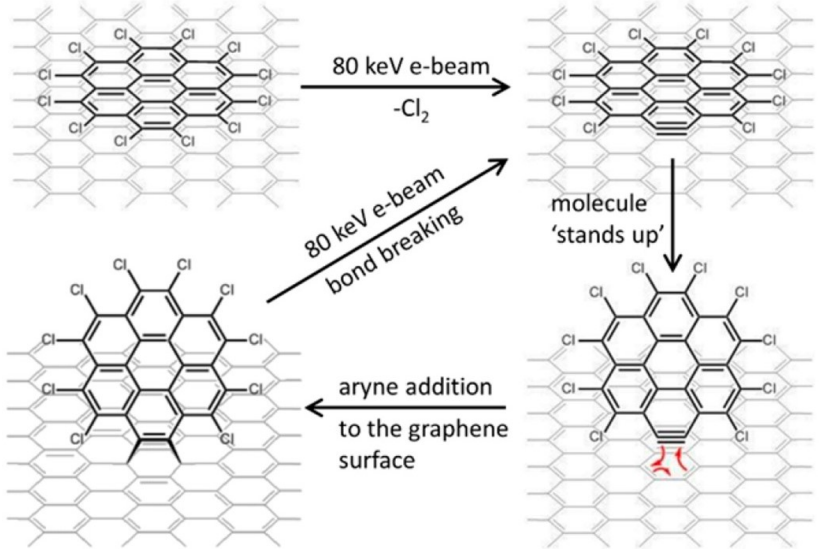

(b)

Figure 2.2. (a, b) Impact of an 80 keV electron onto a carbon atom of PCC breaks a C−Cl bond which leads to formation of an aryne species $C_{24}Cl_{10}$ that can have a face-on (circle) or edge-on (line) orientation. Once edge-on, the aryne species can act as a dienophile and react with the C=C bond of graphene via a Diels-Alder cycloaddition. Reproduced from T. W. Chamberlain *et al.*, *ACS Nano*, 2017, **11**, 2509-2520. Licensed under ACS AuthorChoice.[7]

Markevich *et al.* have explored the electron beam-driven functionalisation of graphene with PCC both theoretically and experimentally using TEM. When adsorbed PCC molecules are irradiated with an 80 keV electron beam, incident electrons transfer up to a maximum of 15.8 eV of kinetic energy via direct knock-on to a carbon atom of PCC (while only 5.3 eV is transferred to a chlorine atom). This energy transfer is large enough to substantially perturb the C−Cl bond (Fig. 2.3), eventually leading to loss of Cl_2 to form an aryne species $C_{24}Cl_{10}$. This aryne can change from a face-on to an edge-on orientation on the graphene surface which allows it to react with the C=C bonds of pristine graphene via a Diels-Alder cycloaddition (Fig. 2.2). This cycloadduct is metastable and bonds can be broken by the electron beam to reform the aryne species.[6,9]

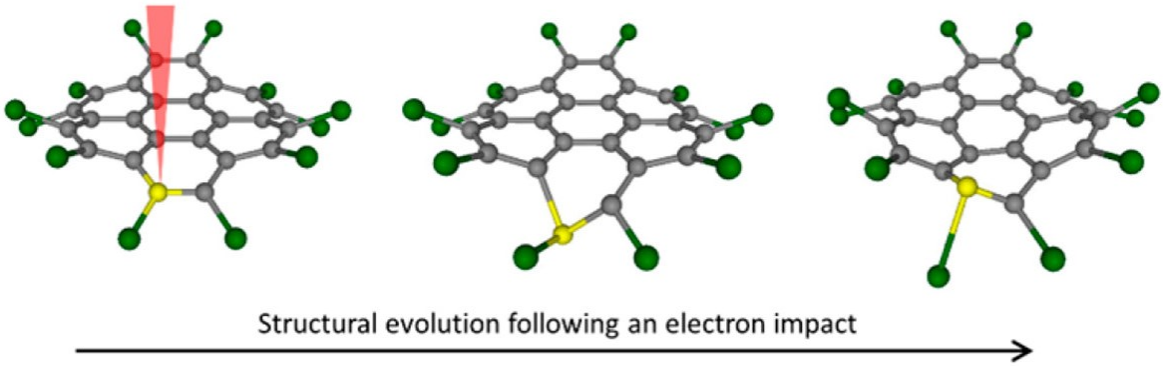

Figure 2.3. Models from density functional theory (DFT) calculations of energy transfer from an incident electron to a carbon atom of PCC, illustrating the significant perturbation of the C−Cl bond from an equilibrium bond distance of 0.174 nm up to 0.28 nm.[7] Reproduced from T. W. Chamberlain *et al.*, *ACS Nano*, 2017, **11**, 2509-2520. Licensed under ACS AuthorChoice.[7]

The Diels-Alder cycloaddition of the PCC aryne species was investigated further by Chamberlain *et al.* in a SWNT system.[7] PCC molecules have a high filling rate into SWNTs because the diameter of the molecule is only slightly smaller than the average internal diameter of the SWNTs. As a result, there are favourable van der Waals interactions between molecules and nanotubes, leading to high filling. PCC molecules have a tendency to form tightly packed stacks inside SWNTs due to π-π interactions (Fig. 2.4), reminiscent of the high periodicity of C_{60} fullerene peapods.[10]

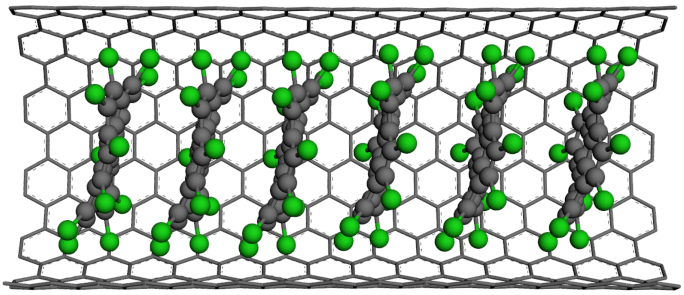

Figure 2.4. Model of PCC inside SWNTs; the diameter of PCC is 1.41 nm while the average diameter of SWNTs used is 1.55 $\pm$ 0.1 nm.

The stack of encapsulated PCC molecules lose Cl_2 under an 80 keV electron beam to form the aryne species in much the same way as when adsorbed onto a graphene substrate. However, instead of reacting with the concave interior of the SWNT, PCC molecules undergo Diels-Alder cycloadditions with each other. The aryne (dienophile) requires a near-orthogonal orientation to the adjacent PCC molecule (diene) in order for a cycloaddition to occur, forming an angular adduct $C_{48}Cl_{22}$. Under continuous electron irradiation, the angular adduct loses another two Cl_2 before undergoing radical rearrangements to form the planar adduct $C_{48}Cl_{18}$. The energy profile of the entire reaction was calculated (Fig. 2.5). The beam stability of the angular adduct is due to the relatively high energy barrier for breaking the C=C bond. Further cycloadditions elongate the adduct to form a chlorine-terminated graphene nanoribbon (Cl-GNR).

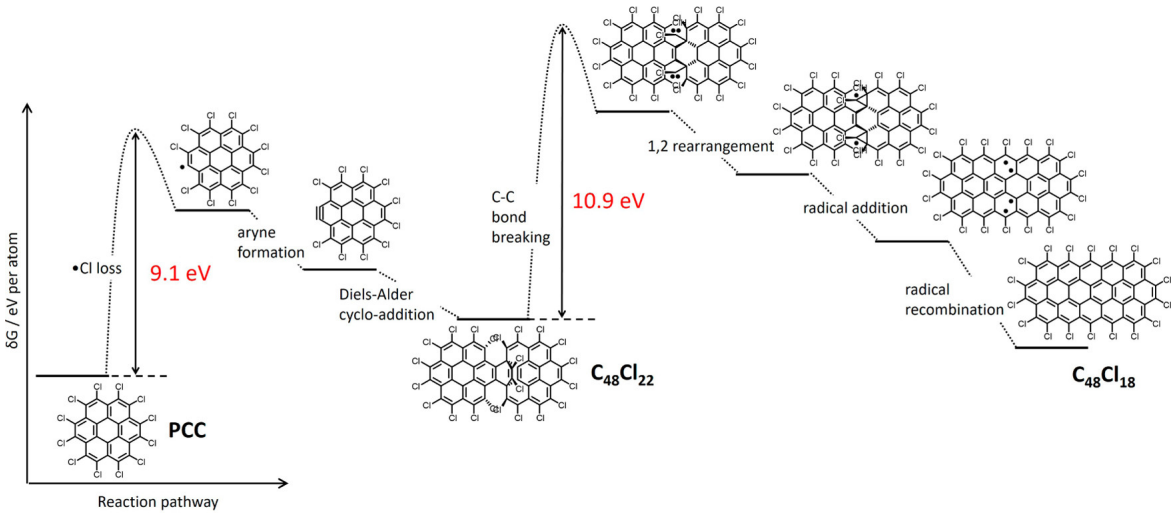

Figure 2.5. The energy profile of PCC dimerisation. Electron beam impact on a carbon atom of PCC causes dissociation of C−Cl bonds, loss of Cl_2, and the formation of a reactive aryne species (the dienophile). The aryne then undergoes a Diels-Alder [2+4]π cyclo-addition with the neighbouring PCC molecule (the diene), leading to the initial angular $C_{48}Cl_{22}$ adduct. Under further irradiation, a C−C bond breaks and the initial adduct loses two Cl_2 molecules before rearranging into the planar $C_{48}Cl_{18}$ adduct with an extended fully aromatic π-system. There are two main energy barriers; 9.1 eV for aryne formation and 10.9 eV for adduct rearrangements. Since the maximum transferrable energy from an 80 keV electron to a carbon atom is 15.8 eV, both of these barriers can be overcome during imaging. Reproduced from T. W. Chamberlain *et al.*, *ACS Nano*, 2017, **11**, 2509-2520. Licensed under ACS AuthorChoice.[7]

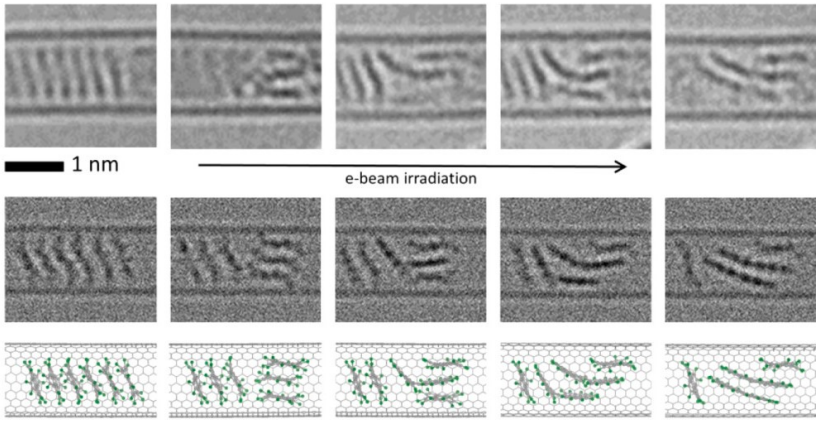

Figure 2.6. Comparison between experimental micrographs (top row) with simulated TEM micrographs (middle row) generated by exposing the corresponding structural models (bottom row) to doses of 1×10^6 e^- nm^{-2} of 80 keV electrons. Both the angular and planar adducts can be seen in the experimental micrographs. Reproduced from T. W. Chamberlain *et al.*, *ACS Nano*, 2017, **11**, 2509-2520. Licensed under ACS AuthorChoice.[7]

Linear polymerisation can only occur inside a SWNT because the nanotube blocks cycloaddition from any other angle (Fig. 2.7) thus templating the formation of a linear graphene nanoribbon, much like the linear polymerisation of $C_{60}O$ inside SWNTs.[11] Were this reaction to occur outside the confines of a nanotube, the product would be a complex polymer with many branches.

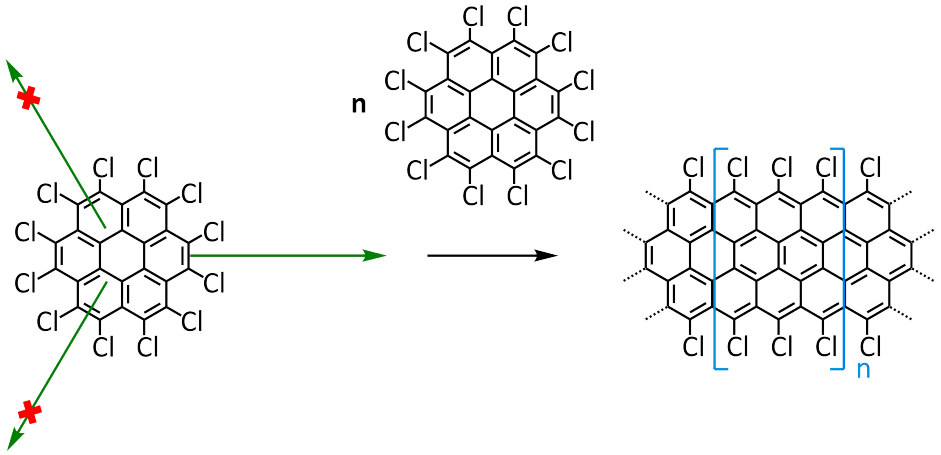

Figure 2.7. PCC can lose Cl_2 from any position around the circumference of the molecule but the SWNT restricts aryne cycloaddition to the one parallel to the nanotube axis, templating the formation of a linear nanoribbon from PCC molecules. Reproduced from T. W. Chamberlain *et al.*, *ACS Nano*, 2017, **11**, 2509-2520. Licensed under ACS AuthorChoice.[7]

This electron beam-induced polymerisation of PCC was recorded as a "stop-frame film" which allowed the elucidation of pathway mechanisms and intermediates, such as the metastable angular adduct (Fig. 2.8).[7] Having introduced the molecule PCC and the relevant high resolution TEM studies carried out on this model molecule, we can say that there is still much we can do to develop our knowledge on PCC polymerisation under the electron beam. This will in turn improve our collective understanding on the effects a high-energy electron beam can have on materials at the atomic level. The work by Chamberlain *et al.* laid solid foundations from which to explore this particular electron beam-induced reaction.

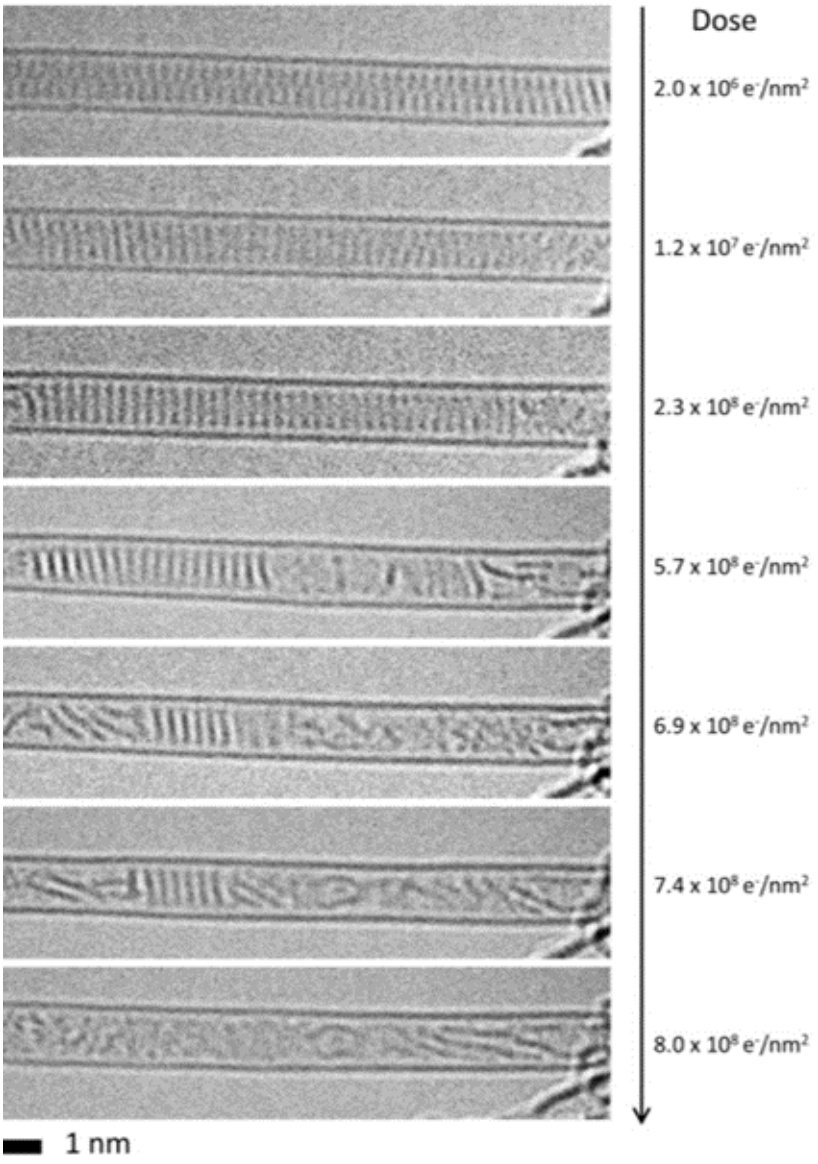

Figure 2.8. A time series of aberration corrected high resolution TEM micrographs showing the polymerisation of PCC into a chlorine-terminated graphene nanoribbon inside the SWNT under an 80 keV electron beam (the cumulative electron doses are shown on the right side of each micrograph). Reproduced from T. W. Chamberlain *et al.*, *ACS Nano*, 2017, **11**, 2509-2520. Licensed under ACS AuthorChoice.[7]

2.2 Aims and Objectives

The aim of this study, applied to PCC polymerisation inside SWNTs, is to develop a general method for studying kinetics at the single-molecule level. This will be the first attempt to follow reaction kinetics in direct-space by counting individual molecules and could be incredibly useful for many other systems. We will also investigate the polymerisation of PCC under different stimuli such as heat and advance the ChemTEM method by decoupling thermal effects from electron beam effects.

Firstly, continued improvements in detector technology will allow the temporal resolution of the reaction to be drastically increased. Use of a more sensitive camera (i.e. one that has a higher pixel count in response to an electron hitting the camera) with a much higher image capture rate (tens to hundreds of images per second) would mean a much lower dose can be used during the reactions for image acquisition. This may reveal more transient intermediates of the reaction. Chamberlain *et al.* used an image capture rate of two images per second. By imaging under a continuous electron beam at a similar dose rate or flux to that used by Chamberlain *et al.*, we can relate the total electron dose required to drive the reaction to completion to the total time taken for the reaction to occur, and therefore study the kinetics of PCC polymerisation.

Secondly, we hope to distinguish between thermal processes and electron beam-induced processes by investigating the effects of temperature on PCC polymerisation. *In situ* heating and cryo sample holders can be used to vary the temperature during imaging from ambient to 1200 ^{o}C as well as cool the sample to liquid nitrogen temperatures. Higher temperatures are likely to increase the rate of reaction, and beyond a threshold temperature polymerisation may occur without the influence of the electron beam. The kinetics of this thermally activated polymerisation can also be studied. Conversely, under cryo temperatures, molecular motion

may become "frozen out" which could significantly slow down polymerisation and increase the lifetimes of intermediates, thus improving the description of the entire reaction.

Thirdly, the use of different stimuli to initiate reactions will be investigated. We can use UV light to initiate the Diels-Alder cycloaddition of two PCC molecules, an idea inspired by the work carried out by Gover *et al.* where the UV laser of a mass spectrometer was used to initiate reactions of carbon-containing molecules such as PAHs.[12]

Finally, we will place the PCC@SWNT system in a wider context by comparison with other large PAHs such as the parent molecule coronene as well as chalcogenide-containing PAHs such as octathio[8]circulene and tetrathio-tetraseleno[8]circulene[13] to see how electron-beam induced reactions and products differ. This will allow for comparison and we can begin to consider trends in stabilities and reactivates of all the PAH molecules involved in this study.

2.3 Results and Discussion

2.3.1 Synthesis and characterisation of PCC

The initial task at hand was to synthesis and characterise PCC itself. PCC was produced through perchlorination of the polycyclic aromatic hydrocarbon (PAH) coronene (the reaction mechanism is shown in Fig. 2.9).[14] Ballester and Molinet discovered the chlorinating agent now known as the BMC reagent, a rather powerful and selective concoction of aluminium (III) chloride, sulfur monochloride, and sulfuryl chloride. The BMC reagent is formed through coordination of sulfur monochloride to aluminium (III) chloride. This attacks the peripheral double bonds of coronene which rearranges to give the chlorine substituent, producing hydrogen chloride as a by-product. The chlorinating agent is then regenerated through abstraction of Cl from sulfuryl chloride (the solvent). Two abstractions produces sulfur dioxide as another by-product. For every substituted chlorine, a molecule of HCl and half a molecule of SO_2 are given off, which boil off as gases. In practice, chlorination of coronene has the unfortunate features of being both hygroscopic and sensitive to moisture. However, typical air sensitive techniques cannot be used because of how much corrosive HCl gas is given off. A compromise of attaching the reaction to a Dreschel bottle containing concentrated sulfuric acid to absorb atmospheric moisture was used. Any tubing used to attach glassware together became thoroughly etched and the setup was usually sweating HCl profusely after the twenty-four-hour long reaction was over. Short of gassing coronene with pure chlorine, this method of electrophilic substitution is the best route, selectively substituting all hydrogens at sp^2 carbon atoms. The BMC reagent is able to push chlorination to completion even while the coronene moiety distorts to accommodate the bulky Cl substituents, further illustrating the high reactivity of the BMC reagent. The yield of PCC was quantitative and analysis of the product showed that only pure PCC is produced.

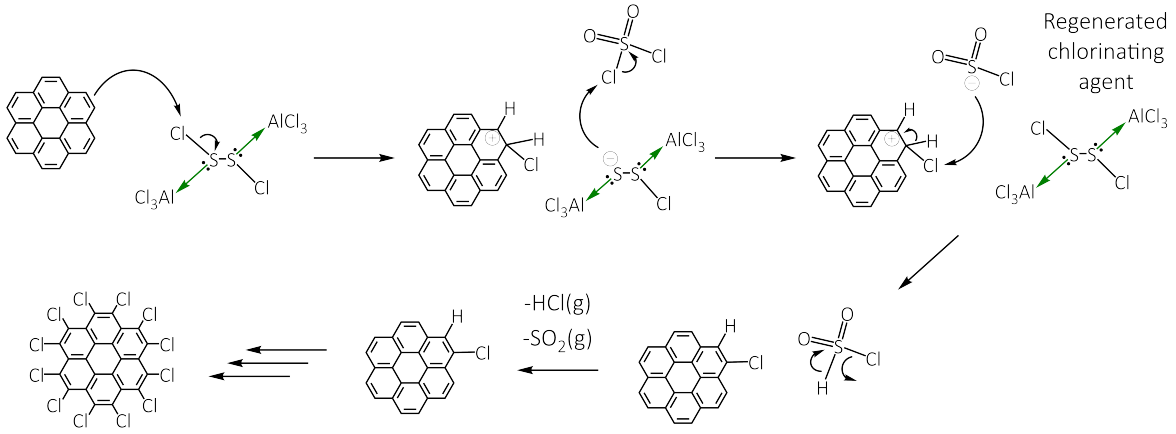

Figure 2.9. The mechanism of the perchlorination of coronene using the BMC chlorinating agent aluminium (III) chloride, sulfur monochloride, and sulfuryl chloride. Sulfur monochloride forms dative bonds (shown as green arrows) with the Lewis acid aluminium (III) chloride to produce an electrophilic source of chlorine which then undergoes electrophilic addition to coronene. The chlorinating agent is regenerated via abstraction of Cl from a sulfuryl chloride solvent molecule.[15,16]

For a long while, the main technique used to characterise PCC was matrix-assisted laser desorption/ionisation time-of-flight (MALDI-ToF) mass spectrometry (Fig. 2.11) due to its stubborn insolubility in most solvents used for nuclear magnetic resonance (NMR) spectroscopy. We were able to collect a high resolution ^{13}C NMR spectrum (Fig. 2.10) by using a long (16 hour) scan on a 500 MHz machine. Both analytical techniques showed that the product was purely PCC and therefore did not require further purification.

Interestingly, the MALDI-ToF spectrum of PCC showed a regular pattern of fragmentation (see Fig. 2.11) where there were peaks at 642, 572, and 500 m/z corresponding to sequential loss of Cl_2 from the parent molecule, forming the species $C_{24}Cl_{10}$, $C_{24}Cl_8$, and $C_{24}Cl_6$ respectively. This was reminiscent of the first step of the irradiation-induced polymerisation of PCC (Fig. 2.3) where there was loss of Cl_2 to produce an aryne. There was no loss of just a single Cl nor further loss after three Cl_2 which immediately suggested that the loss of Cl_2 was symmetrical around the molecule. This arrangement of C=C would have the most planar structure which would reduce steric strain from the bulky Cl groups (Fig. 2.11). There

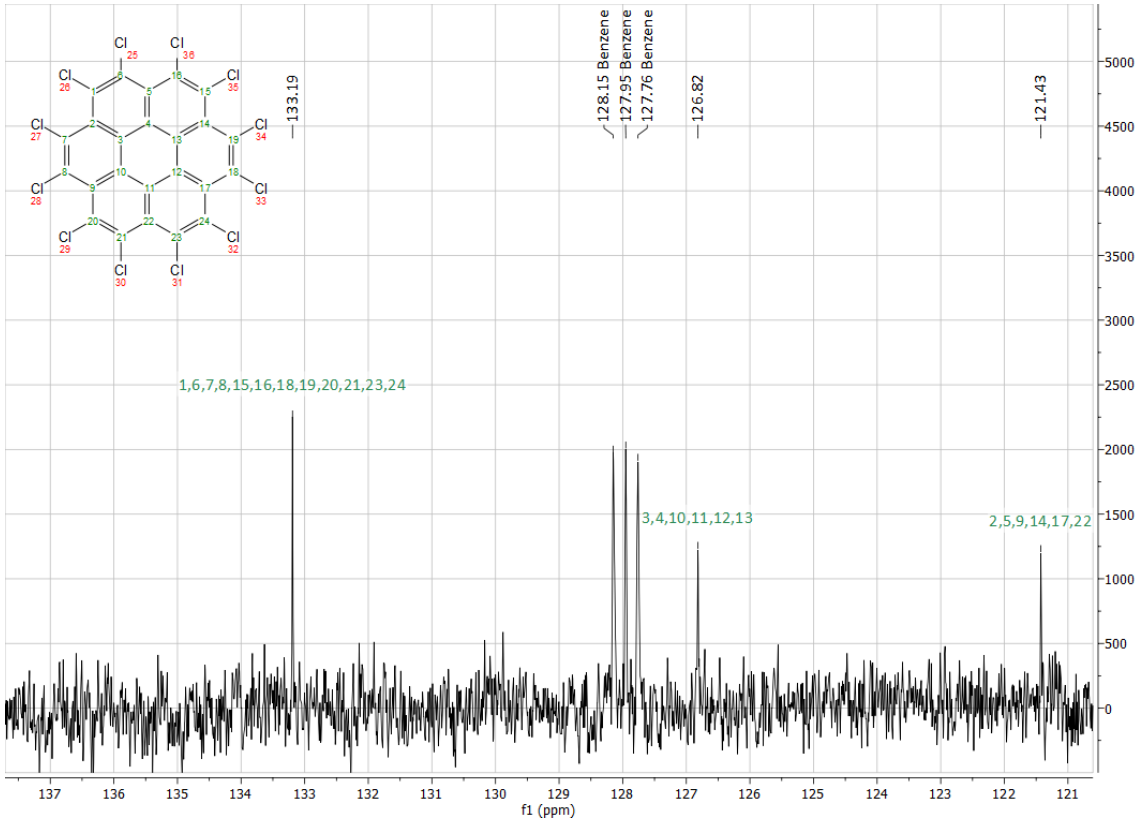

Figure 2.10. The ^{13}C NMR spectrum of PCC. The PCC peaks are labelled with the structure adjacent. The incredibly high sensitivity of this NMR experiment meant that insignificant quantities of benzene were detected. This impurity was likely on the surface of the glass NMR tube since the same tubes are reused for different NMR experiments using different solvents such as deuterated benzene. Therefore benzene is not present in the PCC product.

was no further loss of Cl_2 from the molecule likely because introduction of more C=C bonds would induce too much strain in the molecule. This symmetrical loss of Cl_2 around the molecule also suggested that, without a nanotube as a templating reaction container, PCC would polymerise in those three directions (Fig. 2.7) rather than forming a linear oligomer. The discovery of the reactive aryne species in MALDI-ToF prompted a repeat of the MALDI experiment but at a higher laser power (from 8% to 20% of the 355 nm laser) to see if this increase in power would induce any reactions between PCC molecules and indeed, this was the case (Fig. 2.11).

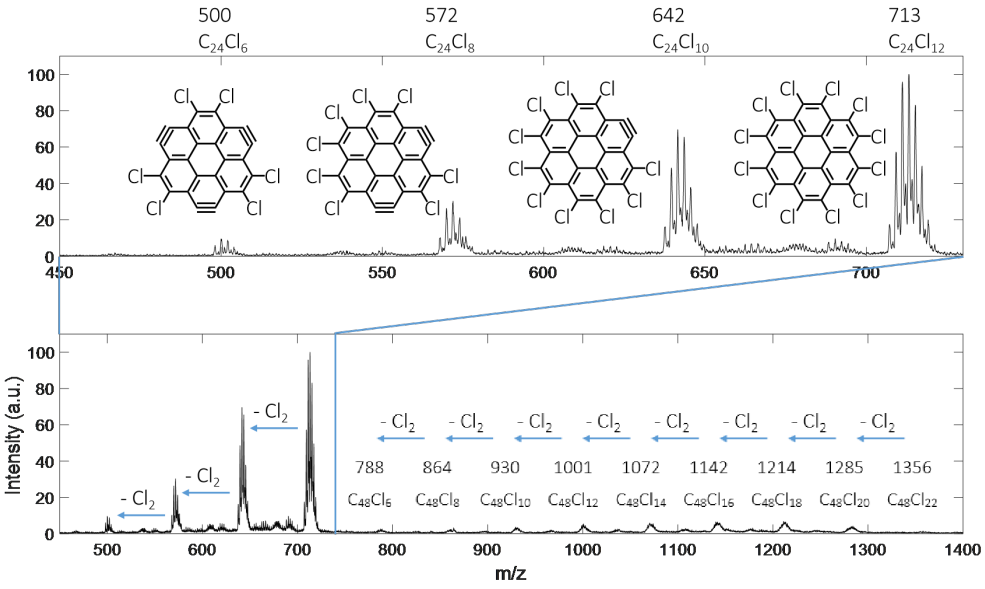

Figure 2.11. The MALDI-ToF mass spectrum of perchlorocoronene (PCC), taken using a 355 nm laser at 20% laser power without use of a matrix. The top spectrum is an expansion of the region showing the molecular ion peaks at 713 m/z as well as fragmentation of the parent ion via successive loss of Cl_2 forming the arynes at 642, 572, and 500 m/z; the bottom spectrum shows the adducts of PCC dimerisation under the UV laser as well as fragmentation peaks due to loss of Cl_2.

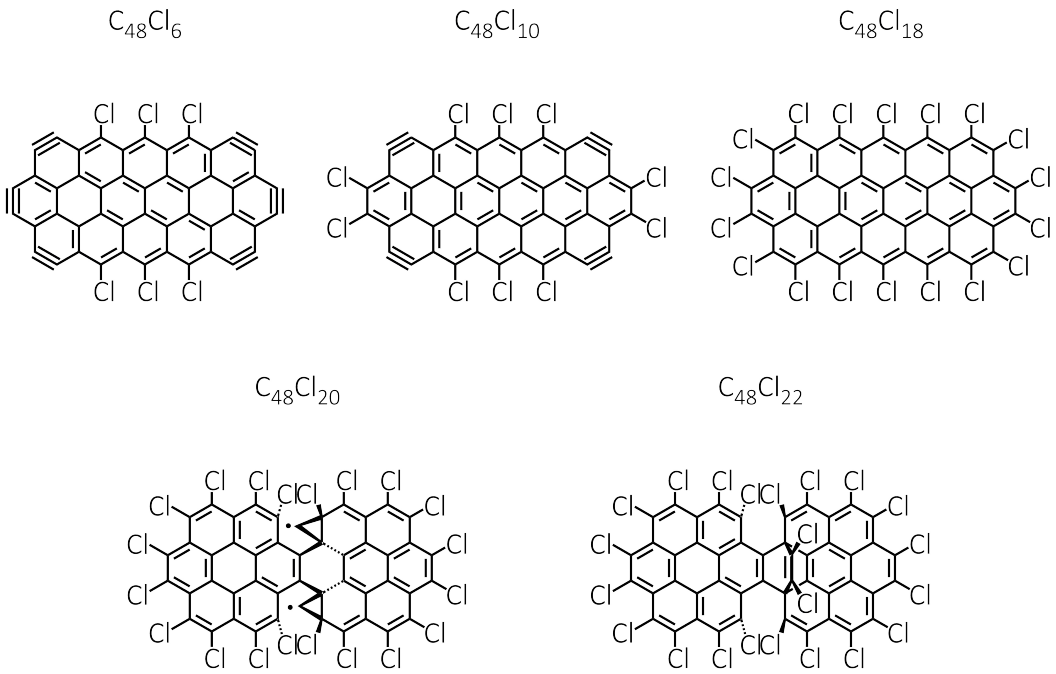

Figure 2.12. Proposed structures of the planar adducts after fragmentation through loss of Cl_2.

As can be seen, there were several peaks with m/z values much greater than that of PCC. There may be a miniscule peak at 1356 m/z corresponding to $C_{48}Cl_{22}$, the initial angular adduct formed from the Diels-Alder [2+4]π cyclo-addition of two PCC molecules (Fig. 2.12). The next peak observed was at 1285 m/z which corresponded to $C_{48}Cl_{20}$, a species likely formed from the loss of Cl_2 from the initial angular adduct (Fig. 2.12). The next peak at 1214 m/z corresponded to the planar adduct (Fig. 2.12), which formed from the loss of Cl_2 and rearrangement from the previous angular adduct. This planar adduct then fragmented in a similar manner to the PCC molecule, sequentially losing six Cl_2 from two adjacent C atoms, forming triple bonds around the curved ends of the adduct. This seemed the most likely path (rather than losing multiple Cl_2 before dimerising) as the most intense peaks are higher in m/z value. As with PCC, the triple bonds were likely to have occupied alternate positions (as shown in Fig. 2.12) until finally 6 Cl_2 molecules were lost from the adduct to give $C_{48}Cl_6$. Inbetween each major peak from loss of Cl_2 were minor peaks which likely corresponded to loss of one Cl atom. These odd-numbered-Cl species were less populated, suggesting that loss of one Cl atom was not as favourable as loss of two. Again, this was attributed to preferential formation of aryne species.

The MALDI-ToF results show that the UV laser can cause similar reactions to those induced by the TEM electron beam which suggests that such electron beam-induced reactions are possible using other energy sources (this was a major theme in the work carried out by Gover *et al.* on PAHs).[12] It is rather interesting to find that electron beam-induced PCC polymerisation is not some isolated incident inside the TEM. This has implications for the beam-induced mechanism. If there is a pathway via UV irradiation, there is likely an equivalent electronic excitation pathway via electron-electron collisions. However, this may not happen when PCC molecules are encapsulated inside conductive SWNTs.

2.3.2 Electron beam-induced polymerisation of PCC in SWNTs

We began by imaging a filled nanotube at ambient temperature under continuous and constant 80 kV irradiation (we used 80 kV throughout this work) so we would have a baseline from which to work on. The following describes our observations.

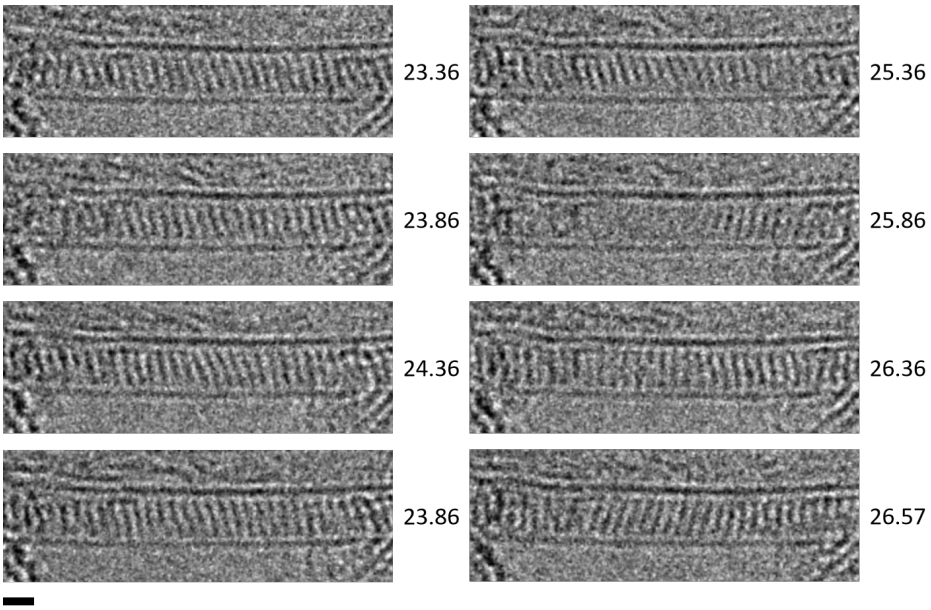

Figure 2.13. A series of micrographs illustrating the PCC stack changing orientation (or "shuffling") inside the nanotube. Shuffling of the stack is required to create sufficient space for the polymerisation reaction. The electron flux used was 2.17×10^{6} e^{-} nm^{-2} s^{-1}. The scale bar is 1 nm. Time stamps are in the format seconds.milliseconds.

There was a distinct "latent" period at the beginning of irradiation when nothing appreciable happened (Fig. 2.13). The stack of PCC molecules did not seem to react and the column orientation flipped slightly from slanting left to slanting right. This "shuffling" is perhaps important for achieving the near-orthogonal orientation requirement of a Diels-Alder cycloaddition. The time required to induce sufficient shuffling is one reason why PCC molecules inside SWNTs are so stable to the electron beam. Cl atoms could still be knocked out to form an aryne and Cl radicals but these reactive species are likely to recombine when the aryne cannot react with an adjacent molecule. In total, at a flux of 2.17×10^{6} e^{-} nm^{-2} s^{-1}, the stack

shuffling took place over 38.45 s before we saw the formation of any dimers. This corresponded to a dose of 8.34×10^{7} e^{-} nm^{-2}.

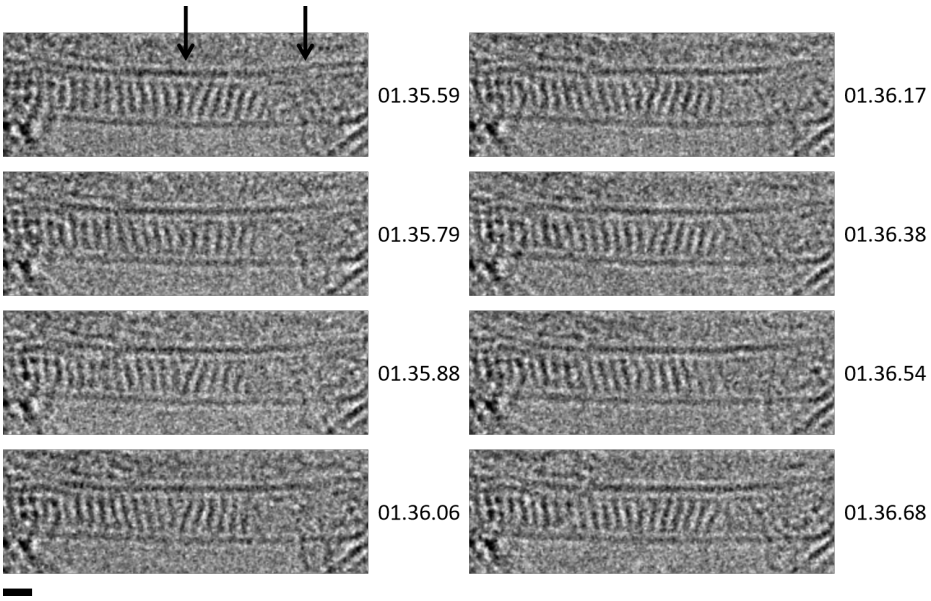

Figure 2.14. A molecule of PCC within the stack changing orientation over a second of imaging. The black arrow on the right of the nanotube indicates a region of blurriness where molecular motion is rapid and polymerisation had begun. The polymer is able to twist, freeing up space for additional movement. This can be seen with the apparently Y-shaped molecule indicated by the black arrow on the left. PCC has no additional appendages and should not be this shape. This is due to movement of a PCC molecule within the stack during image capture, giving the illusion of some Y-shaped entity. The electron flux used was 2.17×10^{6} e^{-} nm^{-2} s^{-1}. The scale bar is 1 nm. Time stamps are in the format minutes.seconds.milliseconds.

Once the reaction had initiated, there was a slow (over several minutes) domino effect where the polymerisation continued along the nanotube from the location where the first dimer was formed. The right side of the nanotube in Fig. 2.14 had some indistinct lines where the nanoribbon had started to form. The soon-to-be-nanoribbon could allow PCC molecules to shuffle more since the polymer could twist and was not pressed into a tight stack formation. The micrographs sometimes appeared to have a Y-shaped molecule in the middle of the nanotube which was not present before the appearance of the first dimer. This was likely when a PCC molecule moved during the image capture. Given that the capture rate was a hun-

dred frames per second, this highlights the increased freedom of movement of PCC molecules once polymerisation had been initiated. Movement of PCC molecules during image capture was also observed by Markevich *et al.* (see Fig. 2.2a).[6]

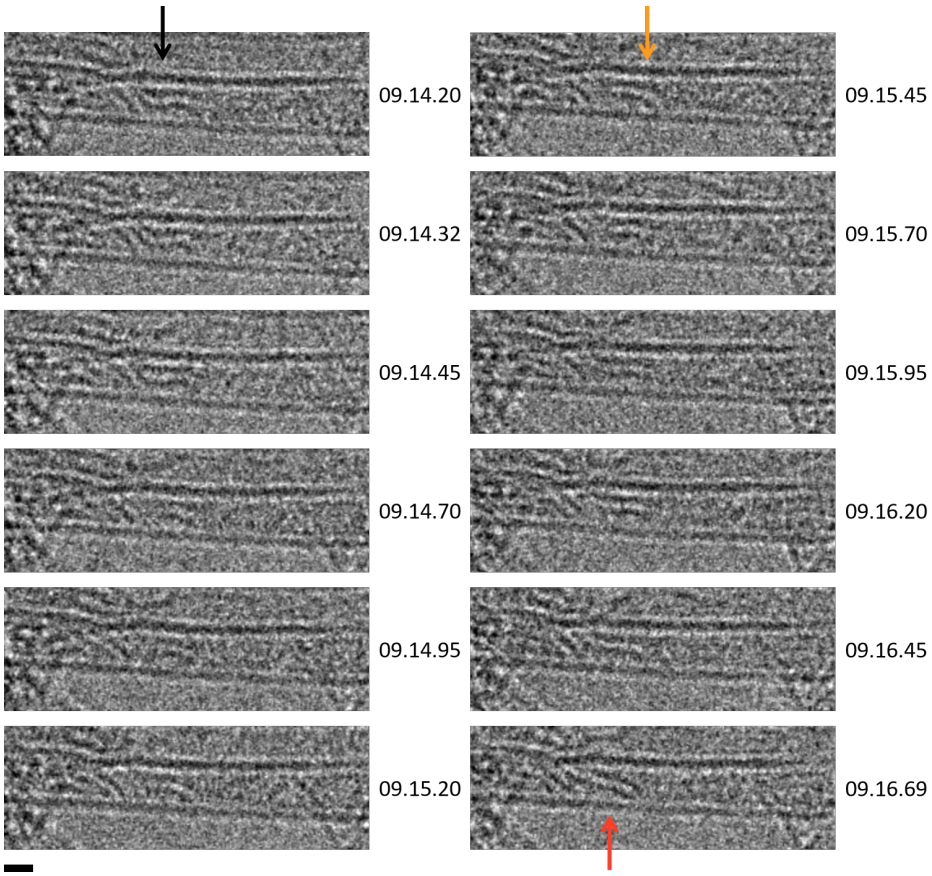

Figure 2.15. A series of micrographs showing the planarisation of two adducts. These adducts are indicated by the black arrow and appear as two parallel wiggly lines. The lines have two "kinks", suggesting two joins between three molecules i.e. the adducts are both trimers. Over a period of imaging (approximately 2.49 s), the two wiggly lines became two straight parallel lines (indicated by the red arrow). The adducts appeared to planarise sequentially; the left sides of both of the angular adducts became planar before the right sides (indicated by the orange arrow). The electron flux used was 2.17×10^6 e^- nm^{-2} s^{-1}. The scale bar is 1 nm. Time stamps are in the format minutes.seconds.milliseconds.

We were able to capture quite a number of frames for some intermediates. An example is illustrated in Fig. 2.15. Two angular trimers indicated by a black arrow (there were two "kinks" in the adducts indicating two joins between three molecules) underwent a series of rearrangements to give planar trimers over approximately

2.49 s (the exact length of time was difficult to determine because the trimers moved during image capture and blurred some images). It appeared as though the parts of the trimers undergoing rearrangement became blurrier, suggesting increased movement or vibration. The left sides of the angular trimers went blurry first, followed by the right sides. The half planar, half angular trimers are shown by the orange arrow. This suggested that the rearrangements occurred sequentially along the trimers rather than simultaneously. Perhaps this was encouraged by the fact that these two trimers were stacked together. Sequential planarisation would maintain maximum π-π stacking between the two trimers. After the rearrangements, the planar trimers appeared as two distinct lines again (indicated by a red arrow).

The overall reaction is shown in Fig. 2.18 which takes place over 9 minutes and 29.09 seconds (or 569.09 s). This corresponds to a total dose of 1.23×10^9 e^- nm^{-2}. By following the reaction over time, we would be able to calculate the electron beam-induced reaction rate constant and subsequently the experimental cross section of the electron beam-induced dimerisation reaction. This prospect was quite exciting for us because we would be able to describe the kinetics of a reaction on the single-molecule level. We should point out here that this kinetics study is *mechanism-agnostic*, meaning that the maths does not depend on the damage mechanisms, whether this be via direct knock-on, radiolysis etc. This is similar to the work by Skowron *et al.* on the reversible Stone-Wales bond rotation.[17] Therefore, we can study the kinetics of electron beam-induced PCC polymerisation and use this information to provide insight into the exact nature of the damage mechanisms. We shall discuss this in more detail later (see the paragraph on the value of k_{obs}).

What can we measure? We can observe either a single molecule (a straight line) or a polymer (curved lines of various lengths) using TEM. After a dimerisation, the molecules are far more mobile and the type of adduct (angular or planar) or

how many PCC molecules had reacted to form this polymer becomes somewhat of a nebulous topic due to rotation and translation of the products. The products also have lower contrast than the starting stack of PCC molecules, making the products more difficult to see in a micrograph. Experimentally, the best way of following the progress of PCC polymerisation is to follow the loss of PCC molecules since the products are often blurred in the images.

In a typical kinetics study, the order of reaction can be found by changing the concentration of various reactants in a solution and observing whether that has an effect on the rate of reaction. This is not possible for the PCC@SWNTs system because PCC molecules self assemble into a stack of molecules separated by their van der Waals radii. Therefore, the "concentration" of PCC molecules inside a SWNTs remains constant and would be impossible to control.

What is concentration at the single-molecule level? Naturally, we cannot describe a concentration for PCC as we would for solution reactions since PCC@SWNTs has no solvent and the concentration would not be mol dm^{-3}. We could describe the "concentration" of PCC@SWNTs as number of molecules per area. The reason for an areal number density is because the driving force for the polymerisation of PCC is the electron beam which is directional. The beam strikes an area of the sample per unit time. The areal number density for PCC@SWNTs could be described as the number of molecules $nPCC$ per area of nanotube A_0. The area of nanotube is defined here as the nanotube width multiplied by the length of nanotube occupied by molecules at the beginning of imaging (i.e. when t = 0 s). The nanotube area does not change over the course of the reaction so we should see a decrease in $nPCC/A_0$ (the “concentration” in our reaction) over time. As this is an electron beam-induced reaction, the reaction proceeds with dose rather than with time. However, since we have kept the flux constant, we can use t to describe the reaction progress since this is more intuitive from a chemist’s perspective.

What is the order of the reaction? We observed a linear decrease in $nPCC/A_0$ over time following the latent period at the beginning of the reaction. This suggests that the observable reaction is zero order. A bulk example might be a catalytic surface saturated with reagents where there is a bottleneck which limits how many reagent molecules can react at the same time. Many enzyme-catalysed reactions are zero order due to saturation of enzyme active sites with the substrate. In our case, the PCC molecules are packed as closely as they physically can be and thus our “concentration” is at a maximum. The strict conformation requirement of the Diels-Alder cycloaddition is the "bottleneck". Therefore, disappearance of individual PCC molecules (which polymerise) has an observable rate constant of k_{obs} (Eq. 2.1).

$$2PCC \xrightarrow{k_{obs}} Dimer$$

Equation 2.1. The dimerisation of PCC has an observable rate constant of k_{obs}.

The differential form of this zero order reaction is written in Eq. 2.2.

$$k_{obs}(nPCC_0/A_0) = -\frac{d(nPCC/A_0)}{dt}$$

Equation 2.2. The zero order differential rate equation of PCC dimerisation with rate constant k_{obs}.

This can be rearranged and integrated to get the integral form of a zero order reaction (Eq. 2.3).

$$(nPCC/A_0) = -k_{obs}t + (nPCC_0/A_0)$$

Equation 2.3. The zero order integrated rate equation of PCC dimerisation with rate constant k_{obs}.

From the zero order rate equation above, we can find the gradient $-k_{obs}$ using the linear plot of $nPCC/A_0$ (concentration) against time (Fig. 2.16).

The linear plot has a gradient of -0.002450 nm^{-2} s^{-1}. Using this value of k_{obs} and the irradiation-induced reaction rate equation from chapter one, the observed reaction cross section σ_{obs} was calculated to be 1.13×10^{-9} nm^2 or 11.3 barn with an error of $\pm$0.574 barn. Errors arise from measurements of the nanotube length which affects the values of $nPCC/A_0$ as well as temporal resolution and deviation in electron flux over the course of imaging. The largest contribution to error was the fluctuation in flux which was largely beyond our control since the electron flux or brightness of the beam was not altered during irradiation.

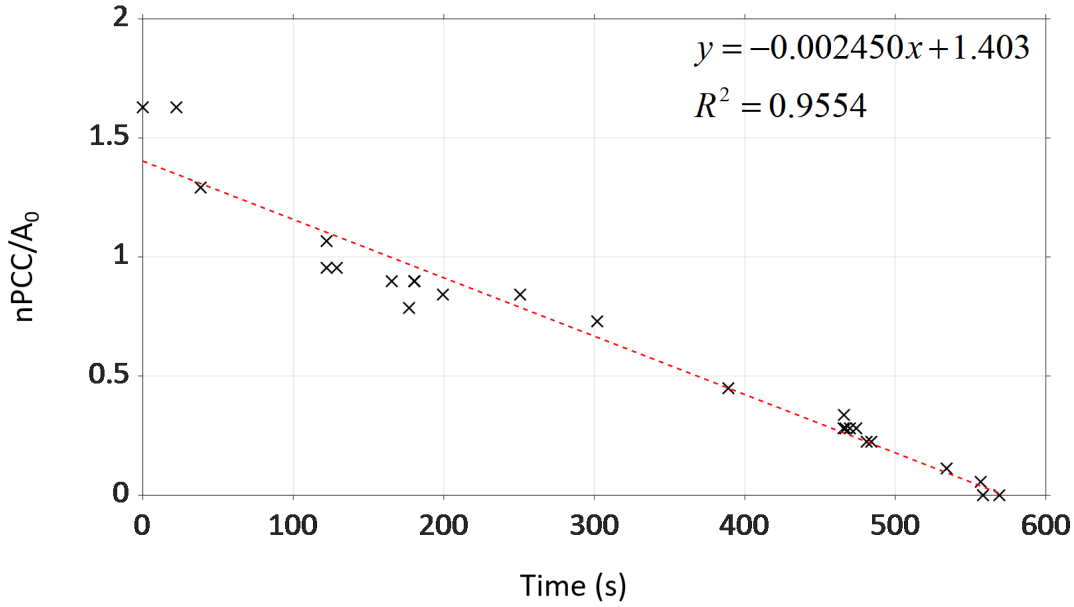

Figure 2.16. The electron beam-induced PCC polymerisation has a linear decrease in number of PCC molecules per total area of nanotube ($nPCC/A_0$) over time. The R-square value of the linear fit is 0.9554. Each data point in this plot corresponds to each time stamped image in Fig. 2.18 apart from t = 0 s when irradiation had not begun (and there is no image) and t = 04.06.31 where the molecules in that image were too blurry to be counted.

The observed reaction cross section σ_{obs} has no physical meaning since this electron beam-induced reaction should not be zero order; the saturation of the system with PCC molecules and the inherent steric requirements of a Diels-Alder cycloaddition led to an apparent zero order reaction. Therefore, we cannot say whether this 11.3 barn is the cross section of a particular process during PCC poly-

merisation. However, this does not mean that calculation of a reaction cross section is irrelevant. The value of 11.3 barn is orders of magnitude lower than what we might expect for a system that reacts via radiolysis.[18]

The upper limit of the cross section of Cl emission from PCC was calculated to be 159 barn by S. T. Skowron (found in the SI by Chamberlain et al.[7]). There can be many orientations and angles between the incident beam and a PCC molecule. Not all collisions will result in Cl emission and formation of the reactive aryne. The orientation where energy can be transferred most efficiently is when the C-Cl and adjacent C-C bonds are parallel to the electron beam. An incident electron transfers energy directly along these bonds which can lead to atom emission. This orientation and angle was used to calculate the cross section (rather than a systematic sweep of all possible orientations and angles). This isotropic approximation of the threshold energy means that the calculated cross section overestimates the emission cross sections and are the upper limits for the process. The calculated cross section is not the cross section for PCC dimerisation, however, as it cannot take into account the Diels-Alder cycloaddition or the orientation requirements of this reaction. Atom emission does not automatically result in dimerisation of PCC. We have seen that stack shuffling took up a significant amount of time, during which any emitted Cl atoms could react back with the aryne because the aryne could not react with any adjacent PCC molecules. The much smaller experimental cross section of 11.3 barn is consistent with direct knock-on damage as the key mechanism for the electron beam-induced polymerisation of PCC. A larger experimental cross section (than the calculated one) would suggest other mechanisms were in play, such as radiolysis.

On a slight tangent, we would like to compare the differences we observed between PCC@SWNTs and nanoscale crystals of PCC. We discuss PCC crystals in more detail in chapter three (including crystallisation, irradiation, and analysis).

We attempted to image nanoscale crystals of PCC at a similar electron flux as PCC@SWNTs. There was a significant difference between the two systems. PCC encapsulated within SWNTs could be imaged easily over a period of several minutes (Fig. 2.18) without much change in the system. The PCC crystal, on the other hand, rapidly became amorphous after seconds of irradiation (Fig. 2.17) and it was not possible to image the d-spacing at an electron flux of 2.25×10^{5} e^{-} nm^{-2} s^{-1}; compare this to the 2.17×10^{6} e^{-} nm^{-2} s^{-1} flux used for PCC@SWNTs.

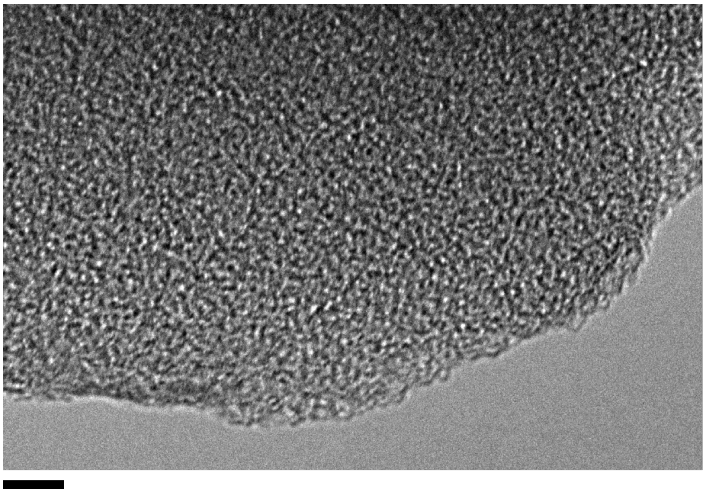

Figure 2.17. A nanoscale crystal of PCC was imaged at an electron flux of 2.25×10^{5} e^{-} nm^{-2} s^{-1}. The scale bar is 5 nm. The electron beam may have been positioned over this crystal for a number of seconds before acquiring this first image. Even before the camera could capture a micrograph of the crystal, it had turned amorphous under the electron beam. This is in stark contrast to the PCC molecules encapsulated within SWNTs, which were stable for many minutes (Fig. 2.18).

The differences in behaviour under the electron beam between PCC in SWNTs and in crystal form suggest that the host SWNT offers beam stability to the encapsulated PCC molecules. This may be because PCC@SWNTs are much thinner than PCC crystals and are electrically and thermally conductive. Charging and heating effects are minimised and direct knock-on likely dominates in conductive materials.[18] Radiolysis, heating, and charging are likely culprits for such rapid disintegration of the PCC crystals. This is further supported by the fact that reducing

the incident flux on the crystals allowed collection of diffraction data and negligible change to the overall crystal structure (see chapter three for the discussion). Reducing the incident flux reduces heating and charging effects on an insulating sample, thereby reducing the rate of beam damage.[18]

Another value which is also important to discuss is k_{obs}. This value can be compared between experiments similar to how the rates of enzyme catalysis can be compared. Key amino acids in an enzyme active site can be substituted, leading to changes in the rate of catalysis. This can give information on the role of those amino acids during catalysis as well as how such amino acid mutations can lead to diseases by affecting the biological functions of the enzyme. Changing experimental conditions such as temperature and accelerating voltage may affect the k_{obs} for PCC polymerisation. For example, heating may increase k_{obs} since increased thermal energy is likely to increase the rate of PCC shuffling within the SWNT. If PCC polymerisation is dominated by knock-on damage, reducing the temperature will not have an effect on k_{obs}. However, if radiolysis is a major component of the reaction, cryogenic temperatures can reduce the rate of radiolysis and therefore k_{obs} would decrease.[18] In summary, comparing values of k_{obs} from different experimental conditions can give information on the precise nature of the reaction mechanism of PCC polymerisation.

This rather exciting adventure into exploring kinetics at the single-molecule level has shown us how to approach such endeavours in the future and could be applied to many other systems in SWNTs.

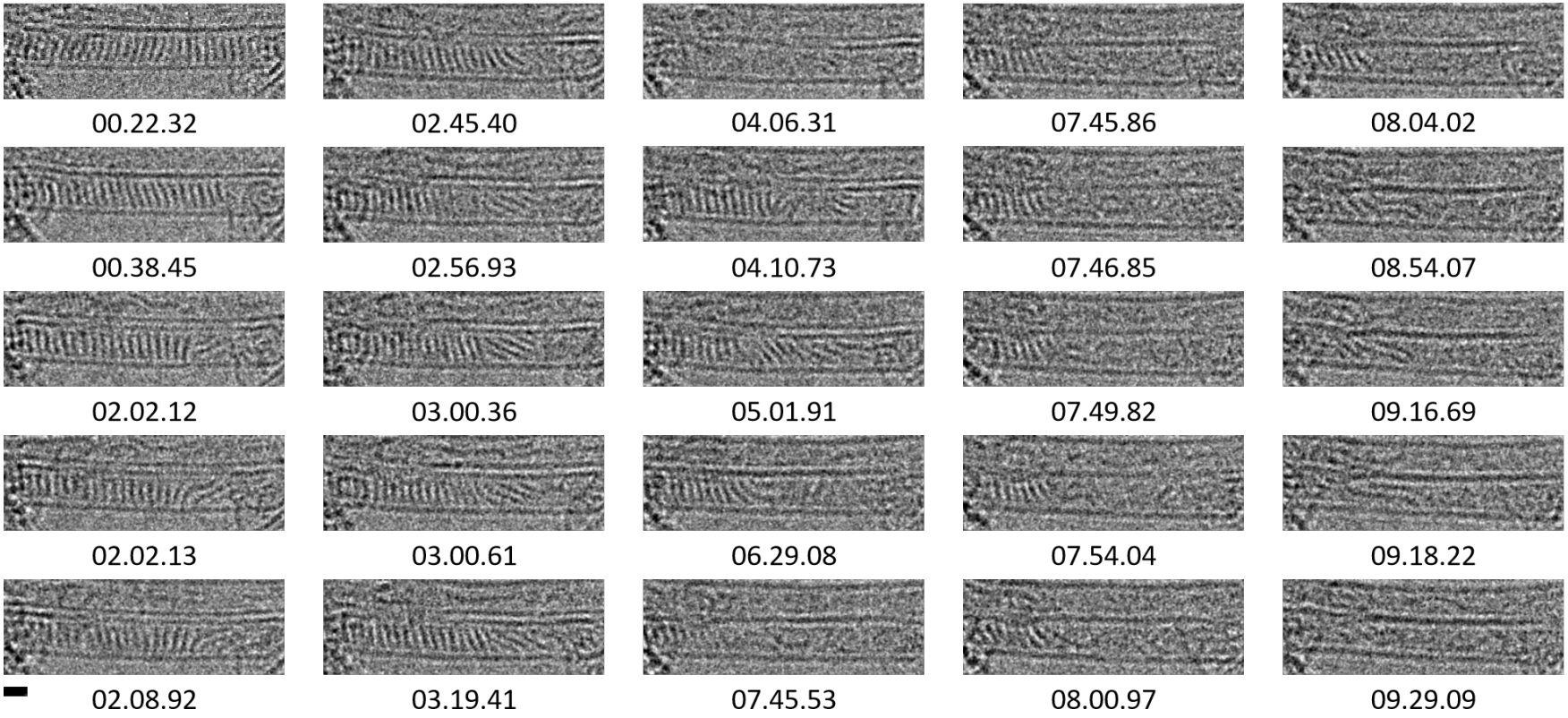

Figure 2.18. The overall electron beam-induced reaction from a stack of PCC molecules inside a nanotube to a chlorine-terminated graphene nanoribbon. Aspects of this reaction have been explored in Figs. 2.13, 2.14, and 2.15. The electron flux used was 2.17×10^{6} e^{-} nm^{-2} s^{-1} over a period of 569.09 s which corresponded to a total dose of 1.23×10^{9} e^{-} nm^{-2}. The scale bar is 1 nm. Time stamps are in the format minutes.seconds.milliseconds.

We then carried out a series of experiments at 23 ^{o}C using electron fluxes on the order of 10^5 e^- nm^{-2} s^{-1} and a slower image capture rate of ten frames per second for comparison to future heating and cryogenic experiments (Fig. 2.19). We reduced the flux by an order of magnitude to reduce the rate of reaction and took frames with a longer exposure time (and therefore fewer frames per second) so we would still have reasonable temporal resolution of the reactions without being completely overwhelmed with data. A sample of PCC@SWNTs does not have any repeating units to image (such as you might find with a sheet of graphene) so hunting for individual nanotubes suspended over vacuum in a (relatively) vast web of nanotube bundles was time consuming. TEMs are known for being terrible at sampling so we must be careful when drawing general conclusions about our sample.

Since nanotubes are of varying lengths, we decided to compare the electron dose required for first dimer formation rather than for the final nanoribbon. We expected some range of doses required since each nanotube (and therefore each molecular stack) was slightly different. However, the doses varied by an order of magnitude, from 5.43×10^6 e^- nm^{-2} to 6.30×10^7 e^- nm^{-2}. Upon closer inspection, the dose required seemed to be related to how the PCC molecules were stacked inside the nanotube. A nanotube with a larger diameter than a PCC molecule (diameter of 1.41 nm) would allow the packing of a stack almost perpendicular to the nanotube wall. This was the case for the nanotube in Fig. 2.19 a) which had a diameter of 1.61 nm. The molecules in this nanotube required the highest dose to form the first dimer (taking over two minutes) which is why there is no final nanoribbon micrograph for this example since that would take a long time (and therefore mean less time would be spent imaging other nanotubes). The filled nanotube in Fig. 2.19 b) had a similar diameter of 1.66 nm. However, the first dimer formation took much less time than the example in Fig. 2.19 a). Since only a smaller section of the

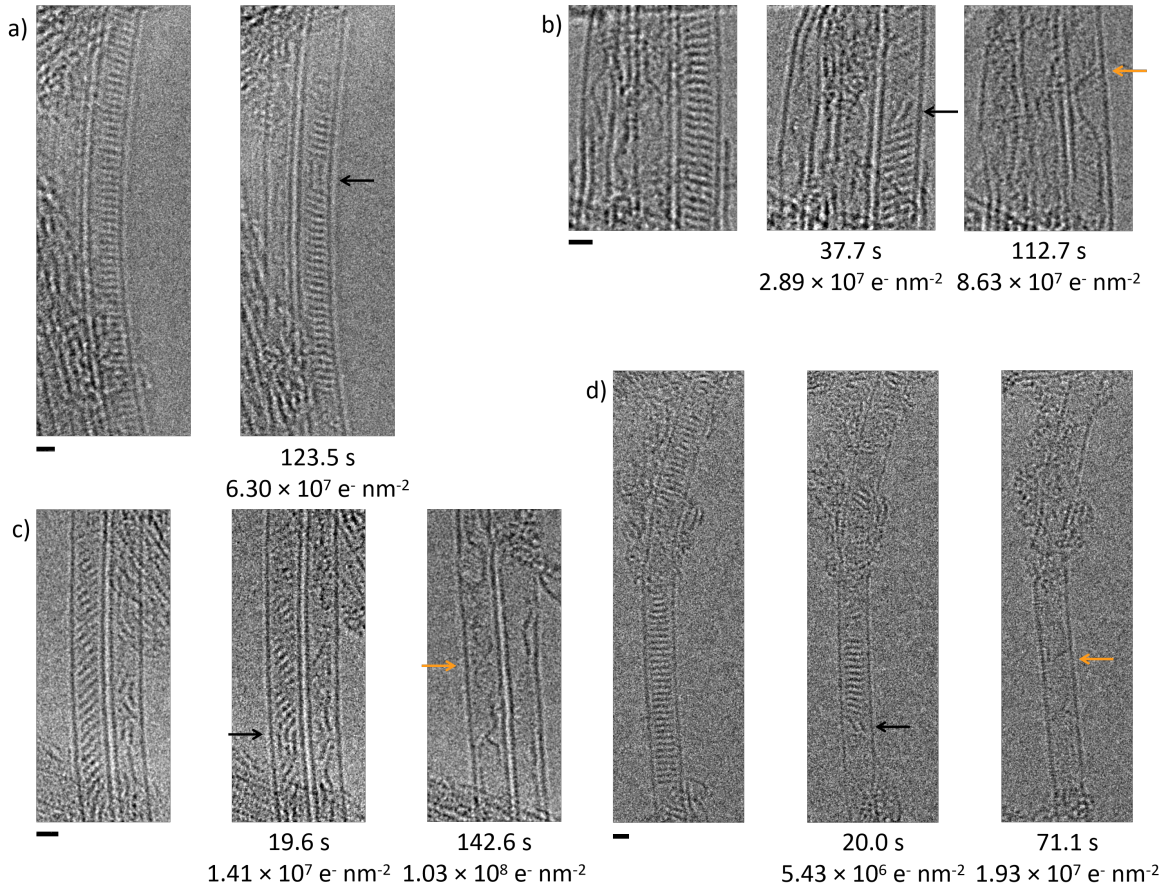

Figure 2.19. Several image series of PCC@SWNT were acquired at 23 ^{o}C for comparison to future heating and cryogenic experiments. For each series of images, the first image is shown alongside the image of the first dimer (black arrows) and, where appropriate, the final image of the nanoribbon (twists in the nanoribbons are indicated with orange arrows). Time stamps and electron doses for the later images have been given. a) This nanotube had a diameter of 1.61 nm. The PCC stack in this nanotube took the longest time (and therefore largest total dose) to form the first dimer. The final nanoribbon is not shown because we did not continue imaging for such a length of time. The electron flux used was 5.10×10^{5} e^{-} nm^{-2} s^{-1}. b) This nanotube had a diameter of 1.66 nm. Images for the first dimer and the final nanoribbon are shown. The electron flux used was 7.65×10^{5} e^{-} nm^{-2} s^{-1}. c) The left nanotube had a diameter of 1.41 nm while the right nanotube had a diameter of 1.33 nm. There were two nanotubes in this particular image series. The nanotube we focused on was the one on the left, however we also discussed the right nanotube in the main text. The electron flux used was 7.20×10^{5} e^{-} nm^{-2} s^{-1}. d) This nanotube had a diameter of 1.79 nm. Images for the first dimer and the final nanoribbon are shown. The electron flux used was 2.72×10^{5} e^{-} nm^{-2} s^{-1}. The scale bars are 1 nm.

nanotube could be imaged, perhaps there were defects in the nanotube elsewhere that allowed for more shuffling of the stack and therefore faster formation of the first dimer. These two similar nanotubes with their different reactions do illustrate the importance of imaging as much of the sample as possible in order to avoid using only a few non-representative areas.

Narrower nanotubes, such as the left nanotube in Fig. 2.19 c) with a diameter of 1.41 nm, can only accommodate a stack of PCC molecules if that stack is at a slant (the PCC plane is at 49° with respect to the nanotube axis). As a result, these slanted molecules took less "shuffling" to achieve the orthogonal orientation required for a Diels-Alder cycloaddition. The right nanotube in Fig. 2.19 c) had an even smaller diameter of 1.33 nm and did not seem to contain any sort of organised stack parallel to the tube. At the beginning of imaging, some of the disorganised molecules in the right nanotube appeared to already have begun reacting.

Similarly, if a nanotube contains some kind of structural defect (such as the one in Fig. 2.19 d) which appeared to have had a slight mishap in the middle), there would be less efficient packing of PCC molecules and therefore more room for re-orientation. This example, which incidentally had the largest diameter of 1.79 nm, required the lowest dose to form both the first dimer and the final nanoribbon. It could be that fewer PCC molecules filled into a nanotube with a defect and so the entire polymerisation would be faster anyway, or the defect allowed for much faster polymerisation because this did not allow PCC molecules to pack as tightly together. These results suggest that confinement in the nanotube (which places a restriction on how the molecules might react) is a significant contribution to the high beam stability of PCC@SWNT.

It is worth noting at this point that we have had to be quite selective with the nanotubes we image. In general, the nanotubes we were able to image were relatively straight because they had to be anchored tightly at both ends. Otherwise,

the nanotubes were likely to bounce in and out of the plane of focus during imaging due to the high energy electron beam. Any movement or vibration in the x/y directions can be compensated for by the fast camera but z movement requires manual correction. We chose not to image nanotubes that moved too much as these image series tended to be blurrier than most (and therefore contain less useful information). If, instead, we could easily image curved and twisted nanotubes, we might see that those molecules inside would be even more inclined to react faster due to the curvature of the nanotube.

2.3.3 *In situ* heating of PCC@SWNTs

A major barrier for the Diels-Alder cycloaddition is the orientation of PCC molecules with respect to one another. The PCC-PCC binding energy in the SWNT would therefore be useful to know. This was calculated by S. E. Mason to be 97.5 kJ mol^{-1} at the B3LYP/6-31G level of theory with counterpoise correction and a 13,13 SWNT represented via the AIRBED (Atomic Interactions Represented By Empirical Dispersion) method.[19] This is essentially the difference in energy between two stacked PCC molecules in their friendly ground state configuration in a SWNT, and the two molecules infinitely separated while still remaining in the nanotube. If a sample of PCC@SWNTs is heated so that this binding energy can be overcome using thermal energy, it will likely increase the rate of stack shuffling and therefore the rate of polymerisation.

Heating of PCC in SWNTs can be carried out *in situ* using a TEM heating stage. Increasing the thermal energy is likely to increase the rate of "shuffling" of PCC molecules which may increase the rate of polymerisation, and therefore the value of k_{obs}. PCC was filled into SWNTs via sublimation under vacuum at 400 ^{o}C so it seemed reasonable to try heating at 400 ^{o}C first to enhance the "shuffling" rate of PCC molecules without activating any thermal reactions. We took a number of

image series in a fresh (non-irradiated) area using electron fluxes on the order of 10^5 e^- nm^{-2} s^{-1} (as we did for the imaging at 23 ^{o}C) while holding the stage at 400 ^{o}C and found that again, there was a disparity in the rates of polymerisation.

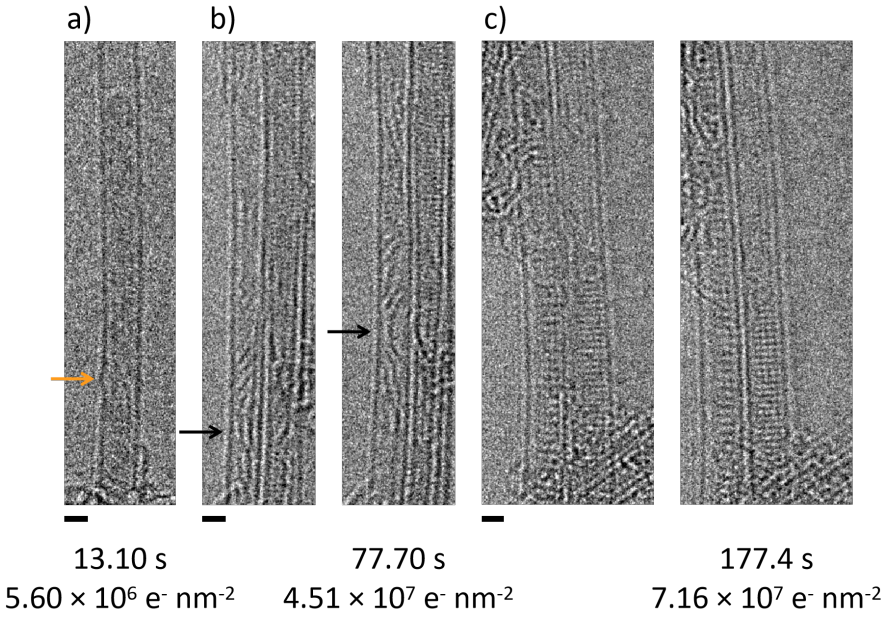

Figure 2.20. Several image series of PCC@SWNT were acquired at 400 ^{o}C. Time stamps and electron doses have been given where appropriate. a) This nanotube had a diameter of 1.48 nm. The PCC molecules in this nanotube had already reacted into a nanoribbon at the beginning of imaging (before the time stamp of 13.10 s, the images were blurry from vibration and movement). An orange arrow indicates a twist in the nanoribbon. The electron flux used was 4.28×10^5 e^- nm^{-2} s^{-1}. b) This nanotube had a diameter of 1.31 nm. The PCC molecules had begun reacting at the beginning of imaging (left image). The electron flux used was 5.81×10^5 e^- nm^{-2} s^{-1}. Adducts are indicated with black arrows. c) The left nanotube had a diameter of 1.64 nm. The PCC stack in this nanotube were incredibly stable to the electron beam even with heating at similar flux of 4.04×10^5 e^- nm^{-2} s^{-1}. The right images in b) and c) have comparable total doses. The scale bars are 1 nm.

The nanotube in Fig. 2.20 a) had a diameter of 1.48 nm. As soon as imaging began (and the electron beam was incident upon the nanotube), the molecules within this nanotube had begun reacting and appeared to already have formed some kind of nanoribbon. There were no features that suggested individual molecules or smaller adducts. This corresponded to a dose of only 5.60×10^6 e^- nm^{-2}; an

order of magnitude lower than the nanotube at 23 ^{o}C in Fig. 2.19 c) which had a comparable diameter of 1.41 nm. The nanotube in Fig. 2.20 b) had an even smaller diameter of 1.31 nm and many adducts had already formed at the beginning of imaging. It is possible this nanotube was poorly filled, such as the right nanotube at 23 ^{o}C in Fig. 2.19 c) that had a diameter of 1.33 nm.

There was also an example of a nanotube of diameter 1.64 nm in Fig. 2.20 c), comparable to the nanotube at 23 ^{o}C in Fig. 2.19 a) which had a diameter of 1.61 nm, where the molecules were incredibly unreactive. Even at 400 ^{o}C, there was no change to the stack of PCC molecules after a dose of 7.16×10^{7} e^{-} nm^{-2}. This is a marked difference from the 1.31 nm nanotube in Fig. 2.20 b). After a similar dose of 4.51×10^{7} e^{-} nm^{-2}, there were extended adducts inside the nanotube of Fig. 2.20 b). The molecules in Fig. 2.20 c) were more stable to the electron beam than some of their ambient temperature counterparts (Fig. 2.19). This is rather intriguing because we originally supposed that at elevated temperatures, the highly favourable van der Waals forces between the molecules in a tightly packed stack might be more easily overcome. Perhaps for such wider nanotubes, a longer period of heating is required to break apart a stack that is packed parallel to the nanotube. These parallel stacks would have larger van der Waals contacts between PCC molecules compared to stacks where PCC molecules are more diagonal to one another i.e. the slant angle is greater with respect to the nanotube axis.

For the two examples at 400 ^{o}C where reactions did occur, we were unable to capture the moment before any reactions. A lower temperature might allow us enough time to catch the process of first dimer formation. We imaged several more series at similar electron fluxes at 200 ^{o}C and found quite the same story. In Fig. 2.21 a) and b), PCC molecules in nanotubes with diameters of 1.36 and 1.44 nm respectively had begun reacting (although not as quickly as at 400 ^{o}C; more individual PCC molecules could be seen). Conversely, the nanotube in Fig. 2.21 c) had a

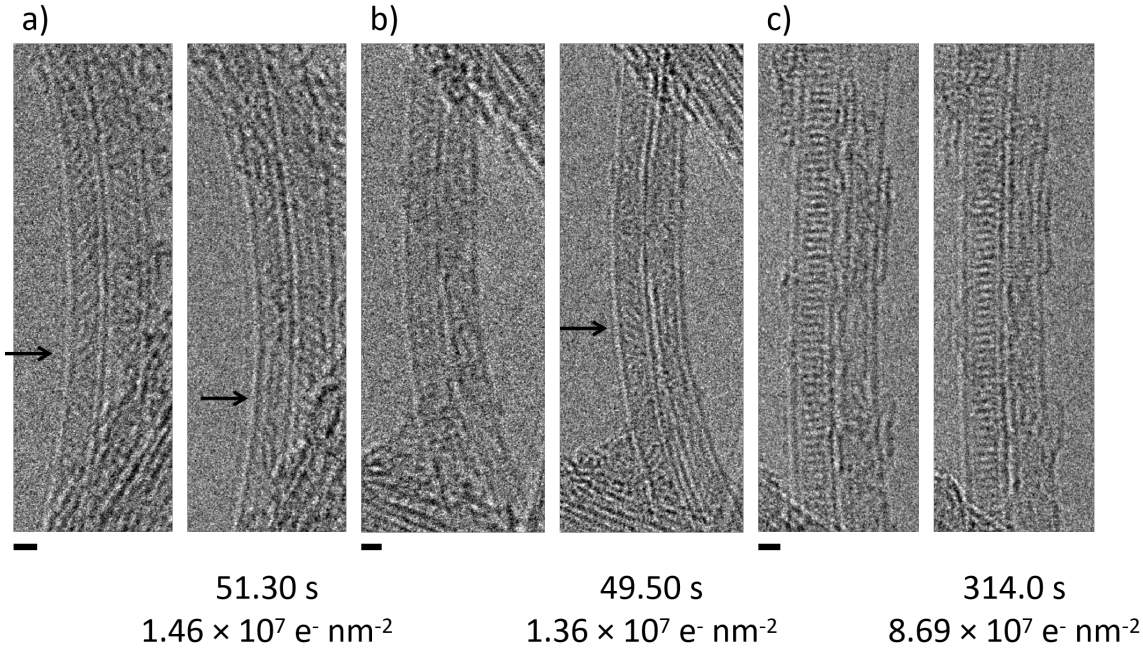

Figure 2.21. Several image series of PCC@SWNT were acquired at 200 ^{o}C. Adducts are indicated with black arrows. a) This nanotube had a diameter of 1.36 nm. Some PCC molecules had begun polymerising at the beginning of imaging. The electron flux used was 2.84$\times$10^{5} e^{-} nm^{-2} s^{-1}. b) The left nanotube had a diameter of 1.44 nm while the right nanotube is even narrower at a diameter of 1.21 nm. Again, it appeared as though some molecules had begun polymerising although this was quite blurry in the first image on the left side. The electron flux used was 2.76$\times$10^{5} e^{-} nm^{-2} s^{-1}. The right images of a) and b) have comparable total doses. c) This nanotube had a diameter of 1.66 nm. The PCC molecules were incredibly stable even with heating at a similar flux of 2.77$\times$10^{5} e^{-} nm^{-2} s^{-1} and after a similar total dose to a) and b), there was still an intact stack of unreacted PCC molecules. The scale bars are 1 nm.

diameter of 1.66 nm and again the molecules inside were quite beam stable. After a dose of 8.69$\times$10^{7} e^{-} nm^{-2} there was still an entire stack of PCC molecules, similar to the example in Fig. 2.20 c).

In summary, heating increased the rate at which the electron beam-induced polymerisation occurred. However, this effect appeared to be much greater for narrower nanotubes that did not allow for perpendicular stacks of molecules. We did not carry out a kinetics study on these reactions because we could not capture any first dimerisation events.

2.3.4 Thermally-induced polymerisation of PCC in SWNTs

We then used beam blanking to remove electrons as a source of energy for any reactions in order to understand the effects of only thermal energy on PCC@SWNTs. The aim was to ramp up the temperature until we reached a point where all nanotubes we came across contained a nanoribbon product. The entire sample was heated to 400 ^{o}C for ten minutes and then cooled back to ambient temperatures (23 ^{o}C). There were still plenty of stacks of PCC molecules in the SWNTs when we imaged across a fresh area (Fig. 2.22). This was repeated on the same sample at 500 ^{o}C for another ten minutes and imaged at ambient temperature (Fig. 2.23). There were fewer areas with stacks of molecules inside but polymerisation had not gone to completion for many of the nanotubes we imaged. Notably, after both 400 and 500 ^{o}C experiments, the nanotubes containing intact stacks of molecules had diameters larger than 1.50 nm. After another bout of heating at 600 ^{o}C for ten minutes, all the nanotubes we imaged did not seem to contain any individual molecules or smaller intermediates, including a couple of nanotubes with diameters larger than 1.50 nm (Fig. 2.24). The thermal energy given during these experiments is enough for complete polymerisation although the exact temperature and length of time for the reaction are uncertain due to our "feeling around in the dark" experimental procedure. This was a series of experiments to test our methodology before using more expensive heating chips.

Fig. 2.24 a i) and a ii) are high magnification micrographs of the same nanotube from Fig. 2.24 a). The products inside the nanotube were not one continuous nanoribbon; there was a gap in the middle. The products appeared much more disordered than the well-defined nanoribbons formed using the electron beam at ambient temperature (Fig. 2.19). Once all the molecules in a stack can move separately from one another at elevated temperatures, it is likely that they will react in much more random ways. For example, the molecules may not polymerise into

one single nanoribbon and instead form several; this seemed to be the case in Fig. 2.24 a). Additionally, rampant dechlorination may occur at such high temperatures since 600 ^{o}C is a high enough temperature to decompose PCC, something we discovered when testing sublimation filling into nanotubes under vacuum at different temperatures. Although the filling experiment at 600 ^{o}C took place over three days and therefore cannot be directly compared to our *in situ* TEM experiments, we can suggest that heating 600 ^{o}C gave enough thermal energy to break C – Cl bonds without requiring input from the electron beam. If this is the case, this could give rise to any number of reactive species such as radicals from homolytic bond dissociation. From this point onwards, subsequent reactions between these species would increase the complexity of the overall product.

We can use this data to calculate the activation energy E_a of the purely thermally induced polymerisation of PCC (Eq. 2.4) which has the rate constant k_T.

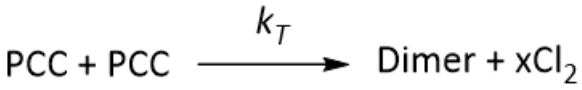

Equation 2.4. The thermally induced dimerisation of PCC molecules where a dimer and x number of moles of Cl_2 are produced. This reaction has the reaction rate constant k_T.

Under the conditions we used, x number of moles of Cl_2 could be produced due to heat-induced cleavage of C – Cl bonds. Because a volume of nanotube was heated, the "concentration" of the thermally induced reactions can be described as the number of PCC molecules $nPCC$ per volume of nanotube V_0 ($nPCC/V_0$). Therefore, the second order rate equation can be written as shown in Eq. 2.5 where $[PCC]_0$ is the initial number of PCC molecules per volume.

$$-\frac{d(nPCC/V_0)}{dt} = (\frac{2}{x+1})k_T{[PCC]_0}^2$$

Equation 2.5. The second order rate equation describing the schematic in Eq. 2.4.

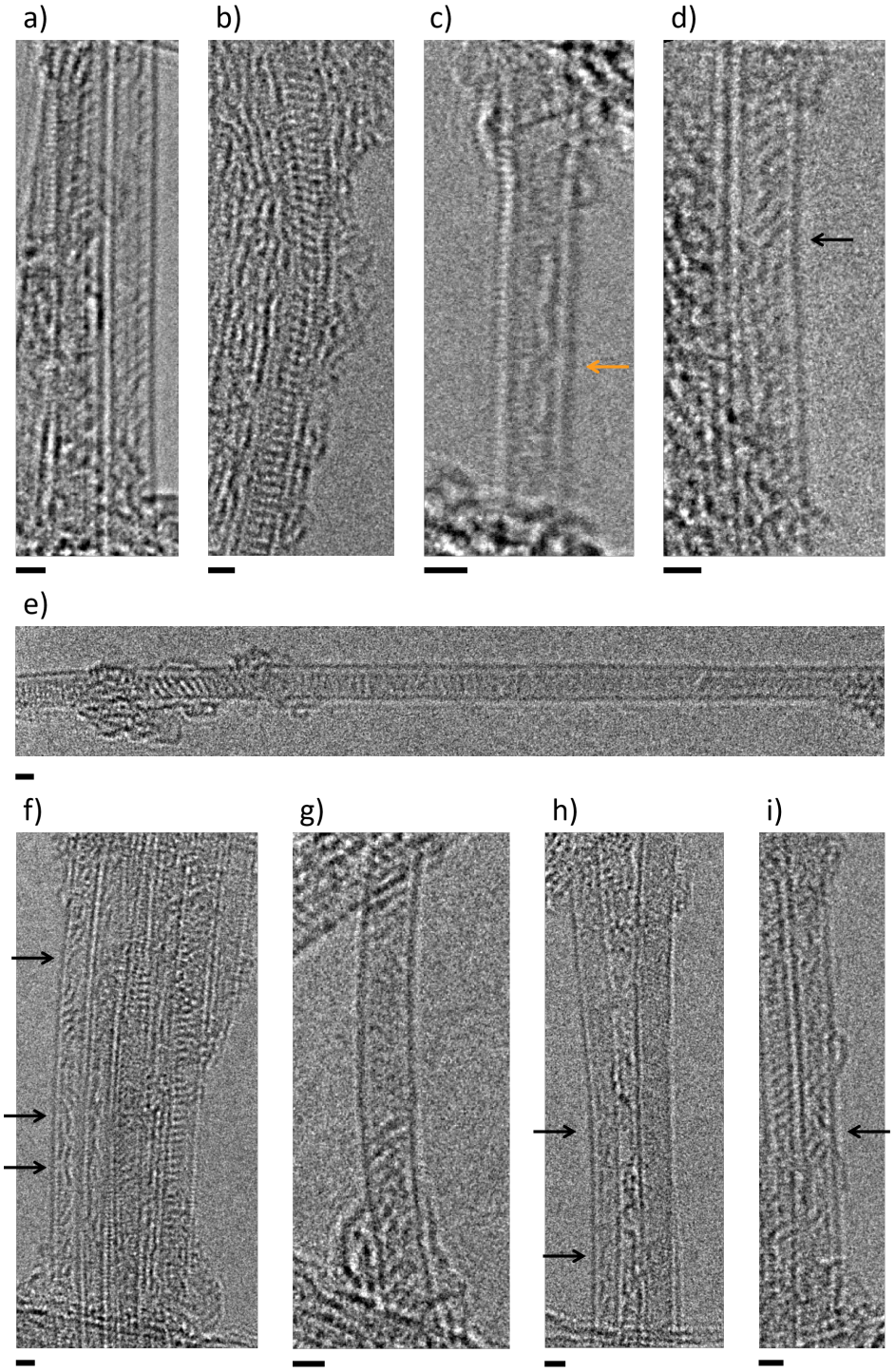

Figure 2.22. Individual snapshots (capture time of 0.5 s) of the sample were taken at 23 ^{o}C after heating at 400 ^{o}C for ten minutes. Adducts are indicated with black arrows while twists in nanoribbons are indicated with orange arrows. The nanotube diameters are as follows: a) 1.41 nm, b) 1.59 nm, c) 1.28 nm, d) 1.52 nm, e) 1.62 nm, f) left is 1.31 nm; right is 1.64 nm, g) 1.54 nm, h) leftmost nanotube is 1.38 nm, and i) 1.23 nm. There are some regions of blurriness in the nanotubes in e) and g) which are likely due to molecular movement. All scale bars are 1 nm.

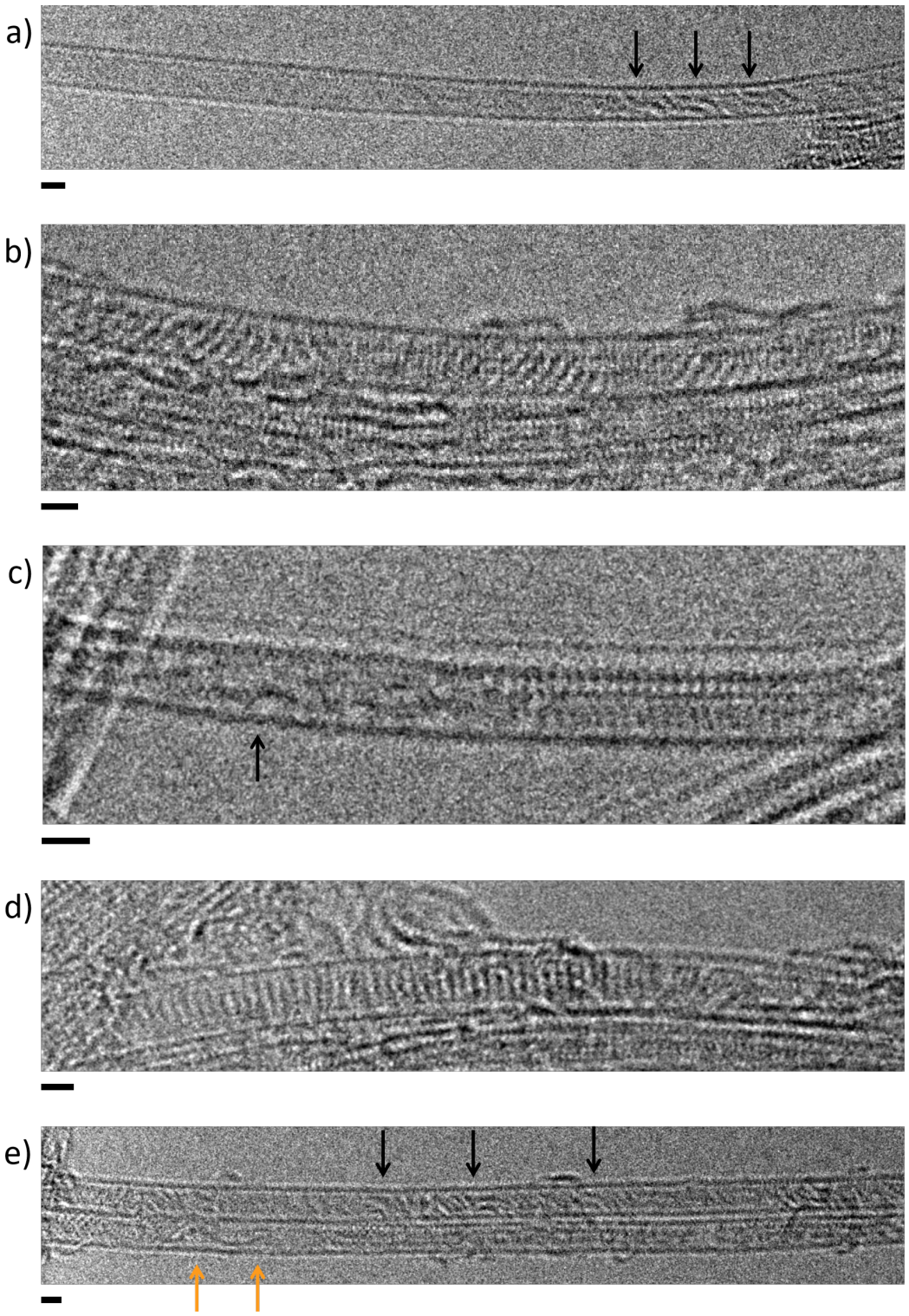

Figure 2.23. Individual snapshots (capture time of 0.5 s) of the sample were taken at 23 ^{o}C after heating at 500 ^{o}C for ten minutes. Adducts are indicated with black arrows while twists in nanoribbons are indicated with orange arrows. The nanotube diameters are as follows: a) 1.39 nm, b) 1.56 nm, c) 1.44 nm, d) 1.75 nm, and e) top nanotube is 1.36 nm; bottom nanotube is 1.25 nm. All scale bars are 1 nm.

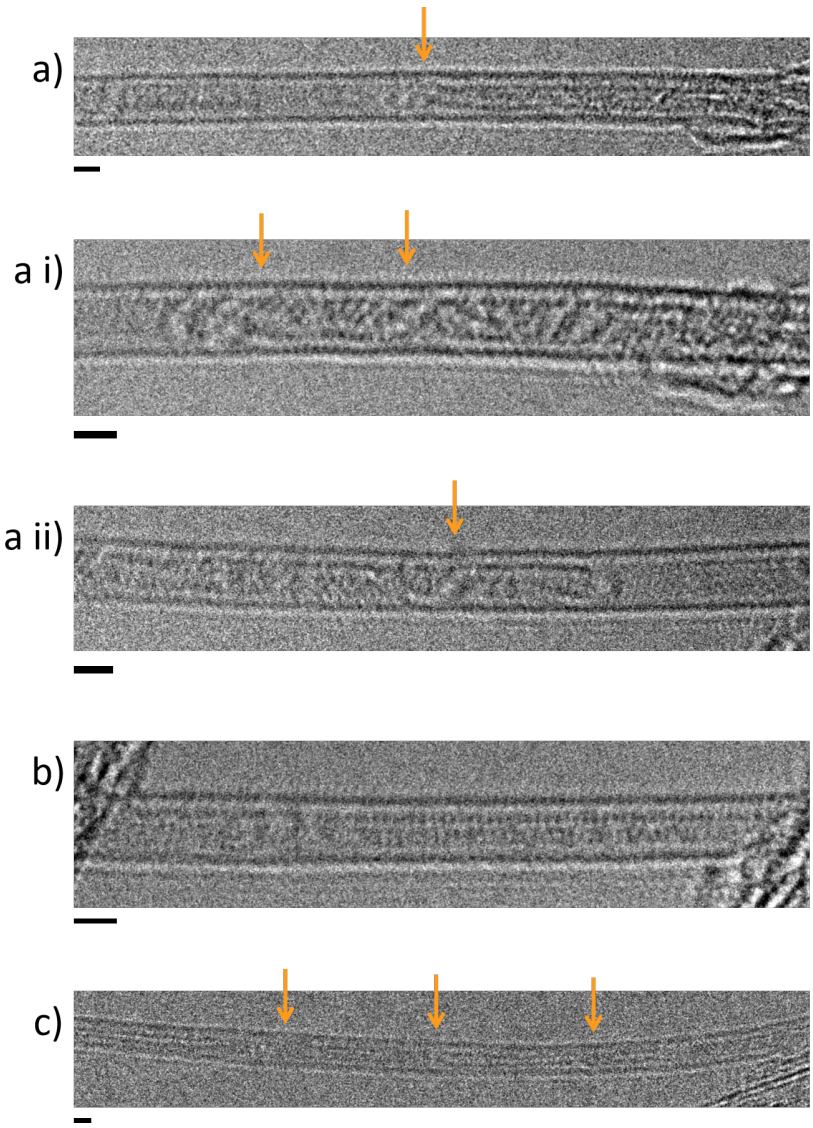

Figure 2.24. Individual snapshots (capture time of 0.5 s) of the sample were taken at 23 ^{o}C after heating at 600 ^{o}C for ten minutes. Suspected twists in the nanoribbon-like products are indicated with orange arrows. The nanotube diameters are as follows: a) 1.61 nm, b) 1.33 nm, and c) 1.59 nm. All scale bars are 1 nm.

However, from previous observations of UV light-induced dimerisation (in the MALDI-ToF), it seemed likely that PCC molecules dimerised *before* losing Cl_2 successively. We simplified Eq. 2.5 into the integrated rate equation in Eq. 2.6 where we assumed only one mole of Cl_2 is produced per dimerisation reaction (there may of course be further reactions that lose more Cl_2). All images shown in previous figures of experiments at 23, 400, 500, and 600 ^{o}C (Figs. 2.19, 2.22, 2.23, and 2.24 respectively) were analysed for number of molecules per volume.

$$\frac{1}{(nPCC/V_0)} = k_T t + \frac{1}{[PCC]_0}$$

Equation 2.6. The integrated second order rate equation of PCC dimerisation.

The images at 23 ^{o}C were used as the unreacted value of $nPCC/V_0$. The nanotube volumes V_0 were then measured for each entire visible nanotube at 400, 500, and 600 ^{o}C. Given the high filling rate of PCC into SWNTs, the nanotubes at higher temperatures were assumed to be completely filled before heating. The values of $nPCC/V_0$ were averaged for each of the four temperatures.

The rate constant k_T can be calculated using the averaged values of $nPCC/V_0$ for each temperature using Eq. 2.7.

$$k_T = \frac{[PCC]_0 - (nPCC/V_0)}{(nPCC/V_0)[PCC]_0 t}$$

Equation 2.7. A rearrangement of Eq. 2.6 to give the rate constant at each temperature k_T.

A linear plot of k_T against $1/T$ using the Arrhenius equation (Eq. 2.8) can be used to calculate the activation energy E_a (Eq. 2.9).

$$k_T = P \times e^{-\frac{E_a}{k_B T}}$$

Equation 2.8. The Arrhenius equation for the thermally-induced PCC polymerisation where k_T is the thermally induced rate constant, T is the temperature, P is the pre-exponential factor, E_a is the activation energy, and k_B is the Boltzmann constant (8.617×10^{-5} eV K^{-1}).

$$lnk_T = -\frac{E_a}{k_B}(\frac{1}{T}) + ln(P)$$

Equation 2.9. A linear plot of the Arrhenius equation in Eq. 2.8 has a gradient of $-\frac{E_a}{k_B}$.

Alternatively, the activation energy can also be found algebraically using the two-point form of the Arrhenius equation (Eq. 2.10), which rearranges to Eq. 2.11. The activation energy of thermally induced PCC polymerisation was calculated to be 0.395$\pm$0.00025 eV per molecule or 38.1$\pm$0.0242 kJ mol^{-1}. The errors came from the temperature of the heating chip which varied by less than a degree, measurements of the nanotube volume, and our timings of the heating period which likely varied by about ten seconds.

$$ln(\frac{k_1}{k_2}) = \frac{E_a}{k_B}(\frac{1}{T_1} - \frac{1}{T_2})$$

Equation 2.10. The two-point form of the Arrhenius equation where two rate constants (k_1 and k_2) and two corresponding temperatures (T_1 and T_2) are substituted into Eq. 2.8.

$$E_a = \frac{k_B T_1 T_2}{(T_1 - T_2)} ln(\frac{k_1}{k_2})$$

Equation 2.11. Rearrangement of Eq. 2.10 to find the activation energy E_a where the rate constants from experiments at 400 and 500 ^{o}C were used.

Due to time and sample limitations, we carried out all heating experiments on the same heating chip. The same batch of PCC@SWNTs was heated at 400 ^{o}C for ten minutes, then 500 ^{o}C, and so on. Because of this experimental setup, the activation energy will be a lower limit. Future experiments to obtain an estimate of the activation energy (rather than a lower limit) would involve use of multiple heating chips, one for each temperature, and carrying out a similar analysis of the data. As with the electron beam-induced reaction, this kinetics study of the thermally induced reaction is a general method that can be applied to other nanoscale systems.

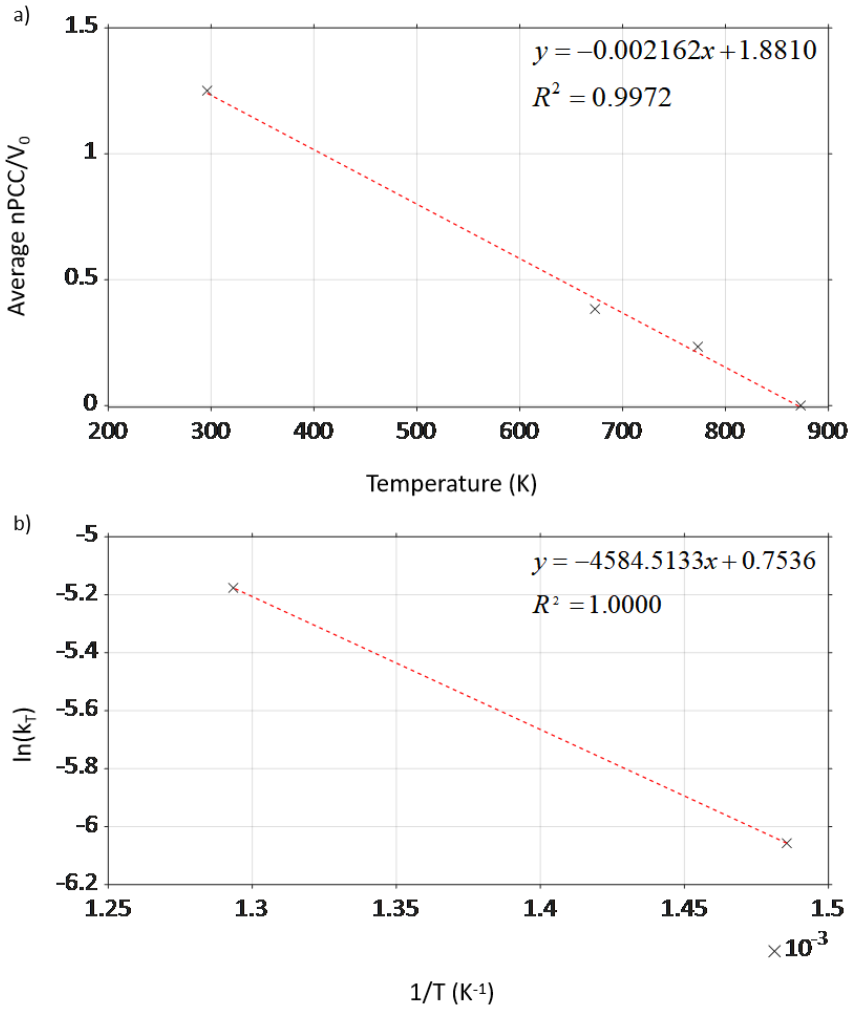

Figure 2.25. a) The thermally induced PCC polymerisation has a linear decrease in average number of PCC molecules per total volume of nanotube ($nPCC/V_0$) against temperature. b) k_T could be calculated for two data points (where there was a change in $nPCC/V_0$ without needing to divide by zero; see Eq. 2.7). The linear plot of $ln(k_T)$ against $1/T$ from Eq. 2.9 can be used to find the gradient $-E_a/k_B$.

2.3.5 PCC@SWNTs under cryogenic conditions

On the other end of the spectrum, we could attempt to limit molecular motion by cooling PCC@SWNTs down to cryogenic temperatures using liquid nitrogen (77 K or -195.79 ^{o}C). This would slow down the rate of polymerisation and potentially allow us to capture atomically resolved micrographs of PCC molecules. So far, we have only managed to image the lines that correspond to one molecule due to molecular vibrations at ambient and elevated temperatures. We decided to use an image capture rate of a hundred frames per second again so that we might reduce the presence of molecular vibration in the micrographs. Under a similar electron flux (10^{5} e^{-} nm^{-2} s^{-1}) as the ambient temperature examples in Fig. 2.19, we were able to capture an atomically resolved stack of PCC molecules at cryogenic temperatures (Fig. 2.26). The stack appeared to be leaning approximately 50^{o} towards the left. The molecules in Fig. 2.26 a) were much more beam stable than the examples at ambient temperature. They received a similar total electron dose to ambient temperature experiments without exhibiting much molecular motion or any polymerisation.

Progressing on from the atomic imaging of PCC molecules, we took another image series at a similar flux to identify how cryogenic temperatures might affect a nanoscale reaction (Fig. 2.31). However, over 39.83 s (corresponding to a total dose of 1.78×10^{7} e^{-} nm^{-2}), the entire nanotube became significantly damaged. We also observed formation of nanometre-sized high contrast crystals, which we shall return to later on in this chapter. The damaged nanotube was unlike any of the previous experiments at ambient or elevated temperatures. Nanotubes in a PCC@SWNT sample tend not to become overly damaged during imaging (which is why many researchers use nanotubes as the substrate for atomically resolved imaging - see chapter one) so we wondered why the "inert" reaction containers were so much more susceptible to beam damage during our cryo experiments.

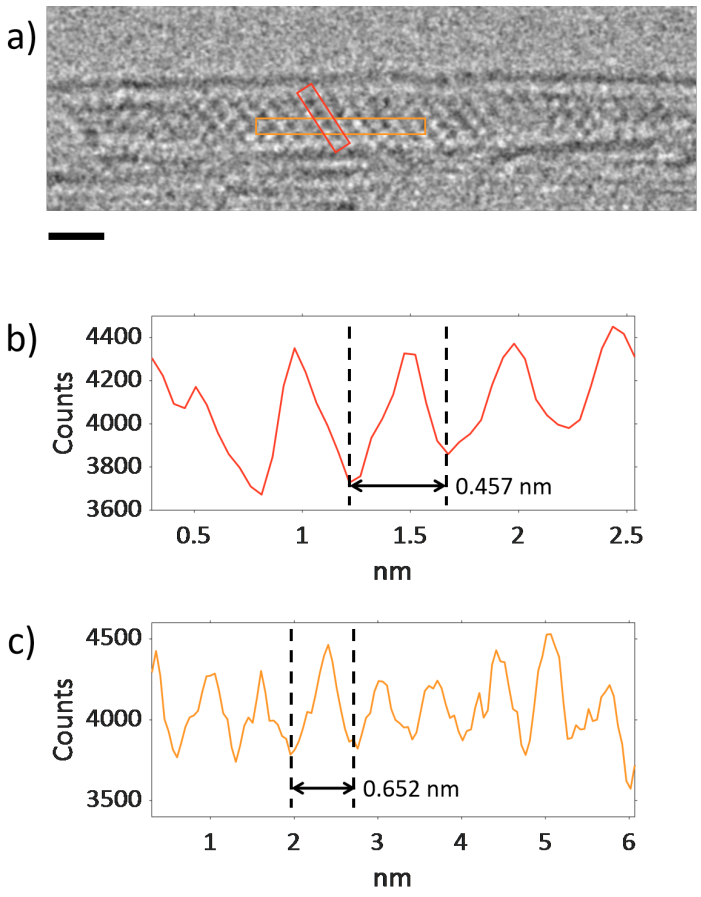

Figure 2.26. PCC@SWNT under cryogenic conditions. a) Atomic resolution was achieved of the PCC stack at an electron flux of 4.74×10^5 e^- nm^{-2} s^{-1} over a period of 192.36 s, which corresponded to a total dose of 9.11×10^7 e^- nm^{-2}. The nanotube has a diameter of 2.56 nm. The scale bar is 1 nm. b) and c) Line profiles of the PCC stack; the colours of the plots correspond to the rectangles in a).

We considered common damage mechanisms in cryo TEM. At all operating voltages of a TEM, the incident electron beam is significantly higher in energy than all covalent bond energies and ionisation energies found in organic molecules. As a result, primary damage can occur where the electron beam excites or ionises the valence electrons of molecules in the sample (otherwise known as radiolysis). This can break bonds, creating radicals and emitting secondary electrons that can partake in further destructive reactions which is known as secondary damage.[20] A major issue for sample stability in cryo TEM is the presence of thick layers of hexagonal or vitreous ice which can form when cooling the sample holder. Typically, a sample

is rapidly cooled by plunging into liquid ethane (90.4 K) which fixes the sample in its current state. However, moisture from the atmosphere during sample preparation or within the TEM vacuum can condense onto the cold sample, contaminating the surface with thicker layers of ice.[21,22] The ice contamination has higher contrast and can undergo radiolysis (as can any water present in the sample). For example, a reaction such as $H_2O \longrightarrow H\cdot + OH\cdot$ might take place. These radicals can recombine or react with nearby organic molecules or proteins like so: $OH\cdot + R-H \longrightarrow RO\cdot + H_2$. This is known as tertiary damage and can severely distort the sample. Eventually, bubbles of hydrogen gas can evolve within the sample which causes significant problems with sample analysis such as changes in image contrast.[20]

The PCC@SWNT sample was synthesised in vacuum at 400 ^{o}C so there should be very little moisture present. The sample was not plunged into liquid ethane and was simply loaded onto the cryo holder and cooled while in the TEM. However, any moisture in the TEM vacuum could condense onto the rapidly cooling sample when liquid nitrogen is added to the sample holder. The water contaminant can undergo radiolysis in the manner described above. In addition to this, hydrogen atoms receive significantly more kinetic energy at 80 kV via direct knock-on than other elements because the maximum transferred energy T_{max} from an incident electron to the atom is inversely proportional to atomic weight M.[2] This results in a significantly higher atom ejection cross-section σ_d. If PCC@SWNT was contaminated with water, both radiolysis and knock-on damage can cause the damage seen in Fig. 2.31.

We imaged empty SWNTs at ambient temperature as a control to show their beam stability. These SWNTs were imaged using a higher flux (an order of magnitude greater than experiments with PCC@SWNTs) of 10^6 e$^-$ nm^{-2} s^{-1} over a period of 609.10 s which corresponded to a total dose of 5.26×10^9 e$^-$ nm^{-2}. As can be seen in Fig. 2.27, the nanotube wall integrity was not compromised during

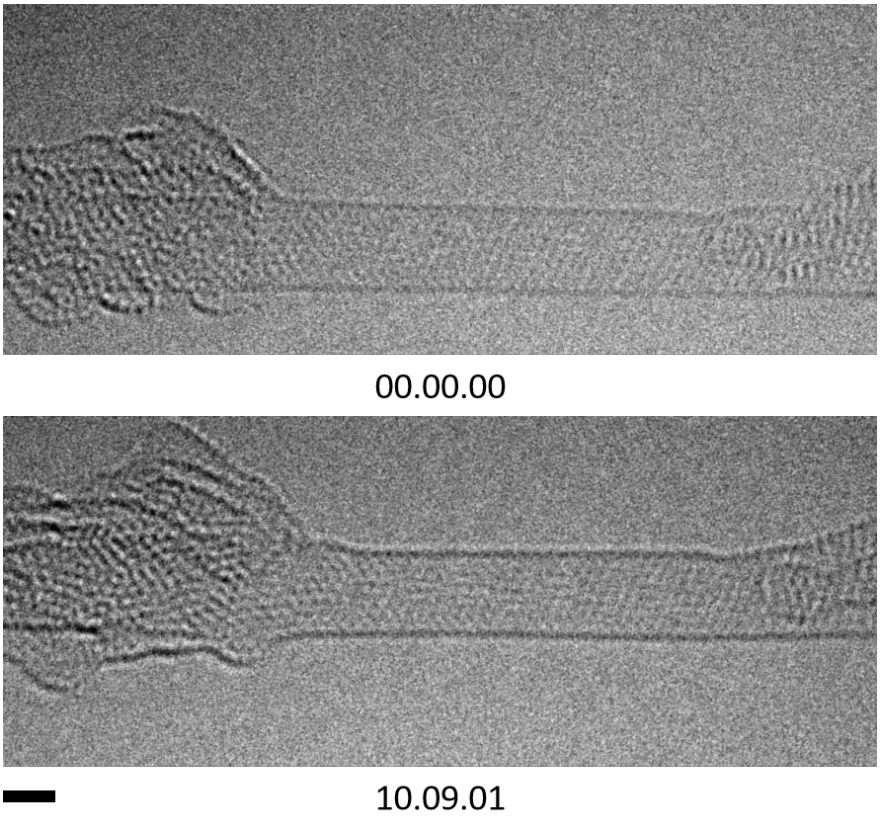

Figure 2.27. A "dry" SWNT was imaged at room temperature using an electron flux of 8.64×10^6 e^- nm^{-2} s^{-1} over 609.10 s which corresponded to a total dose of 5.26×10^9 e^- nm^{-2}. The carbon lattice can be seen in both the initial and the final images. There was very little change to the nanotube. The scale bar is 1 nm. Time stamps are in the format minutes.seconds.milliseconds.

imaging, even though there were some defects towards the left and right sides of the nanotube present from the beginning of imaging. Although the beam stability of carbon nanotubes is not new information, we wanted to acquire a control image series under identical imaging conditions for direct comparison. In addition to this, the atomic resolution of the SWNT in Fig. 2.27 shows that our atomically resolved stack of PCC molecules in Fig. 2.26 is not simply misintepretation of the nanotube lattice; the stack of high contrast dots arranged in rows of four look nothing like the hexagonal pattern of the carbon atoms in the empty SWNT.

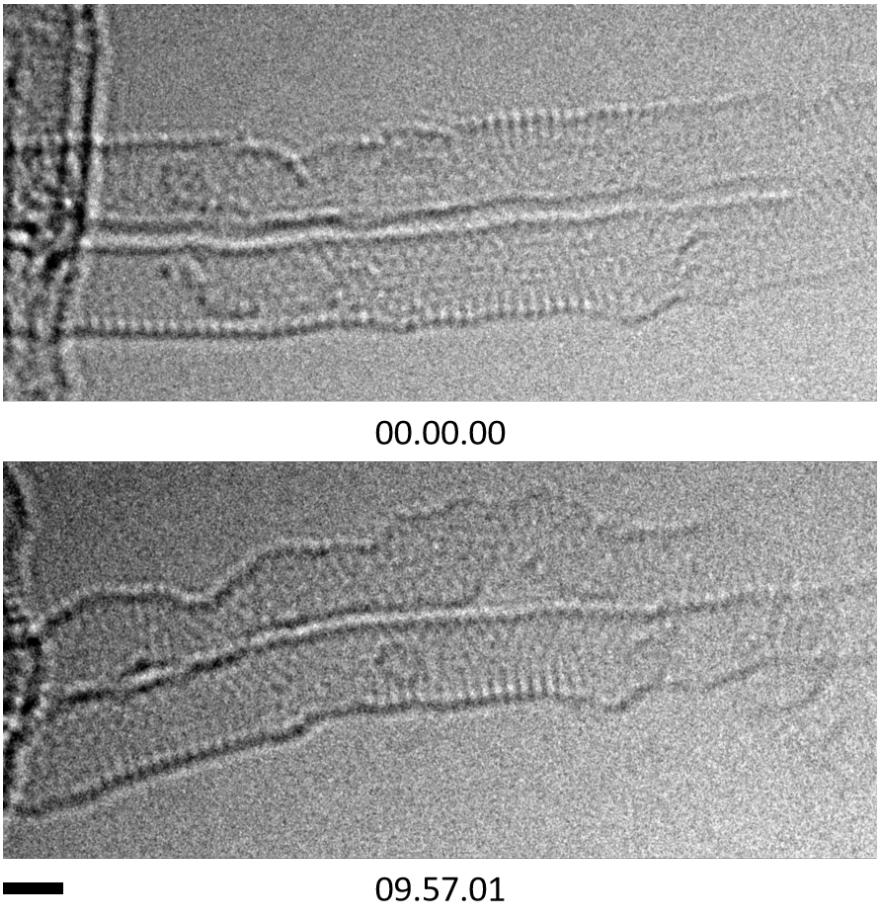

Figure 2.28. Two "wet" SWNTs were imaged under cryogenic conditions using an electron flux of 7.39×10^{6} e^{-} nm^{-2} s^{-1} over 597.10 s which corresponded to a total dose of 4.41×10^{9} e^{-} nm^{-2}. Both nanotubes become significantly damaged during imaging. The scale bar is 1 nm. Time stamps are in the format minutes.seconds.milliseconds.

We then deliberately introduced water into a second empty SWNT sample by sonicating the nanotubes in deionised water before drop casting that suspension onto a TEM grid. Most of the water will have evaporated off but some amount of water may have remained in the sample. The aim here was to image these "wet" empty nanotubes under cryogenic conditions in order to see if they would become as damaged as the example in Fig. 2.31. During insertion of this sample into the TEM column, we cooled the sample holder with liquid nitrogen as soon as the TEM vacuum was ready so that we would increase the likelihood of moisture in the microscope condensing onto the SWNTs, again to deliberately contaminate the

SWNTs with water. We imaged these SWNTs at a flux of 10^6 e^- nm^{-2} s^{-1} over a period of 597.10 s which corresponded to a total dose of 4.41×10^9 e^- nm^{-2}, similar to the ambient temperature SWNT example previously. This time the nanotubes behaved quite differently, gaining defects rapidly and even snapping in twain on the right side (Fig. 2.28). These nanotubes also started off with some defects, but unlike the ambient temperature example in Fig. 2.27, the defects increased in severity during imaging. The same batch of nanotubes was used for both ambient temperature and cryogenic TEM. Similar imaging conditions were also used. The main differences were use of cryogenic conditions and the presence (or lack) of water. All this suggests that our suspect for increasing the rate of damage to the SWNTs in the PCC@SWNTs sample was indeed moisture contamination.

In an attempt to avoid contaminating PCC@SWNT with moisture, we inserted the sample holder into the pumping chamber while still at ambient temperature and allowed the holder to pump down in the vacuum for much longer than before (20 minutes). Then, when the sample of PCC@SWNT was inserted into the microscope, the vacuum was allowed to reach the original value before liquid nitrogen was added to the sample holder. This rather more careful loading of the sample might improve the vacuum before we cooled the sample and therefore reduce water contamination on the surface. The subsequent series of images of PCC polymerisation at cryogenic temperatures is shown in Fig. 2.30. Formation of the first dimer (that was in focus) took 21.3 s or a dose of 1.43×10^7 e^- nm^{-2}. This is of the same order of magnitude as the doses required for first dimer formation at 23 ^{o}C (Fig. 2.19). This suggests that the polymerisation at cryogenic temperatures is comparable to those occurring at room temperature, which is consistent with direct knock-on being the major damage mechanism during PCC polymerisation.[18] Radiolysis is likely to dominate in insulating samples but SWNTs are conducting at all temperatures used in this chapter. Cryogenic temperatures would only improve the

thermal and electrical conductivity of SWNTs. We only have one data point at cryogenic temperatures so we should not draw absolute conclusions about the electron beam-induced polymerisation of PCC in SWNTs. However, so far, all evidence is consistent with direct knock-on being the dominant mechanism of this reaction.

One bizarre thing of note is that a crystal of high contrast began growing on the left side of the nanotubes throughout imaging. This crystal was visible through several nanotubes and had a regular d-spacing pattern of 2.30 Å (this was measured from the final micrograph in the series and is shown in Fig. 2.32). There was also a high contrast crystal from Fig. 2.31 that had a regular d-spacing pattern of 4.03 Å and rotated during imaging to show a different face with d-spacing of 2.05-2.06 Å (Fig. 2.33). Initially we wondered if it could be hexagonal water ice.[23] The d-spacing of 2.30 Å in Fig. 2.32 could correspond to the (3 0 0) plane while the d-spacing of 2.05-2.06 Å in Fig. 2.33 could correspond to the (1 1 3) plane but the d-spacing of 4.03 Å does not match any ice Ih plane. The prolonged stability under the electron beam and high contrast compared to carbon nanotubes did not suggest water ice. In addition to this, we did not observe any high contrast crystals during imaging of empty SWNTs under cryogenic conditions.

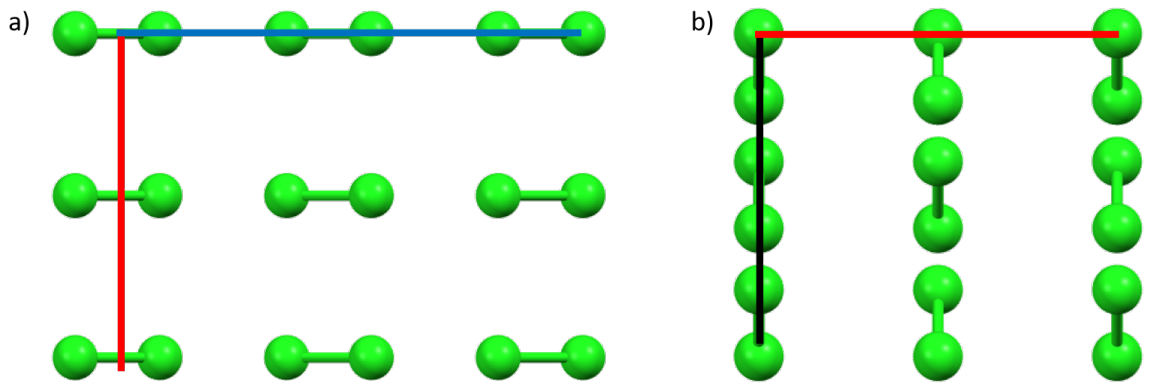

Figure 2.29. a) The unit cell of solid chlorine[24] along the b axis and b) along the c axis. The a axis is red, the b axis is black, and the c axis is blue.

Chlorine is removed from the system during the reaction as radicals which combine to give diatomic chlorine. The operating temperature of the cooling holder is approximately 100 K which is far below the melting point of diatomic chlorine which is at 171.6 K. The crystal structure (shown in Fig. 2.29) of a single crystal of solid chlorine was solved by Collin in 1952[24] and further refined by Donohue *et al.* in 1965.[25] Diffraction data was recorded at around 113 K and the symmetry of the crystal was found to be orthorhombic. The d-spacing of 2.30 Å in Fig. 2.30 may correspond to the (2 0 2) plane. The d-spacing of 2.05-2.06 Å in Fig. 2.31 is a good match for the (0 0 4) plane while the d-spacing of 4.03 in the same Fig. could correspond to the (0 0 2) plane.

The pressure dependence of solid chlorine has not been investigated (although temperature dependence has been[26] and the overall crystal structure did not change significantly). The vacuum at the sample in a TEM may reach up to $\times 10^{-8}$ mbar.[27] The environment inside a TEM is quite alien compared to the conditions used during crystallography of solid chlorine. For one, there is a high input of energy from the electron beam which could excite the crystals and change the crystal structure. While we cannot conclusively say what these crystals are composed of, it is reasonable to suggest that we serendipitously found some nanocrystals of solid chlorine.

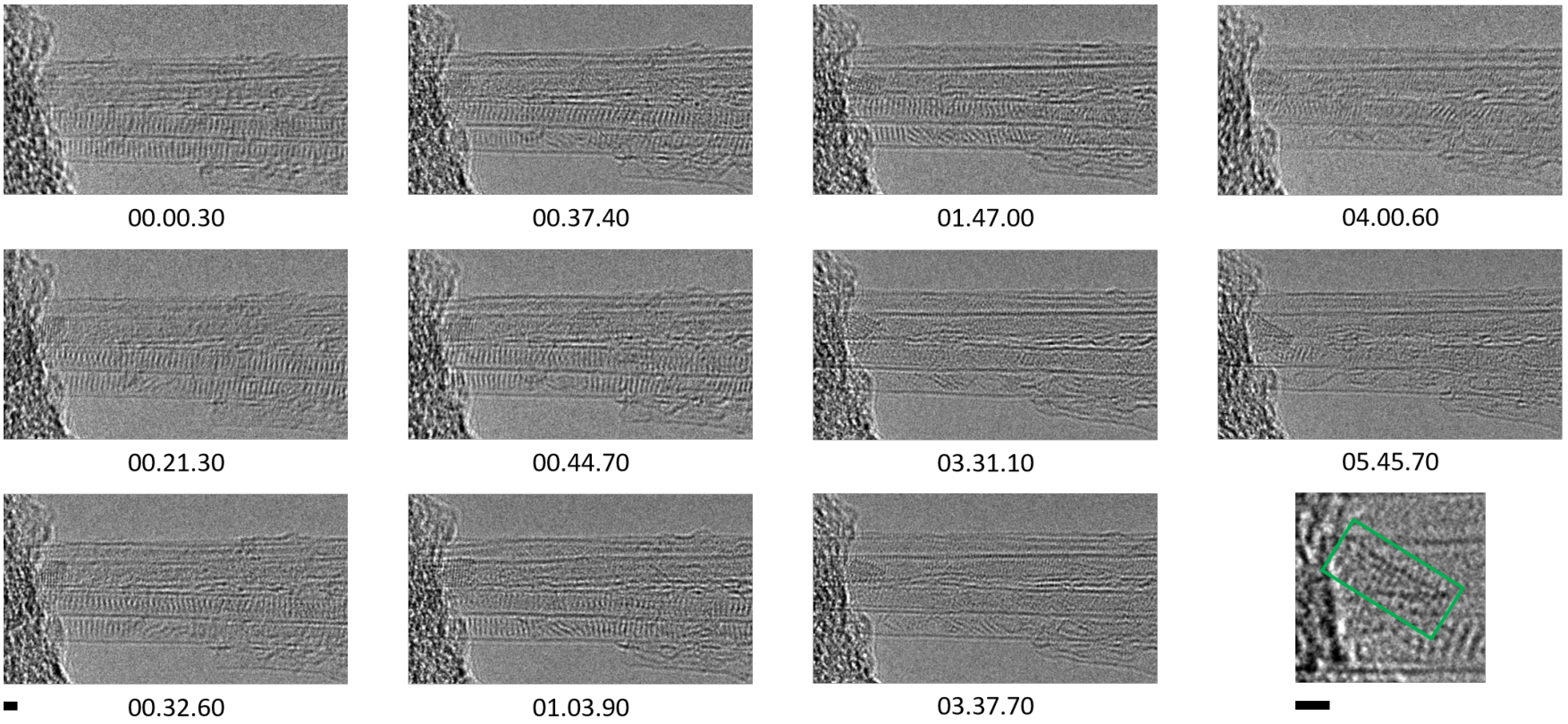

Figure 2.30. PCC@SWNTs imaged under cryogenic conditions. An electron flux of 6.72×10^{5} e^{-} nm^{-2} s^{-1} was used over a period of 288.40 s which corresponded to a total dose of 1.94×10^{8} e^{-} nm^{-2}. First dimer formation was observed at 21.3 s or a dose of 1.43×10^{7} e^{-} nm^{-2}. During imaging, a high contrast crystal formed indicated by the green rectangle. The line profile was measured from the green rectangle and is shown in Fig. 2.32. The scale bars are 1 nm. Time stamps are in the format minutes.seconds.milliseconds.

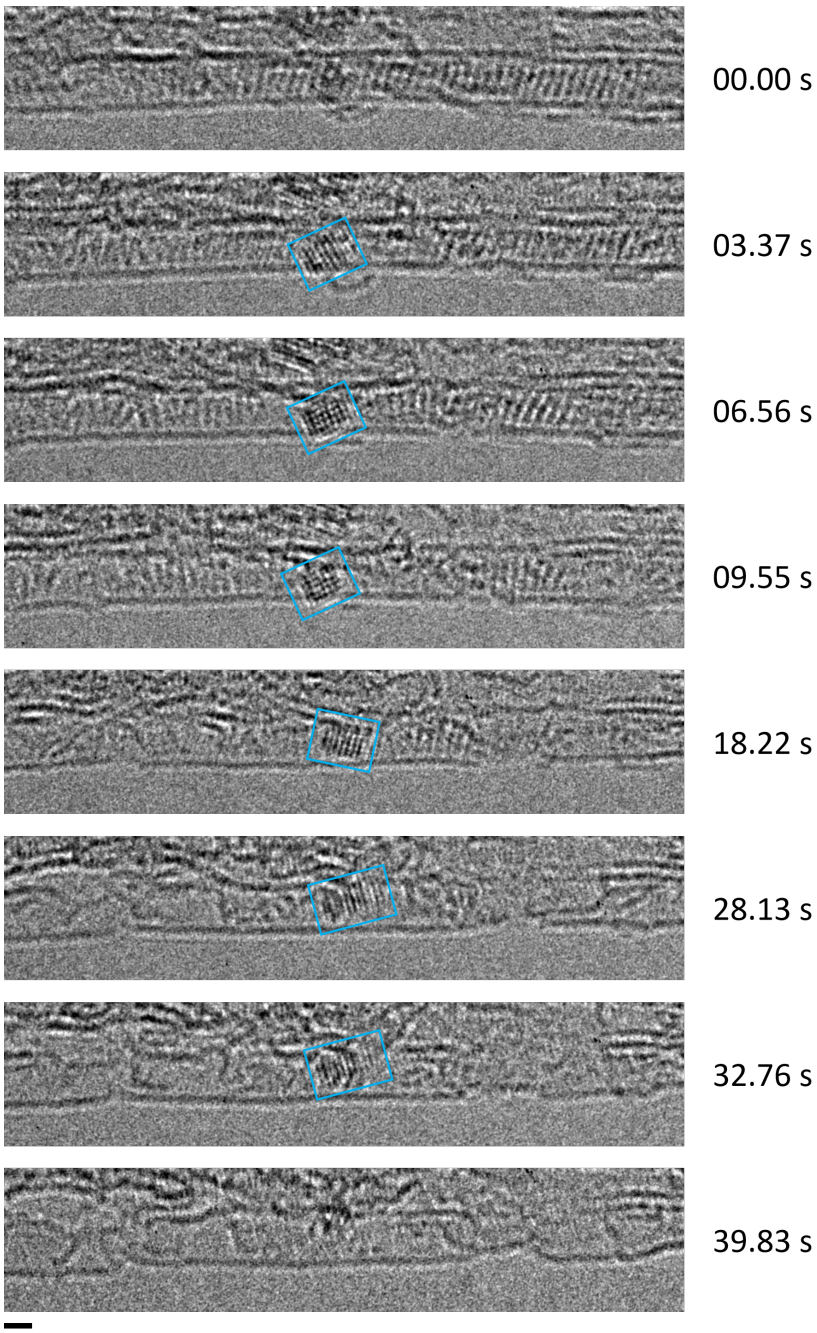

Figure 2.31. PCC@SWNTs imaged under cryogenic conditions. An electron flux of 4.47×10^{5} e^{-} nm^{-2} s^{-1} was used over a period of 39.83 s which corresponded to a total dose of 1.78×10^{7} e^{-} nm^{-2}. The SWNT became damaged and a high contrast crystal formed during imaging. The blue rectangles indicate where the crystal is in each image. Line profiles were measured for each blue rectangle and are shown in Fig. 2.33. The scale bar is 1 nm.

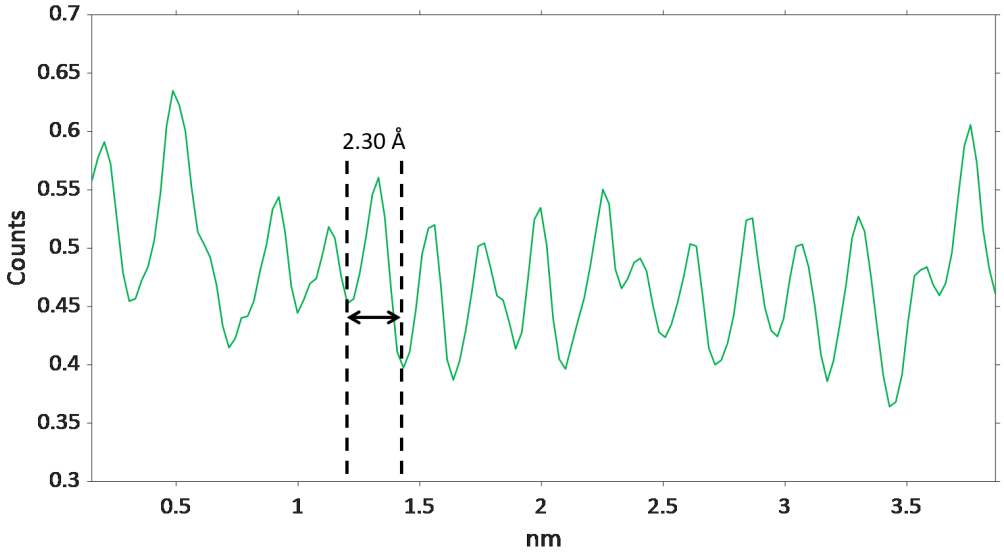

Figure 2.32. Line profile of the crystal from Fig. 2.30, showing a d-spacing of 2.30 Å. The profile was measured from the green rectangle in the image.

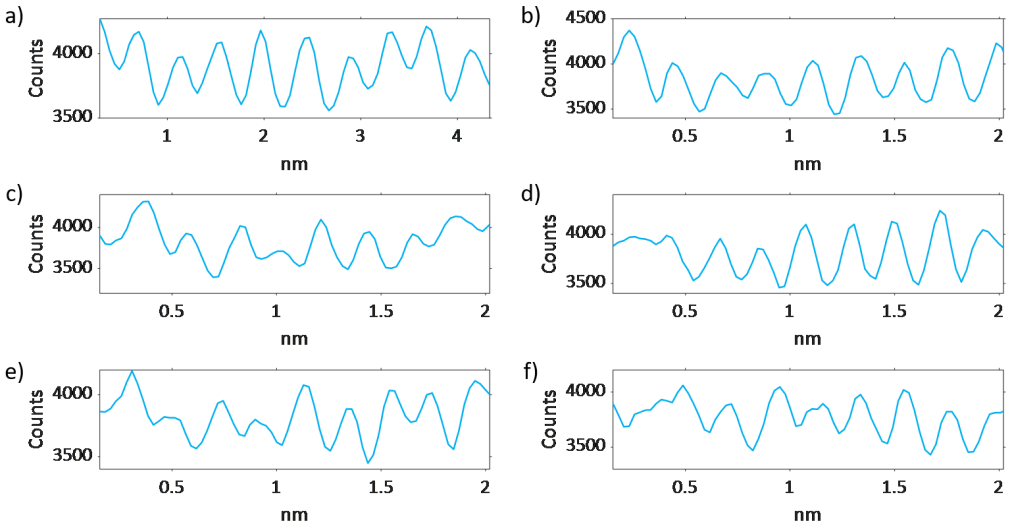

Figure 2.33. Line profiles of the crystal from Fig. 2.31. The profiles were measured from the blue rectangles in the images. The time stamps and d-spacings of each line profile are as follows: a) 03.37 s; 4.03 Å, b) 06.56 s; 2.06 Å, c) 09.55 s; 2.06 Å, d) 18.22 s; 2.05 Å, e) 28.13 s; 2.05 Å, and f) 32.76 s; 2.06 Å.

2.3.6 Other systems for comparison to PCC@SWNT

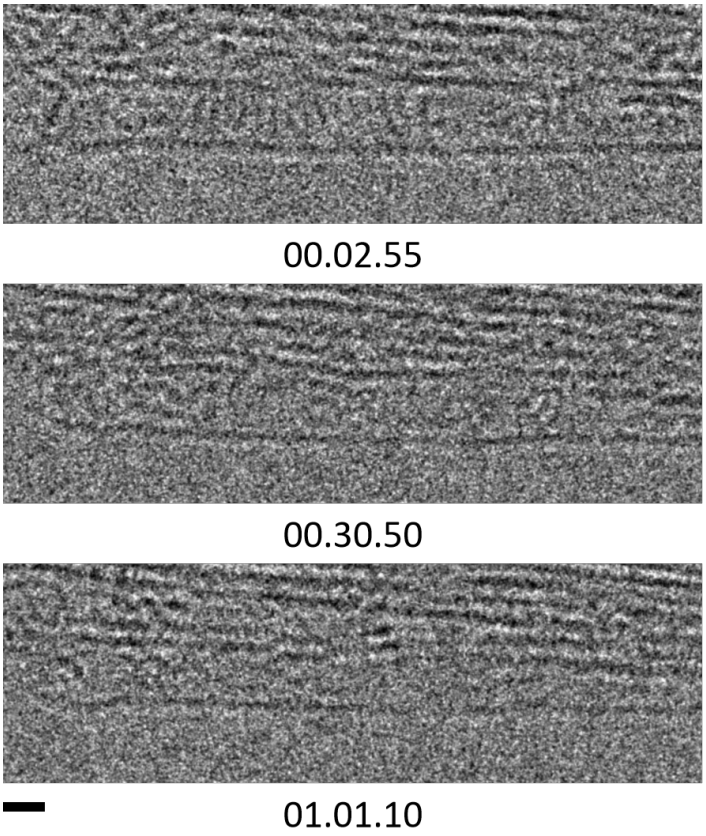

Figure 2.34. Coronene@SWNTs under cryogenic conditions. The coronene molecules were extremely low contrast compared to PCC and reacted significantly faster. An electron flux of 2.49×10^{5} e^{-} nm^{-2} s^{-1} was used over 88.70 s which corresponded to a total dose of 2.21×10^{7} e^{-} nm^{-2}. The scale bar is 1 nm. Time stamps are in the format minutes.seconds.milliseconds.

We carried out a few short studies using similar imaging conditions on other PAHs in SWNTs in order to place the PCC@SWNT system in perspective. The parent molecule coronene was a good candidate to compare the electron beam-induced behaviour of a hydrogenated PAH to the perchlorinated derivative (coronene and deuterated coronene have been studied previously at ambient temperatures by Chamberlain *et al.*[2]). In order to capture as much of the reaction as possible, we imaged coronene@SWNT (Fig. 2.34) under cryogenic conditions and at a faster capture rate of twenty frames per second (compared to ten for PCC). A similar flux of 10^{5} e^{-} nm^{-2} s^{-1} was used for imaging coronene@SWNT. After

approximately 88.70 s or a total dose of 2.21×10^7 e^- nm^{-2}, the entire stack of coronene molecules had reacted. It was difficult to conclusively say when all the molecules had reacted due to the low signal to noise ratio in the micrographs. When PCC@SWNT was imaged under cryogenic conditions using a similar total dose (Fig. 2.30; timestamp of 00.32.60 corresponding to a total dose of 2.19×10^7 e^- nm^{-2}), there was still much of the original stack and only a few dimers had formed. Coronene molecules could lose $H\cdot$, ionise, or become otherwise excited by the electron beam to form reactive species. Several of these processes could occur simultaneously. These species can then react without needing any particular conformation, for example the coronene molecules seemed to react to form an extended disordered carbon structure (Fig. 2.35). The key difference between coronene and PCC is the lack of heavy terminating atoms which dramatically increases the beam stability of PCC by a factor of about 1000.[9] Under the electron beam, the carbon structures may eventually form an internal carbon nanotube within the host nanotube. The chemical transformations of coronene in SWNTs have also been studied by Botka *et al.* where they found much the same behaviour under the electron beam.[28]

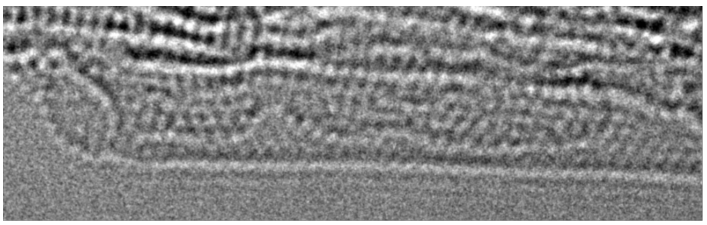

Figure 2.35. A higher magnification image of coronene@SWNT under cryo conditions after irradiation. The scale bar is 1 nm.

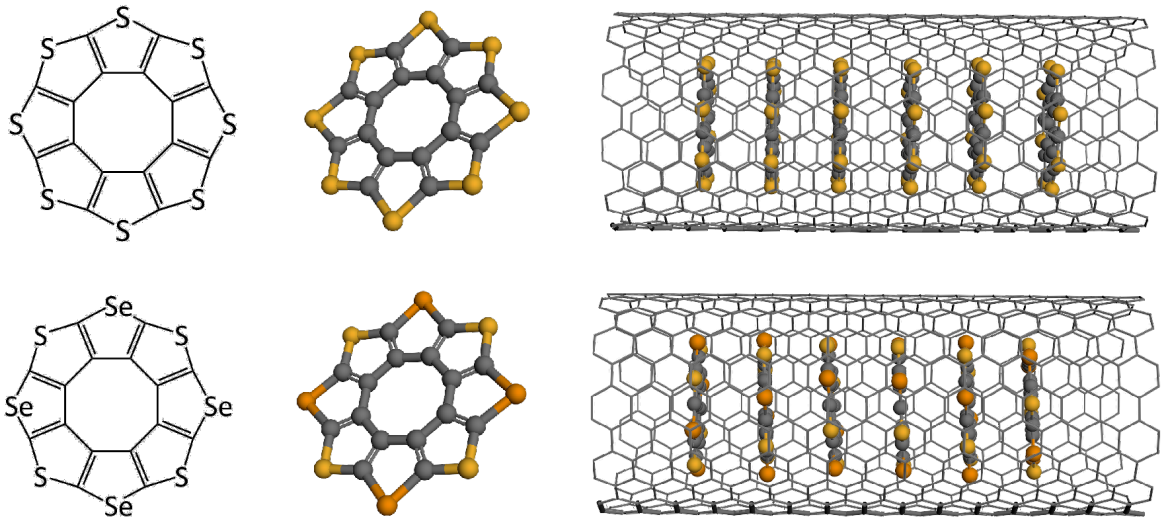

Figure 2.36. The chemical structures, three-dimensional models, and models inside SWNTs of $C_{16}S_8$ octathio[8]circulene (OTC; top) and $C_{16}S_4Se_4$ tetrathiotetraseleno[8]circulene (TTC; bottom) respectively.[13] The diameter of OTC 1.24 nm is while the diameter of TTC is 1.26 nm. The average diameter of SWNTs used is 1.55±0.1 nm.

Likewise, the sulflower molecule octathio[8]circulene[13] (OTC; Fig. 2.36 top) does not require a strict conformation when reacting under the influence of the electron beam. Chamberlain *et al.* have carried out a study into OTC in SWNTs using similar imaging conditions to PCC@SWNT.[7] They discovered that OTC forms radical species upon electron impact which are able to dimerise while adjacent to one another to form a U-shaped adduct (the electron beam-induced reaction mechanism is shown in Fig. 2.38). From this point, the U-shaped adduct can lose a carbon and a sulfur atom from additional electron impacts to form a planar adduct. Continued polymerisation eventually produces an uneven sulfur-terminated nanoribbon inside the SWNT (the imaging carried out by Chamberlain *et al.* is shown in Fig. 2.37).

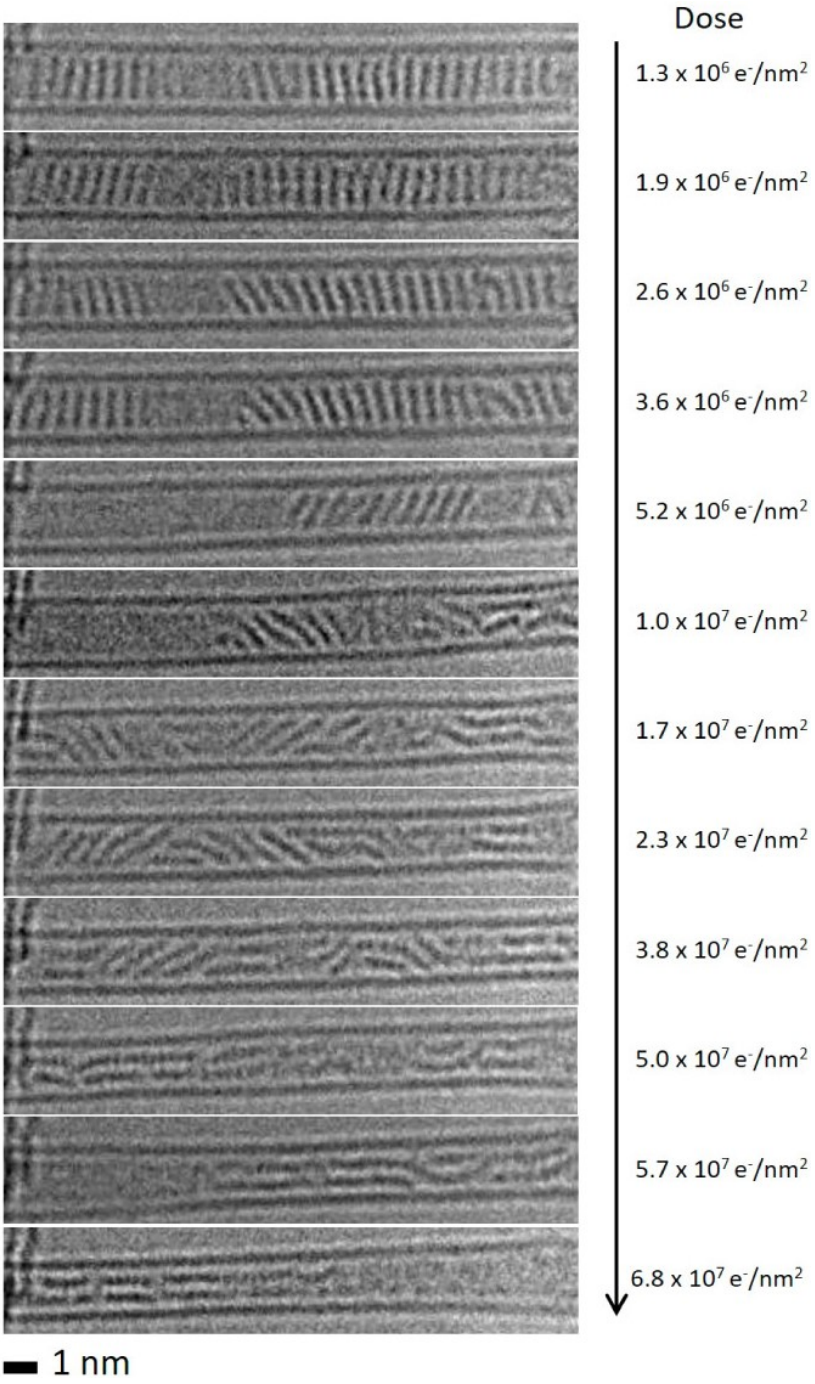

Figure 2.37. A time series of aberration corrected high resolution TEM micrographs showing the polymerisation of OTC molecules ($C_{16}S_8$) into an uneven sulfur-terminated nanoribbon inside the SWNT under an 80 keV electron beam (the cumulative electron doses are shown on the right side of each micrograph). Reproduced from T. W. Chamberlain *et al.*, *ACS Nano*, 2017, **11**, 2509-2520. Licensed under ACS AuthorChoice.[7]

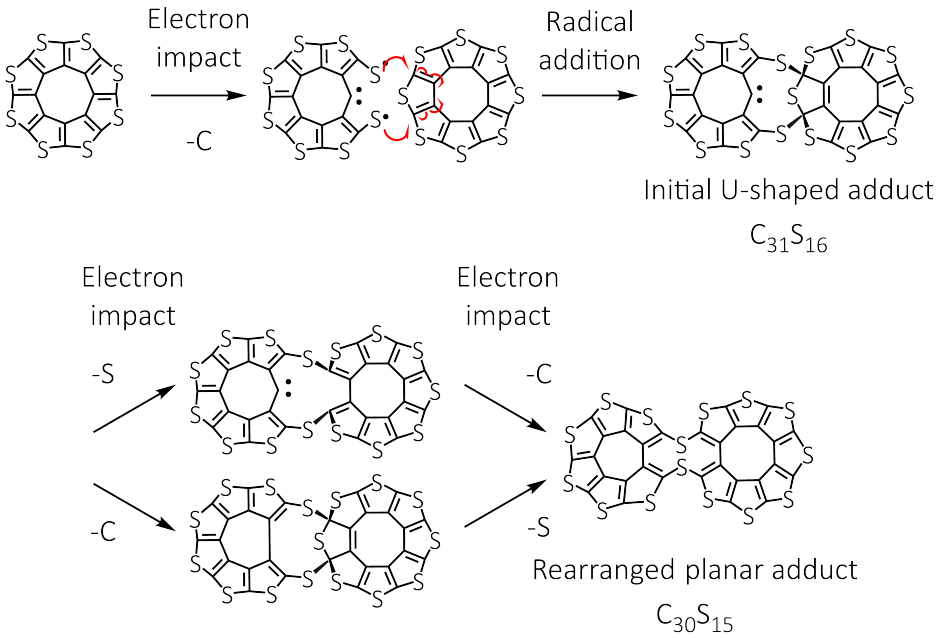

Figure 2.38. The electron beam-induced reaction of two OTC ($C_{16}S_8$) molecules. An incident electron can knock out one of the carbon atoms, forming a thiyl biradical which can attack an adjacent OTC molecule, leading to a U-shaped angular adduct $C_{31}S_{16}$. This adduct can lose either the sextet carbon atom or the out-of-plane sulfur atom via another electron impact to give the planar adduct $C_{30}S_{15}$. Further reactions with OTC molecules eventually leads to a nanoribbon product with an uneven sulfur-terminated edge (Fig. 2.5). Reproduced from T. W. Chamberlain *et al.*, *ACS Nano*, 2017, **11**, 2509-2520. Licensed under ACS AuthorChoice.[7]

A related molecule, tetrathiotetraseleno[8]circulene (TTC; Fig. 2.36 bottom) has not been imaged in a SWNT using TEM before. It was therefore interesting to us to compare both sulflowers to PCC and coronene. In order to do so, both sulflower molecules would need to be imaged under the same conditions as we have used previously. We supposed that, since TTC is so similar in structure to OTC, both molecules might react in similar ways. A proposed electron-beam induced reaction mechanism can be found in Fig. 2.39 which was based upon the OTC reaction mechanism by Chamberlain *et al.* Because there are two types of peripheral atoms in a TTC molecule compared to just the one in OTC, there may be additional forking in the reaction pathways, leading to two possible planar adducts: $C_{30}S_7Se_8$ or $C_{30}S_8Se_7$.

Random population of either type of planar adduct (which likely depends on the orientation of adjacent molecules) will increase the complexity of the final nanoribbon product.

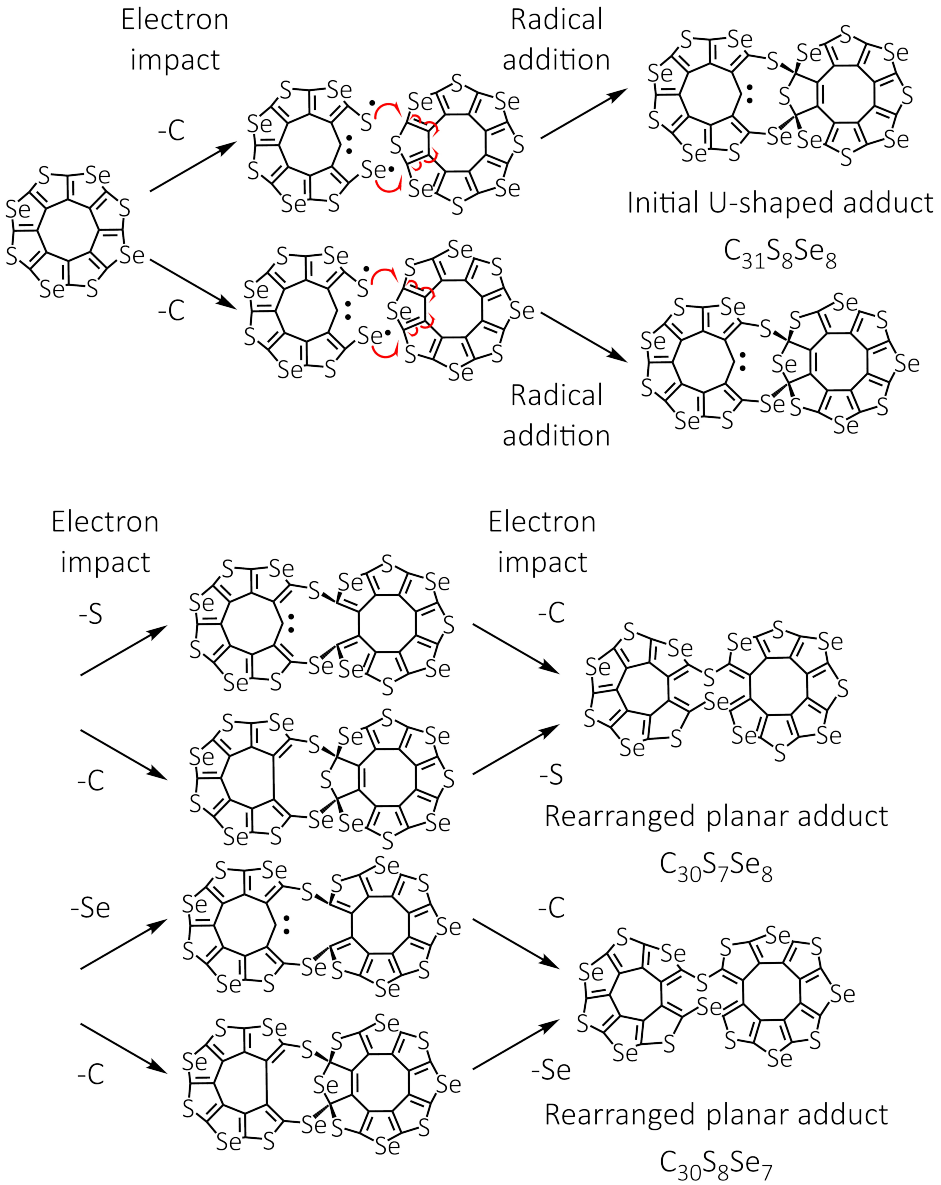

Figure 2.39. Proposed mechanism of the electron beam-induced reaction of two TTC ($C_{16}S_4Se_4$) molecules, based on the OTC ($C_{16}S_8$) reaction mechanism in Fig. 2.38 which was adapted from Chamberlain *et al.*[7]

Both sulflowers were imaged using an electron flux of 10^5 e^- nm^{-2} s^{-1} at ambient temperatures, similar to the fluxes used for imaging PCC. We were unsure of how rapidly the polymerisations might progress and opted to use a much faster image capture rate of a hundred frames per second (compared to ten frames per second for PCC). Therefore, each frame of the sulflowers had a lower signal to noise ratio than the PCC images.

OTC appeared quite the same as the example imaged by Chamberlain *et al.*; a stack of lines in a nanotube. We found that the first dimer formed around 07.86 s which corresponded to a total dose of 9.80×10^5 e^- nm^{-2}. The dimer could be seen as a low contrast tilted U-shape in Fig. 2.40 a) (indicated by the black arrow). The total dose required to give the first dimer was two orders of magnitude lower than the dose used at ambient temperature experiments on PCC@SWNT in Fig. 2.19 b) and c). As the reaction progressed, it became increasingly more difficult to see whether the contrast in the nanotube was due to molecules, intermediates, or the final nanoribbon. TTC also formed stacks of molecules inside nanotubes and had increased image contrast due to the heavier Se peripheral atoms. Almost immediately after imaging began upon this particular area, the reaction had begun. We were unable to capture the point where the first dimer formed. The first image where the nanotube and its contents were in focus was at 04.04 s. This can be seen in Fig. 2.40 b); the image corresponding to a similar total dose for OTC@SWNT at 05.78 s is shown in Fig. 2.40 a) for comparison. Polymerisation had completed by 11.68 s, corresponding to a total dose of 1.83×10^6 e^- nm^{-2}. The nanoribbon products derived from OTC and TTC are shown in Fig. 2.40 c) and d) respectively. Both have uneven edges due to the multiple possibilities during polymerisation. This is particularly noticeable with the TTC nanoribbon in Fig. 2.40 d) where the darker contrast dots (selenium) terminating the nanoribbon appear randomly along the edges.

Without making any gross generalisations using only one image series for each type of sulflower, the immediate impression with the sulflowers was that they seemed more reactive under the electron beam than PCC@SWNT. Both reactions took place over total electron doses that were two orders of magnitude lower than PCC. TTC seemed much more reactive than OTC; substituting S atoms for heavier Se atoms will give different bond strengths and carbon emission threshold energies. We considered some general chemical properties of sulfur and selenium. The dissociation energy of a typical C−S bond is 713.3±1.2 D^o_{298}/kJ mol^{-1} while for a typical C−Se bond, it is 590.4±5.9 D^o_{298}/kJ mol^{-1}.[29] Most C−Se bonds are weaker than C−S bonds which means that the σ^* orbital of the C−Se bond is lower in energy than that of the C−S bond and therefore more reactive as an electron acceptor.[30] Selenium is also more polarisable than sulfur, leading to more rapid electrophilic and nucleophilic substitutions at the element. Selenyl radicals are much more stable than thiyl radicals which allow selenyl radicals to react more reversibly, for example with reactive oxygen species.[30] These differences in properties is why some reactions in nature have evolved to use selenium rather than sulfur. Many reactions occur faster when involving selenium compared to the same reactions involving sulfur. Perhaps generation of selenyl radicals under the electron beam are rapid and require less energy than thiyl radicals. In our experiments, which are quite far removed from biological systems, it may be possible that the faster reactions of TTC under the electron beam are due to selenyl radical additions (see Fig. 2.39) occurring faster than the sulfur analogue.

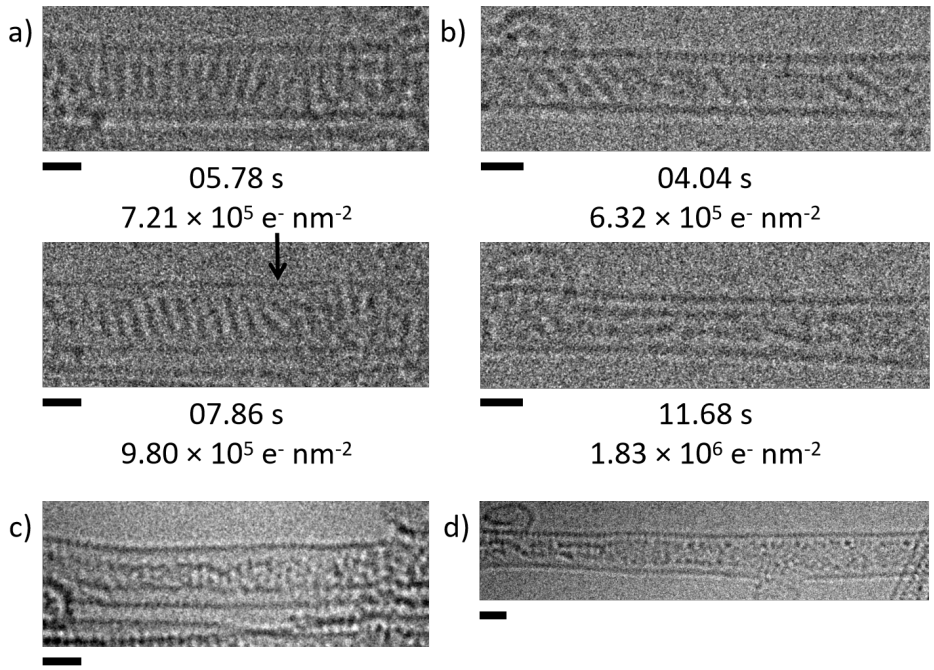

Figure 2.40. a) OTC@SWNTs and b) TTC@SWNTs were imaged under ambient conditions using electron fluxes of 1.25 and 1.57×10^5 e^- nm^{-2} s^{-1} respectively. Formation of the first OTC dimer (indicated by the black arrow) occurred at 07.86 s. TTC molecules had begun reacting at the beginning of imaging so we were unable to capture formation of the first dimer. The first image in focus of TTC@SWNTs was at 04.04 s and the image of OCT@SWNTs corresponding to a similar total dose at 05.78 s is shown side by side for comparison. The final nanoribbon derived from TTC was observed at 11.68 s; however, the OTC polymerisation became too low in contrast during our imaging conditions so the corresponding OTC nanoribbon was not visible. We increased the electron flux to image the final OTC c) and TTC d) nanoribbons. All scale bars are 1 nm.

2.4 Conclusions

Throwing as many reasonable stimuli at PCC as can be found in a typical academic setting has shown us several aspects of PCC polymerisation. PCC dimerisation by the electron beam can be reproduced under a different type of excitation; by using the UV laser of the MALDI-ToF mass spectrometer. This suggests that the electron beam-induced polymerisation might have a route via electronic excitation and therefore the chemistry initiated in the TEM has relevance to more 'typical' chemistry. We could use the TEM to discover new types of reactions. PCC and the dimer adduct as well as several other intermediates were detected in the MALDI-ToF MS, backing up the proposed mechanism by Chamberlain *et al.*[7] An agreement between MALDI-ToF MS, a macroscopic analysis method, and TEM, a local probe method, is an important outcome. Both PCC and the dimer adduct exhibited an aesthetically pleasing symmetical pattern of fragmentation, losing pairs of chlorine atoms around the molecules. This revealed the importance of symmetrical chlorine loss for the stabilities of the intermediates and highlighted the role of the nanotube for templating the linear polymerisation of PCC into a nanoribbon.

Using the vast amount of high resolution TEM data obtained from the electron Physical Science Imaging Centre (ePSIC) at Diamond Light Source, we were able to follow the reaction kinetics on the single-molecule level in direct-space. We were able to calculate the experimental PCC dimerisation cross section and compare this to the theoretical value, thus allowing us to conclude that the key mechanism for the electron beam-induced polymerisation of PCC is direct knock-on damage. The method developed here is general and could be applied to many other molecular systems, thus allowing us to routinely use the TEM to study reactions at the single-molecule level.

The HR-TEM combined with the superfast OneView camera and variable temperature sample stages available at ePSIC gave us the opportunity to investigate

the reactions of individual molecules of PCC under different conditions. The way in which PCC molecules pack within a nanotube significantly influenced polymerisation. The Diels-Alder cycloaddition imposed particularly rigid restrictions upon the orientation requirements for PCC molecules which led to a latent period at the beginning of irradiation where dimerisation did not occur because of a lack of space. The requirement for space meant that molecular packing was far more important than we initially imagined. Nanotubes which were wide enough to allow PCC to stack perpendicular to the nanotube wall seemed to provide more stability to the stack of PCC molecules. These molecules could pack efficiently and thus reduce the amount of space available for stack shuffling. On the other hand, narrower nanotubes could only allow stacking of slanted PCC molecules and so the molecules were not in as much contact with each other. This seemed to increase the rate of shuffling and therefore the rate of polymerisation.

Heating PCC@SWNTs allowed us to decouple thermal effects from electron beam-induced effects. Heating while simultaneously irradiating with the electron beam removed the latent period in some experiments because there was enough thermal energy to overcome the binding energy between PCC molecules in a stack within the SWNT. For certain experiments where there was more efficient molecular packing, there were still latent periods, further highlighting the importance of sterics in this polymerisation reaction as well as the strength of the binding energy between efficiently packed PCC molecules. We also carried out experiments using only heat to initiate reactions. These experiments were used to calculate the activation energy for the thermally activated PCC polymerisation. Although this value is a low limit of the activation energy, we have the means and knowledge with which to improve the thermal kinetics study and acquire an estimate of the activation energy.

Under cryogenic conditions, we were able to reduce molecular motion and vibration and captured atomically resolved images of the PCC stack. However, we did

run into the problem of water which unfortunately plagues most of cryo microscopy. Our samples are not air or moisture sensitive and tend to be quite robust so trial and error with cryo TEM was possible with our samples. We discovered what appeared to be nanocrystals of solid chlorine which formed over the duration of imaging. The nanocrystals were of high image contrast; they did not degrade under the electron beam; and the d-spacings matched quite closely to reported values for solid chlorine. This was the first time the chlorine by-product of PCC polymerisation was captured on camera. This was another important piece of information for understanding the reaction mechanism because it is consistent with the mechanism proposed by Chamberlain *et al.* as well as the data from MALDI-ToF MS in this chapter.

Finally, PCC@SWNTs was briefly compared to coronene and two types of sulflowers in SWNTs. Coronene and the sulflowers reacted much faster under the electron beam than PCC. The major reason why coronene reacts faster is because coronene does not have heavy terminating atoms and therefore receives much more energy via collisions from beam electrons. There are likely a few reasons why the sulflowers reacted faster than PCC. The most obvious reason is that sulflower polymerisation (for both types of sulflowers used in the study) does not have any orientation requirements and therefore molecules can react while still tightly packed together. Therefore, there is no latent period during irradiation. The differences in bond strengths between carbon and the terminating atoms in PCC and the sulflowers likely also had an effect on the rate of reaction.

This chapter has been an in-depth study into the imaging and irradiation of PCC encapsulated within SWNTs. We developed a general method to study the kinetics of electron beam-induced reactions at the single-molecule level. This general method can be combined with macroscopic analysis methods such as MALDI-ToF MS to understand reaction mechanisms. We have decoupled thermal effects from electron beam-induced effects on the polymerisation of PCC. We have also

used cryo TEM to capture atomistic detail of PCC as well as the elusive chlorine by-product of PCC polymerisation. Finally, we have imaged and irradiated other PAHs in SWNTs and compared them to PCC@SWNTs in order to place PCC in a wider context of electron beam-induced reactions at the single-molecule level. TEM of PCC can be found throughout the literature and even with such a long history, we discovered new complexities and nuances with the electron beam-induced reactions of PCC. No doubt there is still much to learn about reactions at the single-molecule level. The work carried out here will likely be useful groundwork for future studies.

2.5 Future Work

Based on the methods developed in this chapter, the JEOL ARM300F at ePSIC is a near-perfect machine for direct-space kinetic studies for a wide range of molecules. The OneView camera is versatile, sensitive, and fast enough to capture many types of reactions. The microscope also has a direct electron detector, the Medipix camera, which is much smaller in size to the OneView but would obviously allow for use of even lower electron fluxes. In terms of the best electron flux to use, this parameter would depend heavily on the system being investigated. An important factor to bear in mind would be the beam stabilities of the molecules. For example, it would be extremely challenging to study the kinetics of the beam-induced reactions of hydrogenated molecules such as coronene@SWNTs because this molecule reacts much too quickly.

The ability to control the temperature of the sample stage with excellent precision is another attractive feature at ePSIC which we have utilised during our experiments. These temperature stages would also be useful for many other direct-space kinetic studies. We would, for example, revisit the thermal kinetics study of PCC@SWNTs, carry out the varied heating experiments on separate heating chips, and calculate an estimate for the activation energy. Cryo microscopy is also worth exploring. For particularly beam stable molecules (i.e. ones with heavy atoms), cryogenic temperatures can assist with atomically resolved imaging by reducing molecular motion and vibration. This could be useful for a plethora of systems, especially inorganic materials encapsulated in SWNTs.

Overall, the methodologies developed in this chapter should prove useful for future studies into direct-space kinetic studies. Indeed, we recently have used similar techniques and equipment for the study of electron beam-induced reactions of polyoxometalates (POMs) in SWNTs.

2.6 Experimental Methods

Reagents were purchased from Sigma Aldrich and used as received. Octathio[8]circulene and tetrathiotetraseleno[8]circulene were given to us by V. G. Nenajdenko from Moscow M.V. Lomonosov State University.

Matrix assisted laser desorption/ionisation time-of-flight mass spectrometry (MALDI-ToF MS) analyses were performed on a Bruker ultraFlexIII instrument (Bruker Daltonik, Bremen, Germany). Samples were deposited on a stainless steel target plate (type MTP384; Bruker Daltonik, Bremen, Germany) and due to the nature of the samples, no matrix was required. A pulsed solid-state UV laser (355nm, 500 μJ, 66.7Hz) was used to ionise the sample. The instrument was operated in reflection mode. Data was acquired through the instrument's flexControl software (v3,B185; Bruker Daltonik, Bremen, Germany), and processed using Bruker's flexAnalysis software (v3,B96; Bruker Daltonik, Bremen, Germany).

Nuclear magnetic resonance (NMR) spectroscopy was carried out in deuterated chloroform using a Bruker AV(III)500 spectrometer by Analytical Chemistry at the University of Nottingham. In particular, special thanks are due to S. Aslam for acquiring the 16 hr-long ^{13}C NMR spectrum of perchlorocoronene. All chemical shifts are quoted in ppm where ^{1}H NMR and ^{13}C spectra are quoted relative to neat trimethylsilate (TMS).

High resolution transmission electron microscopy (HR-TEM) was carried out at the electron Physical Science Imaging Centre (ePSIC) at Diamond Light Source. The microscope JEOL ARM300F is Cs corrected and was operated at 80 kV. Micrographs were acquired using the Gatan OneView camera. In-situ sample heating with single tilt DENS Solutions Wildfire heating holder, temperature range: ambient to 1200 ^{o}C. In-situ sample cooling with liquid nitrogen single tilt Fischione cooling holder, operating temperature -175 ^{o}C. TEM samples were prepared via a drop casting technique, where samples were dispersed in HPLC-grade isopropanol, fol-

lowed by deposition of several drops of the suspension onto copper grid mounted with “lacey” carbon films (Agar Scientific UK), and dried under ambient conditions. All micrographs were processed using Gatan Digital Micrograph and ImageJ Fiji software[31–33] with the ImageJ plugins TurboReg and StackReg.[34]

We thank Diamond Light Source for access and support in use of the electron Physical Science Imaging Centre (Instrument E02 and proposal numbers MG22887, MG23260, and SW23444) that contributed to the results presented here.

2.6.1 Synthesis of PCC and characterisation

Synthesis of PCC was taken from literature[14,15] and is described here. Aluminium chloride (7.5 mg) was dissolved in sulfuryl chloride (3 ml) and heated to reflux (70 ^{o}C). A mixture of coronene (30 mg) and sulfur monochloride (8.89 µl) in sulfuryl chloride (5 ml) was added dropwise to the reflux over 3 min. The reaction turned inky blue upon addition of the coronene mixture. The solvent volume was reduced to approximately 1 ml by distillation and left to reflux (70 ^{o}C) for 28 hours. Additional sulfuryl chloride was added throughout the reflux to maintain the solvent volume. The resulting dark yellow suspension was distilled to dryness and neutralised with deionised water and sodium bicarbonate, heated to 95 ^{o}C for 1 hr, and then acidified with hydrochloric acid (37%, pH 1). The mixture was filtered through a PTFE membrane (0.2 µm pore size), washed with deionised water, and dried under vacuum. No purification was required. The product, perchlorocoronene was a dark yellow powder (72 mg, quant.). ^{13}C NMR δ(500 MHz, $CDCl_3$); 133.2 (Aryl C-Cl), 126.8 (Aryl C), 121.4 (Aryl C). Positive-ion MALDI-ToF MS m/z; 713 ($C_{24}Cl_{12}$), 642 ($C_{24}Cl_{10}$), 571 ($C_{24}Cl_8$), 500 ($C_{24}Cl_6$).

2.6.2 Filling molecules into SWNTs

Single-walled carbon nanotubes (50 mg) were refluxed in nitric acid (3 M, 50 mL) at 120 ^{o}C for 2 hr. The nanotubes were then filtered over PTFE membrane (0.2 µm) and washed with sodium hydroxide (1 M, 50 mL) as well as deionised water (50 mL) and dried under vacuum to give dried, opened SWNTs (49.5mg). Perchlorocoronene (or coronene; octathio[8]circulene; tetrathiotetraseleno[8]circulene) was added to the opened nanotubes in a 3:1 mass ratio, sealed in a glass ampoule under vacuum ($\times$ 10^{-4} mbar) and heated at 400 ^{o}C for 72 hr. The resulting black powder was washed by sonicating in toluene and filtering over PTFE membrane (0.2 µm). Sublimation filling was also carried out at 500 and 600 ^{o}C for perchlorocoronene to test how different temperatures affected filling.

2.7 References

1. T. Baird, J. H. Gall, D. D. MacNicol, P. R. Mallinson and C. R. Michie, *J. Chem. Soc., Chem. Commun.*, 1988, 1471–1473.
2. T. W. Chamberlain, J. Biskupek, S. T. Skowron, P. A. Bayliss, E. Bichoutskaia, U. Kaiser and A. N. Khlobystov, *Small*, 2015, **11**, 622–629.
3. J. R. Fryer, *Ultramicroscopy*, 1984, **14**, 227–236.
4. J. R. Fryer, *J. Electron Microsc. Tech.*, 1989, **11**, 310–325.
5. W. Dong, T. Baird, J. R. Fryer, C. J. Gilmore, D. D. MacNicol, G. Bricogne, D. J. Smith, M. A. O'Keefe and S. Hövmoller, *Nature*, 1992, **355**, 605–609.
6. A. Markevich, S. Kurasch, O. Lehtinen, O. Reimer, X. Feng, K. Müllen, A. Turchanin, A. N. Khlobystov, U. Kaiser and E. Besley, *Nanoscale*, 2016, **8**, 2711–2719.
7. T. W. Chamberlain, J. Biskupek, S. T. Skowron, A. V. Markevich, S. Kurasch, O. Reimer, K. E. Walker, G. A. Rance, X. Feng, K. Müllen, A. Turchanin, M. A. Lebedeva, A. G. Majouga, V. G. Nenajdenko, U. Kaiser, E. Besley and A. N. Khlobystov, *ACS Nano*, 2017, **11**, 2509–2520.
8. M. Koshino, Y. Niimi, E. Nakamura, H. Kataura, T. Okazaki, K. Suenaga and S. Iijima, *Nat. Chem.*, 2010, **2**, 117–124.
9. S. T. Skowron, T. W. Chamberlain, J. Biskupek, U. Kaiser, E. Besley and A. N. Khlobystov, *Acc. Chem. Res.*, 2017, **50**, 1797–1807.
10. B. W. Smith and D. E. Luzzi, *Chem. Phys. Lett.*, 2000, **321**, 169–174.
11. D. A. Britz, A. N. Khlobystov, K. Porfyrakis, A. Ardavan and G. A. D. Briggs, *Chem. Commun.*, 2005, 37–39.
12. R. K. E. Gover, *PhD thesis, University of Nottingham*, 2016.
13. T. Hensel, N. N. Andersen, M. Plesner and M. Pittelkow, *Synlett*, 2016, **27**, 498–525.
14. M. Koshino, H. Kurata and S. Isoda, *Ultramicroscopy*, 2010, **110**, 1465–1474.
15. M. Ballester and C. Molinet, *C. Chem. Ind. (London)*, 1954, 1290.
16. O. Silberrad, *J. Chem. Soc. Trans.*, 1925, **127**, 2677–2684.
17. S. T. Skowron, V. O. Koroteev, M. Baldoni, S. Lopatin, A. Zurutuza, A. Chuvilin and E. Besley, *Carbon*, 2016, **105**, 176–182.

18. R. F. Egerton, *Microsc. Res. Tech.*, 2012, **75**, 1550–1556.

19. S. E. Mason, P. H. Beton and N. A. Besley, *J. Chem. Theory Comput.*, 2019, **15**, 5628–5634.

20. L. A. Baker and J. L. Rubinstein, *Methods Enzymol.*, 2010, **481**, 371–388.

21. R. F. Thompson, M. Walker, C. A. Siebert, S. P. Muench and N. A. Ranson, *Methods*, 2016, **100**, 3–15.

22. L. E. Franken, E. J. Boekema and M. C. A. Stuart, *Adv. Sci.*, 2017, **4**, 1600476.

23. J. D. Bernal and R. H. Fowler, *J. Chem. Phys.*, 1933, **1**, 515–548.

24. R. L. Collin, *Acta Cryst.*, 1952, **5**, 431–432.

25. J. Donohue and S. H. Goodman, *Acta Cryst.*, 1965, **18**, 568–569.

26. B. M. Powell, K. M. Heal and B. H. Torrie, *Mol. Phys.*, 1984, **53**, 929–939.

27. H. Sawada, N. Shimura, K. Satoh, E. Okunishi, S. Morishita, T. Sasaki, Y. Jimbo, Y. Kohno, F. Hosokawa, T. Naruse, M. Hamochi, T. Sato, K. Terasaki, T. Suzuki, M. Terao, S. Waki, T. Nakamichi, A. Takano, Y. Kondo and T. Kaneyama, *JEOL News*, 2014, **49**, 51–57.

28. B. Botka, M. E. Füstös, H. M. Tóháti, K. Németh, G. Klupp, Z. Szekrényes, D. Kocsis, M. Utczás, E. Székely, T. Váczi, G. Tarczay, R. Hackl, T. W. Chamberlain, A. N. Khlobystov and K. Kamarás, *Small*, 2014, **10**, 1369–1378.

29. *"Bond Dissociation Energies" in CRC Handbook of Chemistry and Physics*, ed. J. Rumble, CRC Press/Taylor & Francis, Boca Raton, FL, 100th Edition (Internet Version), 2019.

30. H. J. Reich and R. J. Hondal, *ACS Chem. Biol.*, 2016, **11**, 821–841.

31. C. A. Schneider, W. S. Rasband and K. W. Eliceiri, *Nat. Methods*, 2012, **9**, 671–675.

32. J. Schindelin, C. T. Rueden and M. C. Hiner, *Mol. Reprod. Dev.*, 2015, **82**, 518–529.

33. J. Schindelin, I. Arganda-Carreras, E. Frise, V. Kaynig, M. Longair, T. Pietzsch, S. Preibisch, C. Rueden, S. Saalfeld, B. Schmid, J. Y. Tinevez, D. J. White, V. Hartenstein, K. Eliceiri, P. Tomancak and A. Cardona, *Nat. Methods*, 2012, **9**, 676–682.

34. P. Thévenaz, U. E. Ruttimann and M. Unser, *IEEE Trans. Image Process.*, 1998, **7**, 27–41.

CHAPTER 3

Polyheterocyclic aromatic hydrocarbon crystals

3.1 Introduction

Moving on from polycyclic aromatic hydrocarbon (PAH) molecules in single-walled carbon nanotubes (SWNTs), we shall now discuss our studies on crystals of polyheterocyclic aromatic molecules, in particular hexaazatrinaphthylene (HAT) derivatives (Fig. 3.1). HATs are nitrogen-containing polyheterocyclic aromatic molecules easily synthesised through condensation of hexaketocyclohexane and 1,2-diaminobenzene (Fig. 3.2). A wide variety of derivatives are available through post-synthetic modifications of HATs, allowing fine tuning of properties such as ionisation potentials and electron affinities.[1] HAT derivatives are able to self-organise into discotic liquid crystals wth strongly electron-deficient characters and therefore electron-accepting behaviours which may be useful properties for organic electronic applications.[2,3] Because of this, there has been research into use of HAT derivatives in perovskite solar cells.[4,5]

HATs functionalised with alkylamides can form self-assembled supramolecular nanofibres which can be crosslinked using chemical or photochemical means and patterned onto a surface for use as nanoscale optoelectronic devices.[6] Self-

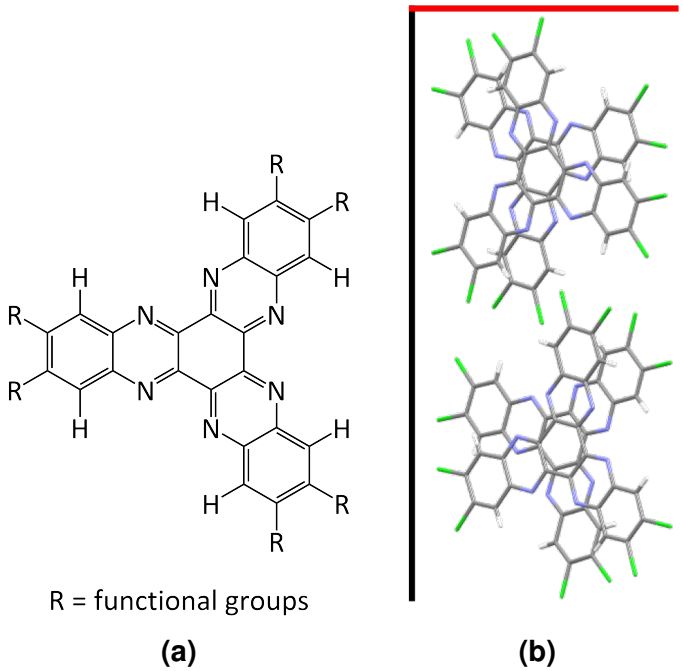

Figure 3.1. (a) Chemical structure of 5,6,11,12,17,18-hexaazatrinaphthylene (H-HAT) where R can be any functional group. (b) Unit cell along the c axis of a solvent-free 2,3,8,9,14,15-hexachloro-5,6,11,12,17,18-hexaazatrinaphthylene (Cl_6-HAT) crystal synthesised via sublimation in vacuum.[1] The a axis is indicated with a red line; the b axis with black.

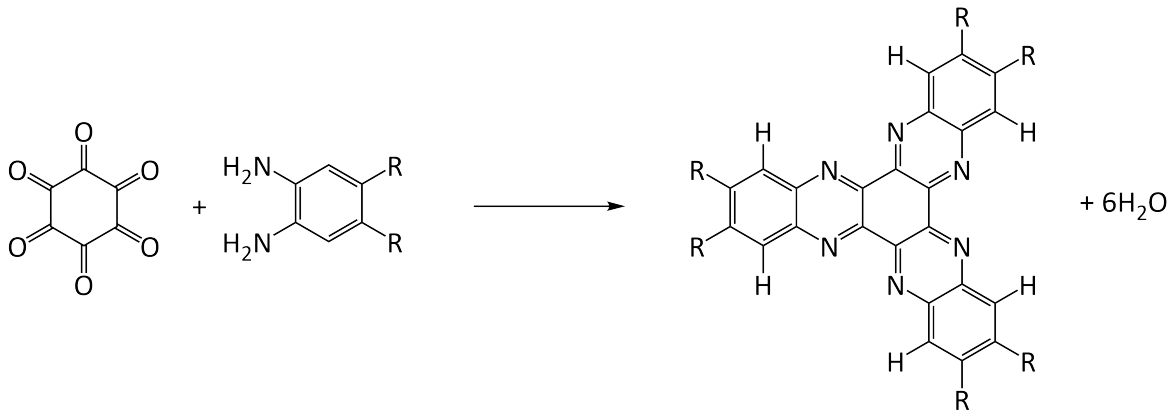

Figure 3.2. Typical synthesis of HAT molecules where R can be any functional groups; if R on the diaminobenzene are two additional amine groups, polycondensation can occur to form an extended structure.

assembled fibres functionalised with aromatic and aliphatic amines can also be used to gelate solvents of different polarity. These highly stable organogels with organised morphologies are interesting candidates for n-type semiconductors.[7] Porous polymers incorporating various HAT groups have also been synthesised.[8] Because a wide range of properties are accessible through the use of different functional units, these materials are promising candidates for chemo-selective adsorption and heterogeneous catalysis as well as organic cathodes for lithium ion batteries.[9–13] However, polymers made from HAT building blocks are often highly disordered and non-crystalline due to the irreversible nature of the polycondensations used to synthesise HAT-based polymers.[14] As an example, condensation of the hexaketocyclohexane and tetra-diaminobenzene (to form an extended network rather than a single HAT molecule) could occur linearly which introduces defects into the overall covalent organic framework or COF (see Fig.3.3).[15] As such, some properties of HAT-derived materials such as electron transport can be negatively affected.

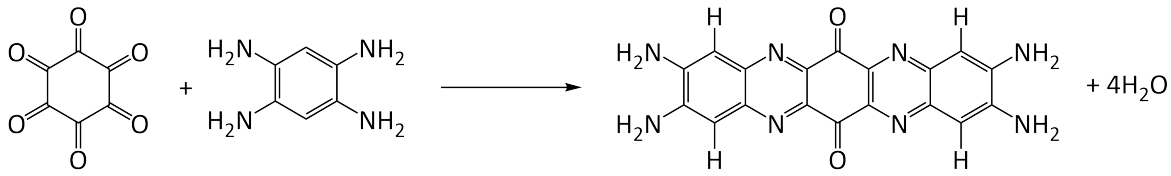

Figure 3.3. Linear condensation of hexaketocyclohexane and tetra-diaminobenzene that introduces defects into the extended structure because further condensation cannot occur when the ketone groups are opposite one another.

At this point, allow us to take a detour here to discuss how the electron beam is often used for crosslinking materials and whether this might be useful for HAT-derived framework synthesis. We shall focus on materials made from aromatic molecules as this is most relevant to the current topic at hand. Electron beams can be focused into very small spots (<1 nm) and are therefore widely used in electron beam lithography (EBL) for fabrication of nanoscale structures. Irradiated resist ma-

terials either become soluble (positive resist) or insoluble (negative resist) in specific solvents. Aromatic self-assembled monolayers (SAMs) deposited on substrates such as gold or silicon are used as ultrathin organic resists and can be crosslinked by the electron beam to form negative resists.[16–19] SAMs have also been selectively modified by the electron beam; nitro groups on aromatic SAMs were converted to amino groups under low energy (50 eV) electron irradiation. The aromatic part of the SAM was dehydrogenated and crosslinked.[20] This is particularly interesting from a chemist's perspective because this electron-induced reduction of the nitro groups occurred without any external reducing or hydrogenating agents. Therefore, the hydrogen must come from the aromatic part of the monolayer itself. The C−H bonds were first cleaved by both primary (the electron beam) and secondary electrons (emitted from the metal substrate) which lead to crosslinking of the aromatic groups (formation of both single and double bonds) and hydrogenation of the nitro groups.[21] The amino groups can be further modified using electrophilic agents to produce localised molecularly patterned surfaces.

"Chemical lithography" has been carried on further by Angelova *et al.* who used an electron beam (either 50 or 100 eV) to crosslink SAMs composed of a variety of aromatic molecules, ranging from oligophenyl derivatives to polycyclic aromatic hydrocarbons, into ultrathin free-standing carbon nanomembranes (CNMs) (Fig. 3.4). The properties of the CNMs such as thickness, conductivity, chemical functionalisation, and presence of nanopores depended on the type of precursor molecule in the SAM.[22]

In terms of synthesising an extended, crystalline frameworks from HAT building blocks, we could utilise the lone pairs on the nitrogen atoms of HAT molecules. These are available for coordinating to metals such as titanium,[23] cobalt,[24] copper,[25] palladium,[26] rhenium,[26,27] and dysprosium.[28] We might imagine a metal organic framework (MOF) utilising HATs as the linkers where each HAT molecule acts

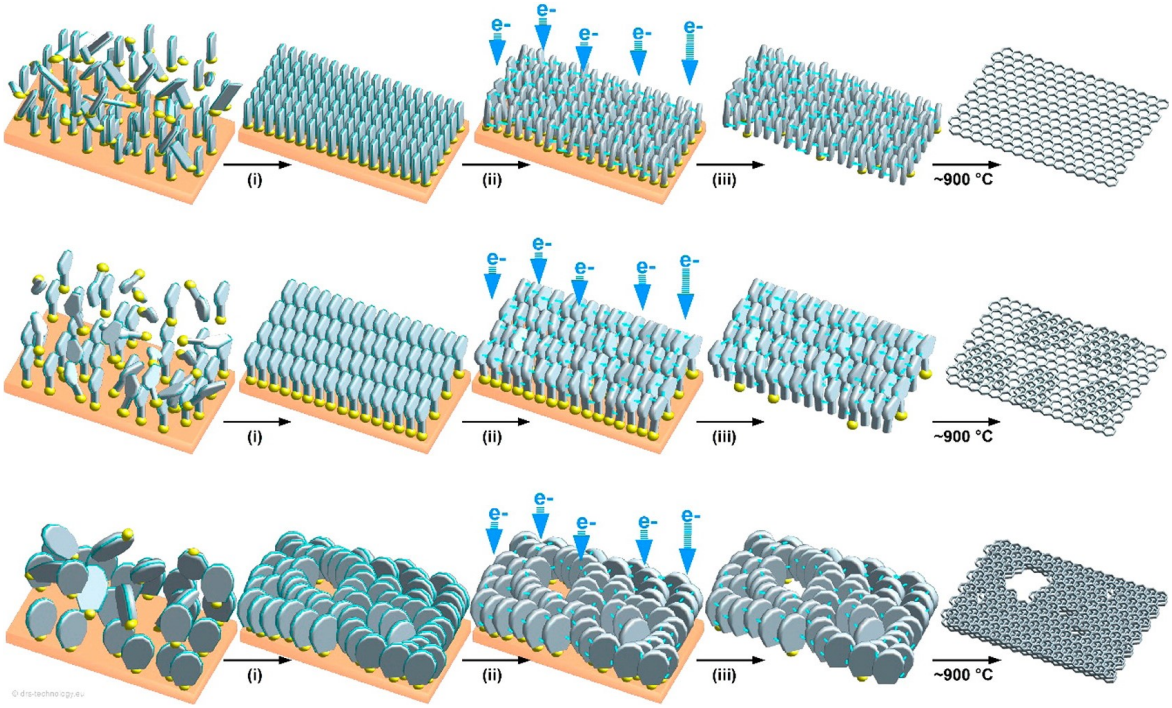

Figure 3.4. Schematics illustrating the formation of carbon nanomembranes (CNMs) and subsequently graphene from self-assembled monolayers (SAMs) composed of "linear" precursor molecules such as nonfused oligophenyl derivatives (top), small polycyclic hydrocarbons (PAHs) such as naphthalene (middle), or "bulky" aromatic hydrocarbons such as hexabenzocoronene (bottom). The SAMs are prepared on a substrate (i) and irradiated with an electron beam to form the CNM (ii), released from the underlying substrate (iii), and then further annealed at 900 °C (iv) to form graphene. Oligophenyls and small PAHs crosslink to form homogenous CNMs while the bulkier molecular precursors assemble in a less-ordered monolayer and as a result, form CNMs with nanopores. All these features were retained when the CNMs were annealed to form graphene.[22] Reprinted (adapted) with permission from P. Angelova *et al.*, *ACS Nano*, 2013, **7**, 6489-6497. Copyright (2013) American Chemical Society.

as a tris-bidentate ligand. Due to the rigid, bulky nature of HATs, the metal centre would need to accept a tetrahedral conformation. However, as with synthesis of porous polymers from HATs, MOF production is complicated to control and is often a delicate balance of reaction conditions leading to a mixture of thermodynamic and kinetic products. Therefore it is difficult to scale up MOF production and process the MOF powders for use in applications.[29]

EBL is therefore worth exploring for fabrication of HAT-derived COFs. There is little in the literature on the behaviour of HAT crystals under an electron beam so studying the electron beam-induced reactions of HAT molecules using transmission electron microscopy (TEM) is an obvious first step. Of course, this may not be directly comparable to how EBL could be used to fabricate materials out of HATs since EBL irradiation relies on secondary and backscattered electrons from the substrate. However, it would still be useful to have an understanding of electron beam-induced processes and at this point we have much experience using TEM for this purpose.

3.2 Aims and Objectives

There is much literature on the topic of imaging crystals with the aim of reducing damage for structural characterisation (as discussed in chapter one). The work in this chapter will build upon that by expanding our knowledge on imaging crystals in order to use the electron beam as a synthetic tool. The aim of the work in this chapter is to understand the electron beam-induced reactions of HAT-derived frameworks, an essential step towards carrying out electron beam fabrication of these large polyheterocyclic aromatic molecules. To this end, three molecules are chosen for comparative analysis: hexaazatrinaphthylene (HAT) and its semi-chlorinated (Cl_6-HAT) and semi-fluorinated (F_6-HAT) cousins because syntheses and purification of these three molecules are straightforward and have been described in the literature (general reaction scheme is shown in Fig. 3.2).[1]

TEM analysis will be performed at 80 kV to correspond with the voltage used by the electron beam lithography (EBL) facility at the University of Nottingham. Therefore any results obtained during this study would be more comparable to products from a scaled up process using EBL. For all three molecules, the critical doses at 80 kV will be determined. The critical dose values will be useful numbers to know to aid fabrication of materials from HATs. The critical dose is defined here as the total electron dose the crystal can take *before* all crystallinity is destroyed. This will be determined by following the disappearance of the diffraction pattern, similar to how crystals were originally studied in the TEM (as discussed in chapter one). Determination of critical doses from diffraction patterns is discussed in more detail later on in this chapter.

As the solvent free crystal structures for the parent HAT and F_6-HAT have not been solved in the literature, we shall use the expertise of resident crystallographers and the facilities at Diamond Light Source to carry out single-crystal X-ray diffraction (SCXRD) as part of this study. The crystal structures will be necessary for under-

standing how these crystals react under the electron beam in three-dimensional space as well as assignments of the diffraction patterns.

Because the beam stabilities of HAT-type crystals have seemingly not been studied in the TEM, it will also be a useful objective to compare and contrast HATs with other polycyclic aromatic molecules that have been extensively studied in the TEM such as the old favourites copper(II) phthalocyanine (CuPc) and perchlorocoronene (PCC) which we introduced back in the first and second chapters respectively.

3.3 Results and Discussion

The HAT molecules were synthesised as described in the literature (the procedure and characterisation can be found in Experimental Methods and the Appendix)[1] while PCC was synthesised in chapter two. We grew most of the crystals via sublimation under high vacuum, with the exception of the fully-chlorinated hexadecachloro-copper(II) phthalocyanine (Cl_{16}-CuPc), which decomposed upon heating. We resorted to using the brilliant green powder Cl_{16}-CuPc as purchased. Avoiding the presence of solvent during crystallisation was an important aspect of this study since any solvent molecules would complicate the crystals' behaviour under the electron beam and likely increase the rate of beam damage.

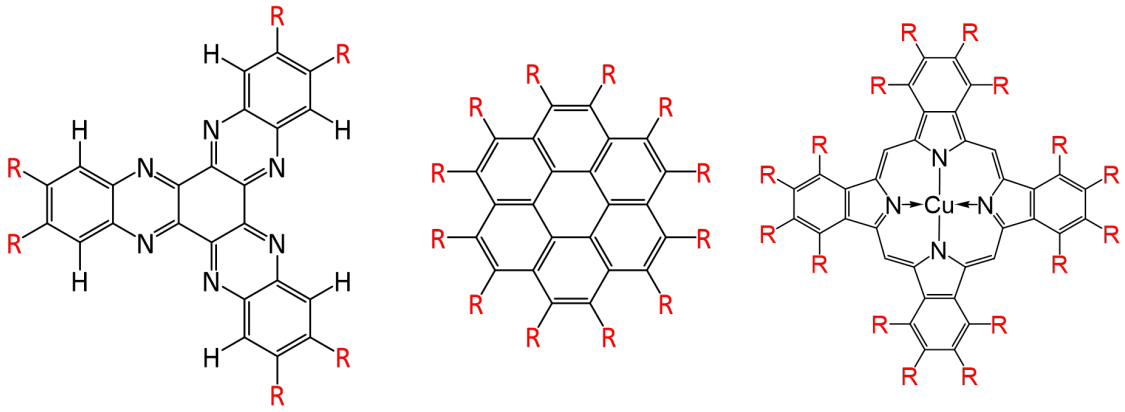

R = H: 5,6,11,12,17,18-hexaazatrinaphthylene (H-HAT)
R = F: 2,3,8,9,14,15- hexafluoro-5,6,11,12,17,18-hexaazatrinaphthylene (F_6-HAT)
R = Cl: 2,3,8,9,14,15- hexachloro-5,6,11,12,17,18-hexaazatrinaphthylene (Cl_6-HAT)

R = H: coronene
R = Cl: perchlorocoronene (PCC)

R = H: copper(II) phthalocyanine (CuPc)
R = Cl: hexadecachloro-copper(II) phthalocyanine (Cl_{16}-CuPc)

Figure 3.5. Structures of all the molecules studied in this chapter.

Crystalline powders of HATs, coronene, PCC, CuPc, and Cl_{16}-CuPc (Fig. 3.5) were gently pressed onto TEM grids and imaged under the same conditions (see Experimental Methods). Thin, similarly-sized nanocrystals of all the molecules were selected for imaging to limit the heating and charging effects as well as production of secondary electrons which would contribute to chemical transformations and therefore complicate our interpretations of electron dose-induced transformations in the TEM. Thin crystals would also be more comparable to the few-layer crystals we would ideally irradiate in EBL. Several image series were acquired for each type of crystal using comparable electron fluxes. For ease of reading, diffraction patterns have been labelled with time stamps rather than electron doses.

For the molecules where there are crystal structures in literature or where the structure could be solved using single crystal X-ray diffraction (SCXRD), the software package CrysTBox[30–32] was used to assign Miller indices to the diffraction patterns. The planes corresponding to the pairs of diffraction spots were generated using CrysTBox which gave us information on the planes of atoms that were indirectly observed over time. For some diffraction patterns, CrysTBox was unable to find the crystal lattice either because there were not enough data points (diffraction spots) for the program to work with or multiple crystal orientations were present. We chose pairs of diffraction spots with similar d-spacings (for each type of crystal) that could be tracked for the entire time series. We shall begin by discussing the irradiation of PCC and Cl_{16}-CuPc crystals.

The solvent-free unit cell of PCC[33] is shown in three orientations in Fig. 3.6. However, SCXRD data of Cl_{16}-CuPc could not be found in literature, with or without solvent. Since we could not grow our own solvent-free crystals via sublimation, we did not carry out assignments of the Cl_{16}-CuPc diffraction patterns. The overall diffraction patterns for both PCC (Figs. 3.8 and 3.9) and Cl_{16}-CuPc (Figs. 3.10 and 3.11) crystals did not seem to disappear during irradiation. However, both types

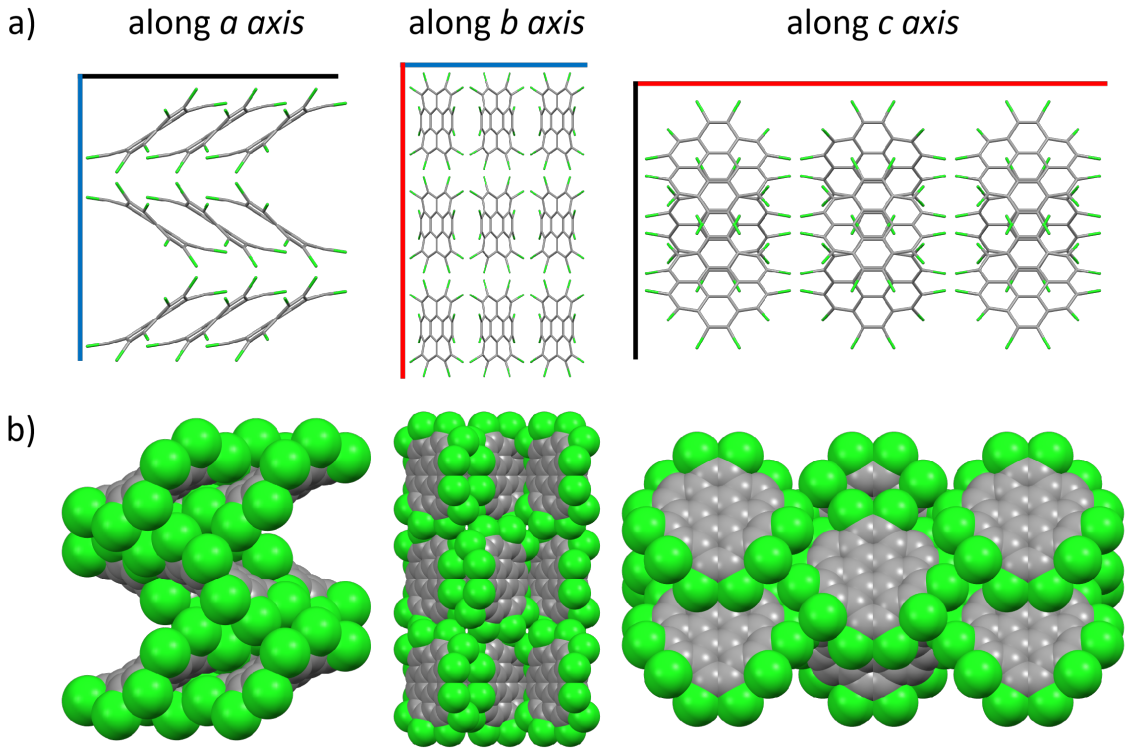

Figure 3.6. The unit cell of perchlorocoronene (PCC)[33] with the a (red), b (black), and c (blue) axes indicated. Three orientations of the unit cell along the axes are shown as both a) stick and b) space-filling models.

of nanoscale crystals were quite mobile during irradiation, rotating, translating, and sometimes even launching themselves off camera (this was the case with all irradiated crystals in this study). As a result, the diffraction spot intensities were prone to increasing and decreasing during irradiation (Fig. 3.7) and we could not use a decrease in intensity to e^{-1} of the maximum intensity to calculate the critical dose (as has been used before in the literature - see chapter one). Therefore, we used critical dose in our study to mean the total electron dose a crystal was irradiated with before crystallinity was destroyed. The intensities I in the diffraction patterns of PCC and Cl_{16}-CuPc crystals (as well as other crystals in this study) were normalised into percentages using I/I_{Max} where I_{Max} was the maximum intensity over the entire duration of irradiation. For PCC and Cl_{16}-CuPc crystals, we placed a self-imposed limit of a total electron dose of 4.00 $\times$ 10^4 e^- nm^{-2} (corresponding to some four

hundred or so seconds) to compare to other molecules since the crystallinities of PCC and Cl_{16}-CuPc crystals were still intact after ten minutes of irradiation. Strictly speaking, 4.00 $\times$ 10^4 e^- nm^{-2} is not the critical dose for PCC and Cl_{16}-CuPc; the critical doses for these two molecules are above 4.00 $\times$ 10^4 e^- nm^{-2}. However, given the low electron fluxes used in this study and the beam stability afforded from perchlorination of aromatic molecules, it may have taken far too long to find those critical dose values and it became more important to irradiate the other molecules in this study.

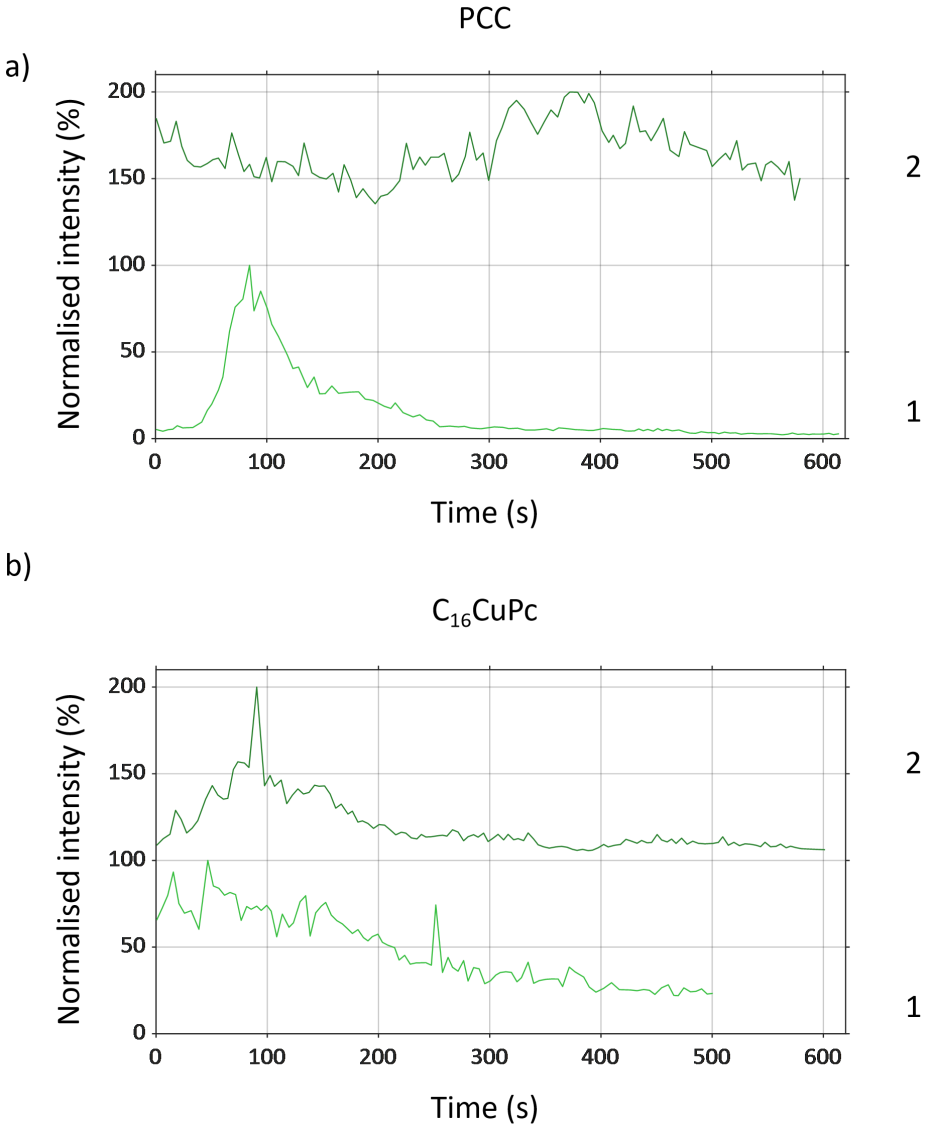

Figure 3.7. Normalised intensities over time of a) PCC1 (light green), PCC2 (dark green), b) Cl_{16}-CuPc1 (light green), and Cl_{16}-CuPc2 (dark green). PCC2 and Cl_{16}-CuPc2 have been offset by 100% for clarity, appearing between 100 and 200% on the plot. All crystals were irradiated with electron fluxes on the order of 10 e^{-} nm^{-2} s^{-1}. Note that for PCC1, the diffraction spot intensity appears to be negligible at the beginning of irradiation. This is not the case; see Fig. 3.8 where the diffraction pattern of PCC1 is apparent. The crystal rotating and/or translating during irradiation led to a huge increase in the intensity of the tracked pair of diffraction spots, leading to a seemingly low diffraction spot intensity at the beginning.

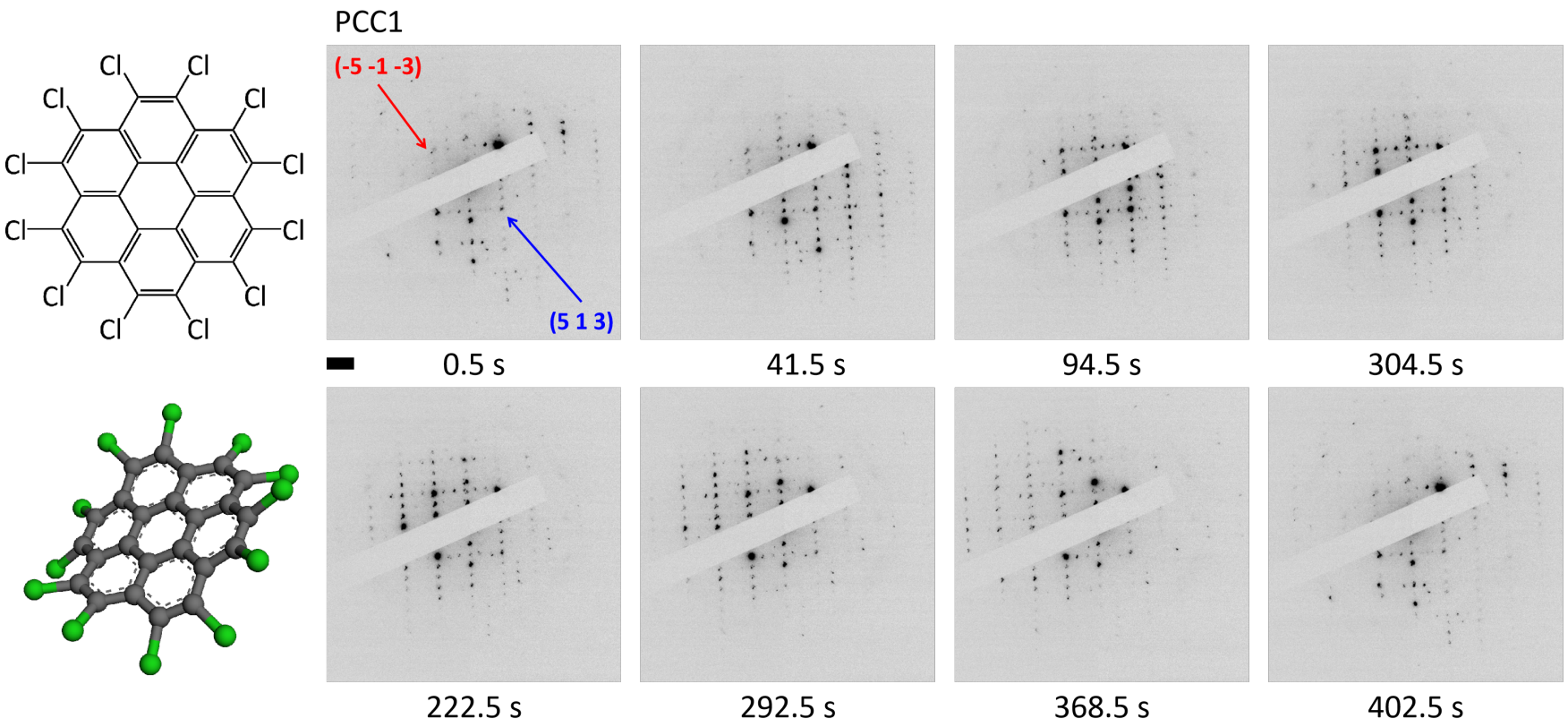

Figure 3.8. A diffraction pattern time series of a nanocrystal of perchlorocoronene (PCC1). The time stamps are shown below each pattern. The scale bar is 2 1/nm. The tracked pair of diffraction spots have a d-spacing of 3.01 Å. More information on the planes corresponding to the diffraction spots can be found in Fig. 3.45 in the Appendix. The nanocrystal of PCC1 was irradiated using an electron flux of 9.94 $\times$ 10 e^- nm^{-2} s^{-1} over a period of 402.5 s for a total electron dose of 4.00 $\times$ 10^4 e^- nm^{-2}. The structure and model of PCC are shown on the left.

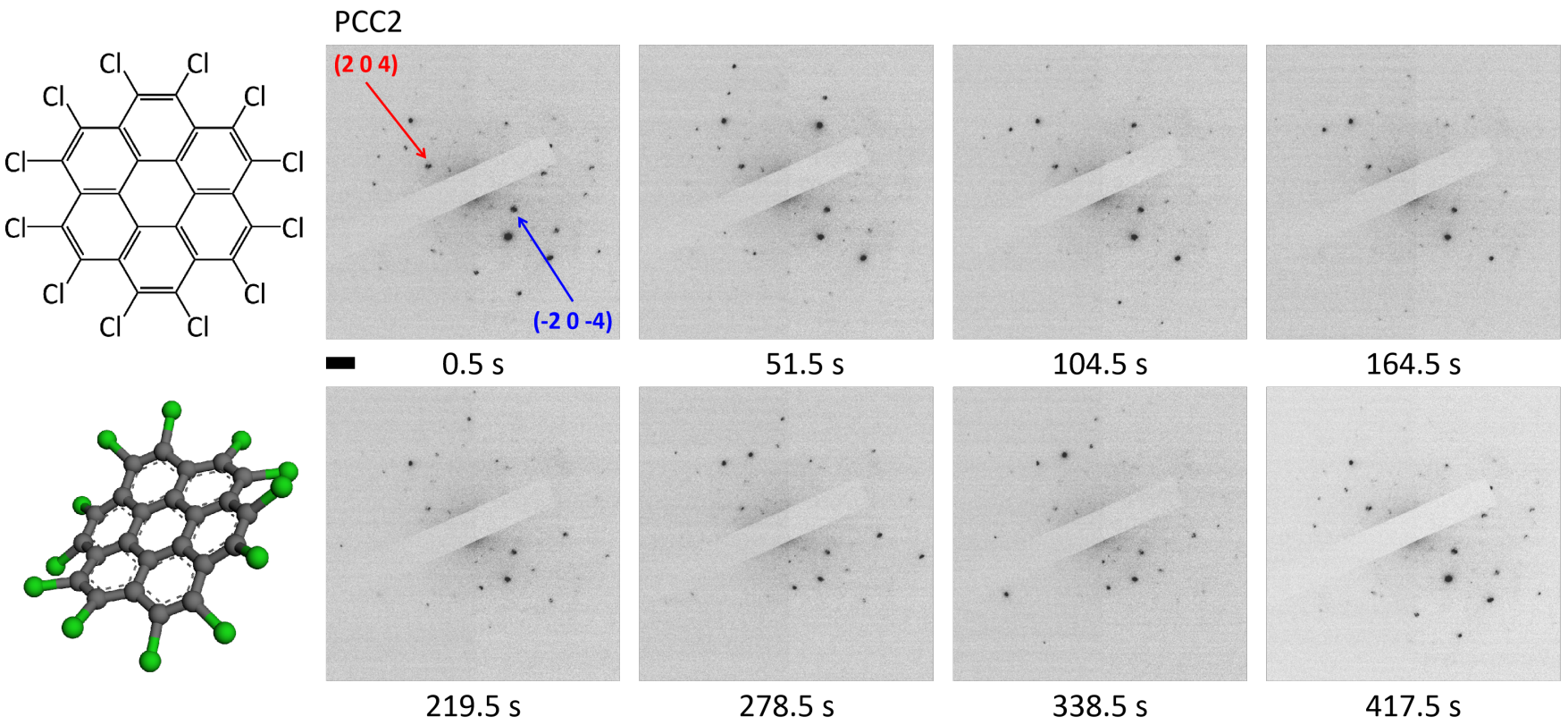

Figure 3.9. A diffraction pattern time series of a nanocrystal of perchlorocoronene (PCC2). The time stamps are shown below each pattern. The scale bar is 2 1/nm. The tracked pair of diffraction spots have a d-spacing of 2.96 Å. More information on the planes corresponding to the diffraction spots can be found in Fig. 3.45 in the Appendix. The nanocrystal of PCC2 was irradiated using an electron flux of 9.65 $\times$ 10 e^- nm^{-2} s^{-1} over a period of 417.5 s for a total electron dose of 4.03 $\times$ 10^4 e^- nm^{-2}. The structure and model of PCC are shown on the left.

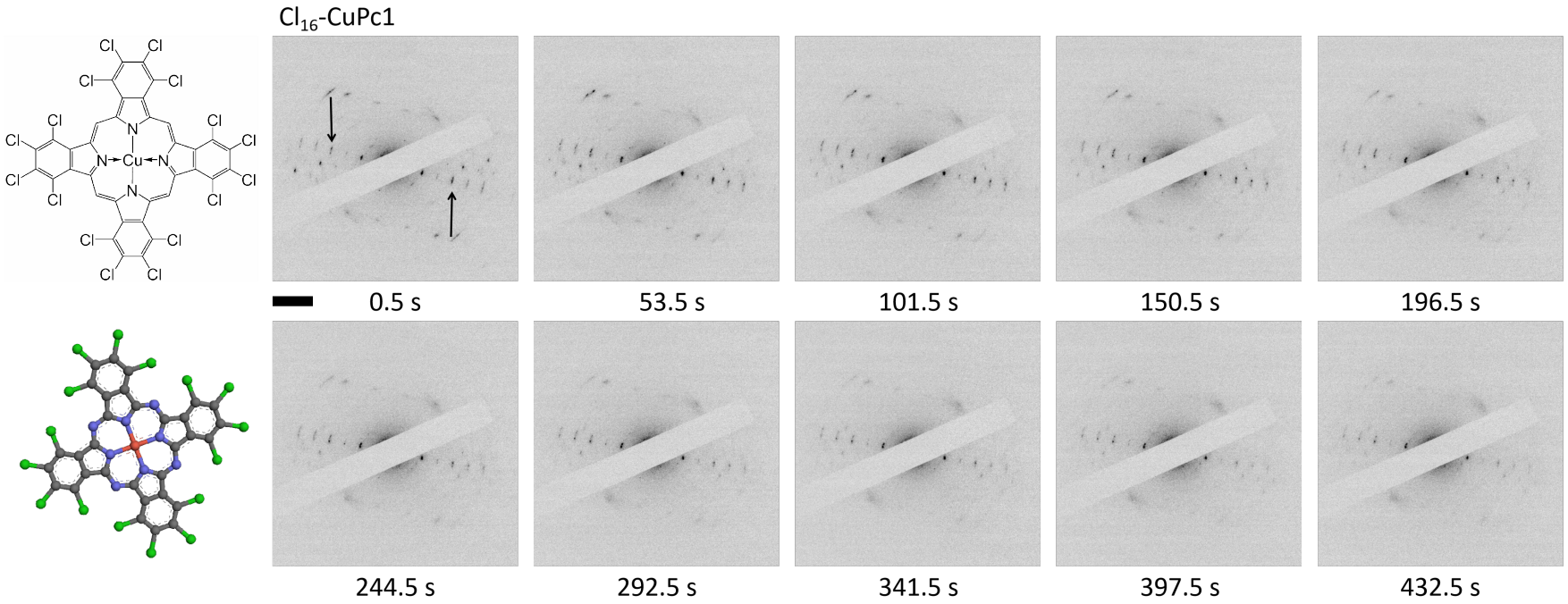

Figure 3.10. A diffraction pattern time series of a nanocrystal of hexadecachloro-copper(II) phthalocyanine (Cl_{16}-CuPc). The time stamps are shown below each pattern. The scale bar is 2 1/nm. The tracked pair of diffraction spots have a d-spacing of 3.27 Å. The nanocrystal of Cl_{16}-CuPc was irradiated using an electron flux of 9.25×10 e^- nm^{-2} s^{-1} over a period of 432.5 s for a total electron dose of 4.00×10^4 e^- nm^{-2}. The structure and model of Cl_{16}-CuPc are shown on the left.

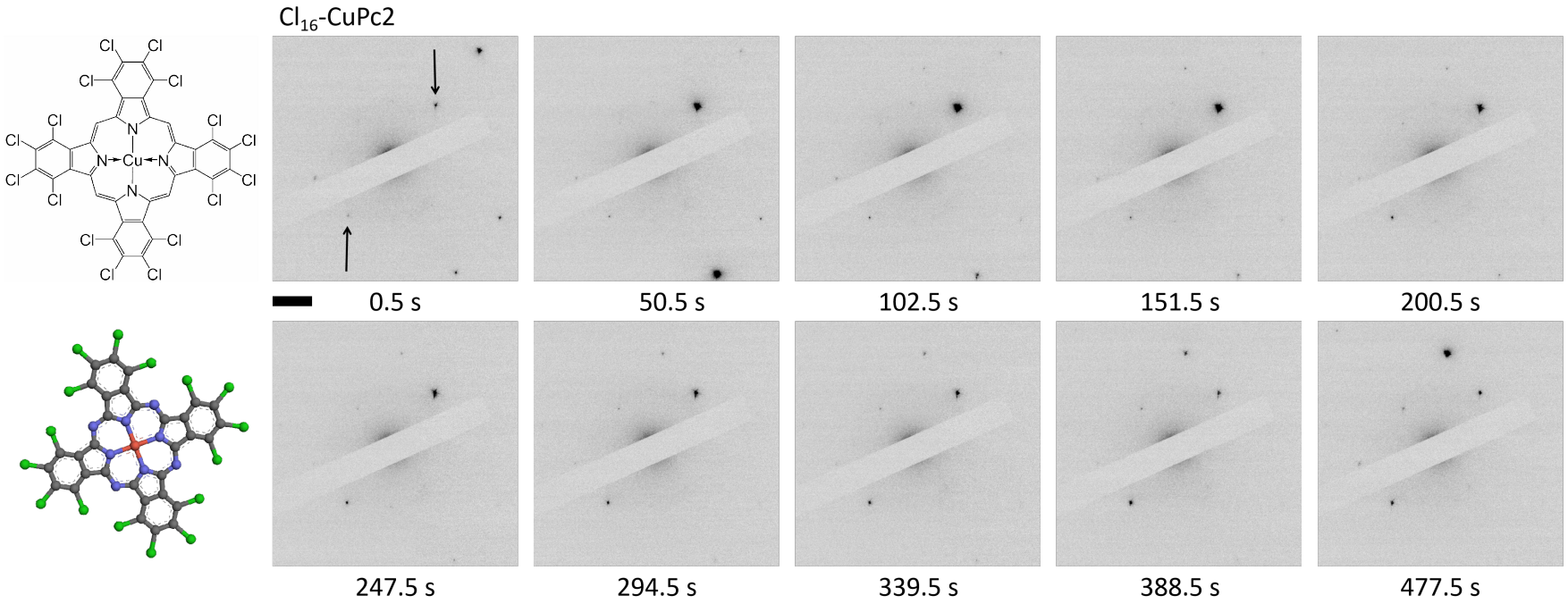

Figure 3.11. A diffraction pattern time series of a nanocrystal of hexadecachloro-copper(II) phthalocyanine (Cl_{16}-CuPc). The time stamps are shown below each pattern. The scale bar is 2 1/nm. The tracked pair of diffraction spots have a d-spacing of 2.85 Å. The nanocrystal of Cl_{16}-CuPc was irradiated using an electron flux of 8.38 $\times$ 10 e^- nm^{-2} s^{-1} over a period of 477.5 s for a total electron dose of 4.00 $\times$ 10^4 e^- nm^{-2}. The structure and model of Cl_{16}-CuPc are shown on the left.

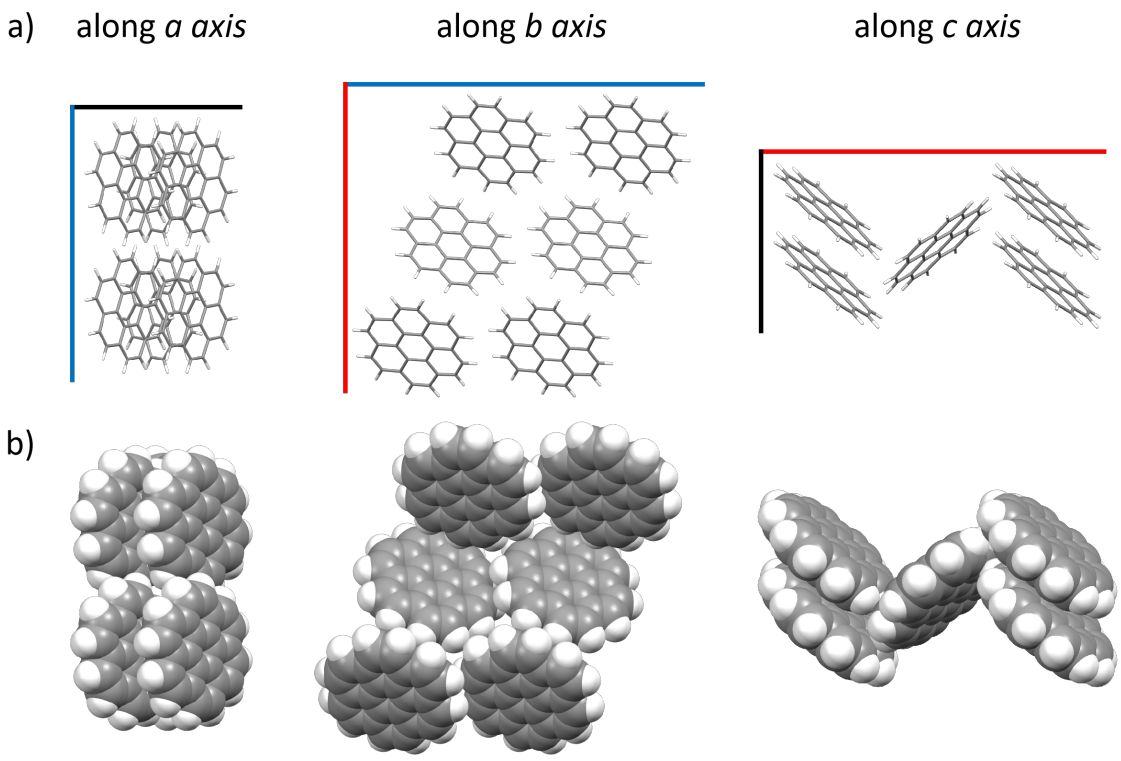

Figure 3.12. The unit cell of coronene[34] with the a (red), b (black), and c (blue) axes indicated. Three orientations of the unit cell along the axes are shown as both a) stick and b) space-filling models.

Conversely, the changes in diffraction patterns of both coronene and CuPc crystals were rapid. Their unit cells are shown in Figs. 3.12 and 3.13 respectively. After an average total electron dose of 1.31 $\times$ 10^4 e^- nm^{-2} for coronene and 1.17 $\times$ 10^4 e^- nm^{-2} for CuPc, the pair of diffraction spots tracked in each pattern had faded (see Fig. 3.14 for the intensities over time). The timing between each micrograph was approximately 5 s (but could be more depending on how slow the software decided to be). Therefore if we chose to use micrographs with amorphous rings as the end point of the series, we could be overestimating the critical doses. An underestimation of the total dose will be less damaging to the crystals and more useful to us should we progress onto using the electron beam to create extended cross-linked structures from these molecules. We used the penultimate micrographs *before* the diffraction spots had entirely disappeared and so these micrographs still contained

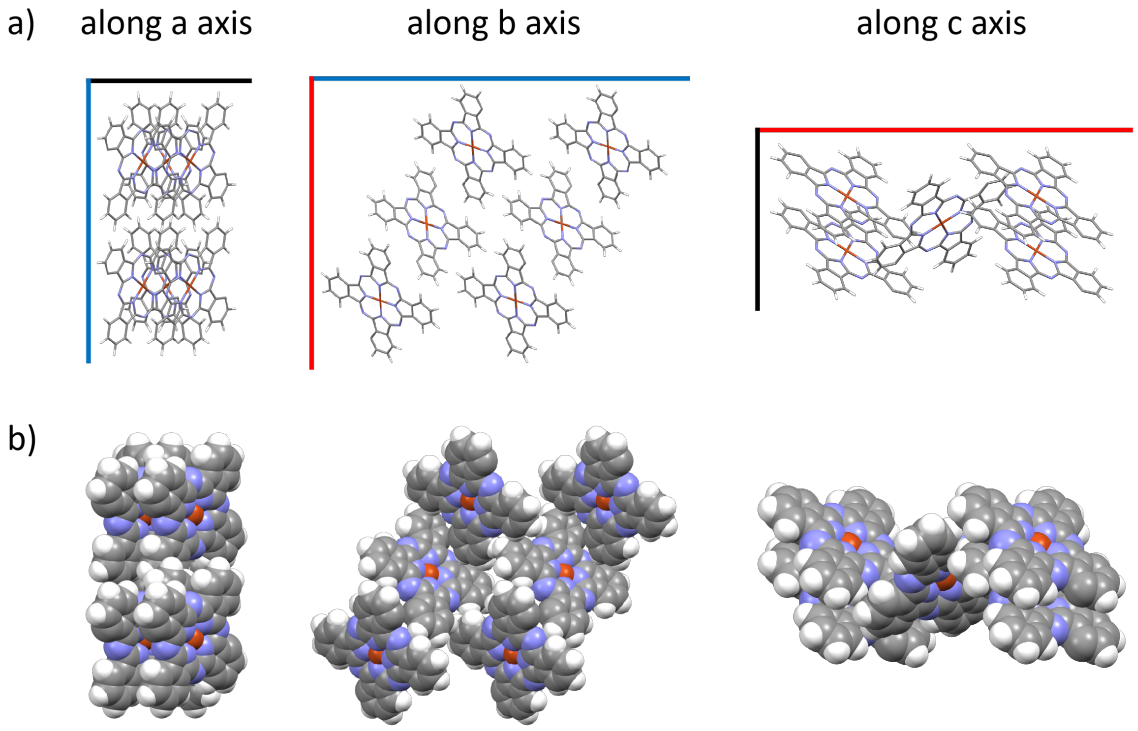

Figure 3.13. The unit cell of copper(II) phthalocyanine (CuPc)[35] with the a (red), b (black), and c (blue) axes indicated. Three orientations of the unit cell along the axes are shown as both a) stick and b) space-filling models.

some diffraction spots rather than fully amorphous rings. The final data points in all of the plots in Fig. 3.14 (and subsequent intensity plots) correspond to the final micrographs in each irradiation series where the diffraction spot intensities had faded to slightly above background noise.

Crystals of organic molecules suffer greatly from radiolysis under the electron beam[36] so again, the results with coronene and CuPc were unsurprisingly similar to literature. Multiple studies into radiation damage of organic molecules have shown that these molecules can be incredibly sensitive to the electron beam.[36–47] Coronene has also been investigated while encapsulated inside SWNTs.[43] In this case, the main source of damage is via direct knock-on since the coronene molecules are encapsulated within thermally and electrically conducting carbon nanotubes. The direction in which incident electrons strike a molecule can affect

how the molecule is damaged. Coronene molecules in SWNTs are all parallel to the electron beam. Any bonds parallel to the electron beam are more susceptible to electron beam damage than other bonds in the molecule because the momentum of an incident electron is transferred along those bonds.[43] In our studies, the crystals were deposited in different orientations and irradiated along different crystallographic directions. This was due in part to random deposition of crystals on the TEM grids as well as movement of the crystals during irradiation. The critical doses for the coronene and CuPc crystals did not vary hugely (see Fig. 3.25 for the standard error bars). This suggests that the critical dose does not depend significantly on the orientation of the crystal with respect to the electron beam. Damage from radiolysis does not change significantly with direction since ionisation can occur regardless of how the molecule is orientated with respect to the beam.

Replacing hydrogen with halogens improves the stability of molecules under the electron beam.[36,42,48] As we have seen in the literature as well as in the results presented so far, fully halogenated organic molecules are significantly more stable to the electron beam than their hydrogenated counterparts. PCC and Cl_{16}-CuPc crystals appear entirely unperturbed after being irradiated with a total electron dose of 4.00 $\times$ 10^4 e^- nm^{-2} whereas in about a quarter of that dose, both coronene and CuPc crystals had amorphised. Additionally, ejected chlorine atoms are much more sterically hindered compared to hydrogen atoms. The surrounding molecules in the crystal prevent chlorine from escaping easily; this is known as the "cage effect". Therefore chlorine atoms have a higher probability of recombining with their molecule. Meanwhile, hydrogen atoms are much more likely to be ejected into the vacuum of the TEM, escaping entirely.[36,42] After loss of hydrogen atoms, the peripheral carbon atoms are incredibly unstable. It is possible that, in order to form stable C – C bonds, the molecules reorder themselves in the crystal so that they can react and cross-link with one another. The energy for molecular motion (rotation,

translation etc.) can be provided by the electron beam. One can imagine this process to be quite random, leading to an amorphous carbon structure at the end of irradiation.

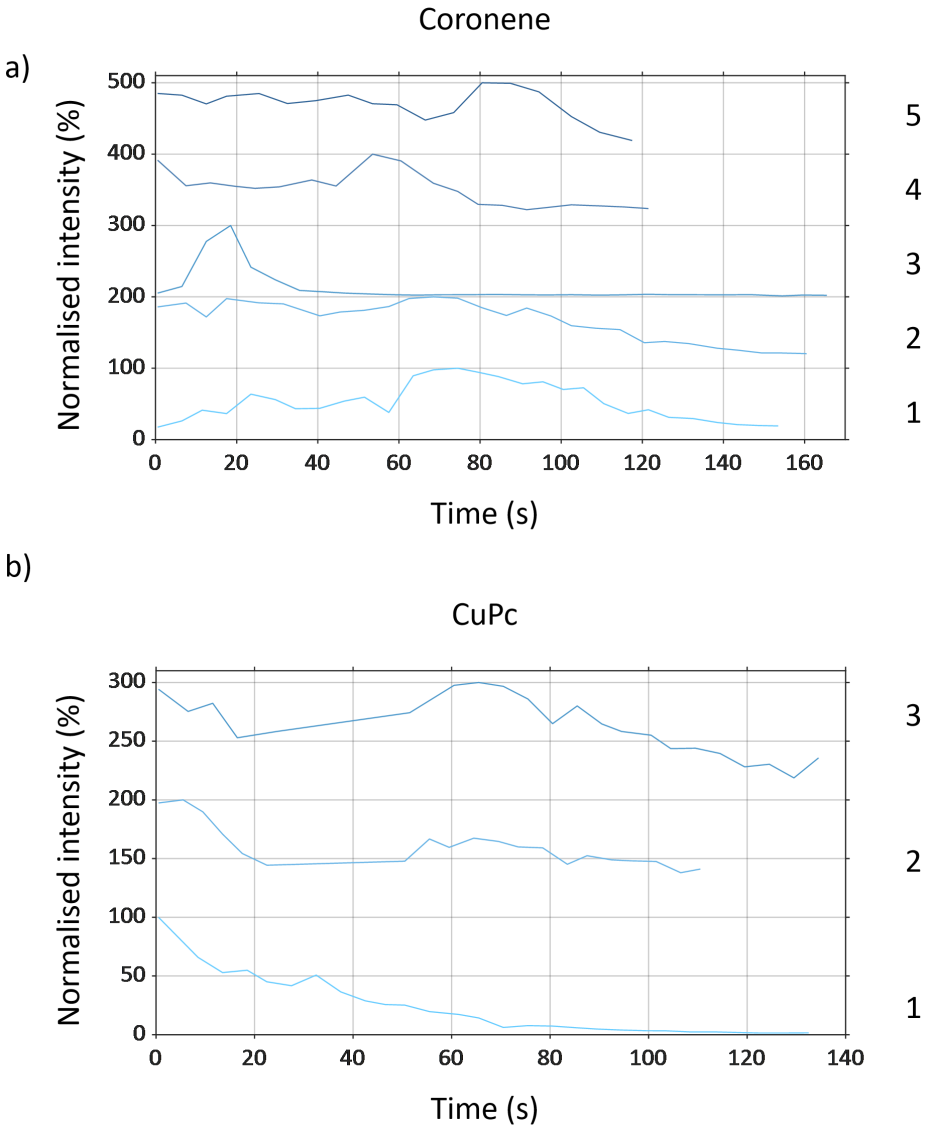

Figure 3.14. Normalised intensities over time of a) Coronene1-5 from bottom to top and b) CuPc1-3 from bottom to top. All plots have been offset from one another by 100% for clarity. All crystals were irradiated with electron fluxes on the order of 10 e^{-} nm^{-2} s^{-1}.

Studying these four well-known molecules under our imaging conditions gave us a critical dose scale on which to compare the unknown HAT molecules. It would be reasonable to expect the same trend with the HAT molecules, namely that the halogenated derivatives, F_6-HAT and Cl_6-HAT, would be more stable to the electron beam than H-HAT itself.

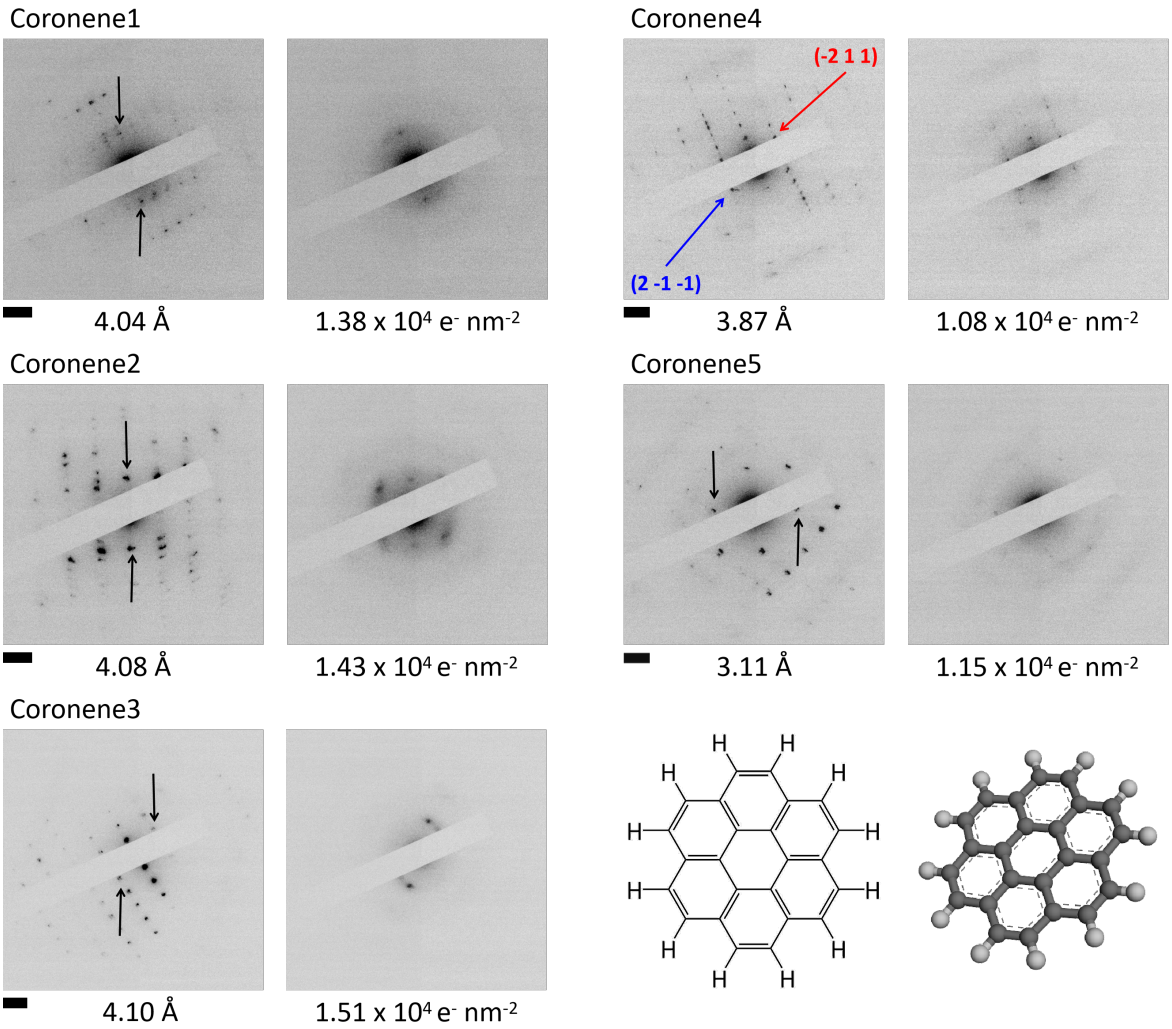

Figure 3.15. Diffraction patterns of nanocrystals of coronene. The d-spacings of the tracked pairs of diffraction spots and the critical doses are shown below the micrographs. More information on the planes corresponding to the diffraction spots of Coronene4 can be found in Fig. 3.46 in the Appendix. The scale bars are 2 1/nm. The nanocrystals were irradiated using an average electron flux of 9.14 $\times$ 10 e^- nm^{-2} s^{-1} over an average period of 143.7 s for an average total electron dose of 1.31 $\times$ 10^4 e^- nm^{-2}. The structure and model of coronene are shown in the bottom right.

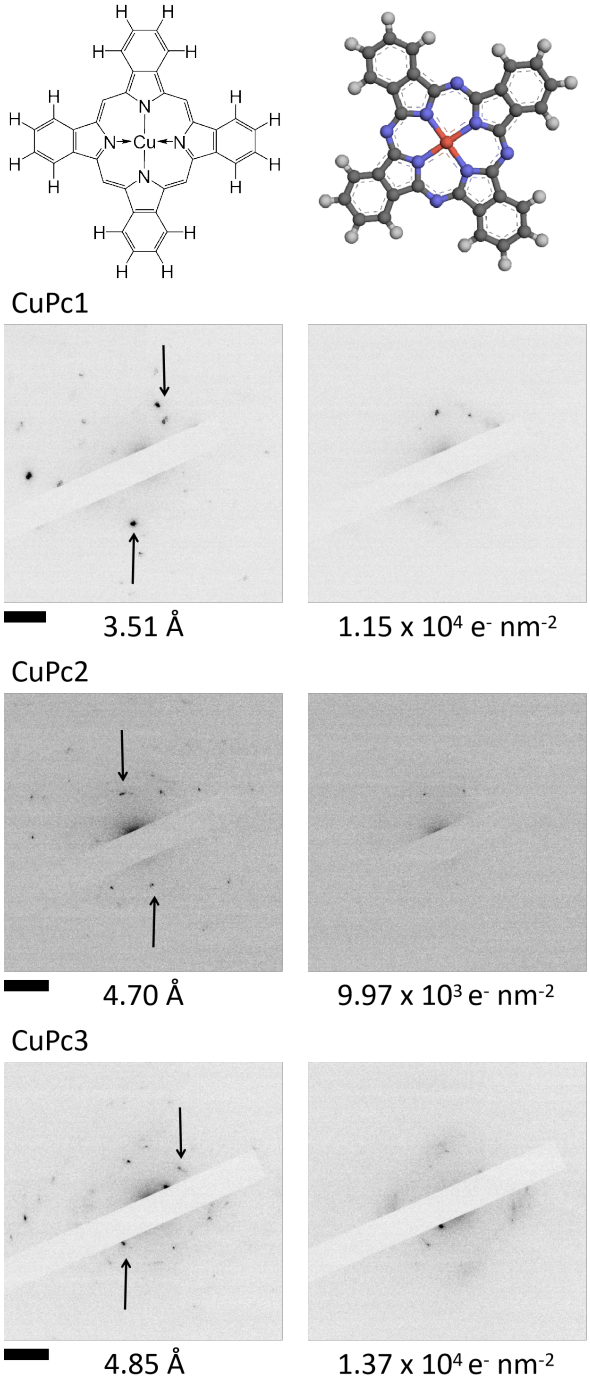

Figure 3.16. Diffraction pattern time series of nanocrystals of copper(II) phthalocyanine (CuPc). The d-spacings of the tracked pairs of diffraction spots and the critical doses are shown below the micrographs. The scale bars are 2 1/nm. The nanocrystals were irradiated using an average electron flux of 9.29 $\times$ 10 e^{-} nm^{-2} s^{-1} over an average period of 125.8 s for an average total electron dose of 1.17 $\times$ 10^{4} e^{-} nm^{-2}. The structure and model of CuPc are shown at the top.

The hydrogenated HAT, H-HAT, appeared to behave similarly to coronene and CuPc under the electron beam. The average critical dose for H-HAT was 1.24 $\times$ 10^4 e^- nm^{-2} (Fig. 3.19) which is comparable to the average critical dose for coronene and CuPc (see Fig. 3.18 for plots of intensities over time for H-HAT). All three molecules share similar structural motifs although presence of nitrogen atoms and even copper do not seem to have a significant impact on the reactivity and stability of these molecules under the electron beam. This suggests that the core of the molecule is not heavily involved in the electron beam-induced reactions which makes sense from a chemical perspective. Any reactions with the central part of a molecule would require breaking of multiple bonds and this would take more energy than breaking peripheral bonds.

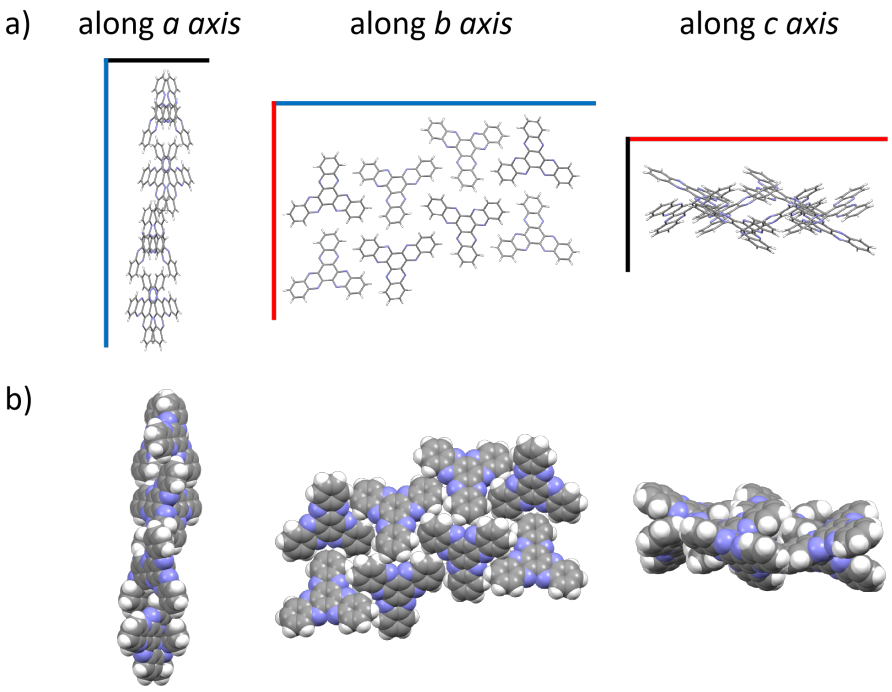

Figure 3.17. The unit cell of 5,6,11,12,17,18- hexaazatrinaphthylene (H-HAT) with the a (red), b (green), and c (blue) axes indicated. Three orientations of the unit cell along the axes are shown as both a) stick and b) space-filling models.

In order to fully interpret the diffraction patterns of the HATs, we needed a piece of missing information. The crystal structure of H-HAT was not in the literature so, using crystals from the same batch of sublimations for TEM imaging, S. Argent (X-ray Crystallography Service Manager at the University of Nottingham) solved the crystal structure for us using SCXRD. H-HAT molecules exhibited the usual π-π stacking with 'interlocking' between the propeller-like ends of the molecules (Fig. 3.17). Using this information, we were able to assign Miller indices to one pair of diffraction spots (Fig. 3.19). The other diffraction patterns likely did not contain enough information for CrysTBox to find the crystal lattice.

Energy dispersive X-ray spectroscopy (EDXS) was carried out after irradiation on three crystals (H-HAT1-3; Fig. 3.19) and showed presence of a nitrogen peak. This suggests that the amorphous material remaining after irradiation contained both carbon and nitrogen. High magnification imaging on H-HAT4 showed that the material remaining had no ordered structure to it (Fig. 3.19).

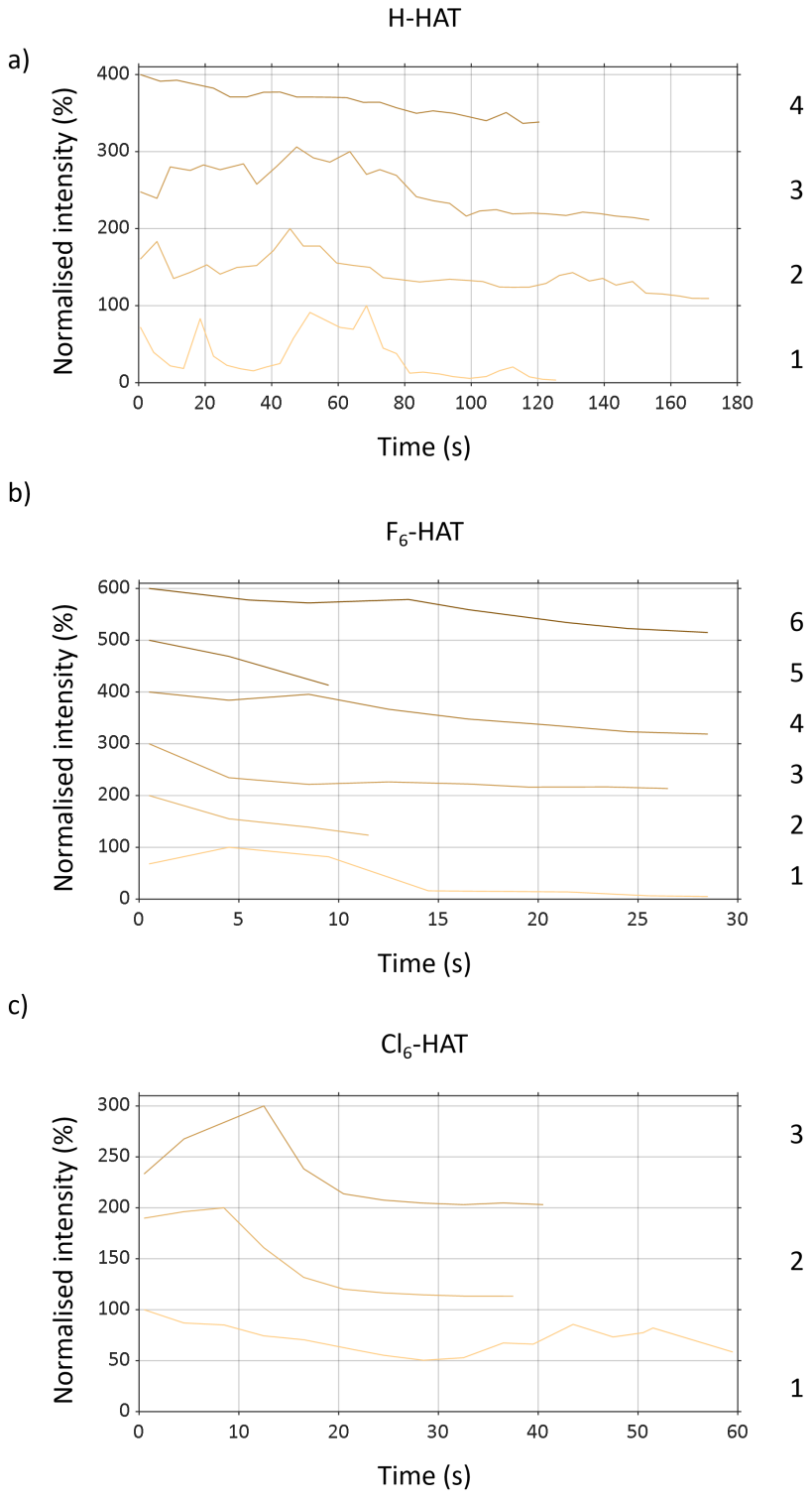

Figure 3.18. Normalised intensities over time of a) H-HAT1-4 from bottom to top, b) F_6-HAT1-6 from bottom to top, and c) Cl_6-HAT1-3 from bottom to top. All plots have been offset from one another by 100% for clarity. All crystals were irradiated with electron fluxes on the order of 10-10^2 e^- nm^{-2} s^{-1}.

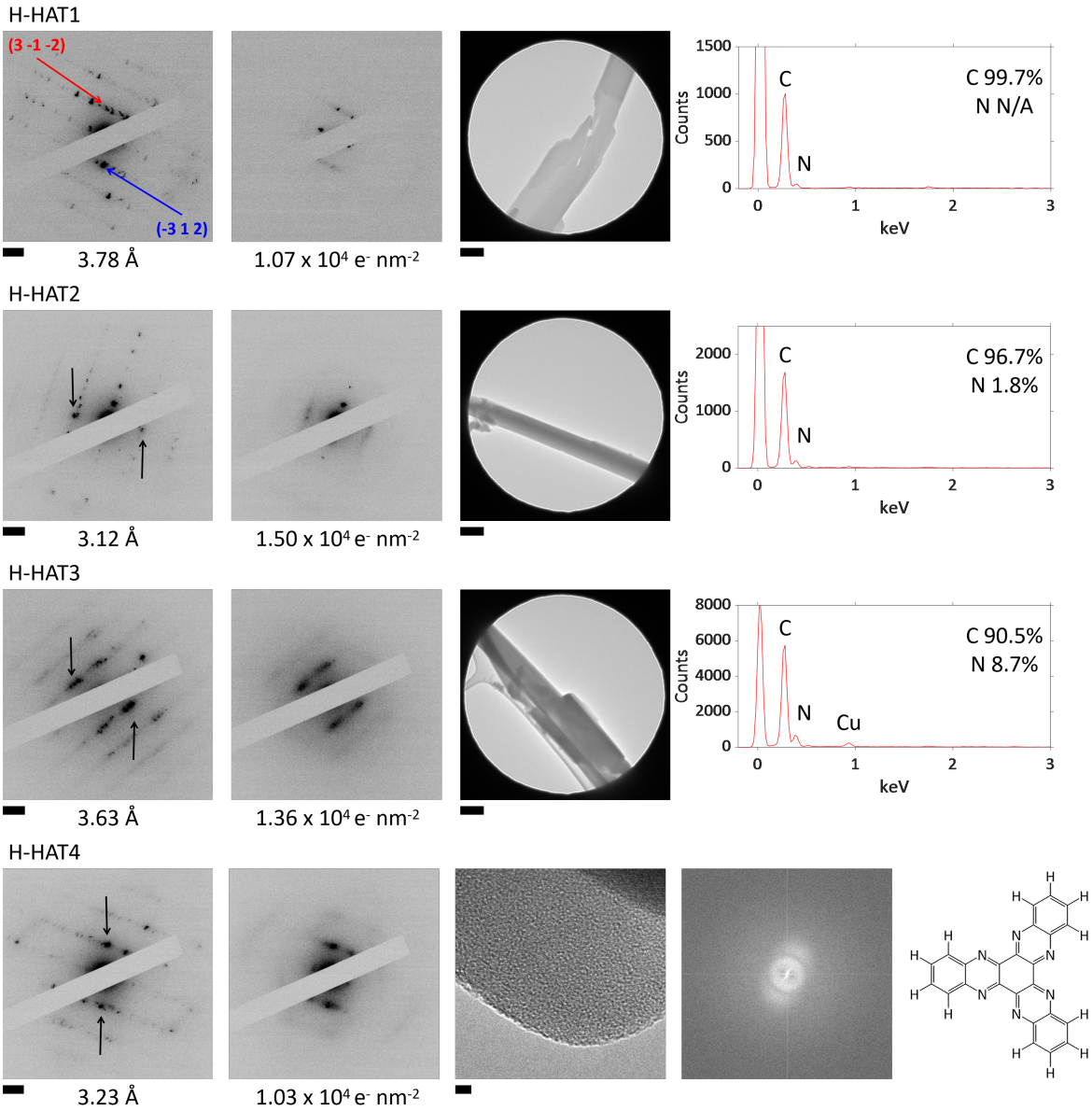

Figure 3.19. Diffraction pattern time series of nanocrystals of 5,6,11,12,17,18-hexaazatrinaphthylene (H-HAT). The d-spacings of the tracked pairs of diffraction spots and the critical doses are shown below the micrographs. More information on the planes corresponding to the diffraction spots of H-HAT1 can be found in Fig. 3.47 in the Appendix. The scale bars are 2 1/nm. The nanocrystals were irradiated using an average electron flux of 8.69 $\times$ 10 e^- nm^{-2} s^{-1} over an average period of 142.8 s for an average total electron dose of 1.24 $\times$ 10^4 e^- nm^{-2}. For crystals 1-3, energy dispersive X-ray spectroscopy (EDXS) was carried out on the regions indicated in the images (third from the left). The scale bars for those images are 0.25 µm. The spectra are shown on the right with labelled peaks and atomic % of C and N. A high magnification image (scale bar 5 nm) and the Fourier transform are shown for H-HAT4. The structure of H-HAT is shown in the bottom right.

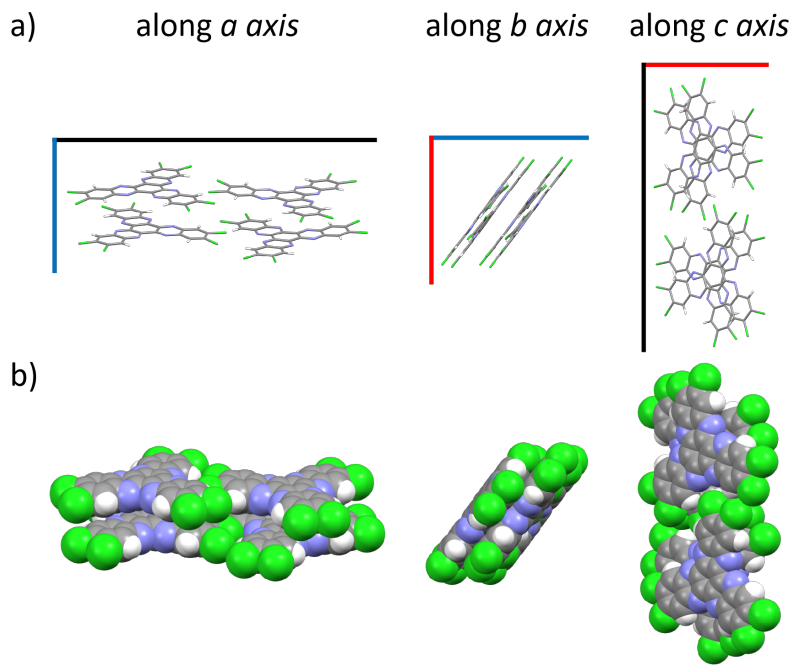

Figure 3.20. The unit cell of 2,3,8,9,14,15- hexachloro- 5,6,11,12,17,18- hexaazatrinaphthylene (Cl_6-HAT)[1] with the a (red), b (green), and c (blue) axes indicated. Three orientations of the unit cell along the axes are shown as both a) stick and b) space-filling models.

The Cl_6-HAT solvent-free crystal structure can be found in literature[1] (Fig. 3.20) and similar conditions to the literature were used to make our crystals. A brief run on the diffractometer by S. Argent confirmed that the crystals had the same structure as in the literature. Cl_6-HAT crystals were surprisingly much more sensitive to the electron beam than H-HAT, requiring an average critical dose of 6.00×10^3 e^- nm^{-2} for the tracked pairs of diffraction spots to fade away (see Figs. 3.18 and 3.22). The initial reaction initiated by the electron beam is likely similar to H-HAT, coronene, and CuPc where radiolysis leads to peripheral C–H bond scission. However, after loss of hydrogen, it is likely energetically favourable for HX to leave from the semi-halogenated HAT, forming arynes. The large HX or X$\cdot$ (compared to H_2 or H$\cdot$) may be trapped within the crystal due to the cage effect and these species can react further with other molecules, causing more rapid wide-scale damage to the crystal lattice.

EDXS carried out on three of the five crystals studied showed quite a variation in the Cl:N ratios (Fig. 3.23). In pristine molecules of Cl_6-HAT, the Cl:N ratio should be 1:1. Loss of Cl from the crystal structure would lead to an increase in the relative amount of nitrogen. A decrease in the relative amount of nitrogen suggests that some N was removed during crystal degradation. Nitrogen atoms could react with H or Cl radicals to form N−H or N−Cl radical species, which may react further leading to breakdown of the HAT moiety. These species may defuse out of the crystal, leading to a drop in the relative amount of nitrogen.

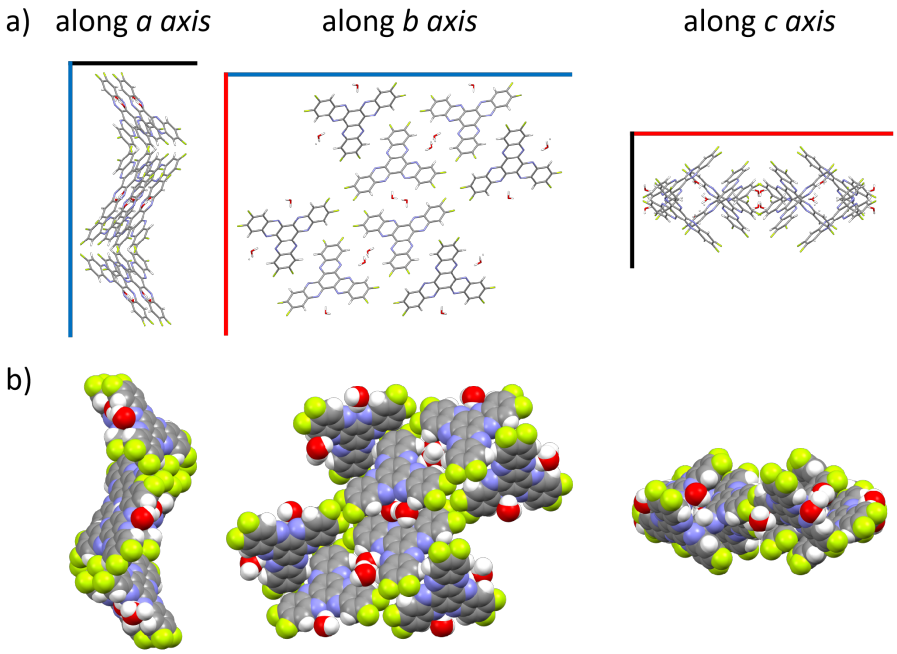

Figure 3.21. The unit cell of 2,3,8,9,14,15- hexafluoro- 5,6,11,12,17,18- hexaazatrinaphthylene (F_6-HAT) with the a (red), b (green), and c (blue) axes indicated. Three orientations of the unit cell along the axes are shown as both a) stick and b) space-filling models.

The F_6-HAT crystal structure was also solved by S. Argent (Fig. 3.21) and it could not be more different from the other HATs; the molecules had co-crystallised with water. The SCXRD data also suggests hydrogen bonding between the water and F_6-HAT molecules and that the unit cell contains two water molecules per molecule of F_6-HAT (see the Appendix at the end of this chapter). There are two

lengths of H...acceptor bonds where the acceptor is N from the F_6-HAT: around 2.3 and 1.9 Å. The IR spectrum of F_6-HAT crystals (Fig. 3.43 in the Appendix) contain two strong, sharp water peaks at 3468 and 3323 wavenumbers which supports the SCXRD data. These sharp peaks in the IR indicate that O – H are hydrogen bonded in specific orientations. IR absorptions of the two lengths of O – H bonds will occur at similar frequencies, leading to two sharp peaks. Synthesis of these molecules took place in acetic acid so presence of water in the product was not surprising. F_6-HAT is also likely much more hygroscopic than the other HATs since F is extremely electronegative and would withdraw electron density from the nitrogens, allowing N to hydrogen bond with water.

The average critical dose for F_6-HAT was an order of magnitude lower than for H-HAT, at 2.10 $\times$ 10^3 e^- nm^{-2} (Figs. 3.24. Out of all of the crystals investigated in this chapter, F_6-HAT was the most vulnerable to the electron beam. The SCXRD and IR data explained why the F_6-HAT crystals were so much more beam sensitive than both H-HAT and Cl_6-HAT crystals. As we saw in chapter two, presence of water increases the rate of beam damage by undergoing radiolysis, generating reactive species such as H$\cdot$ and OH$\cdot$ which lead to further damage to F_6-HAT molecules and general destruction of the crystal. EDXS of the six crystals mostly showed a decrease in the F to N ratio; in a pristine F_6-HAT molecule, the atomic ratio of F:N should be 1:1. Four out of the six crystals showed a reduction in the amount of F after irradiation (F_6-HAT1,2,3, and 6; Fig. 3.24). The two crystals that showed either an increase in the amount of F (F_6-HAT 4, Fig. 3.24) or the same ratio of F to N (F_6-HAT 5, Fig. 3.24) had some thicker material close by (shown in the images of the EDXS acquisition areas). Both areas surrounding the two crystals were irradiated but, due to their thickness, more F may have been retained in the surrounding crystals (the cage effect) rather than emitted out, resulting in a higher amount of F in the EDXS.

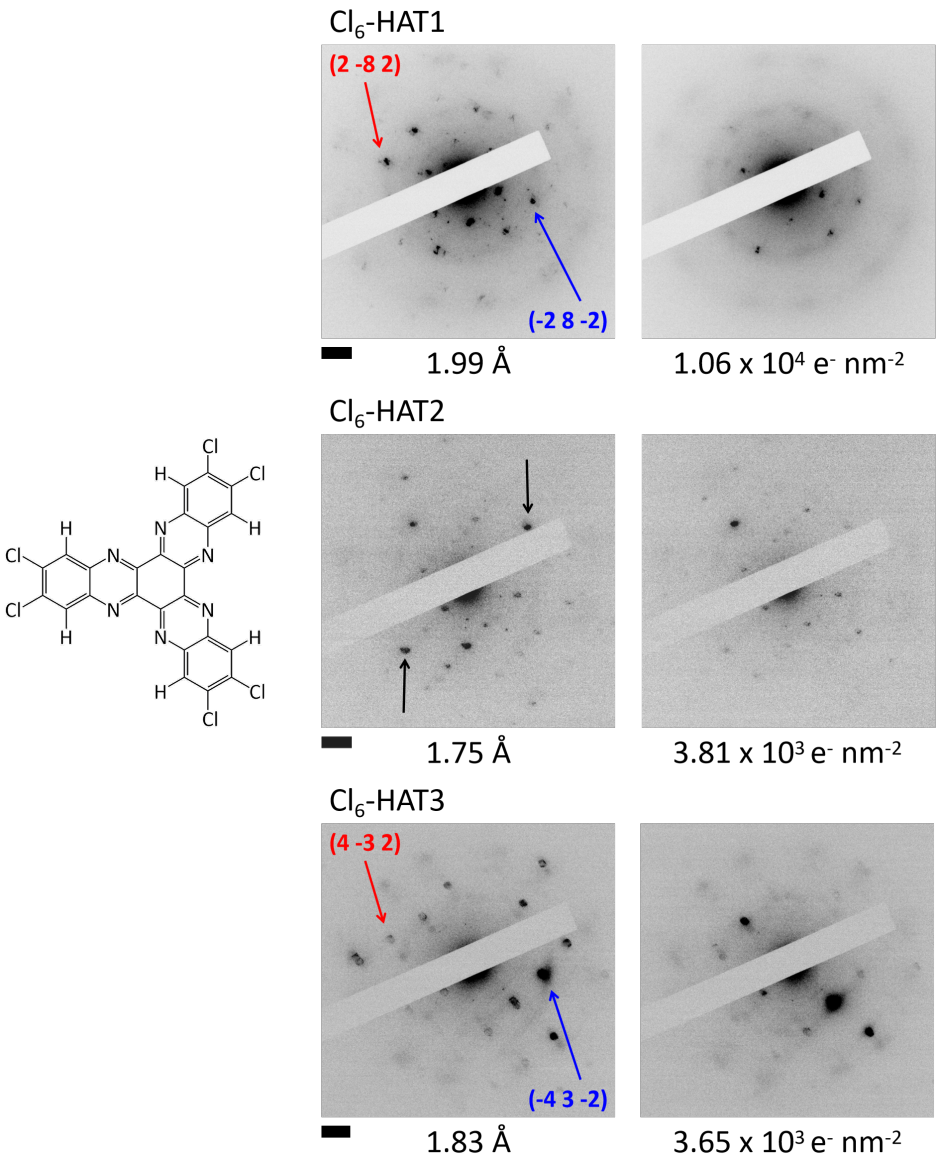

Figure 3.22. Diffraction pattern time series of nanocrystals of 2,3,8,9,14,15-hexachloro- 5,6,11,12,17,18- hexaazatrinaphthylene (Cl_6-HAT). The d-spacings of the tracked pairs of diffraction spots and the critical dose for each nanocrystal is shown below the final micrographs. More information on the planes corresponding to the diffraction spots of Cl_6-HAT1 and Cl_6-HAT3 can be found in Fig. 3.49 in the Appendix. The scale bars are 2 1/nm. The tracked pairs of diffraction spots have d-spacings of 1.99, 1.75, and 1.83 Å for crystals 1 to 3 respectively. The nanocrystals were irradiated using an average electron flux of 1.12 $\times$ 10^2 e^- nm^{-2} s^{-1} over an average period of 45.8 s for an average total electron dose of 6.00 $\times$ 10^3 e^- nm^{-2}. The structure of Cl_6-HAT is shown on the left.

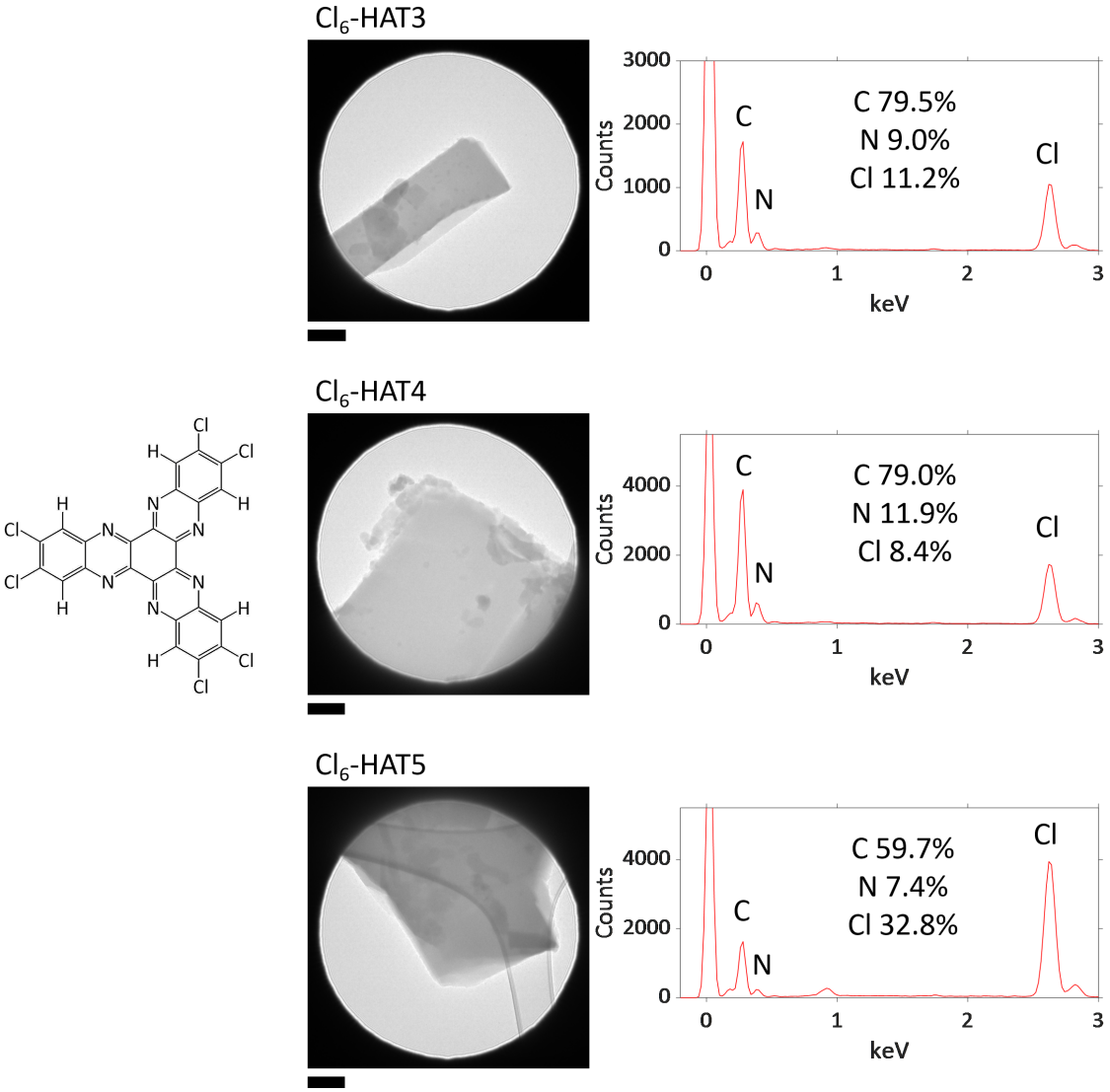

Figure 3.23. Energy dispersive X-ray spectroscopy (EDXS) was carried out on three Cl_6-HAT nanocrystals on the regions indicated in the images after irradiation using an average electron flux of 1.12×10^2 e^- nm^{-2} s^{-1} over similar time periods as previously used for Cl_6-HAT (Cl_6-HAT3 is the same crystal as that in Fig. 3.22). However, the critical doses could not be calculated for crystals 4 and 5 because crystal movement resulted in rapidly changing diffraction patterns and therefore a pair of diffraction spots could not be tracked from start to end (and therefore the total time for the critical doses were unknown). The scale bars for the images are 0.25 µm. The spectra are shown on the right with labelled peaks and atomic % of C, N and Cl, showing that these crystals are of Cl_6-HAT (there was a large contribution to the C signal from the supporting amorphous carbon film). The structure of Cl_6-HAT is shown on the left.

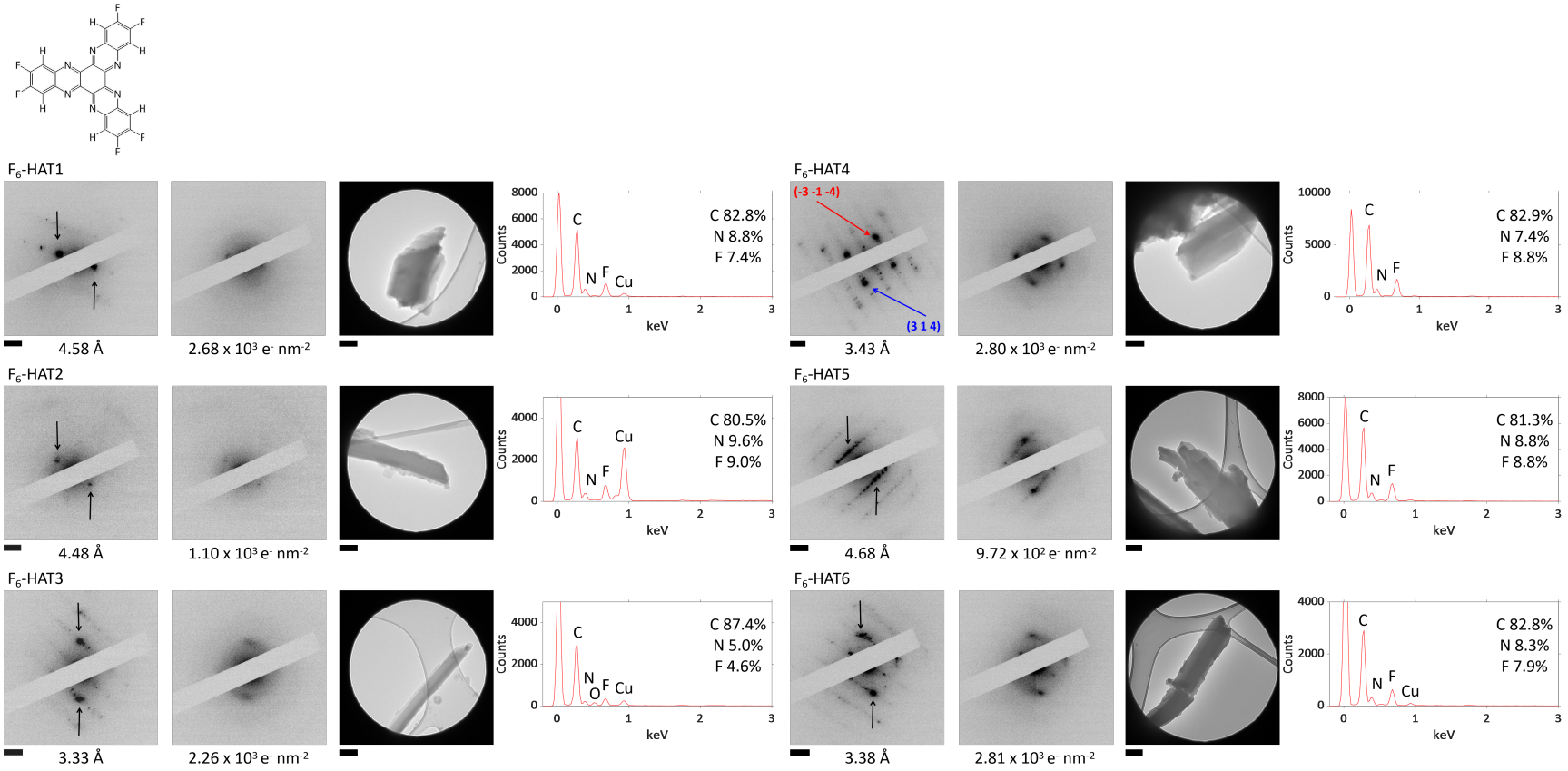

Figure 3.24. Diffraction pattern time series of nanocrystals of 2,3,8,9,14,15- hexafluoro- 5,6,11,12,17,18- hexaazatrinaphthylene (F_6-HAT). The d-spacings of the tracked pairs of diffraction spots and the critical doses are shown below the micrographs. More information on the planes corresponding to the diffraction spots of F_6-HAT4 can be found in Fig. 3.48 in the Appendix. The scale bars are 2 1/nm. The nanocrystals were irradiated using an average electron flux of 9.75 $\times$ 10 e^- nm^{-2} s^{-1} over an average period of 22.2 s for an average total electron dose of 2.10 $\times$ 10^3 e^- nm^{-2}. Energy dispersive X-ray spectroscopy (EDXS) was carried out on the regions indicated in the images (third from the left). The scale bars for those images are 0.25 µm. The spectra are shown on the right with labelled peaks and atomic % of C, N and F. The structure of F_6-HAT is shown on the left.

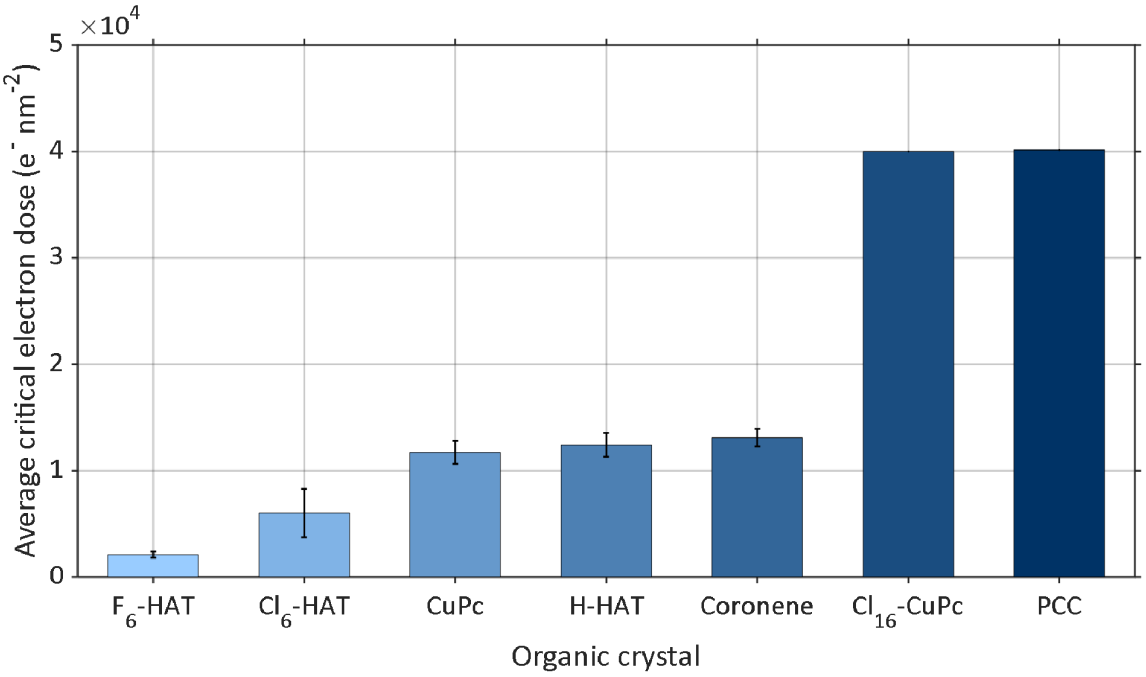

Figure 3.25. A graph showing the average critical dose for each type of crystal with standard error bars shown. The average critical doses are as follows in ascending order: 2.10 $\times$ 10^3 e^- nm^{-2} for F_6-HAT; 6.00 $\times$ 10^3 e^- nm^{-2} for Cl_6-HAT; 1.17 $\times$ 10^4 e^- nm^{-2} for CuPc; 1.24 $\times$ 10^4 e^- nm^{-2} for H-HAT; 1.31 $\times$ 10^4 e^- nm^{-2} for coronene; and over 4.00 $\times$ 10^4 e^- nm^{-2} for both Cl_{16}-CuPc and PCC.

The electron beam stabilities and behaviours of all crystals have been discussed relative to one another (an overview of the data is shown in Fig. 3.25). As expected, crystals of the fully chlorinated molecules PCC and Cl_{16}-CuPc were extremely stable to the electron beam in comparison to the other crystals. Halogenation can improve beam stability by reducing knock-on damage, increasing the energy required for ionisation or bond scission, reducing the lifetime of excited triplet states which increases the probability of recombination, and increasing steric hindrance due to the cage effect.[49]

The surprising result was how much more unstable the semi-halogenated HAT analogues were compared to H-HAT. There may be a few reasons why partial halogenation reduces beam stability of molecules. While the C–X bond requires more energy to break via direct knock-on or ionisation and bond scission, there are path-

ways for halogens to leave quite readily via reactions with radiolysis by-products such as hydrogen radicals, forming HX species for example. In fully halogenated molecules, peripheral atoms are all much less susceptible to electron beam damage. Once reactive halogen species are produced, they can react further with other molecules in the crystal and generally increase the chaos. Halogen species (especially chlorine) have much larger van der Waals radii than hydrogen radicals which mean that reactive halogen species are more likely to remain trapped inside the crystal for longer due to the cage effect, prolonging the damage they can cause to the crystal structure. Eliminated halogen atoms also increase the empty space in the crystal structure compared to hydrogen atoms in H-HAT crystals, increasing the beam sensitivity of partially halogenated crystals[50,51]

The lower stability of F_6-HAT, however, is most likely due to co-crystallisation of water, leading to rapid radiolysis and damage to the crystals under the electron beam. Even without the presence of water, it is likely that F_6-HAT crystals will be most susceptible to beam damage because these crystals have the lowest effective molecular occupancy out of all the crystals studied in this chapter. Effective molecular occupancy is the volume of space occupied by a molecule in the crystal and, in the case of F_6-HAT, co-crystallisation with water occurred in order to fill out the empty space in the crystal structure. Increased empty space in a crystal lowers the stability of that crystal structure and increases the intermolecular moveable space which leads to higher beam sensitivity. Koshino *et al.* found that fluorination does not always improve beam stability of organic molecules because these crystals have lower effective molecular occupancy compared to their hydrogenated counterparts.[49] Presence of water was also a significant factor in beam stability of clay mineral nanosheets. Akita *et al.* used electron diffraction, much like we did, to determine the critical doses of mono-, double-, and triple-layer clay. Mono-layers were far more stable than double- or triple-layers because there was no interlayer

space for encapsulation of water molecules. Water is extremely difficult to remove from clay samples, even with heating and drying. Presence of water would increase radiolysis events and lead to faster degradation of the clay.[52] There also appears to be a correlation between critical dose (radiation stability) and decomposition temperature (thermal stability) i.e. crystals that were more thermally stable also happened to be more beam stable as well.[51] This trend is present in our work; F_6-HAT sublimes at 300 °C while H-HAT and Cl_6-HAT sublimes at 450 °C.

All crystals involved in this study are insulating and therefore also susceptible to damage via charging and heating. These damage mechanisms and pathways will likely be quite similar to those found in EBL, with additional damage mechanisms via secondary backscattered electrons. Overall, the data presented in this study will be useful for future experiments involving fabrication of extended structures using EBL.

3.4 Conclusions

Chemical methods are the major way in which highly crystalline organic frameworks are synthesised. These materials have many interesting properties and applications but synthesis can be challenging to carry out and scale up. Electron beam-induced cross linking using EBL could be a viable alternative for bulk synthesis of organic frameworks. The molecules we chose to work with, HATs, can be precursors for organic frameworks and were synthesised in a straightforward manner in this study. The behaviour of these molecules under the electron beam are not known in the literature however, so irradiation studies and comparisons to other well-known molecules were carried out in order to understand the electron beam-induced reactions.

Electron diffraction time series were acquired for each type of HAT crystal under the same irradiation conditions at 80 kV and used to calculate the critical doses of each type of crystal. These values were then compared to those of well studied molecules: PCC, fully chlorinated copper(II) phthalocyanine (Cl_{16}-CuPc), coronene, and copper(II) phthalocyanine (CuPc). The diffraction patterns which contained enough information from multiple planes were assigned Miller indices using crystal structures either in the literature or solved with data from Diamond Light Source.

Both PCC and Cl_{16}-CuPc were extremely stable while coronene and CuPc had comparable critical doses to H-HAT. Fully halogenated molecules are well-known from the literature to be particularly stable to the electron beam. Coronene, CuPc, and H-HAT are all large, polycyclic aromatic hydrocarbons so it was unsurprising that their beam stabilities were comparable. It is interesting to note that presence of N or even a heavy Cu atom did not seem to have a significant imapct on the reactivity and stability of these molecules, suggesting that the peripheral bonds are more important than the core of the molecule for electron beam-induced reactions.

However, the semi-halogenated HATs were much less stable than H-HAT. This may be due to terminating halogen atoms readily reacting with radiolysis by-products such as hydrogen radicals and leaving as reactive halogen species such as HX. These large species would not penetrate as much through the crystal lattice compared to H$\cdot$ due to the cage effect and therefore could initiate many more reactions, leading to wide-scale damage of the crystal. Eliminated halogen substituents also increase the empty space in the crystal structure which will further lower the beam stability of the overall crystal. The incredible beam sensitivity of crystals of F_6-HAT was discovered to be due to the presence of water which had co-crystallised with the F_6-HAT molecules. Acquiring this information was only possible when SCXRD was carried out for us at Diamond Light Source. Any TEM sample containing water can undergo radiolysis which is a major cause of sample damage.

The critical doses and information on chemical reactions from this study will be useful for future irradiation experiments using EBL. We hope to continue with these molecules and develop procedures for synthesising porous materials from HATs using EBL.

3.5 Future Work

H-HAT seems the most promising candidate for EBL experiments because these crystals do not react too rapidly, unlike Cl_6-HAT and F_6-HAT. However it will certainly be interesting to study any products from EBL irradiation of other types of HAT molecules. Under the right irradiation conditions, H-HAT may crosslink to form a porous organic framework. Extremely high beam stability, such as that of Cl_{16}-CuPc and PCC, may also be inappropriate for framework synthesis using EBL because irradiation times to achieve a framework may be impractically long. Additionally, since we have also acquired information on the critical doses of CuPc and coronene, these molecules could also be carried on forwards for framework synthesis. Aromatic molecules are widely used in EBL as negative resists but we could also use the electron beam for "chemical lithography",[22] selectively converting layers of aromatic molecules into potentially crystalline, crosslinked frameworks. Typical negative resists use doses on the order of tens of μC cm^{-2} or 0.1 e^- nm^{-2}. We would expect to use a much lower dose for EBL experiments due to backscattering from substrates such as silicon chips. For comparison, the standard positive resist poly methyl methacrylate (PMMA) uses doses on the order of hundreds of μC cm^{-2} or 10 e^- nm^{-2}.

Our approach to EBL would likely use a standard method of depositing thin layers of the molecule onto a silicon chip. This could be via dropcasting a dilute solution, placing the silicon chip into the solution to allow slow deposition of layers, or sublimation under inert gas flow. The critical doses obtained in this chapter can then be used to guide the EBL experiments. Subsequent analysis of the irradiation products could involve more TEM, XRD if appropriate, atomic force microscopy which can map out the surface topology with atomic precision, and various spectroscopic techniques to probe elemental composition and structure.

3.6 Experimental Methods

Reagents were purchased from Sigma Aldrich, Alfa Aesar, Fischer Scientific, or Acros Organics and used as received. Perchlorocoronene was synthesised as before (in the second chapter).

Nuclear magnetic resonance (NMR) spectra were recorded using a Bruker AV400 spectrometer at the University of Nottingham. All chemical shifts are quoted in ppm where ^{1}H NMR and ^{13}C spectra are quoted relative to neat trimethylsilate (TMS).

Matrix assisted laser desorption/ionisation time-of-flight mass spectrometry (MALDI-ToF MS) analyses were performed on a Bruker ultraFlexIII instrument (Bruker Daltonik, Bremen, Germany). Samples were deposited on a stainless steel target plate (type MTP384; Bruker Daltonik, Bremen, Germany) and due to the nature of the samples, no matrix was required. A pulsed solid-state UV laser (355nm, 500 µJ, 66.7Hz) was used to ionise the sample. The instrument was operated in reflection mode. Data was acquired through the instrument's flexControl software (v3,B185; Bruker Daltonik, Bremen, Germany), and processed using Bruker's flexAnalysis software (v3,B96; Bruker Daltonik, Bremen, Germany).

IR spectra were recorded using a Bruker Alpha FTIR spectrometer using a Bruker Platinum ATR module attachment on powdered solids.

Transmission electron microscopy (TEM) was performed using a JEOL 2100F TEM with an accelerating voltage of 80 kV (field emission electron gun, information limit 0.19 nm) at the Nanoscale and Microscale Research Centre at the University of Nottingham. TEM samples were prepared by gently grinding the crystals in an agate mortar and pestle before pressing onto a copper grid mounted with "lacey" carbon films (Agar Scientific UK). The specific imaging conditions used the second smallest condenser aperture (40 µm), alpha 3, spot size 5, at 8000x magnification with the beam completely spread. The images were acquired with a 0.5 s capture time. All images were processed using Gatan Digital Micrograph and ImageJ Fiji

software.[53–55] Energy dispersive X-ray spectroscopy (EDXS) was acquired using an Oxford Instruments INCA X-ray microanalysis system. Kα values were used for carbon (0.277 keV), nitrogen (0.392 kev), fluorine (0.677 keV), and chlorine (2.622 keV).

3.6.1 H-HAT synthesis

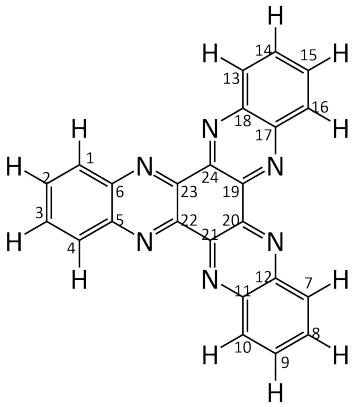

Figure 3.26. 5,6,11,12,17,18- hexaazatrinaphthylene.

H-HAT was prepared according to literature.[1] 1,2-diaminobenzene (31.2 mg, 0.288 mmol) and hexaketocyclohexane octahydrate (30 mg, 0.096 mmol) were refluxed in 1:1 glacial acetic acid/ethanol (3 mL) for 24 hrs at 140 ℃. After reflux, the blue reaction mixture was filtered under reduced pressure while hot and washed with hot glacial acetic acid (118 ℃, 50 mL) until the filtrate was colourless. The resulting green solid was refluxed in nitric acid (30%, 5 mL) at 90 ℃ for 3 hrs. Upon mixing, the solid and nitric acid solvent turned bright yellow. After reflux, 5,6,11,12,17,18- hexaazatrinaphthylene was recovered as a yellow solid by filtering under reduced pressure and washed with deionised water (10 mL), then dried under vacuum (12.1 mg, 0.0315 mmol, 33%). ^{1}H NMR ($CDCl_3$, 400 MHz) δ 8.71 (6H, dd, J 6.53, J 3.51, H-1), 8.06 (6H, dd, J 6.59, J 3.45, H-2). ^{13}C NMR ($CDCl_3$, 101 MHz) δ 143.74 (s, 5), 143.71 (s, 19), 132.44 (s, 1), 130.82 (s, 2). m/z 384.1 ($C_{24}H_{12}N_6^-$, 100%), 279.9 ($C_{18}H_8N_4^-$, 11.6%). IR (ATR)/cm^{-1} ν_{max}: 3060 (C−H).

3.6.2 F_6-HAT synthesis

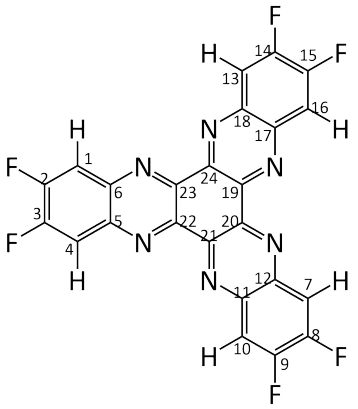

Figure 3.27. 2,3,8,9,14,15- hexafluoro- 5,6,11,12,17,18- hexaazatrinaphthylene.

F_6-HAT was prepared according to literature.[1] 4,5-difluoro-1,2-diaminobenzene (43.8 mg, 0.304 mmol) and hexaketocyclohexane octahydrate (30 mg, 0.096 mmol) were refluxed in degassed glacial acetic acid (3 mL) for 16 hrs at 118 ℃. After reflux, the dark purple reaction mixture was cooled to room temperature and filtered under reduced pressure. Washing with room temperature glacial acetic acid and drying under reduced pressure gave 2,3,8,9,14,15- hexafluoro-5,6,11,12,17,18- hexaazatrinaphthylene as a grey-green solid (28.1 mg, 0.616 mmol, 64 %). ^{1}H NMR ($CDCl_3$, 400 MHz) δ 8.43 (6H, t, J 9.10, H-1). ^{19}F NMR ($CDCl_3$, 400 MHz) δ -122.95 (6F, t, J 9.10, F-2). ^{19}F(H) NMR ($CDCl_3$, 400 MHz) δ -122.96 (6F, s, F-2). ^{13}C NMR ($CDCl_3$, 101 MHz) δ 154.70 (dd, J 264.67, J 18.35, 2), 143.20 (s, 5), 141.61 (t, J 6.34, 19), 115.95 (dd, J 13.08, J 6.90, 1). m/z 492.1 ($C_{24}H_6N_6F_6^-$, 100%). IR (ATR)/cm^{-1} ν_{max}: 3041 (C−H).

3.6.3 Cl_6-HAT synthesis

Cl_6-HAT was prepared according to literature.[1] 4,5-dichloro-1,2-diaminobenzene (95.4 mg, 0.54 mmol) and hexaketocyclohexane octahydrate (31.4 mg, 0.101 mmol) were refluxed in 1:1 glacial acetic acid/ethanol (3 mL) for 24 hrs at 140 ℃. Upon

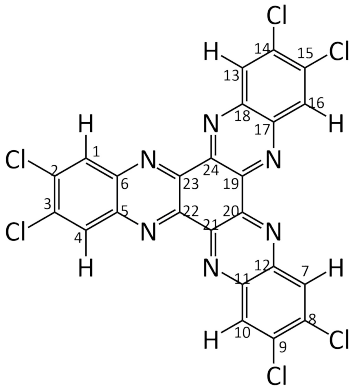

Figure 3.28. 2,3,8,9,14,15- hexachloro- 5,6,11,12,17,18- hexaazatrinaphthylene.

mixing, a dark red suspension formed. After reflux, the resulting dark green reaction mixture was filtered under reduced pressure while hot and washed with hot glacial acetic acid (100 ℃, 20 mL) to give a dark green solid and pale yellow filtrate. The solid was refluxed in nitric acid (30%, 8 mL) at 90 ℃ for 3 hrs, then filtered under reduced pressure and washed with deionised water (10 mL) to yield a colourless filtrate and bright green solid (46.8 mg, 0.0792 mmol, 78 %). The green solid was then refluxed in glacial acetic acid (120 ℃) for 1 hr, then filtered under reduced pressure while hot, washed with hot glacial acetic acid, then dried under reduced pressure to give 2,3,8,9,14,15- hexachloro- 5,6,11,12,17,18- hexaazatrinaphthylene as a bright yellow solid (37.5 mg, 0.0636 mmol, 22 %) ^{1}H NMR ($CDCl_3$, 400 MHz) δ 8.81 (6H, s, H-1). ^{13}C NMR ($CDCl_3$, 101 MHz) δ 143.93 (s, 5), 142.36 (s, 19), 138.29 (s, 2), 131.00 (s, 1). m/z 589.1 ($C_{24}H_6N_6Cl_6^-$, 100%). IR (ATR)/cm^{-1} ν_{max}: 3090 (C – H).

3.6.4 Preparation of crystals for TEM and SCXRD

Crystals (1 mg) were prepared via sublimation in a sealed, flame-dried ampoule under reduced pressure (10^{-4} mbar). One end of the ampoule was introduced to a hot furnace while the other end remained at room temperature. Over the course of the sublimation (over an hr), crystals of the sublimed compound grew slowly at

the cooler end of the ampoule. After sublimation, the ampoule was opened and the sublimed crystals collected.

F_6-HAT was sublimed at 300 °C; coronene and PCC at 400 °C; H-HAT and Cl_6-HAT 450 °C; and phthalocyanine blue at 500 °C. Phthalocyanine green was found to decompose upon sublimation so the powder was used as purchased for the TEM diffraction studies.

3.6.5 SCXRD at Diamond Light Source Beamline i19

All SCXRD data collection and refinements were carried out by S. Argent, the X-ray Crystallography Service Manager at the University of Nottingham.

X-ray diffraction measurements were performed in Experiments Hutch 1 (EH1) of Beamline I19, at Diamond Light Source.[56] The data were collected at a wavelength of 0.6889 Å on a Fluid Film Devices 3-circle fixed-chi diffractometer using a Dectris Pilatus 2M detector. The crystals were mounted on a MiTeGen micromounts using a perfluoropolyether oil, flash frozen in liquid nitrogen before being transported to the Synchrotron where they were cooled for data collection by a Cryostream nitrogen-gas stream.[57] The collected frames were integrated using DIALS[58] software and the data were corrected for absorption effects using AIMLESS,[59] an empirical method. The structure was solved by dual-space methods[60] and refined by least-squares refinement on all unique measured F2 values.[61]

3.6.6 Refinement details for 5,6,11,12,17,18- hexaazatrinaphthylene

The very fine needle-like crystals grown by sublimation diffracted weakly with a low-resolution diffraction limit, despite the use of synchrotron radiation. Restraints were applied to the geometry and anisotropic displacement parameters of the struc-

ture to aid refinement and support the consequently low data to parameter ratio of 5.36. The geometries of the two three-fold symmetric residues were restrained to have similar and symmetric geometries (SAME). Rigid bond and similarity restraints (RIGU, SIMU) were applied to the anisotropic displacement parameters of all atoms in the structure. All hydrogen atoms were geometrically placed and refined using a riding model.

3.6.7 Refinement details for 2,3,8,9,14,15- hexafluoro-5,6,11,12,17,18- hexaazatrinaphthylene

The very thin lath-like crystals diffracted weakly despite the use of synchrotron radiation; the data used in the refinement was truncated to a resolution of 0.95 Å. All hydrogen atoms were observed in the electron density map. The aryl hydrogen atoms were geometrically placed before being refined with a riding model. The water hydrogen atoms are refined with their 1,2 and 1,3 distances restrained to have suitable geometries. The isotropic displacement parameters of all hydrogen atoms are fixed at 1.2×Ueq (aryl) and 1.5×Ueq (water) of their parent atoms. One of the hydrogen atoms of water O2W is disordered over two sites which are fixed at half occupancy each. The two disorder sites are parted such that the hydrogen atoms are in separate parts to their symmetry equivalents on adjacent water residues. One of the hydrogen atoms in O1W donates a hydrogen bond to an adjacent symmetry equivalent O1W residue. The hydrogen atom is modelled at half-occupancy and parted to be in a different disorder component to its symmetry equivalent. The remaining half-occupancy hydrogen site at O1W will likely donate a hydrogen bond to one of the other two proximate symmetry equivalent O1W residues. This other hydrogen position is not apparent in the electron density map and is not included in the model, however, it is included in the unit cell contents all derived parameters.

3.7 References

1. S. Barlow, Q. Zhang, B. R. Kaafarani, C. Risko, F. Amy, C. K. Chan, B. Domercq, Z. A. Starikova, M. Y. Antipin, T. V. Timofeeva, B. Kippelen, J.-L. Brédas, A. Kahn and S. R. Marder, *Chem. Eur. J.*, 2007, **13**, 3537–3547.
2. H. Bock, A. Babeau, I. Seguy, P. Jolinat and P. Destruel, *Chem. Phys. Chem.*, 2002, **3**, 532–535.
3. B. R. Kaafarani, T. Kondo, J. Yu, Q. Zhang, D. Dattilo, C. Risko, S. C. Jones, S. Barlow, B. Domercq, F. Amy, A. Kahn, J.-L. Brédas, B. Kippelen and S. R. Marder, *J. Am. Chem. Soc.*, 2005, **127**, 16358–16359.
4. D. Zhao, Z. Zhu, M.-Y. Kuo, C.-C. Chueh and A. K.-Y. Jen, *Angew. Chem. Int. Ed.*, 2016, **55**, 8999–9003.
5. Z. Zhu, D. Zhao, C.-C. Chueh, X. Shi, Z. Li and A. K.-Y. Jen, *Joule*, 2018, **2**, 168–183.
6. H.-L. Yip, J. Zou, H. Ma, Y. Tian, N. M. Tucker and A. K.-Y. Jen, *J. Am. Chem. Soc.*, 2006, **128**, 13042–13043.
7. D. G. Veláquez, A. G. Orive, A. H. Creus, R. Luque and Á. G. Ravelo, *Org. Biomol. Chem.*, 2011, **9**, 6524–6527.
8. A. Thomas, *Angew. Chem. Int. Ed.*, 2010, **49**, 8328–8344.
9. P. M. Budd, B. Ghanem, K. Msayib, N. B. McKeown and C. Tattershall, *J. Mater. Chem.*, 2003, **13**, 2721–2726.
10. K. E. Maly, *J. Mater. Chem.*, 2009, **19**, 1781–1787.
11. J. Wang, Y. Lee, K. Tee, S. N. Riduan and Y. Zhang, *Chem. Commun.*, 2018, **54**, 7681–7684.
12. J. Wang, C. S. Chen and Y. Zhang, *ACS Sustainable Chem. Eng*, 2018, **6**, 1772–1779.
13. D. Taylor, S. J. Dalgarno, Z. Xu and F. Vilela, *Chem. Soc. Rev.*, 2020, **Advance Article**.
14. F. Xu, X. Chen, Z. Tang, D. Wu, R. Fu and D. Jiang, *Chem. Commun.*, 2014, **50**, 4788–4790.
15. C. T. Stoppiello, H. Isla, M. Martínez-Abadía, M. W. Fay, C. D. J. Parmenter, M. J. Roe, B. Lerma-Berlanga, C. Martí-Gastaldo, A. Mateo-Alonso and A. N. Khlobystov, *Nanoscale*, 2019, **11**, 2848–2854.

16. W. Geyer, V. Stadler, W. Eck, M. Zharnikov, A. Gölzhäuser and M. Grunze, *Appl. Phys. Lett*, 1999, **75**, 2401–2403.

17. T. Weimann, W. Geyer, P. Hinze, V. Stadler, W. Eck and A. Gölzhäuser, *Microelectron. Eng.*, 2001, **57-58**, 903–907.

18. T. Felgenhauer, C. Yan, W. Geyer, H.-T. Rong and A. Gölzhäuser, *Appl. Phys. Lett.*, 2001, **79**, 3323–3325.

19. A. Küller, M. A. El-Desawy, V. Stadler, W. Geyer, W. Eck and A. Gölzhäuser, *J. Vac. Sci. Technol. B*, 2004, **22**, 1114–1117.

20. W. Eck, V. Stadler, W. Geyer, M. Zharnikov, A. Gölzhäuser and M. Grunze, *Adv. Mater.*, 2000, **12**, 805–808.

21. A. Turchanin, D. Käfer, M. El-Desawy, C. Wöll, G. Witte and A. Gölzhäuser, *Langmuir*, 2009, **25**, 7342–7352.

22. P. Angelova, H. Vieker, N.-E. Weber, D. Matei, O. Reimer, I. Meier, S. Kurasch, J. Biskupek, D. Lorbach, K. Wunderlich, L. Chen, A. Terfort, M. Klapper, K. Müllen, U. Kaiser, A. Gölzhäuser and A. Turchanin, *ACS Nano*, 2013, **7**, 6489–6497.

23. I. M. Piglosiewicz, R. Beckhaus, G. Wittstock, W. Saak and D. Haase, *Inorg. Chem.*, 2007, **46**, 7610–7620.

24. W.-H. Wu, M.-J. Huang, Q. Zeng, W.-R. Xian, W.-M. Liao and J. He, *Inorg. Chem. Commun.*, 2019, **103**, 149–153.

25. S. J. Lind, T. J. Walsh, A. G. Blackman, M. I. J. Polson, G. I. S. Irwin and K. C. Gordon, *J. Phys. Chem. A*, 2009, **113**, 3566–3575.

26. V. J. Catalano, W. E. Larson, M. M. Olmstead and H. B. Gray, *Inorg. Chem.*, 1994, **33**, 4502–4509.

27. M. G. Fraser, C. A. Clark, R. Horvath, S. J. Lind, A. G. Blackman, X.-Z. Sun, M. W. George and K. C. Gordon, *Inorg. Chem.*, 2011, **50**, 6093–6106.

28. C. A. Gould, L. E. Darago, M. I. Gonzalez, S. Demir and J. R. Long, *Angew. Chem. Int. Ed.*, 2017, **56**, 10103–10107.

29. M. Rubio-Martinez, C. Avci-Camur, A. W. Thornton, I. Imaz, D. Maspoch and M. R. Hill, *Chem. Soc. Rev.*, 2017, **46**, 3453–3480.

30. M. Klinger and A. Jäger, *J. Appl. Crystallogr.*, 2015, **48**.

31. M. Klinger, *CrysTBox - Crystallographic Toolbox*, Institute of Physics of the Czech Academy of Sciences, 2015.

32. M. Klinger, M. Němec, L. Plívka, V. Gärtnerová and A. Jäger, *Ultramicroscopy*, 2015, **150**, 88–95.

33. T. Baird, J. H. Gall, D. D. MacNicol, P. R. Mallinson and C. R. Michie, *J. Chem. Soc., Chem. Commun.*, 1988, 1471–1473.

34. J. K. Fawcett and J. Trotter, *Proc. R. Soc. Lond. A*, 1966, **289**, 366–376.

35. C. J. Brown, *J. Chem. Soc. A*, 1968, 2488–2493.

36. R. F. Egerton, P. Li and M. Malac, *Micron*, 2004, **35**, 399–409.

37. J. R. Fryer and F. Holland, *Ultramicroscopy*, 1983, **11**, 67–70.

38. J. R. Fryer, *Ultramicroscopy*, 1984, **14**, 227–236.

39. J. R. Fryer, C. McNee and F. M. Holland, *Ultramicroscopy*, 1984, **14**, 357–358.

40. R. Henderson and R. Glaeser, *Ultramicroscopy*, 1985, **16**, 139–150.

41. J. R. Fryer, *J. Electron Microsc. Tech.*, 1989, **11**, 310–325.

42. R. F. Egerton, *Ultramicroscopy*, 2013, **127**, 100–108.

43. T. W. Chamberlain, J. Biskupek, S. T. Skowron, P. A. Bayliss, E. Bichoutskaia, U. Kaiser and A. N. Khlobystov, *Small*, 2015, **11**, 622–629.

44. J. Cattle, M. S'ari, N. Hondow, P. Abellán, A. P. Brown and R. M. D. Brydson, *J. Phys.: Conf. Ser.*, 2015, **644**, 012030.

45. M. S'ari, J. Cattle, N. Hondow, H. Blade, S. Cosgrove, R. M. D. Brydson and A. P. Brown, *J. Phys.: Conf. Ser.*, 2015, **644**, 012038.

46. M. S'ari, H. Blade, R. Brydson, S. D. Cosgrove, N. Hondow, L. P. Hughes and A. Brown, *Mol. Pharmaceutics*, 2018, **15**, 5114–5123.

47. R. F. Egerton, *Micron*, 2019, **119**, 72–87.

48. T. W. Chamberlain, J. Biskupek, S. T. Skowron, A. V. Markevich, S. Kurasch, O. Reimer, K. E. Walker, G. A. Rance, X. Feng, K. Müllen, A. Turchanin, M. A. Lebedeva, A. G. Majouga, V. G. Nenajdenko, U. Kaiser, E. Besley and A. N. Khlobystov, *ACS Nano*, 2017, **11**, 2509–2520.

49. M. Koshino, Y. H. Masunaga, T. Nemoto, H. Kurata and S. Isoda, *Micron*, 2005, **36**, 271–279.

50. M. Koshino, H. Kurata and S. Isoda, *Micros. Microanal.*, 2005, **11**, S02.

51. M. Koshino, H. Kurata and S. Isoda, *Microsc. Microanal.*, 2007, **13**, 96–107.

52. I. Akita, Y. Ishida and T. Yonezawa, *Phys. Chem. Chem. Phys.*, 2020, **22**, 25095.

53. C. A. Schneider, W. S. Rasband and K. W. Eliceiri, *Nat. Methods*, 2012, **9**, 671–675.

54. J. Schindelin, C. T. Rueden and M. C. Hiner, *Mol. Reprod. Dev.*, 2015, **82**, 518–529.

55. J. Schindelin, I. Arganda-Carreras, E. Frise, V. Kaynig, M. Longair, T. Pietzsch, S. Preibisch, C. Rueden, S. Saalfeld, B. Schmid, J. Y. Tinevez, D. J. White, V. Hartenstein, K. Eliceiri, P. Tomancak and A. Cardona, *Nat. Methods*, 2012, **9**, 676–682.

56. D. R. Allan, H. Nowell, S. A. Barnett, M. R. Warren, A. Wilcox, J. Christensen, L. K. Saunders, A. Peach, M. T. Hooper, L. Zaja, S. Patel, L. Cahill, R. Marshall, S. Trimnell, A. J. Foster, T. Bates, S. Lay, M. A. Williams, P. V. Hathaway, G. Winter, M. Gerstel and R. W. Wooley, *Crystals*, 2017, 22.

57. J. Crosier and A. M. Glazer, *J. Appl. Crystallogr.*, 1986, 105–107.

58. G. Winter, D. G. Waterman, J. M. Parkhurst, A. S. Brewster, R. J. Gildea, M. Gerstel, L. Fuentes-Montero, M. Vollmar, T. Michels-Clark, I. D. Young, N. K. Sauter and G. Evans, *Acta Crystallogr. Sect. D-Struct. Biol.*, 2018, 85–97.

59. P. R. Evans and G. N. Murshudov, *Acta Cryst.*, 2013, 1204–1214.

60. G. M. Sheldrick, *Acta Cryst.*, 2015, A71, 3–8.

61. G. M. Sheldrick, *Acta Cryst.*, 2015, C71, 3–8.

3.8 Appendix

The Appendix contains the characterisation data for the three HAT molecules: crystal parameters for SCXRD, NMR, MALDI-ToF MS, IR, and crystal plane assignments for some of the diffraction patterns.

SCXRD data for 5,6,11,12,17,18- hexaazatrinaphthylene.

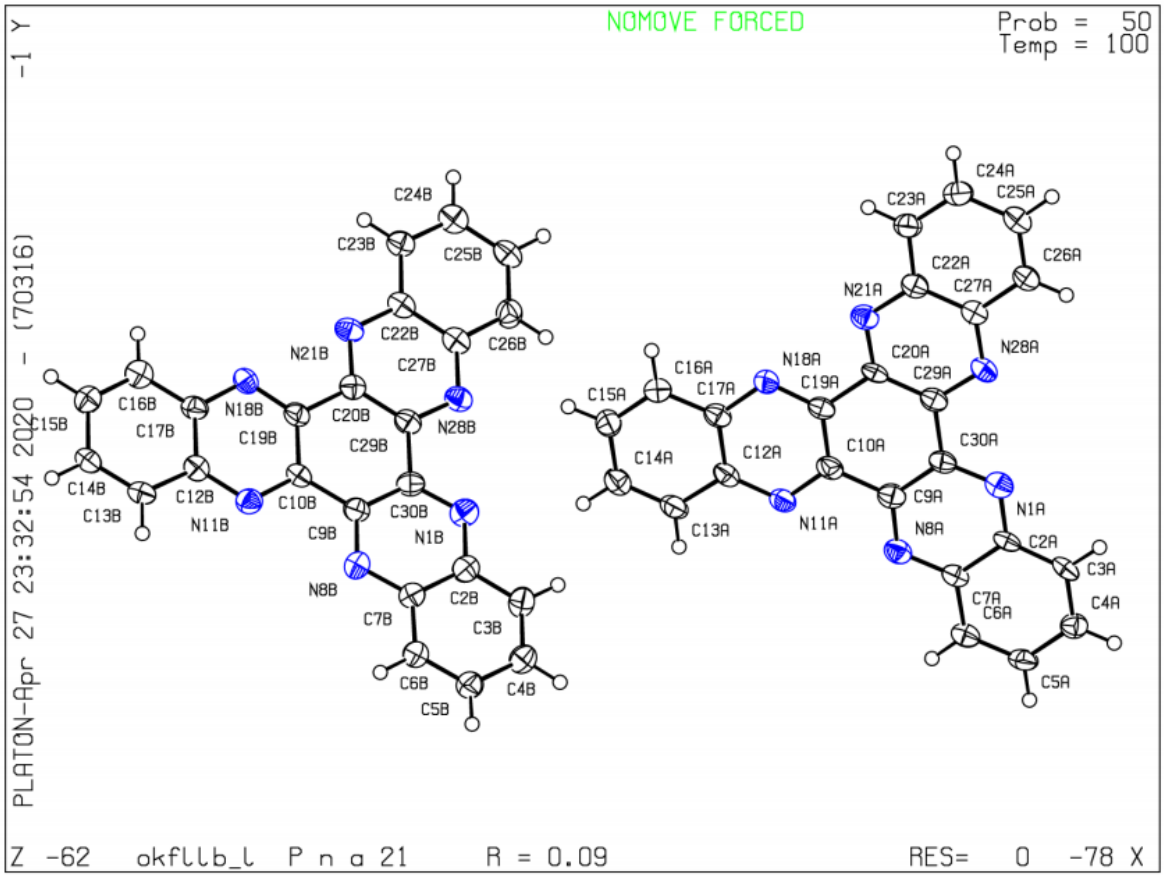

Figure 3.29. Ellipsoid plot of the unit cell of 5,6,11,12,17,18-hexaazatrinaphthylene.

Crystal data and structure refinement for 5,6,11,12,17,18- hexaazatrinaphthylene.

Empirical formula	$C_{24}H_{12}N_6$
Formula weight	384.40
Temperature/K	100(2)
Crystal system	orthorhombic
Space group	$Pna2_1$
a/Å	21.7922(18)
b/Å	3.8884(3)
c/Å	39.449(3)
$\alpha/^o$	90.0
$\beta/^o$	90.0
$\gamma/^o$	90.0
Volume/$Å^3$	3342.8(3)
Z	8
ρcalcg/cm^3	1.528
μ/mm^{-1}	0.090
F(000)	1584.0
Crystal size/mm^3	$0.15\times0.005\times0.002$
Radiation	Synchrotron (λ=0.6889)
2Θ range for data collection/^{o}	2.002 to 47.798
Index ranges	$-25\leq h\leq25$, $-4\leq k\leq4$, $-46\leq l\leq46$
Reflections collected	30591
Independent reflections	5690 [R_{int} =0.1654, R_{sigma} = 0.0973]
Data/restraints/parameters	5690/1891/542
Goodness-of-fit on F^2	1.040
Final R indexes [I>=2σ (I)]	R_1 =0.0908, wR_2 =0.2209
Final R indexes [all data]	R_1 =0.1197, wR_2 =0.2379

Largest diff. peak/hole/eÅ^{-3}	0.42/−0.32
Flack parameter	−0.7(10)

Fractional Atomic Coordinates ($\times 10^4$) and Equivalent Isotropic Displacement Parameters (Å$^2 \times 10^3$) for 5,6,11,12,17,18- hexaazatrinaphthylene. U_{eq} is defined as 1/3 of of the trace of the orthogonalised U_{IJ} tensor.

Atom	x	y	z	U(eq)
N1A	6000(3)	-1483(19)	6939.4(18)	33.0(16)
C2A	5540(3)	-3250(20)	7088(2)	28.0(18)
C3A	5568(3)	-4040(20)	7436(2)	32.5(19)
C4A	5104(3)	-5830(20)	7589(2)	33.1(19)
C5A	4571(4)	-6740(20)	7403(2)	34(2)
C6A	4521(4)	-5950(20)	7067(2)	31.8(19)
C7A	4999(3)	-4190(20)	6897.9(19)	30.3(19)
N8A	4948(3)	-3433(19)	6563.3(18)	33.8(17)
C9A	5408(4)	-1750(20)	6423(2)	32.1(19)
C10A	5372(3)	-810(20)	6060.5(19)	31.4(19)
N11A	4867(3)	-1701(18)	5889.9(18)	31.8(17)
C12A	4833(3)	-770(20)	5561(2)	32.5(19)
C13A	4309(4)	-1630(20)	5364(2)	37(2)
C14A	4272(4)	-700(20)	5035(2)	35(2)
C15A	4745(4)	1220(20)	4877(2)	37(2)
C16A	5261(4)	2070(20)	5056(2)	35(2)
C17A	5315(3)	1140(20)	5402.7(19)	30.2(18)
N18A	5837(3)	2018(19)	5578.4(18)	31.7(17)
C19A	5858(3)	1080(20)	5903.3(19)	29.2(18)
C20A	6415(3)	2000(20)	6098(2)	28.1(19)
N21A	6860(3)	3651(19)	5937.6(18)	32.8(17)

C22A	7368(3)	4400(20)	6123(2)	30.3(18)
C23A	7865(4)	6090(20)	5967(2)	35(2)
C24A	8381(4)	6860(20)	6152(2)	37(2)
C25A	8420(4)	5870(20)	6497(2)	35(2)
C26A	7949(3)	4240(20)	6658(2)	30.0(18)
C27A	7406(4)	3510(20)	6473(2)	29.2(18)
N28A	6946(3)	1777(18)	6633.1(19)	32.2(17)
C29A	6451(3)	1100(20)	6445.0(19)	31.2(18)
C30A	5944(3)	-780(20)	6611.4(19)	29.3(18)
N1B	3283(3)	3481(18)	4437.4(19)	36.6(18)
C2B	2789(4)	4630(20)	4616.7(19)	35(2)
C3B	2752(4)	3910(20)	4967(2)	39(2)
C4B	2250(4)	4940(20)	5145(2)	38(2)
C5B	1773(4)	6830(20)	4987(2)	38(2)
C6B	1794(4)	7530(20)	4651(2)	34(2)
C7B	2303(4)	6400(20)	4454(2)	36(2)
N8B	2315(3)	7155(18)	4116.4(19)	32.2(17)
C9B	2807(3)	6090(20)	3946.1(19)	31.3(18)
C10B	2846(4)	6870(20)	3584(2)	28.9(18)
N11B	2383(3)	8530(19)	3438.0(18)	33.5(17)
C12B	2433(3)	9270(20)	3103.2(19)	28.9(18)
C13B	1957(4)	11020(20)	2932(2)	33(2)
C14B	1998(4)	11780(20)	2595(2)	33(2)
C15B	2538(4)	10800(20)	2413(2)	33.7(19)
C16B	3003(4)	9070(20)	2565(2)	35(2)
C17B	2962(4)	8230(20)	2914(2)	31.2(19)
N18B	3439(3)	6571(18)	3064.5(17)	29.8(16)
C19B	3377(3)	5860(20)	3392.5(19)	31.4(19)

C20B	3881(3)	3990(20)	3560.2(19)	28.8(17)
N21B	4374(3)	3185(18)	3376.8(19)	31.7(17)
C22B	4839(4)	1500(20)	3537(2)	30.1(18)
C23B	5381(4)	710(20)	3356(2)	34(2)
C24B	5846(4)	-990(20)	3518(2)	39(2)
C25B	5788(4)	-2110(20)	3858(2)	37(2)
C26B	5264(4)	-1420(20)	4036(2)	38(2)
C27B	4778(4)	430(20)	3882(2)	33.0(19)
N28B	4269(3)	1309(18)	4064.0(18)	33.5(17)
C29B	3829(4)	3070(20)	3908(2)	31.4(19)
C30B	3289(3)	4220(20)	4109(2)	32.2(19)

Anisotropic Displacement Parameters ($Å^2 \times 10^3$) for 5,6,11,12,17,18- hexaaza-trinaphthylene. The Anisotropic displacement factor exponent takes the form: $-2\pi^2$[$h^2a^{*2}U_{11}$+2hka*b*U_{12}+...].

Atom	U11	U22	U33	U23	U13	U12
N1A	30(4)	27(4)	42(4)	0(3)	0(3)	1(3)
C2A	15(4)	30(4)	40(5)	-2(4)	2(3)	4(3)
C3A	16(4)	36(5)	45(5)	0(4)	-5(3)	2(3)
C4A	32(4)	33(5)	34(5)	-3(4)	3(3)	1(3)
C5A	22(4)	35(5)	46(5)	6(4)	6(4)	-3(3)
C6A	25(4)	28(5)	43(5)	-1(4)	2(3)	1(3)
C7A	21(4)	33(5)	37(4)	-3(4)	1(3)	-1(3)
N8A	27(4)	36(4)	38(4)	-5(3)	1(3)	3(3)
C9A	30(4)	30(4)	37(5)	-4(4)	3(3)	2(4)
C10A	23(4)	35(5)	36(4)	-6(4)	2(3)	8(3)
N11A	23(4)	34(4)	38(4)	2(3)	1(3)	2(3)
C12A	21(4)	37(5)	39(4)	-1(4)	-2(3)	4(3)

C13A	22(5)	47(6)	42(5)	-3(4)	0(4)	1(4)
C14A	30(4)	37(5)	38(5)	-7(4)	-4(3)	2(4)
C15A	33(4)	43(5)	33(4)	-2(4)	-2(3)	4(4)
C16A	30(4)	42(5)	34(4)	1(4)	4(4)	0(4)
C17A	25(4)	29(4)	37(4)	-5(4)	1(3)	2(3)
N18A	26(4)	39(4)	30(4)	-1(3)	1(3)	3(3)
C19A	22(4)	29(4)	36(4)	-3(4)	4(3)	9(3)
C20A	15(4)	32(5)	37(5)	-2(4)	3(3)	5(3)
N21A	29(4)	32(4)	37(4)	-5(3)	2(3)	1(3)
C22A	28(4)	26(4)	37(4)	-2(4)	1(3)	3(3)
C23A	28(4)	38(5)	40(5)	4(4)	4(4)	-1(4)
C24A	33(5)	36(5)	42(5)	5(4)	8(4)	2(4)
C25A	28(4)	33(5)	44(5)	-4(4)	-4(4)	0(4)
C26A	27(4)	24(4)	38(5)	-3(4)	0(3)	6(3)
C27A	25(4)	27(4)	36(5)	-2(4)	0(3)	0(3)
N28A	23(4)	33(4)	40(5)	0(3)	-2(3)	5(3)
C29A	25(4)	31(5)	38(4)	-2(4)	2(3)	6(3)
C30A	23(4)	27(4)	38(4)	-2(4)	4(3)	7(3)
N1B	40(4)	32(4)	38(4)	0(4)	4(3)	5(3)
C2B	38(4)	33(5)	33(4)	-2(4)	1(3)	-5(4)
C3B	45(5)	39(5)	33(4)	1(4)	-2(4)	5(4)
C4B	44(5)	35(5)	35(5)	3(4)	2(4)	0(4)
C5B	36(5)	44(5)	34(4)	-2(4)	1(4)	-2(4)
C6B	34(5)	35(5)	33(5)	2(4)	0(4)	0(4)
C7B	33(4)	44(5)	31(4)	1(4)	2(3)	-2(4)
N8B	39(4)	28(4)	30(4)	0(3)	0(3)	-1(3)
C9B	27(4)	34(5)	33(4)	-4(4)	1(3)	-1(3)
C10B	22(4)	29(4)	35(4)	-1(4)	-2(3)	-1(3)

N11B	32(4)	35(4)	34(4)	0(3)	1(3)	-4(3)
C12B	30(4)	23(4)	33(4)	-5(4)	-2(3)	-1(3)
C13B	23(4)	35(5)	41(5)	0(4)	3(3)	1(3)
C14B	24(4)	35(5)	40(5)	1(4)	-3(4)	0(3)
C15B	39(5)	30(5)	33(5)	0(4)	1(4)	-3(4)
C16B	38(5)	29(5)	37(4)	-8(4)	0(4)	0(3)
C17B	26(4)	28(5)	40(5)	6(4)	2(3)	1(3)
N18B	27(4)	27(4)	34(4)	-3(3)	-5(3)	-5(3)
C19B	25(4)	34(5)	35(4)	0(4)	-2(3)	-5(3)
C20B	30(4)	25(4)	32(4)	-5(3)	0(3)	-4(3)
N21B	27(4)	28(4)	40(5)	-5(3)	2(3)	-2(3)
C22B	28(4)	22(4)	41(5)	-4(4)	-2(3)	-1(3)
C23B	31(4)	32(5)	38(5)	-4(4)	1(3)	0(4)
C24B	38(5)	34(5)	45(5)	-5(4)	-1(4)	2(4)
C25B	28(4)	36(5)	47(5)	-3(4)	-4(4)	4(4)
C26B	40(5)	42(5)	32(5)	-5(4)	-2(4)	5(4)
C27B	30(4)	27(4)	42(5)	-2(4)	-2(3)	0(3)
N28B	29(4)	34(4)	38(4)	-3(3)	0(3)	-3(3)
C29B	27(4)	30(4)	37(5)	-3(4)	0(3)	2(3)
C30B	31(4)	29(5)	37(4)	0(4)	4(3)	-3(3)

Bond lengths for 5,6,11,12,17,18- hexaazatrinaphthylene.

Atom	Atom	Length/Å	Atom	Atom	Length/Å
N1A	C2A	1.349(10)	N1B	C2B	1.363(9)
N1A	C30A	1.328(9)	N1B	C30B	1.327(10)
C2A	C3A	1.406(10)	C2B	C3B	1.413(10)
C2A	C7A	1.444(10)	C2B	C7B	1.418(10)
C3A	C4A	1.369(10)	C3B	C4B	1.360(11)

C4A	C5A	1.418(10)	C4B	C5B	1.419(11)
C5A	C6A	1.367(11)	C5B	C6B	1.351(11)
C6A	C7A	1.414(10)	C6B	C7B	1.425(10)
C7A	N8A	1.357(10)	C7B	N8B	1.363(10)
N8A	C9A	1.319(10)	N8B	C9B	1.331(10)
C9A	C10A	1.479(10)	C9B	C10B	1.463(10)
C9A	C30A	1.435(10)	C9B	C30B	1.430(10)
C10A	N11A	1.337(9)	C10B	N11B	1.329(9)
C10A	C19A	1.429(10)	C10B	C19B	1.438(10)
N11A	C12A	1.348(10)	N11B	C12B	1.356(10)
C12A	C13A	1.421(10)	C12B	C13B	1.409(10)
C12A	C17A	1.431(10)	C12B	C17B	1.432(10)
C13A	C14A	1.354(11)	C13B	C14B	1.365(11)
C14A	C15A	1.417(11)	C14B	C15B	1.431(10)
C15A	C16A	1.367(10)	C15B	C16B	1.357(10)
C16A	C17A	1.419(10)	C16B	C17B	1.417(10)
C17A	N18A	1.375(9)	C17B	N18B	1.360(9)
N18A	C19A	1.334(9)	N18B	C19B	1.330(9)
C19A	C20A	1.480(10)	C19B	C20B	1.473(9)
C20A	N21A	1.325(10)	C20B	N21B	1.332(9)
C20A	C29A	1.415(10)	C20B	C29B	1.424(10)
N21A	C22A	1.357(9)	N21B	C22B	1.362(9)
C22A	C23A	1.410(10)	C22B	C23B	1.413(10)
C22A	C27A	1.427(10)	C22B	C27B	1.429(10)
C23A	C24A	1.374(11)	C23B	C24B	1.368(10)
C24A	C25A	1.416(11)	C24B	C25B	1.417(11)
C25A	C26A	1.363(10)	C25B	C26B	1.367(11)
C26A	C27A	1.418(10)	C26B	C27B	1.416(10)

C27A	N28A	1.364(9)	C27B	N28B	1.367(9)
N28A	C29A	1.335(9)	N28B	C29B	1.329(10)
C29A	C30A	1.479(10)	C29B	C30B	1.487(10)

Bond angles for 5,6,11,12,17,18- hexaazatrinaphthylene.

Atom	Atom	Atom	Angle/^{o}	Atom	Atom	Atom	Angle/^{o}
C30A	N1A	C2A	117.4(7)	C30B	N1B	C2B	116.4(7)
N1A	C2A	C3A	120.2(7)	N1B	C2B	C3B	119.2(7)
N1A	C2A	C7A	120.6(7)	N1B	C2B	C7B	120.9(7)
C3A	C2A	C7A	119.2(7)	C3B	C2B	C7B	119.8(7)
C4A	C3A	C2A	120.7(7)	C4B	C3B	C2B	119.5(8)
C3A	C4A	C5A	120.2(8)	C3B	C4B	C5B	120.9(8)
C6A	C5A	C4A	120.8(7)	C6B	C5B	C4B	120.8(8)
C5A	C6A	C7A	120.4(7)	C5B	C6B	C7B	120.0(8)
C6A	C7A	C2A	118.6(7)	C2B	C7B	C6B	118.9(7)
N8A	C7A	C2A	121.2(7)	N8B	C7B	C2B	122.2(7)
N8A	C7A	C6A	120.1(7)	N8B	C7B	C6B	118.9(7)
C9A	N8A	C7A	116.9(7)	C9B	N8B	C7B	116.2(7)
N8A	C9A	C10A	119.3(7)	N8B	C9B	C10B	118.3(7)
N8A	C9A	C30A	122.2(7)	N8B	C9B	C30B	121.5(7)
C30A	C9A	C10A	118.6(7)	C30B	C9B	C10B	120.2(7)
N11A	C10A	C9A	117.7(7)	N11B	C10B	C9B	118.7(7)
N11A	C10A	C19A	121.7(7)	N11B	C10B	C19B	121.1(7)
C19A	C10A	C9A	120.6(6)	C19B	C10B	C9B	120.2(7)
C10A	N11A	C12A	117.3(7)	C10B	N11B	C12B	117.7(7)
N11A	C12A	C13A	120.4(7)	N11B	C12B	C13B	120.7(7)
N11A	C12A	C17A	121.3(7)	N11B	C12B	C17B	120.7(7)
C13A	C12A	C17A	118.3(7)	C13B	C12B	C17B	118.6(7)

C14A	C13A	C12A	120.7(8)	C14B	C13B	C12B	121.5(7)
C13A	C14A	C15A	121.3(7)	C13B	C14B	C15B	119.0(7)
C16A	C15A	C14A	120.0(8)	C16B	C15B	C14B	121.5(8)
C15A	C16A	C17A	120.3(8)	C15B	C16B	C17B	119.8(7)
C16A	C17A	C12A	119.5(7)	C16B	C17B	C12B	119.5(7)
N18A	C17A	C12A	121.1(7)	N18B	C17B	C12B	121.5(7)
N18A	C17A	C16A	119.4(7)	N18B	C17B	C16B	119.0(7)
C19A	N18A	C17A	116.4(7)	C19B	N18B	C17B	116.5(7)
C10A	C19A	C20A	120.4(7)	C10B	C19B	C20B	120.0(7)
N18A	C19A	C10A	122.2(7)	N18B	C19B	C10B	122.3(7)
N18A	C19A	C20A	117.4(7)	N18B	C19B	C20B	117.7(6)
N21A	C20A	C19A	118.0(7)	N21B	C20B	C19B	118.2(7)
N21A	C20A	C29A	122.7(7)	N21B	C20B	C29B	121.9(7)
C29A	C20A	C19A	119.3(7)	C29B	C20B	C19B	119.8(6)
C20A	N21A	C22A	116.4(7)	C20B	N21B	C22B	117.5(7)
N21A	C22A	C23A	119.5(7)	N21B	C22B	C23B	119.5(7)
N21A	C22A	C27A	121.2(7)	N21B	C22B	C27B	120.8(7)
C23A	C22A	C27A	119.3(7)	C23B	C22B	C27B	119.7(7)
C24A	C23A	C22A	119.9(8)	C24B	C23B	C22B	119.2(8)
C23A	C24A	C25A	120.0(8)	C23B	C24B	C25B	121.7(8)
C26A	C25A	C24A	121.9(8)	C26B	C25B	C24B	120.1(8)
C25A	C26A	C27A	118.8(7)	C25B	C26B	C27B	120.1(8)
C26A	C27A	C22A	119.9(7)	C26B	C27B	C22B	119.2(7)
N28A	C27A	C22A	121.6(7)	N28B	C27B	C22B	120.3(7)
N28A	C27A	C26A	118.3(7)	N28B	C27B	C26B	120.4(7)
C29A	N28A	C27A	115.7(7)	C29B	N28B	C27B	118.2(7)
C20A	C29A	C30A	120.6(7)	C20B	C29B	C30B	120.1(7)
N28A	C29A	C20A	122.3(7)	N28B	C29B	C20B	121.2(7)

N28A	C29A	C30A	117.0(7)	N28B	C29B	C30B	118.6(7)
N1A	C30A	C9A	121.7(7)	N1B	C30B	C9B	122.8(7)
N1A	C30A	C29A	117.7(6)	N1B	C30B	C29B	117.6(7)
C9A	C30A	C29A	120.6(7)	C9B	C30B	C29B	119.6(7)

Torsion angles for 5,6,11,12,17,18- hexaazatrinaphthylene.

A	B	C	D	Angle/^{o}	A	B	C	D	Angle/^{o}
N1A	C2A	C3A	C4A	179.9(8)	N1B	C2B	C3B	C4B	-177.8(9)
N1A	C2A	C7A	C6A	-178.2(8)	N1B	C2B	C7B	C6B	179.5(8)
N1A	C2A	C7A	N8A	2.5(13)	N1B	C2B	C7B	N8B	-2.3(14)
C2A	N1A	C30A	C9A	2.3(12)	C2B	N1B	C30B	C9B	-0.3(13)
C2A	N1A	C30A	C29A	-178.9(7)	C2B	N1B	C30B	C29B	178.6(8)
C2A	C3A	C4A	C5A	-3.6(13)	C2B	C3B	C4B	C5B	-2.2(14)
C2A	C7A	N8A	C9A	-1.5(12)	C2B	C7B	N8B	C9B	0.7(12)
C3A	C2A	C7A	C6A	-1.7(12)	C3B	C2B	C7B	C6B	2.0(13)
C3A	C2A	C7A	N8A	179.0(8)	C3B	C2B	C7B	N8B	-179.8(9)
C3A	C4A	C5A	C6A	2.1(13)	C3B	C4B	C5B	C6B	2.8(14)
C4A	C5A	C6A	C7A	-0.4(13)	C4B	C5B	C6B	C7B	-1.0(14)
C5A	C6A	C7A	C2A	0.2(12)	C5B	C6B	C7B	C2B	-1.4(14)
C5A	C6A	C7A	N8A	179.5(9)	C5B	C6B	C7B	N8B	-179.6(8)
C6A	C7A	N8A	C9A	179.3(8)	C6B	C7B	N8B	C9B	178.9(8)
C7A	C2A	C3A	C4A	3.4(13)	C7B	C2B	C3B	C4B	-0.2(14)
C7A	N8A	C9A	C10A	-179.0(8)	C7B	N8B	C9B	C10B	-179.1(8)
C7A	N8A	C9A	C30A	0.9(12)	C7B	N8B	C9B	C30B	0.9(12)
N8A	C9A	C10A	N11A	0.5(12)	N8B	C9B	C10B	N11B	-1.8(12)
N8A	C9A	C10A	C19A	178.7(8)	N8B	C9B	C10B	C19B	178.2(8)
N8A	C9A	C30A	N1A	-1.3(14)	N8B	C9B	C30B	N1B	-1.2(14)
N8A	C9A	C30A	C29A	179.8(8)	N8B	C9B	C30B	C29B	180.0(8)

C9A	C10A	N11A	C12A	178.7(8)	C9B	C10B	N11B	C12B	179.1(8)
C9A	C10A	C19A	N18A	-178.9(8)	C9B	C10B	C19B	N18B	-178.7(8)
C9A	C10A	C19A	C20A	2.5(12)	C9B	C10B	C19B	C20B	0.6(12)
C10A	C9A	C30A	N1A	178.6(7)	C10B	C9B	C30B	N1B	178.9(8)
C10A	C9A	C30A	C29A	-0.3(12)	C10B	C9B	C30B	C29B	0.0(12)
C10A	N11A	C12A	C13A	-180.0(8)	C10B	N11B	C12B	C13B	179.8(8)
C10A	N11A	C12A	C17A	-0.9(12)	C10B	N11B	C12B	C17B	1.4(12)
C10A	C19A	C20A	N21A	177.9(7)	C10B	C19B	C20B	N21B	-178.0(8)
C10A	C19A	C20A	C29A	-2.2(12)	C10B	C19B	C20B	C29B	2.7(12)
N11A	C10A	C19A	N18A	-0.7(12)	N11B	C10B	C19B	N18B	1.3(13)
N11A	C10A	C19A	C20A	-179.4(8)	N11B	C10B	C19B	C20B	-179.4(7)
N11A	C12A	C13A	C14A	179.8(8)	N11B	C12B	C13B	C14B	-179.8(8)
N11A	C12A	C17A	C16A	-179.8(8)	N11B	C12B	C17B	C16B	-179.4(8)
N11A	C12A	C17A	N18A	1.7(13)	N11B	C12B	C17B	N18B	-2.2(13)
C12A	C13A	C14A	C15A	-1.4(14)	C12B	C13B	C14B	C15B	-0.4(13)
C12A	C17A	N18A	C19A	-1.8(12)	C12B	C17B	N18B	C19B	2.4(12)
C13A	C12A	C17A	C16A	-0.8(12)	C13B	C12B	C17B	C16B	2.1(13)
C13A	C12A	C17A	N18A	-179.3(8)	C13B	C12B	C17B	N18B	179.4(8)
C13A	C14A	C15A	C16A	2.1(14)	C13B	C14B	C15B	C16B	1.4(13)
C14A	C15A	C16A	C17A	-2.1(13)	C14B	C15B	C16B	C17B	-0.6(13)
C15A	C16A	C17A	C12A	1.5(13)	C15B	C16B	C17B	C12B	-1.2(13)
C15A	C16A	C17A	N18A	-179.9(8)	C15B	C16B	C17B	N18B	-178.5(8)
C16A	C17A	N18A	C19A	179.7(7)	C16B	C17B	N18B	C19B	179.7(8)
C17A	C12A	C13A	C14A	0.7(13)	C17B	C12B	C13B	C14B	-1.3(13)
C17A	N18A	C19A	C10A	1.3(12)	C17B	N18B	C19B	C10B	-2.0(12)
C17A	N18A	C19A	C20A	-180.0(7)	C17B	N18B	C19B	C20B	178.7(7)
N18A	C19A	C20A	N21A	-0.9(11)	N18B	C19B	C20B	N21B	1.3(11)
N18A	C19A	C20A	C29A	179.0(8)	N18B	C19B	C20B	C29B	-178.0(8)

C19A	C10A	N11A	C12A	0.5(12)	C19B	C10B	N11B	C12B	-0.9(12)
C19A	C20A	N21A	C22A	-178.8(7)	C19B	C20B	N21B	C22B	179.3(7)
C19A	C20A	C29A	N28A	178.4(8)	C19B	C20B	C29B	N28B	178.1(8)
C19A	C20A	C29A	C30A	0.8(12)	C19B	C20B	C29B	C30B	-4.5(12)
C20A	N21A	C22A	C23A	178.7(8)	C20B	N21B	C22B	C23B	-177.4(8)
C20A	N21A	C22A	C27A	-1.6(12)	C20B	N21B	C22B	C27B	4.3(12)
C20A	C29A	C30A	N1A	-178.4(8)	C20B	C29B	C30B	N1B	-175.7(8)
C20A	C29A	C30A	C9A	0.5(12)	C20B	C29B	C30B	C9B	3.2(12)
N21A	C20A	C29A	N28A	-1.7(13)	N21B	C20B	C29B	N28B	-1.2(13)
N21A	C20A	C29A	C30A	-179.3(8)	N21B	C20B	C29B	C30B	176.2(8)
N21A	C22A	C23A	C24A	180.0(8)	N21B	C22B	C23B	C24B	-179.9(8)
N21A	C22A	C27A	C26A	178.4(8)	N21B	C22B	C27B	C26B	178.0(8)
N21A	C22A	C27A	N28A	2.3(13)	N21B	C22B	C27B	N28B	-4.7(13)
C22A	C23A	C24A	C25A	1.5(14)	C22B	C23B	C24B	C25B	2.6(13)
C22A	C27A	N28A	C29A	-2.5(12)	C22B	C27B	N28B	C29B	2.0(12)
C23A	C22A	C27A	C26A	-2.0(12)	C23B	C22B	C27B	C26B	-0.3(13)
C23A	C22A	C27A	N28A	-178.0(8)	C23B	C22B	C27B	N28B	177.0(8)
C23A	C24A	C25A	C26A	-1.8(14)	C23B	C24B	C25B	C26B	-1.7(14)
C24A	C25A	C26A	C27A	0.1(13)	C24B	C25B	C26B	C27B	-0.2(14)
C25A	C26A	C27A	C22A	1.8(12)	C25B	C26B	C27B	C22B	1.1(13)
C25A	C26A	C27A	N28A	177.9(7)	C25B	C26B	C27B	N28B	-176.1(8)
C26A	C27A	N28A	C29A	-178.6(7)	C26B	C27B	N28B	C29B	179.2(8)
C27A	C22A	C23A	C24A	0.3(13)	C27B	C22B	C23B	C24B	-1.6(13)
C27A	N28A	C29A	C20A	2.2(12)	C27B	N28B	C29B	C20B	0.8(12)
C27A	N28A	C29A	C30A	179.9(7)	C27B	N28B	C29B	C30B	-176.6(8)
N28A	C29A	C30A	N1A	3.8(11)	N28B	C29B	C30B	N1B	1.7(12)
N28A	C29A	C30A	C9A	-177.3(8)	N28B	C29B	C30B	C9B	-179.4(8)
C29A	C20A	N21A	C22A	1.3(12)	C29B	C20B	N21B	C22B	-1.4(12)

C30A	N1A	C2A	C3A	-179.3(8)	C30B	N1B	C2B	C3B	179.5(8)
C30A	N1A	C2A	C7A	-2.8(12)	C30B	N1B	C2B	C7B	1.9(13)
C30A	C9A	C10A	N11A	-179.4(8)	C30B	C9B	C10B	N11B	178.1(8)
C30A	C9A	C10A	C19A	-1.2(12)	C30B	C9B	C10B	C19B	-1.9(13)

Hydrogen Atom Coordinates (Å$\times 10^4$) and Isotropic Displacement Parameters (Å$^2\times 10^3$) for 5,6,11,12,17,18- hexaazatrinaphthylene.

Atom	x	y	z	U(eq)
H3A	5913.02	-3323.07	7565.09	39
H4A	5138.87	-6457.21	7821.09	40
H5A	4245.76	-7911.34	7513.91	41
H6A	4162.36	-6592.91	6945.22	38
H13A	3981.36	-2878.57	5465.45	44
H14A	3921.31	-1340.21	4906.01	42
H15A	4704.71	1922.41	4647.65	44
H16A	5583.79	3292.22	4948.29	42
H23A	7843.12	6703.25	5733.87	42
H24A	8712.47	8051.44	6048.45	45
H25A	8784.31	6365.17	6619.52	42
H26A	7984.03	3603.98	6889.29	36
H3B	3074.58	2707.15	5077.72	47
H4B	2217.99	4385.34	5379.27	46
H5B	1435.73	7621.18	5117.54	46
H6B	1469.02	8770.17	4547.24	40
H13B	1600.47	11675.38	3054.28	40
H14B	1672.09	12938.5	2483.21	40
H15B	2571.05	11367.3	2179.34	40
H16B	3355.81	8429.33	2438.88	42

H23B	5421.8	1355.93	3124.66	41
H24B	6216.51	-1432.87	3399.21	47
H25B	6113	-3339.26	3962.87	44
H26B	5225.23	-2173.64	4264.19	46

SCXRD data for 2,3,8,9,14,15- hexafluoro- 5,6,11,12,17,18- hexaazatrinaphthylene.

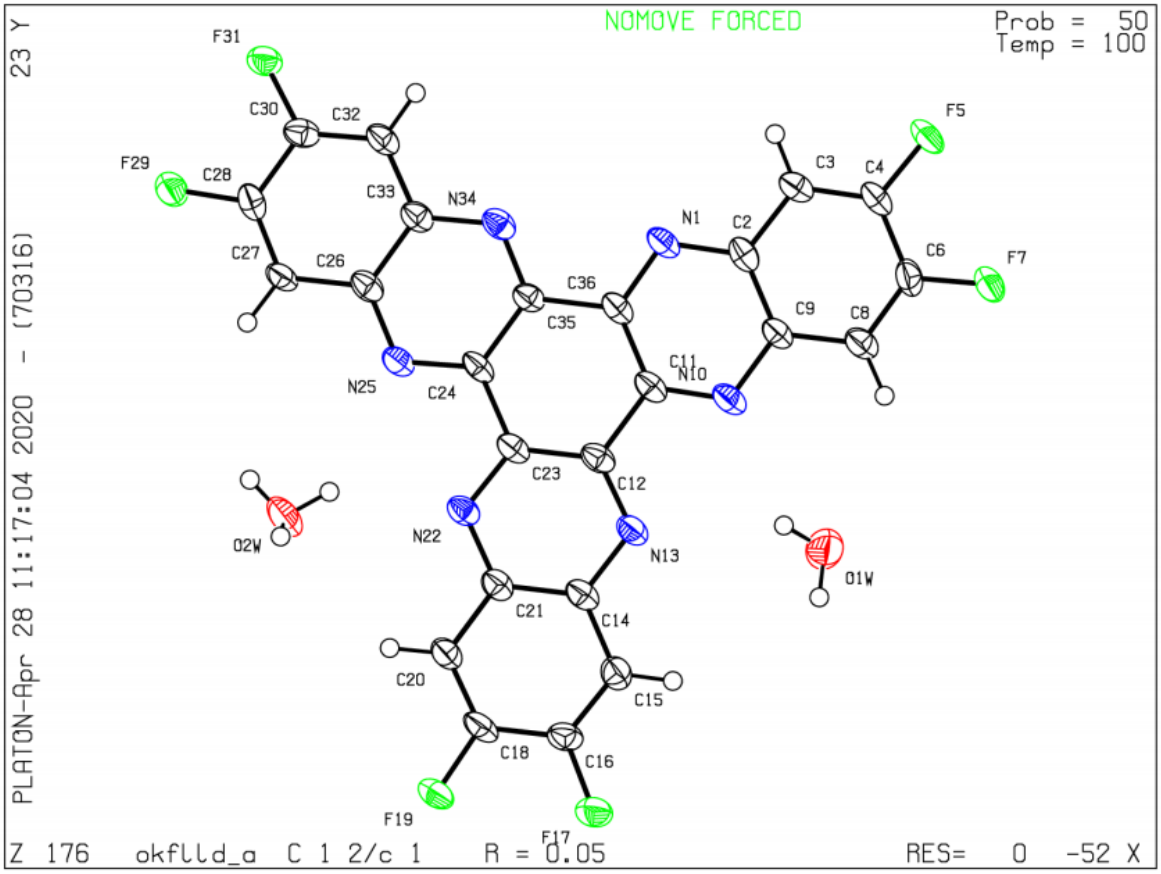

Figure 3.30. Ellipsoid plot of the unit cell of 5,6,11,12,17,18-hexaazatrinaphthylene.

Crystal data and structure refinement for 2,3,8,9,14,15- hexafluoro-5,6,11,12,17,18- hexaazatrinaphthylene.

Empirical formula	$C_{24}H_{10}F_6N_6O_2$
Formula weight	528.38
Temperature/K	100(2)
Crystal system	monoclinic
Space group	C2/c
a/Å	34.4280(6)
b/Å	4.48900(10)
c/Å	29.9864(4)
$\alpha/^o$	90
$\beta/^o$	120.1050(10)
$\gamma/^o$	90
Volume/$Å^3$	4009.18(13)
Z	8
ρcalcg/cm^3	1.751
μ/mm^{-1}	0.144
F(000)	2128.0
Crystal size/mm^3	0.2×0.005×0.005
Radiation	Synchrotron (λ=0.6889)
2Θ range for data collection/^{o}	4.604 to 42.51
Index ranges	$-36 \leq h \leq 34$, $-4 \leq k \leq 4$, $-31 \leq l \leq 31$
Reflections collected	6742
Independent reflections	2401 [R_{int} =0.0483, R_{sigma} =0.0641]
Data/restraints/parameters	2401/8/358
Goodness-of-fit on F^2	1.044
Final R indexes [I>=2σ (I)]	R_1 =0.0522, wR_2 =0.1451
Final R indexes [all data]	R_1 =0.0676, wR_2 =0.1541

Largest diff. peak/hole/eÅ^{-3}	0.32/−0.29

Fractional Atomic Coordinates ($\times 10^4$) and Equivalent Isotropic Displacement Parameters (Å$^2 \times 10^3$) for 2,3,8,9,14,15- hexafluoro- 5,6,11,12,17,18- hexaazatrinaphthylene. U_{eq} is defined as 1/3 of of the trace of the orthogonalised U_{IJ} tensor.

Atom	x	y	z	U(eq)
N1	6348.1(11)	4460(7)	6822.0(11)	29.7(8)
C2	6006.7(13)	5762(9)	6850.2(14)	28.3(10)
C3	5921.7(13)	4922(8)	7250.7(14)	30.0(10)
C4	5576.1(13)	6174(9)	7273.3(14)	29.8(10)
F5	5481.2(8)	5381(5)	7638.1(8)	40.6(6)
C6	5294.6(13)	8308(9)	6901.8(15)	32.6(10)
F7	4958.4(8)	9451(5)	6950.3(8)	40.5(6)
C8	5365.1(14)	9182(9)	6516.6(15)	31.1(10)
C9	5719.2(13)	7888(8)	6476.4(14)	27.0(9)
N10	5788.1(11)	8735(7)	6087.7(11)	30.7(8)
C11	6118.7(13)	7408(8)	6059.0(14)	26.7(9)
C12	6188.7(13)	8260(8)	5629.5(14)	27.3(10)
N13	5914.0(11)	10267(7)	5294.1(12)	28.8(8)
C14	5980.8(13)	10972(8)	4897.0(14)	27.8(10)
C15	5693.6(13)	13093(8)	4526.7(14)	30.2(10)
C16	5772.5(13)	13799(8)	4139.7(15)	30.6(10)
F17	5512.8(8)	15806(5)	3781.2(8)	38.0(6)
C18	6119.9(14)	12455(9)	4090.8(15)	32.2(10)
F19	6175.2(8)	13373(5)	3701.2(8)	42.4(7)
C20	6397.7(13)	10430(8)	4433.5(14)	29.8(10)
C21	6330.2(13)	9608(8)	4847.4(14)	27.9(10)
N22	6608.4(10)	7567(7)	5195.1(11)	27.1(8)

C23	6531.9(13)	6863(8)	5574.9(14)	26.5(9)
C24	6828.2(13)	4655(8)	5956.4(14)	25.5(9)
N25	7145.0(11)	3419(7)	5885.9(11)	27.7(8)
C26	7412.6(13)	1377(8)	6240.0(14)	27.5(10)
C27	7755.6(13)	-25(8)	6179.7(14)	28.5(10)
C28	8013.0(13)	-2079(9)	6529.3(15)	30.6(10)
F29	8339.1(8)	-3524(5)	6488.9(8)	38.8(6)
C30	7948.1(13)	-2931(8)	6941.8(14)	28.7(10)
F31	8219.8(7)	-5082(4)	7259.2(8)	33.4(6)
C32	7632.8(13)	-1605(8)	7016.9(14)	28.7(10)
C33	7350.9(13)	535(8)	6658.6(14)	27.6(9)
N34	7024.2(11)	1844(7)	6723.6(12)	28.5(8)
C35	6765.3(13)	3834(8)	6376.8(14)	25.3(9)
C36	6402.1(13)	5277(8)	6429.0(14)	27.3(10)
O1W	5051.5(10)	12665(7)	5343.2(13)	52.9(9)
O2W	7256.8(11)	5007(7)	4915.5(11)	45.3(8)

Anisotropic Displacement Parameters ($Å^2 \times 10^3$) for 2,3,8,9,14,15- hexafluoro-5,6,11,12,17,18- hexaazatrinaphthylene. The Anisotropic displacement factor exponent takes the form: $-2\pi^2$[$h^2a^{*2}U_{11}$+2hka*b*U_{12}+...].

Atom	U11	U22	U33	U23	U13	U12
N1	44(2)	28.2(18)	27.5(18)	-0.7(15)	25.5(16)	-3.4(16)
C2	33(2)	32(2)	27(2)	-7.3(19)	20.2(19)	-7(2)
C3	40(2)	30(2)	25(2)	-0.7(17)	20.2(19)	-4.6(19)
C4	40(2)	32(2)	29(2)	-4.0(19)	26(2)	-7(2)
F5	55.3(15)	48.2(15)	36.9(13)	5.7(11)	36.9(12)	4.3(12)
C6	39(2)	34(2)	39(2)	-4(2)	29(2)	2(2)
F7	53.9(15)	42.7(14)	44.0(14)	6.1(11)	38.8(13)	9.1(12)

C8	46(3)	26(2)	30(2)	-1.1(18)	26(2)	-1.9(19)
C9	36(2)	26(2)	27(2)	-1.3(18)	21.9(19)	-4.3(19)
N10	45(2)	29.9(19)	26.8(18)	-1.1(15)	24.8(17)	-3.0(16)
C11	35(2)	26(2)	26(2)	-3.6(18)	20.4(19)	-8.5(19)
C12	41(2)	22(2)	24(2)	-3.9(18)	20(2)	-5.7(19)
N13	39(2)	26.7(19)	29.7(19)	1.6(16)	24.2(17)	-1.6(16)
C14	40(2)	23(2)	27(2)	-2.9(18)	22(2)	-6.3(19)
C15	37(2)	26(2)	36(2)	-0.4(19)	24(2)	-0.7(19)
C16	45(3)	21(2)	30(2)	3.5(19)	22(2)	0(2)
F17	52.4(15)	31.0(13)	38.0(14)	9.8(11)	28.0(12)	6.3(11)
C18	49(3)	30(2)	32(2)	2(2)	30(2)	-5(2)
F19	60.4(16)	42.7(15)	41.4(14)	14.2(11)	38.4(13)	9.6(12)
C20	42(2)	27(2)	31(2)	-0.4(19)	26(2)	-1(2)
C21	36(2)	25(2)	29(2)	-1.9(19)	20.9(19)	-4.5(19)
N22	40(2)	19.8(18)	27.6(18)	-1.8(15)	22.0(16)	-3.9(16)
C23	39(2)	23(2)	25(2)	-2.8(18)	21.3(19)	-5.9(19)
C24	40(2)	20(2)	27(2)	-5.4(17)	24.9(19)	-9.4(18)
N25	41(2)	22.8(18)	27.6(18)	-0.5(15)	23.3(16)	-2.1(16)
C26	38(2)	25(2)	24(2)	-6.0(18)	19.5(19)	-6.6(19)
C27	45(2)	22(2)	29(2)	2.4(18)	27(2)	-0.5(19)
C28	37(2)	29(2)	38(2)	-6(2)	28(2)	-4(2)
F29	53.8(15)	34.1(14)	43.2(14)	5.2(11)	35.3(12)	7.8(11)
C30	40(2)	23(2)	23(2)	-1.2(18)	15.4(19)	-3(2)
F31	48.5(14)	25.4(13)	32.7(12)	4.9(10)	25.1(11)	4.0(11)
C32	43(3)	26(2)	27(2)	-3.5(18)	24(2)	-4.5(19)
C33	38(2)	23(2)	27(2)	-2.8(18)	20.5(19)	-4.6(19)
N34	42(2)	22.5(18)	27.7(18)	-3.9(15)	22.7(16)	-4.8(16)
C35	37(2)	18(2)	25(2)	-1.7(18)	19.3(19)	-3.3(19)

C36	39(2)	23(2)	28(2)	-4.6(18)	24(2)	-6.9(19)
O1W	53(2)	44(2)	76(2)	18.3(17)	43.0(19)	10.9(16)
O2W	64(2)	46(2)	49.0(19)	0.2(15)	45.5(18)	-2.1(16)

Bond lengths for 2,3,8,9,14,15- hexafluoro- 5,6,11,12,17,18- hexaazatrinaphthylene.

Atom	Atom	Length/Å	Atom	Atom	Length/Å
N1	C2	1.353(5)	C16	C18	1.412(6)
N1	C36	1.333(5)	C18	F19	1.339(4)
C2	C3	1.422(5)	C18	C20	1.346(5)
C2	C9	1.426(5)	C20	C21	1.421(5)
C3	C4	1.348(5)	C21	N22	1.357(5)
C4	F5	1.337(4)	N22	C23	1.329(5)
C4	C6	1.420(6)	C23	C24	1.470(5)
C6	F7	1.339(4)	C24	N25	1.332(5)
C6	C8	1.352(5)	C24	C35	1.430(5)
C8	C9	1.409(5)	N25	C26	1.354(5)
C9	N10	1.355(5)	C26	C27	1.428(5)
N10	C11	1.325(5)	C26	C33	1.425(5)
C11	C12	1.474(5)	C27	C28	1.343(5)
C11	C36	1.419(5)	C28	F29	1.354(4)
C12	N13	1.328(5)	C28	C30	1.415(5)
C12	C23	1.418(5)	C30	F31	1.349(4)
N13	C14	1.359(5)	C30	C32	1.352(5)
C14	C15	1.420(5)	C32	C33	1.405(5)
C14	C21	1.423(5)	C33	N34	1.367(5)
C15	C16	1.355(5)	N34	C35	1.321(5)
C16	F17	1.343(4)	C35	C36	1.485(5)

Bond angles for 2,3,8,9,14,15- hexafluoro- 5,6,11,12,17,18- hexaazatrinaphthylene.

Atom	Atom	Atom	Angle/^{o}	Atom	Atom	Atom	Angle/^{o}
C36	N1	C2	116.6(3)	C18	C20	C21	118.5(4)
N1	C2	C3	119.4(4)	C20	C21	C14	119.8(4)
N1	C2	C9	121.5(3)	N22	C21	C14	121.2(3)
C3	C2	C9	119.0(4)	N22	C21	C20	119.0(4)
C4	C3	C2	119.5(4)	C23	N22	C21	116.9(3)
C3	C4	C6	121.0(4)	C12	C23	C24	120.1(3)
F5	C4	C3	120.9(4)	N22	C23	C12	121.9(4)
F5	C4	C6	118.1(3)	N22	C23	C24	117.9(3)
F7	C6	C4	117.4(3)	N25	C24	C23	117.5(3)
F7	C6	C8	121.1(4)	N25	C24	C35	122.0(3)
C8	C6	C4	121.4(4)	C35	C24	C23	120.5(3)
C6	C8	C9	119.2(4)	C24	N25	C26	116.5(3)
C8	C9	C2	119.9(3)	N25	C26	C27	118.7(3)
N10	C9	C2	120.8(3)	N25	C26	C33	121.8(4)
N10	C9	C8	119.3(4)	C33	C26	C27	119.5(4)
C11	N10	C9	117.2(3)	C28	C27	C26	117.9(3)
N10	C11	C12	117.5(4)	C27	C28	F29	120.7(3)
N10	C11	C36	121.9(3)	C27	C28	C30	122.4(4)
C36	C11	C12	120.6(4)	F29	C28	C30	116.8(3)
N13	C12	C11	118.1(4)	F31	C30	C28	116.9(3)
N13	C12	C23	122.0(3)	F31	C30	C32	121.9(3)
C23	C12	C11	119.8(4)	C32	C30	C28	121.2(4)
C12	N13	C14	116.9(3)	C30	C32	C33	118.6(4)
N13	C14	C15	118.9(3)	C32	C33	C26	120.3(4)
N13	C14	C21	121.0(3)	N34	C33	C26	120.6(4)

C15	C14	C21	120.0(3)	N34	C33	C32	119.1(3)
C16	C15	C14	117.8(4)	C35	N34	C33	117.2(3)
C15	C16	C18	122.2(4)	C24	C35	C36	119.2(3)
F17	C16	C15	120.2(4)	N34	C35	C24	121.9(4)
F17	C16	C18	117.5(3)	N34	C35	C36	118.9(3)
F19	C18	C16	117.2(4)	N1	C36	C11	122.1(4)
F19	C18	C20	121.1(4)	N1	C36	C35	118.1(3)
C20	C18	C16	121.6(4)	C11	C36	C35	119.8(3)

Hydrogen bonds for 2,3,8,9,14,15- hexafluoro- 5,6,11,12,17,18- hexaazatrinaphthylene.

D	H	A	d(D−H)/Å	d(H−A)/Å	d(D−A)/Å	D−H−A/^{o}
O1W	H1WA	N10	0.850(4)	2.29(3)	2.975(4)	138(4)
O1W	H1W	O1W[1]	0.850(4)	1.984(8)	2.833(6)	176(7)
O2W	H2WB	N22	0.849(4)	2.26(3)	2.981(4)	143(4)
O2W	H2WA	O2W[2]	0.850(4)	1.98(5)	2.697(6)	142(7)
O2W	H2W	O2W[3]	0.850(5)	1.842(9)	2.687(6)	172(5)

[1]1-X,3-Y,1-Z; [2]3/2-X,1/2-Y,1-Z; [3]3/2-X,3/2-Y,1-Z

Torsion angles for 2,3,8,9,14,15- hexafluoro- 5,6,11,12,17,18- hexaazatrinaphthylene.

A	B	C	D	Angle/^{o}	A	B	C	D	Angle/^{o}
N1	C2	C3	C4	-178.7(3)	F17	C16	C18	F19	2.6(5)
N1	C2	C9	C8	179.6(4)	F17	C16	C18	C20	179.7(3)
N1	C2	C9	N10	-1.9(6)	C18	C20	C21	C14	-1.3(6)
C2	N1	C36	C11	0.2(5)	C18	C20	C21	N22	180.0(3)
C2	N1	C36	C35	-178.3(3)	F19	C18	C20	C21	178.1(3)
C2	C3	C4	F5	178.5(3)	C20	C21	N22	C23	-179.9(3)

C2	C3	C4	C6	0.3(6)	C21	C14	C15	C16	-1.6(6)
C2	C9	N10	C11	2.9(5)	C21	N22	C23	C12	-2.6(5)
C3	C2	C9	C8	1.8(5)	C21	N22	C23	C24	179.9(3)
C3	C2	C9	N10	-179.7(3)	N22	C23	C24	N25	-2.4(5)
C3	C4	C6	F7	-180.0(3)	N22	C23	C24	C35	179.3(3)
C3	C4	C6	C8	-0.7(6)	C23	C12	N13	C14	-1.1(5)
C4	C6	C8	C9	1.6(6)	C23	C24	N25	C26	-179.6(3)
F5	C4	C6	F7	1.8(5)	C23	C24	C35	N34	179.6(3)
F5	C4	C6	C8	-178.9(3)	C23	C24	C35	C36	-1.1(5)
C6	C8	C9	C2	-2.1(6)	C24	N25	C26	C27	179.6(3)
C6	C8	C9	N10	179.3(3)	C24	N25	C26	C33	1.6(5)
F7	C6	C8	C9	-179.1(3)	C24	C35	C36	N1	179.5(3)
C8	C9	N10	C11	-178.5(3)	C24	C35	C36	C11	1.0(5)
C9	C2	C3	C4	-0.8(6)	N25	C24	C35	N34	1.3(6)
C9	N10	C11	C12	178.5(3)	N25	C24	C35	C36	-179.3(3)
C9	N10	C11	C36	-2.5(6)	N25	C26	C27	C28	-178.9(3)
N10	C11	C12	N13	-0.9(5)	N25	C26	C33	C32	179.6(3)
N10	C11	C12	C23	-178.7(3)	N25	C26	C33	N34	-1.9(6)
N10	C11	C36	N1	0.9(6)	C26	C27	C28	F29	178.9(3)
N10	C11	C36	C35	179.5(3)	C26	C27	C28	C30	1.5(6)
C11	C12	N13	C14	-178.9(3)	C26	C33	N34	C35	1.8(5)
C11	C12	C23	N22	-179.7(3)	C27	C26	C33	C32	1.6(6)
C11	C12	C23	C24	-2.3(5)	C27	C26	C33	N34	-179.9(3)
C12	C11	C36	N1	179.9(3)	C27	C28	C30	F31	178.1(3)
C12	C11	C36	C35	-1.5(5)	C27	C28	C30	C32	-3.0(6)
C12	N13	C14	C15	179.6(3)	C28	C30	C32	C33	3.6(6)
C12	N13	C14	C21	0.0(5)	F29	C28	C30	F31	0.6(5)
C12	C23	C24	N25	-179.9(3)	F29	C28	C30	C32	179.5(3)

C12	C23	C24	C35	1.8(5)	C30	C32	C33	C26	-2.9(6)
N13	C12	C23	N22	2.5(6)	C30	C32	C33	N34	178.5(3)
N13	C12	C23	C24	180.0(3)	F31	C30	C32	C33	-177.6(3)
N13	C14	C15	C16	178.8(3)	C32	C33	N34	C35	-179.7(3)
N13	C14	C21	C20	-178.8(3)	C33	C26	C27	C28	-0.9(6)
N13	C14	C21	N22	-0.1(6)	C33	N34	C35	C24	-1.5(5)
C14	C15	C16	F17	-179.5(3)	C33	N34	C35	C36	179.1(3)
C14	C15	C16	C18	1.4(6)	N34	C35	C36	N1	-1.1(5)
C14	C21	N22	C23	1.4(5)	N34	C35	C36	C11	-179.6(3)
C15	C14	C21	C20	1.5(6)	C35	C24	N25	C26	-1.3(5)
C15	C14	C21	N22	-179.8(3)	C36	N1	C2	C3	178.0(3)
C15	C16	C18	F19	-178.4(3)	C36	N1	C2	C9	0.3(5)
C15	C16	C18	C20	-1.2(6)	C36	C11	C12	N13	-180.0(3)
C16	C18	C20	C21	1.1(6)	C36	C11	C12	C23	2.2(6)

Hydrogen Atom Coordinates (Å$\times 10^4$) and Isotropic Displacement Parameters (Å$^2\times 10^3$) for 2,3,8,9,14,15- hexafluoro- 5,6,11,12,17,18- hexaazatrinaphthylene.

Atom	x	y	z	U(eq)
H3	6107.2	3489.94	7500.49	36
H8	5178.34	10649.7	6276.04	37
H15	5453.95	13986.83	4549.4	36
H20	6633.56	9568.13	4399.43	36
H27	7800.34	478.78	5900.97	34
H32	7602.52	-2110.06	7305.68	34
H1WA	5326(5)	12150(110)	5491(18)	79
H1W	5030(18)	14030(160)	5140(30)	79
H2WB	7129(12)	5060(100)	5095(13)	68
H2WA	7487(16)	3920(160)	5090(20)	68

H2W	7400(30)	6660(90)	4980(30)	68

Atomic occupancy for 2,3,8,9,14,15- hexafluoro- 5,6,11,12,17,18- hexaazatrinaphthylene.

Atom	Occupancy	Atom	Occupancy	Atom	Occupancy
H1W	0.5	H2WA	0.5	H2W	0.5

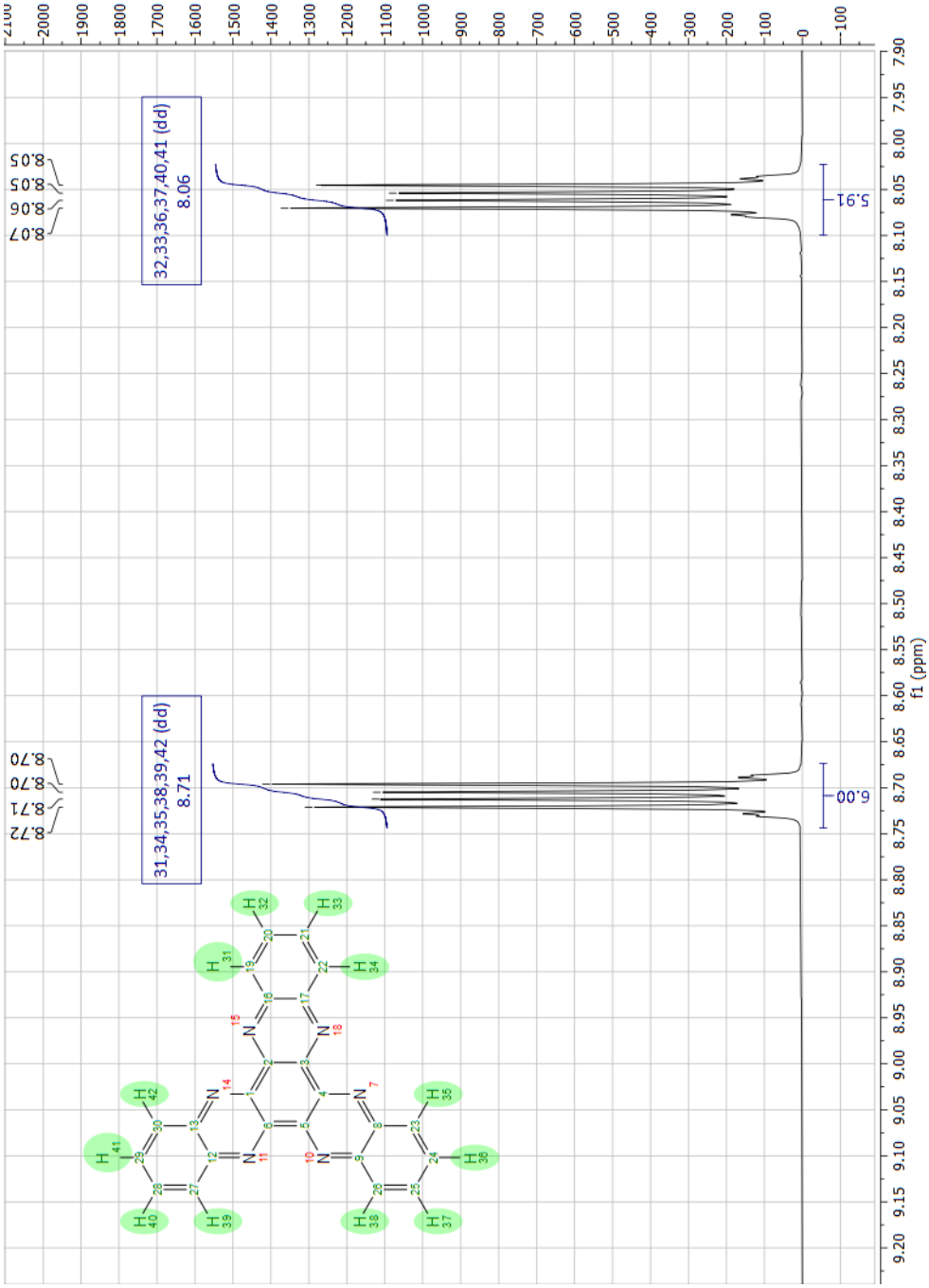

Figure 3.31. Proton NMR for 5,6,11,12,17,18- hexaazatrinaphthylene.

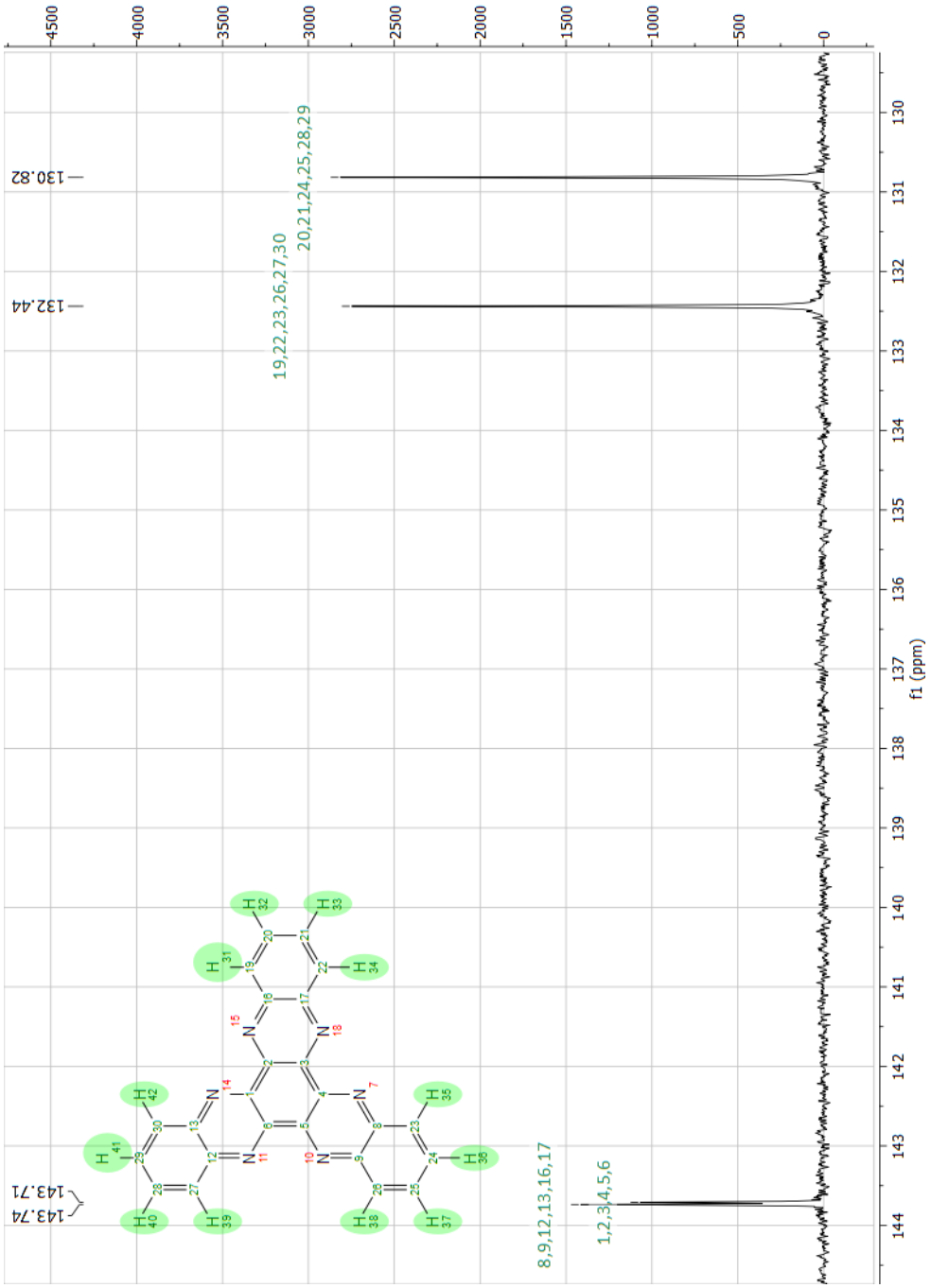

Figure 3.32. Carbon (proton-decoupled) NMR for 5,6,11,12,17,18- hexaazatrinaphthylene.

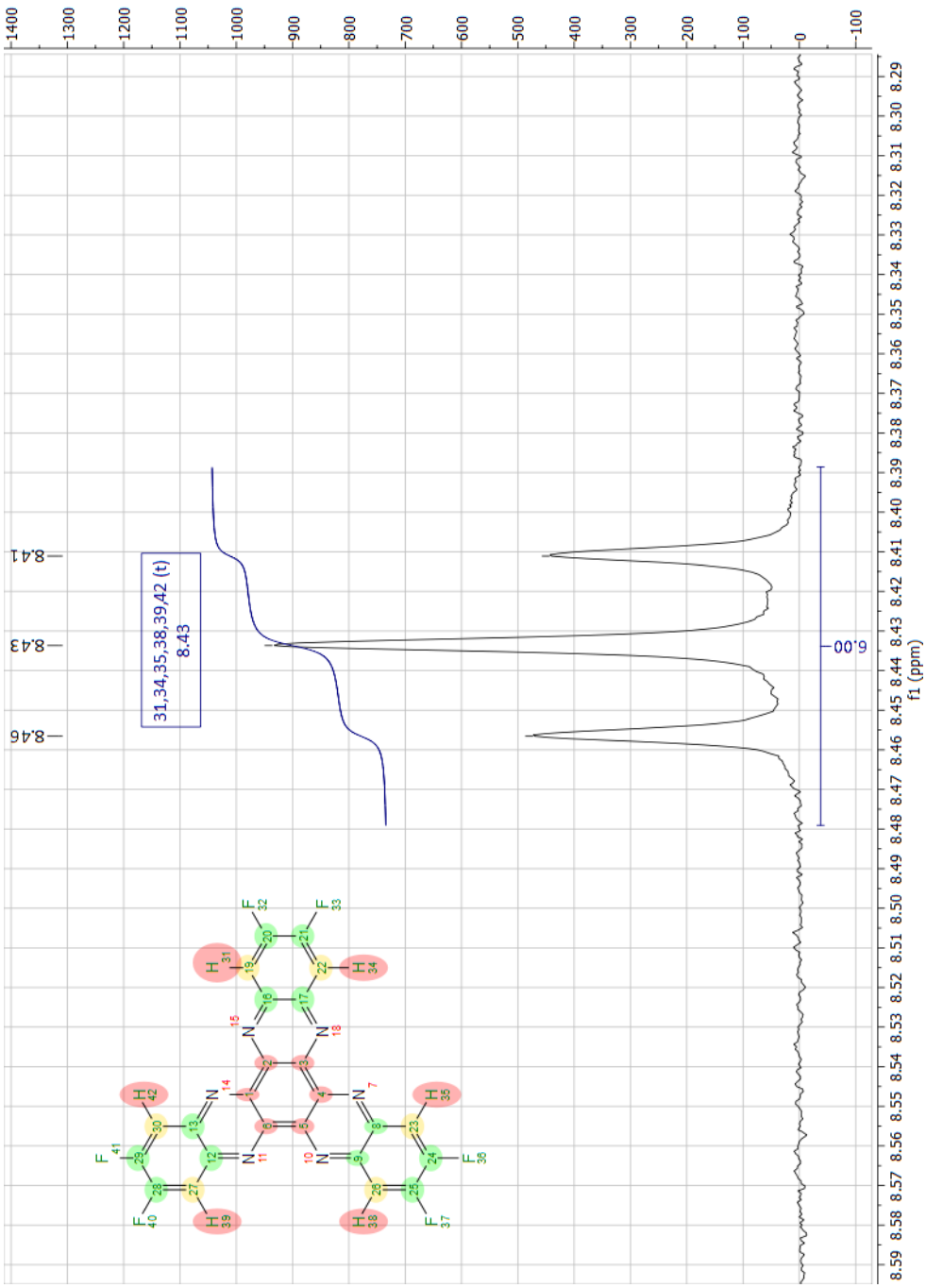

Figure 3.33. Proton NMR for 2,3,8,9,14,15- hexafluoro- 5,6,11,12,17,18- hexaazatrinaphthylene.

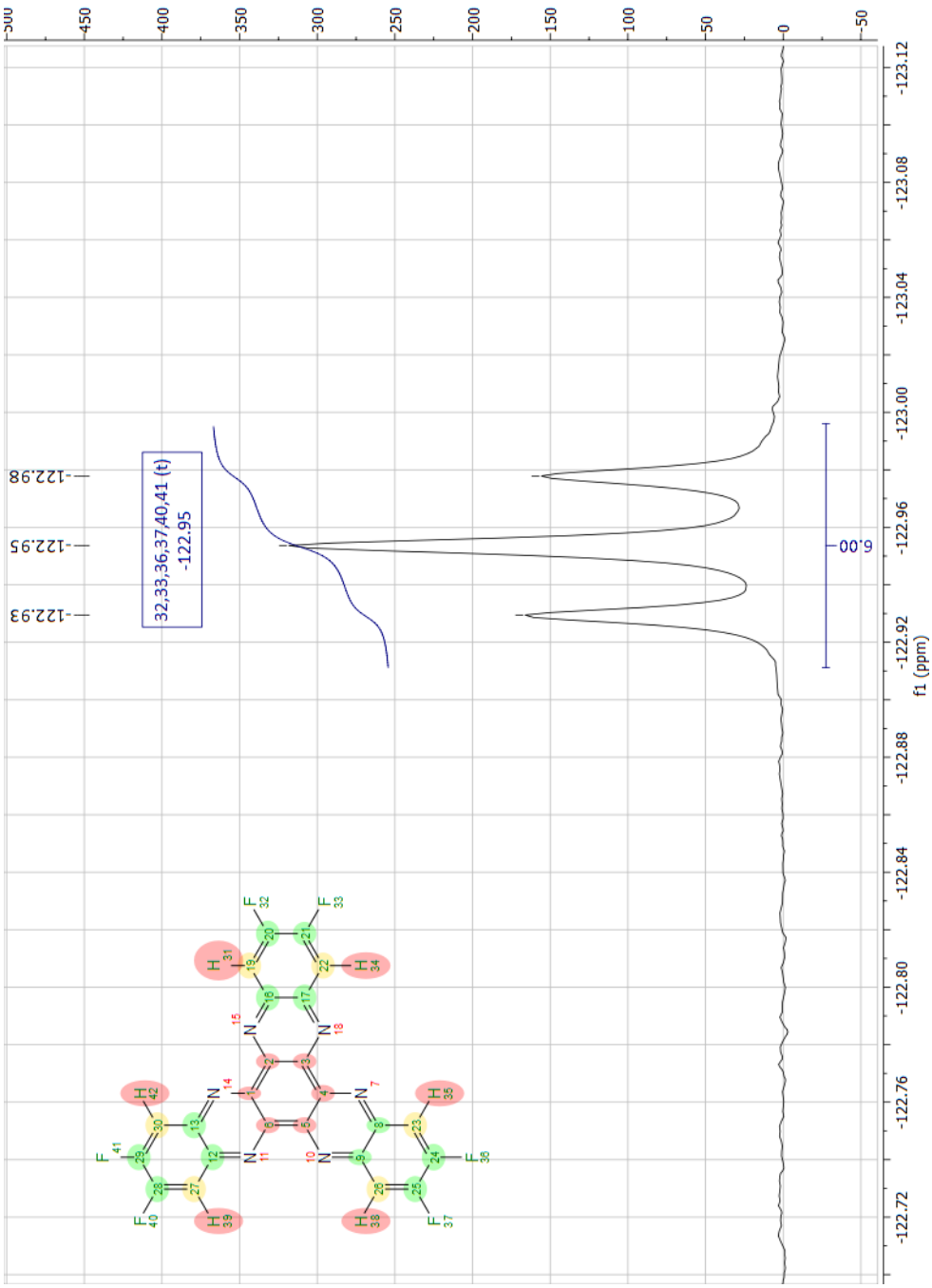

Figure 3.34. Fluorine NMR for 2,3,8,9,14,15- hexafluoro- 5,6,11,12,17,18- hexaazatrinaphthylene.

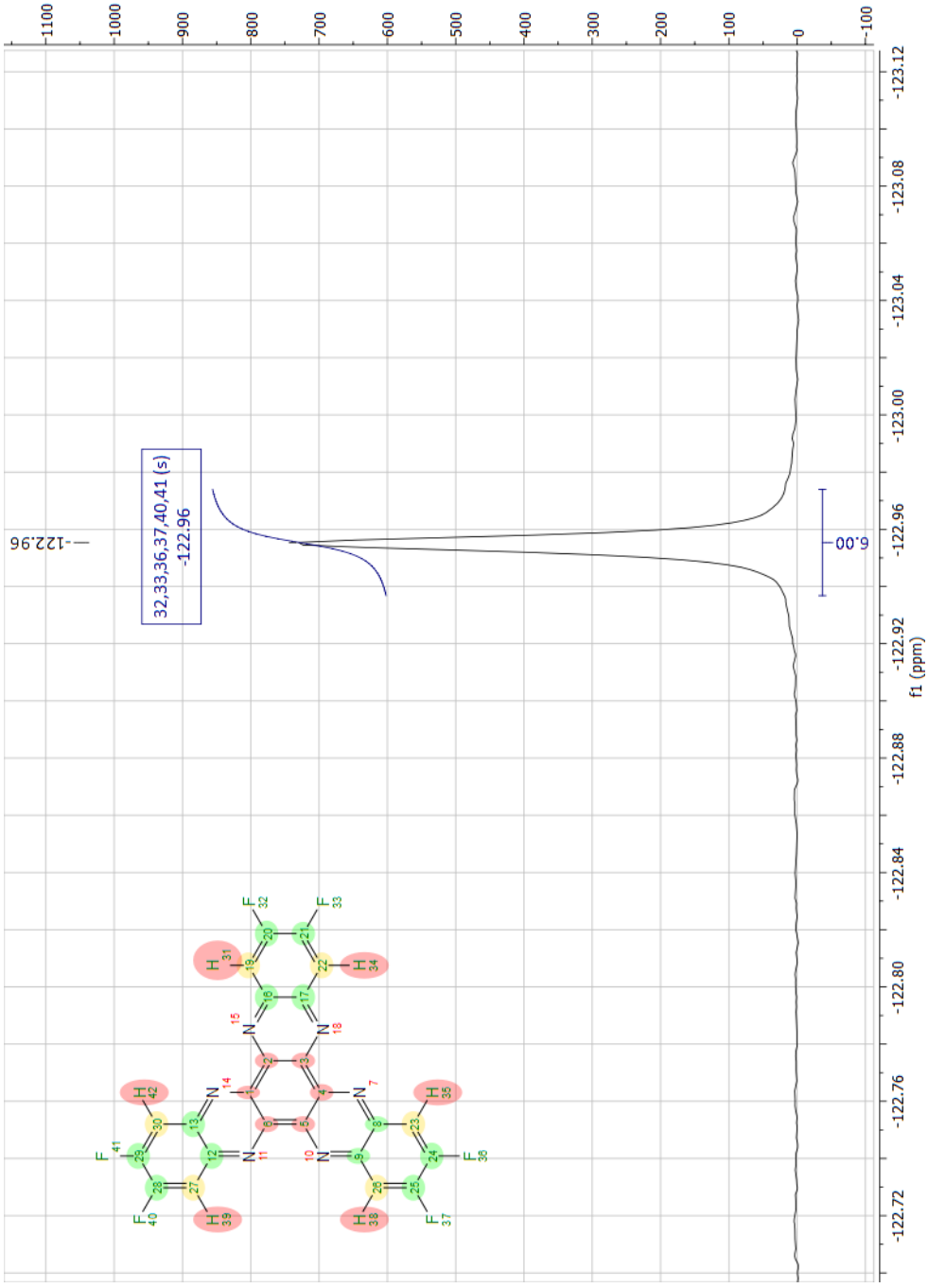

Figure 3.35. Proton-decoupled fluorine NMR for 2,3,8,9,14,15- hexafluoro- 5,6,11,12,17,18- hexaazatrinaphthylene.

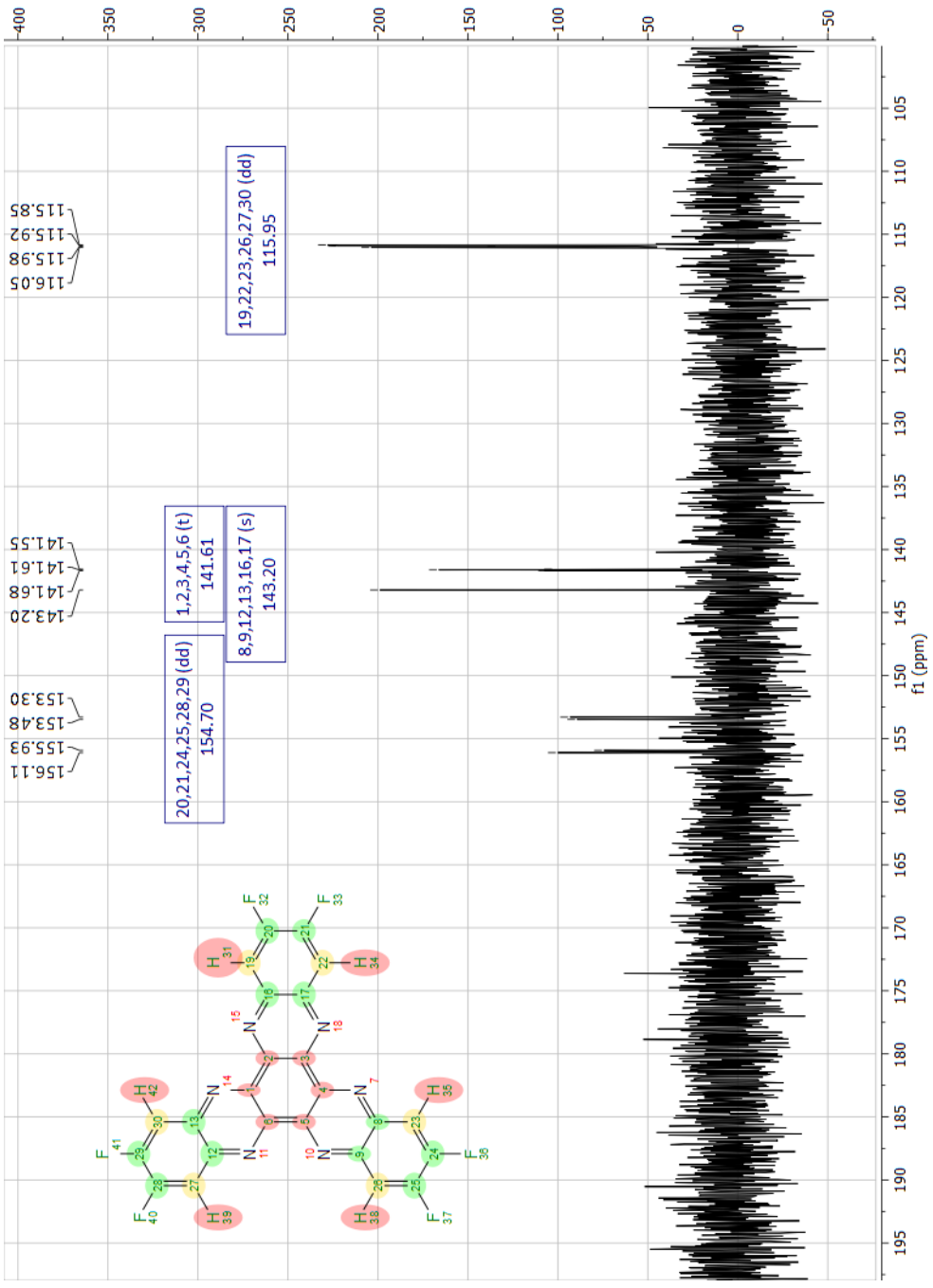

Figure 3.36. Carbon (proton-decoupled) NMR for 2,3,8,9,14,15- hexafluoro- 5,6,11,12,17,18- hexaazatrinaphthylene.

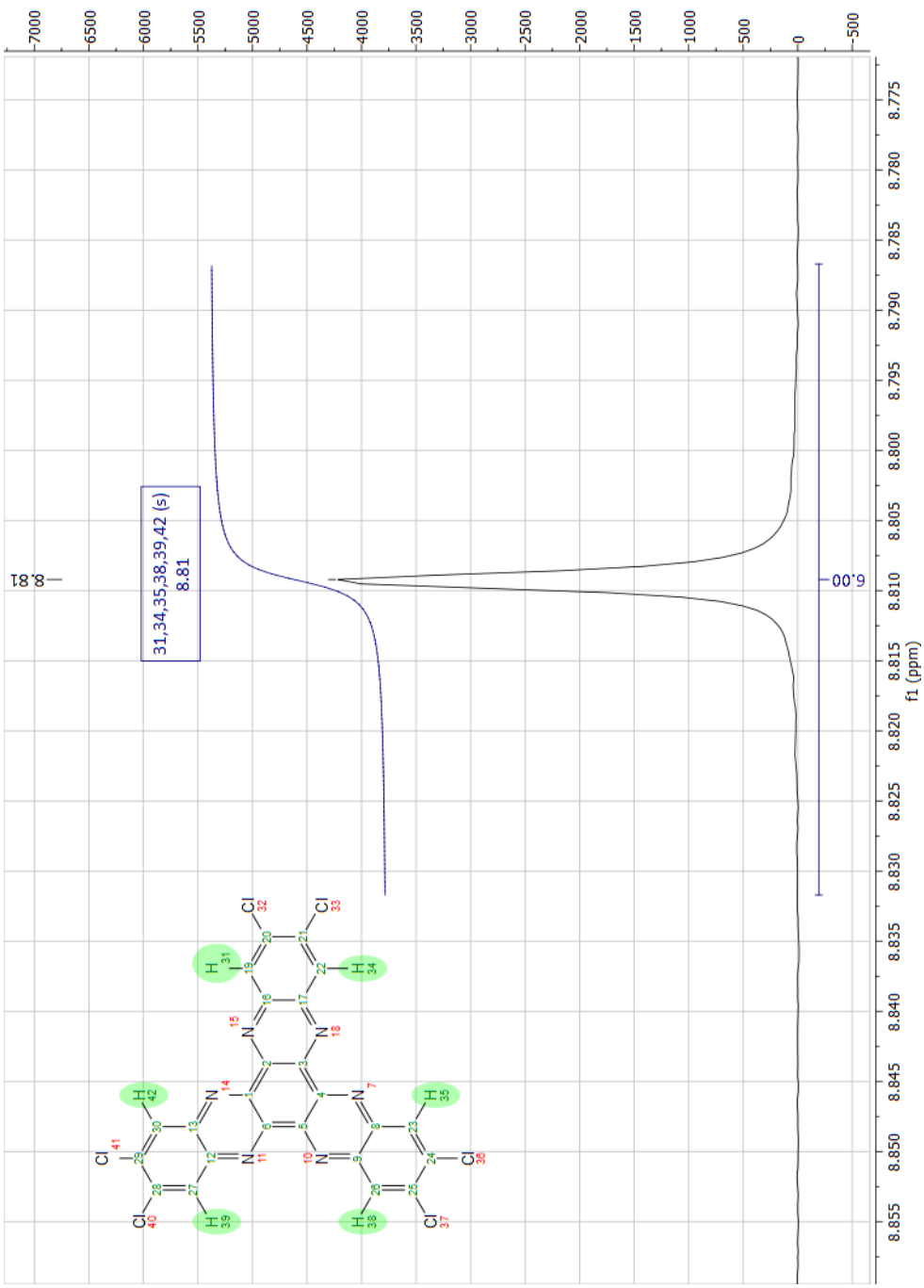

Figure 3.37. Proton NMR for 2,3,8,9,14,15- hexachloro- 5,6,11,12,17,18- hexaazatrinaphthylene.

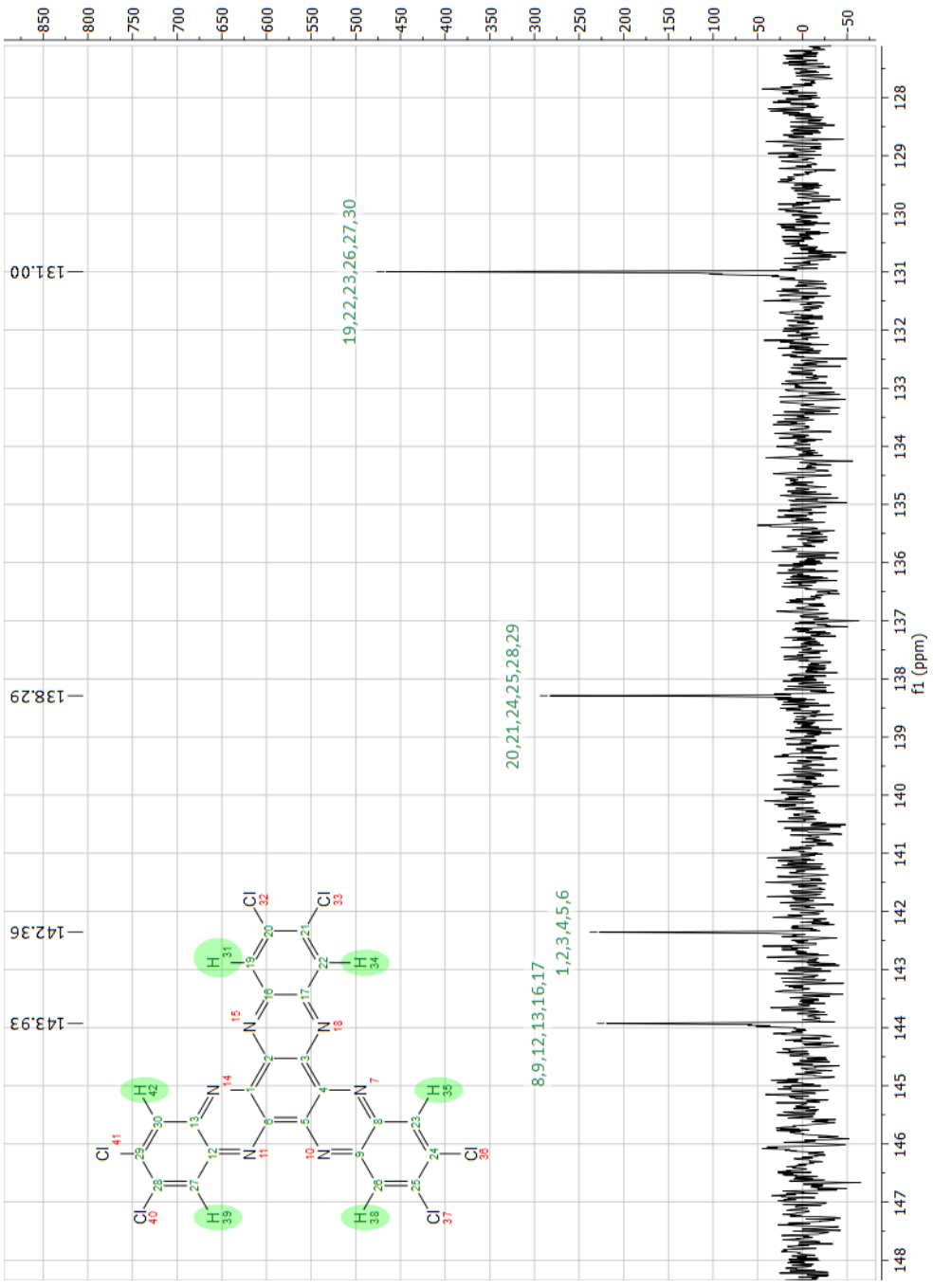

Figure 3.38. Carbon (proton-decoupled) NMR for 2,3,8,9,14,15- hexachloro- 5,6,11,12,17,18- hexaazatrinaphthylene.

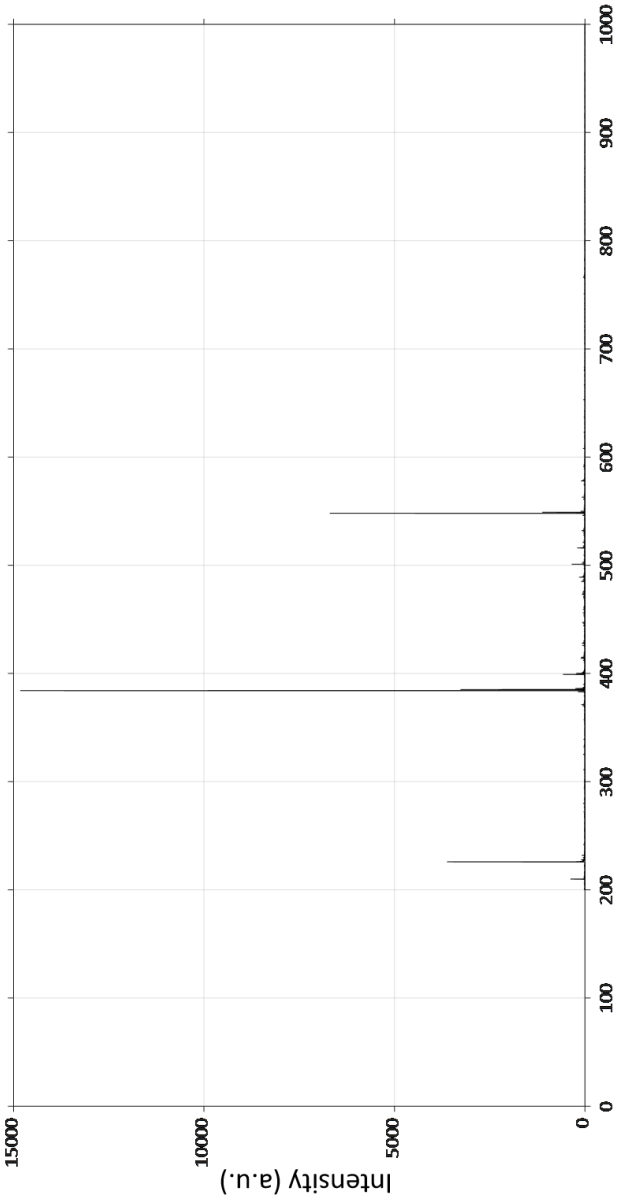

Figure 3.39. MALDI-ToF MS for 5,6,11,12,17,18- hexaazatrinaphthylene.

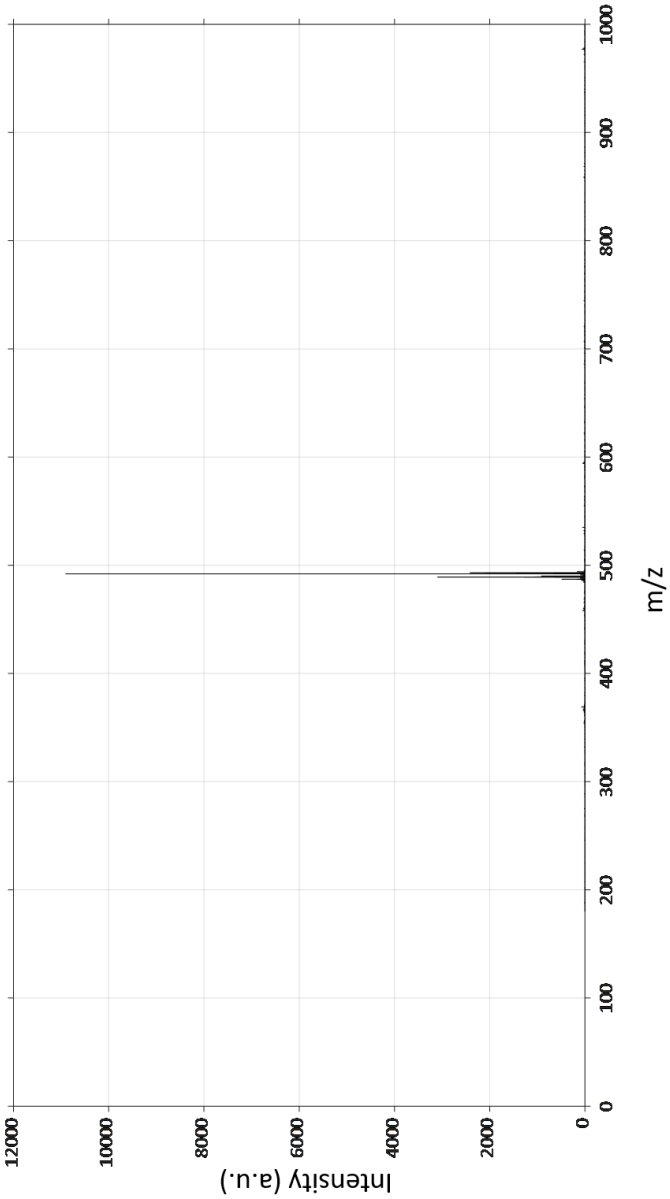

Figure 3.40. MALDI-ToF MS for 2,3,8,9,14,15- hexafluoro- 5,6,11,12,17,18- hexaazatrinaphthylene.

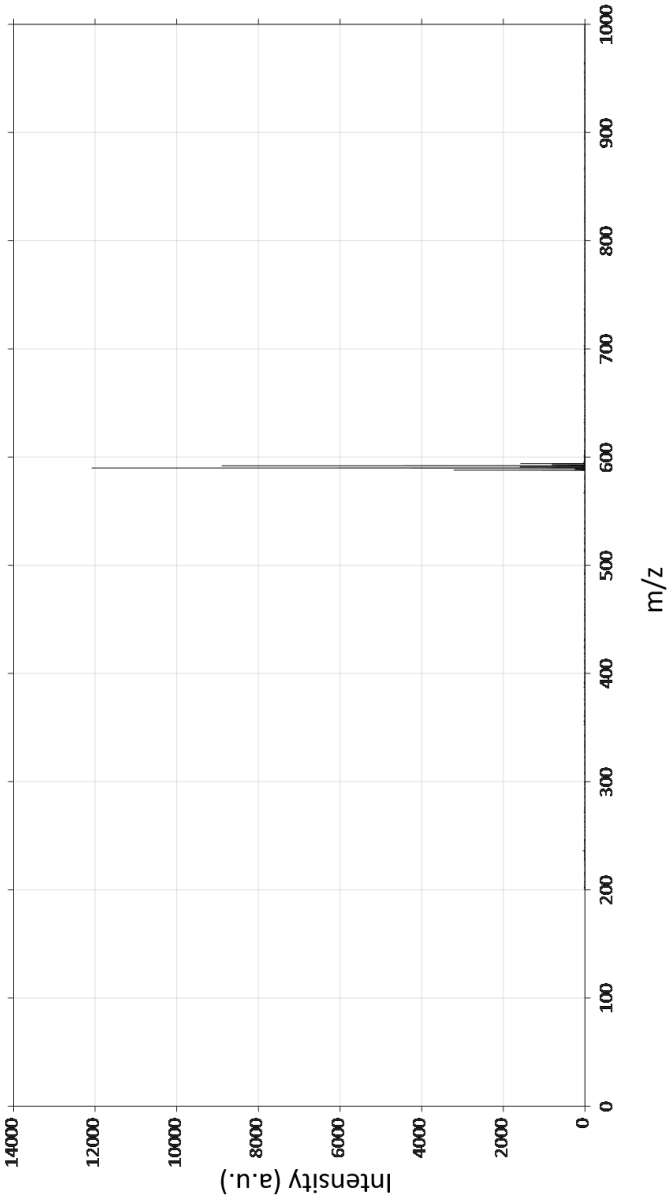

Figure 3.41. MALDI-ToF MS for 2,3,8,9,14,15- hexachloro- 5,6,11,12,17,18- hexaazatrinaphthylene.

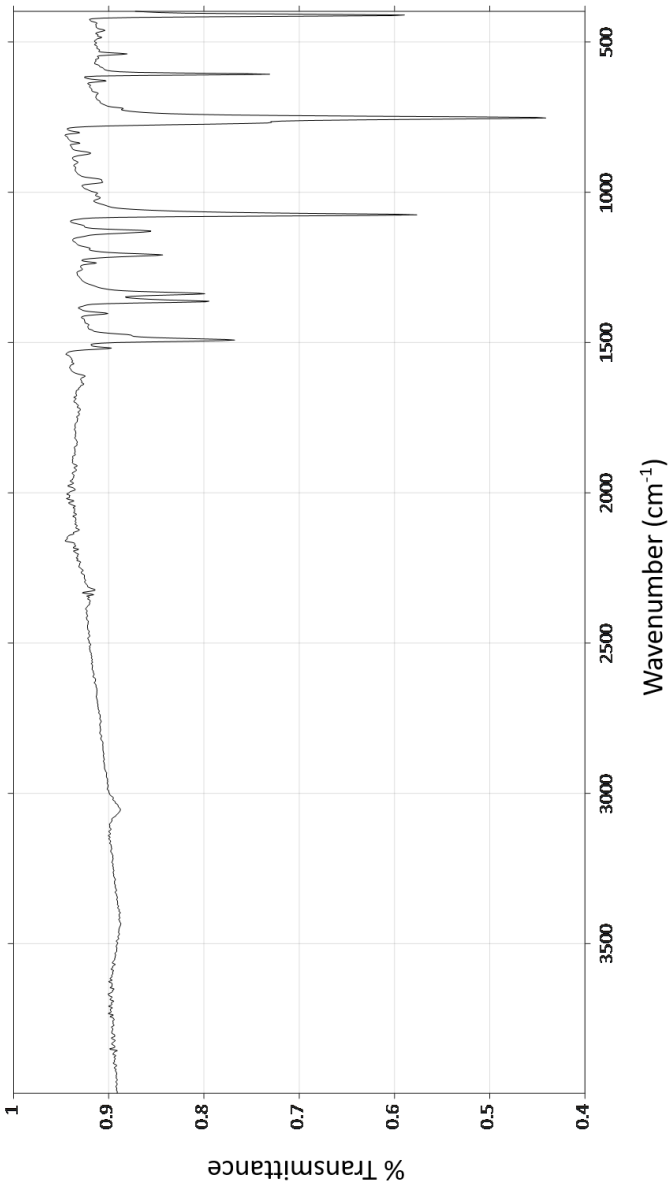

Figure 3.42. IR for 5,6,11,12,17,18- hexaazatrinaphthylene.

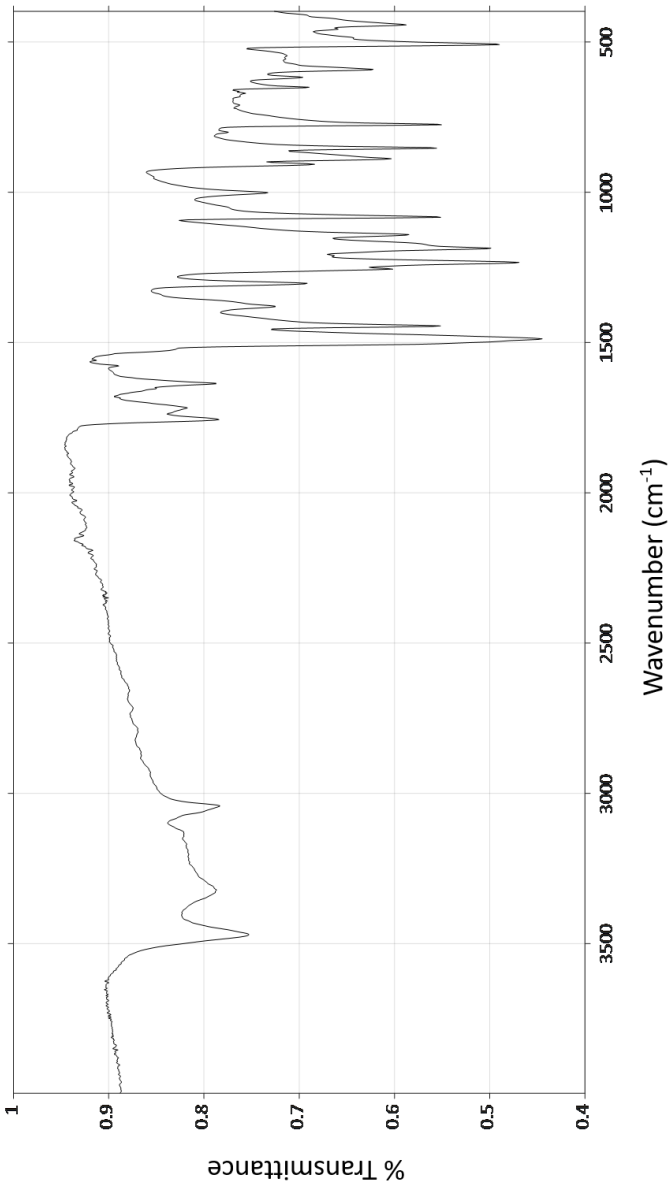

Figure 3.43. IR for 2,3,8,9,14,15- hexafluoro- 5,6,11,12,17,18- hexaazatrinaphthylene.

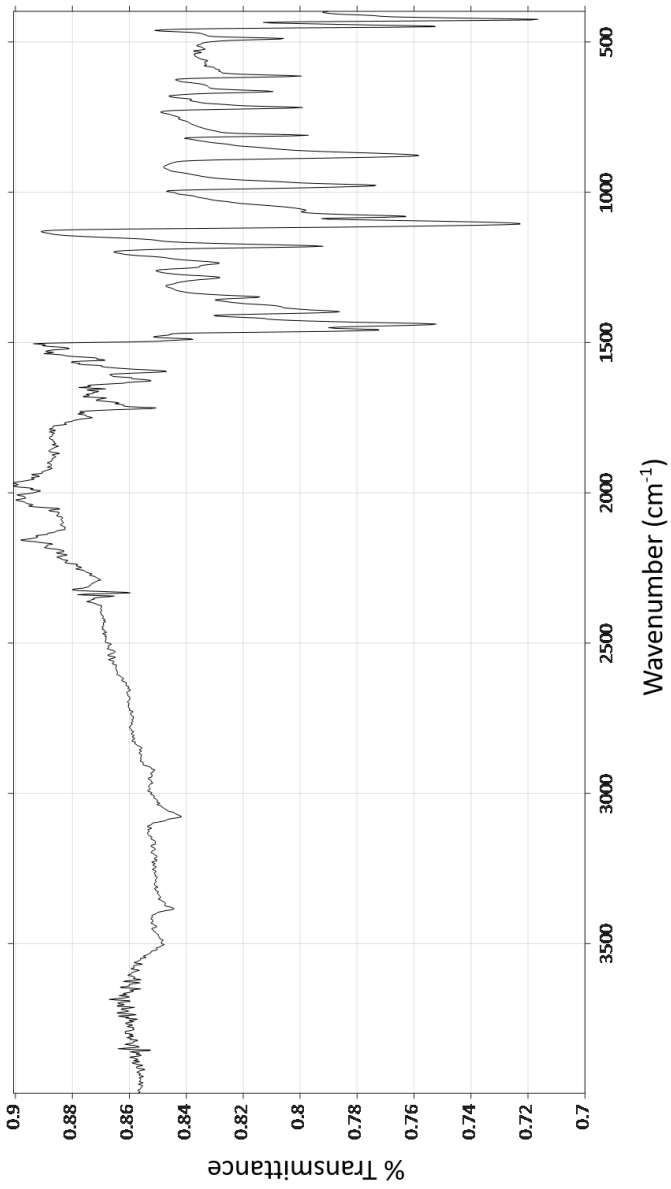

Figure 3.44. IR for 2,3,8,9,14,15- hexachloro- 5,6,11,12,17,18- hexaazatrinaphthylene.

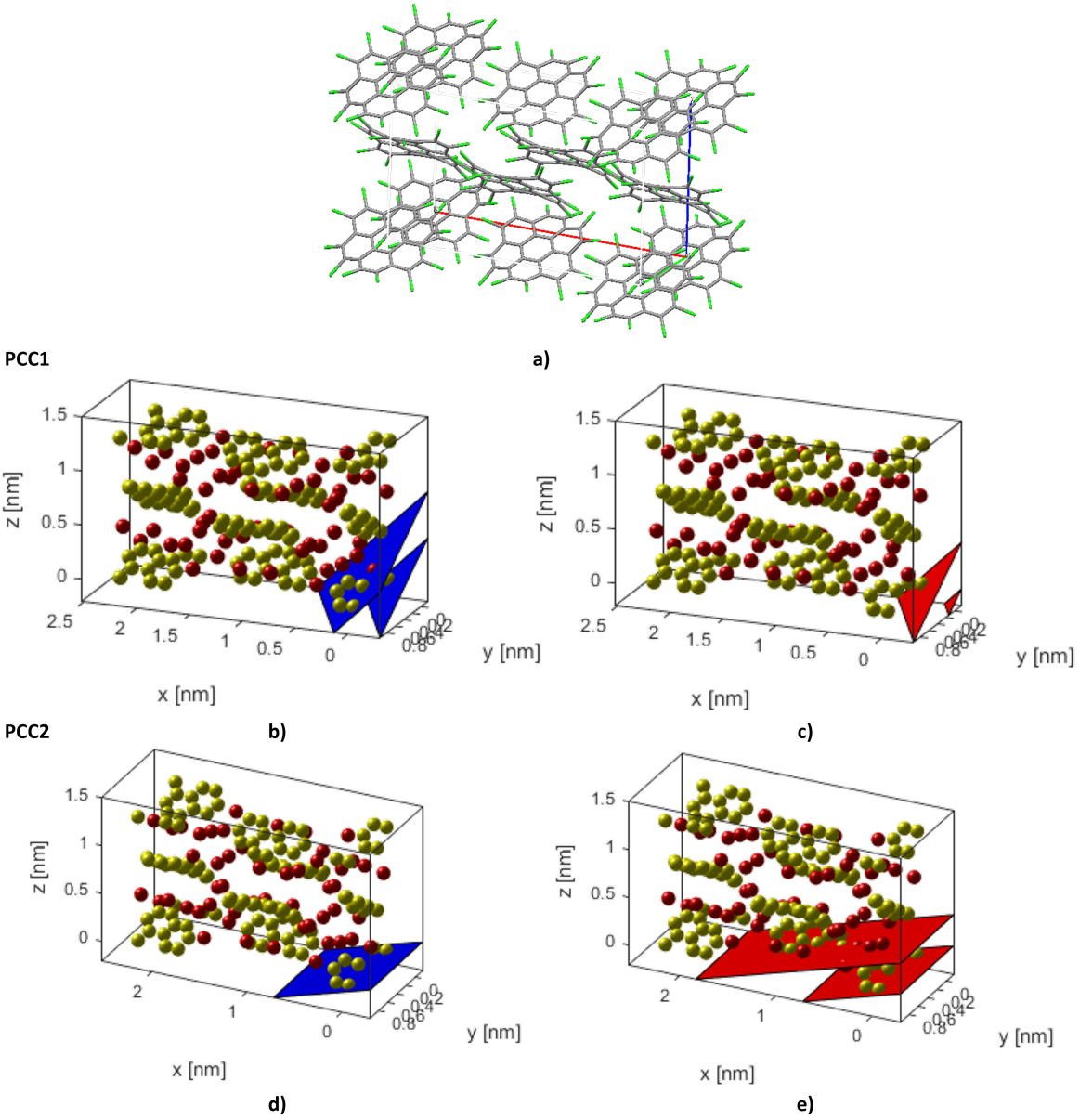

Figure 3.45. a) The unit cell of perchlorocoronene (PCC).[33] b) and c) The unit cell of PCC with the same orientation as a) where blue corresponds to the (5 1 3) plane and red corresponds to the (-5 -1 -3) plane. These planes correspond to the tracked pair of diffraction spots for the PCC1 crystal (Fig. 3.8). d) and e) The unit cell of PCC with the same orientation as a) where blue corresponds to the (-2 0 -4) plane and red corresponds to the (2 0 4) plane. These planes correspond to the tracked pair of diffraction spots for the PCC2 crystal (Fig. 3.9). Images were generated by the cellViewer program in CrysTBox. The assignments for PCC1 and PCC2 were carried out using the diffractGUI program in CrysTBox, giving a d-spacing standard deviation of 0.0013 and 0.0023, and structural factor deviations (R-square values) of 0.9816 and 1.0000 respectively.

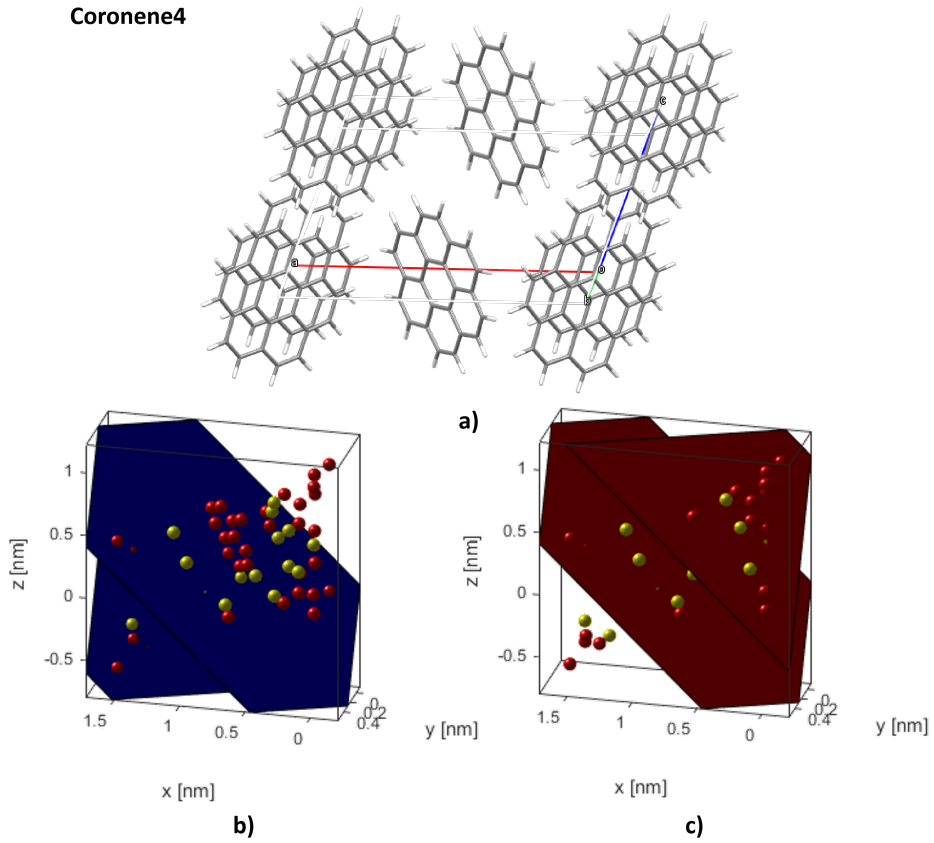

Figure 3.46. a) The unit cell of coronene.[34] b) and c) The unit cell of coronene with the same orientation as a) where blue corresponds to the (2 -1 -1) plane and red corresponds to the (-2 1 1) plane. These planes correspond to the tracked pair of diffraction spots for the coronene4 crystal (Fig. 3.15). Images were generated by the cellViewer program in CrysTBox. The assignments for coronene4 were carried out using the diffractGUI program in CrysTBox, giving a d-spacing standard deviation of 0.0016 and a structural factor deviation (R-square value) of 0.9814.

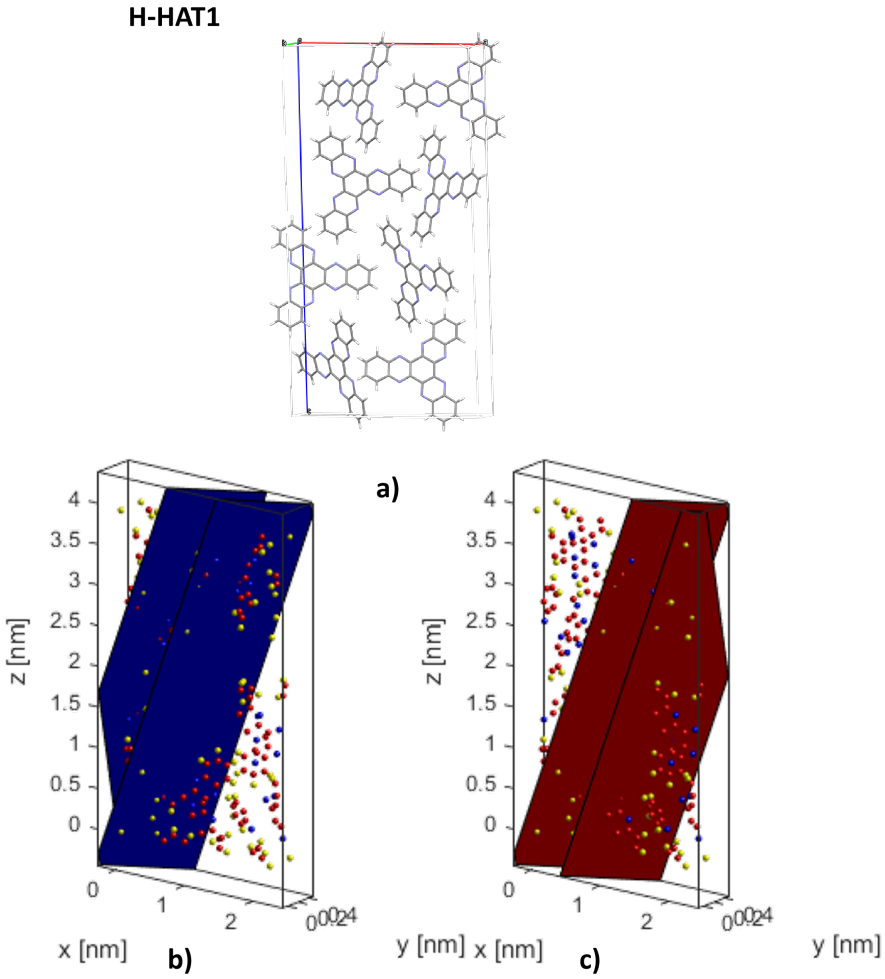

Figure 3.47. a) The unit cell of 5,6,11,12,17,18- hexaazatrinaphthylene (H-HAT) solved by S. Argent (X-ray Crystallography Service Manager at the University of Nottingham). b) and c) The unit cell of H-HAT with the same orientation as a) where blue corresponds to the (-3 1 2) plane and red corresponds to the (3 -1 -2) plane. These planes correspond to the tracked pair of diffraction spots for the H-HAT1 crystal (Fig. 3.19). Images were generated by the cellViewer program in CrysTBox. The assignments for H-HAT1 were carried out using the diffractGUI program in CrysTBox, giving a d-spacing standard deviation of 0.0042 and a structural factor deviation (R-square value) of 0.9119.

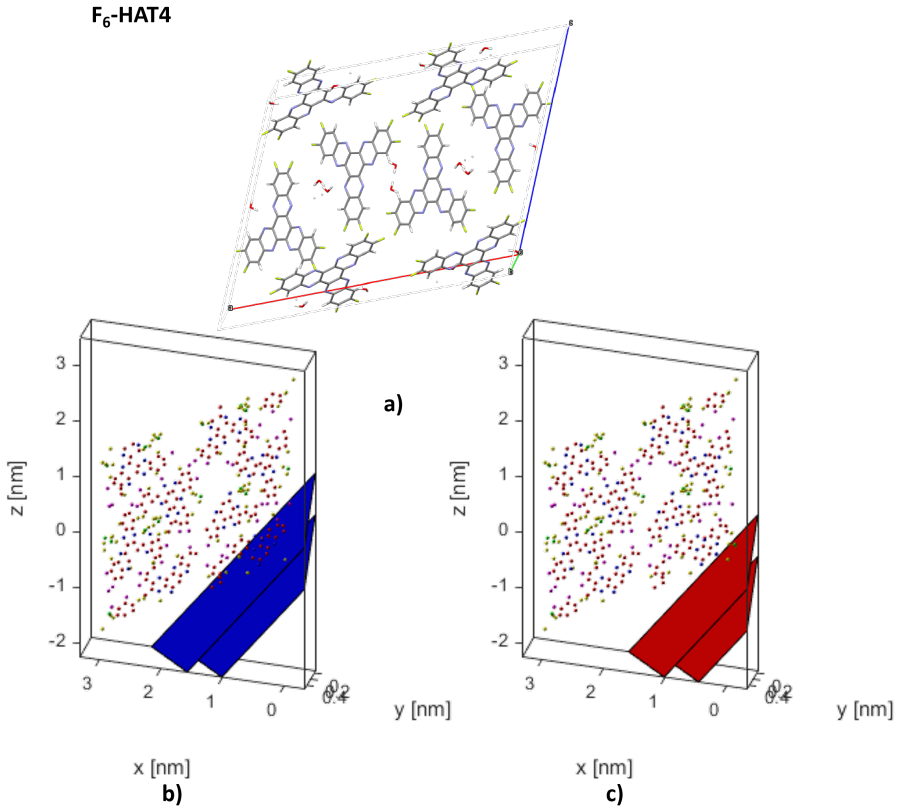

Figure 3.48. a) The unit cell of 2,3,8,9,14,15- hexafluoro- 5,6,11,12,17,18-hexaazatrinaphthylene (F_6-HAT) solved by S. Argent (X-ray Crystallography Service Manager at the University of Nottingham). b) and c) The unit cell of F_6-HAT with the same orientation as a) where blue corresponds to the (3 1 4) plane and red corresponds to the (-3 -1 -4) plane. These planes correspond to the tracked pair of diffraction spots for the F_6-HAT4 crystal (Fig. 3.24). Images were generated by the cellViewer program in CrysTBox. The assignments for F_6-HAT4 were carried out using the diffractGUI program in CrysTBox, giving a d-spacing standard deviation of 0.0014 and a structural factor deviation (R-square value) of 0.9253.

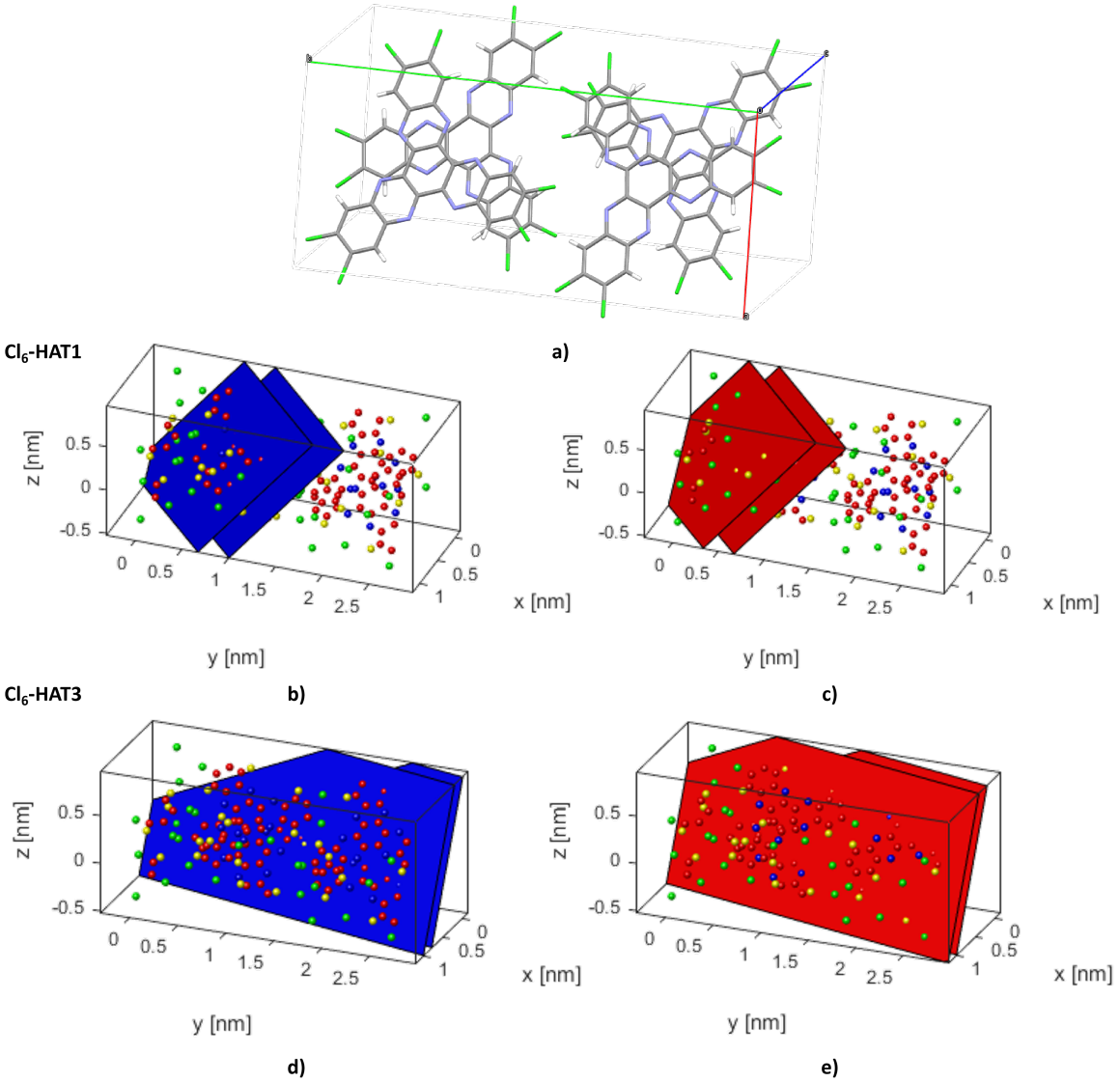

Figure 3.49. a) The unit cell of 2,3,8,9,14,15- hexachloro- 5,6,11,12,17,18-hexaazatrinaphthylene.[1] b) and c) The unit cell of Cl_6-HAT with the same orientation as a) where blue corresponds to the (-2 8 -2) plane and red corresponds to the (2 -8 2) plane. d) and e) The unit cell of Cl_6-HAT with the same orientation as a) where blue corresponds to the (-4 3 -2) plane and red corresponds to the (4 -3 2) plane. Images were generated by the cellViewer program in CrysTBox. The assignments for Cl_6-HAT1 and Cl_6-HAT3 were carried out using the diffractGUI program in CrysTBox, giving d-spacing standard deviations of 0.0026 and 0.0009 and structural factor deviations (R-square values) of 0.8722 and 0.9680 respectively.

CHAPTER 4

Endohedral fullerene HF@C_{60}

4.1 Introduction

Having mentioned endohedral fullerenes with brevity in the first chapter, we shall now discuss what endohedral fullerenes are, how they are synthesised, what examples exist in the literature, and finally why there has been such prolific interest in these materials. Endohedral fullerenes are fullerene cages that contain an encapsulated moiety inside, whether it be a single atom or a molecule. Heath *et al.* discovered that the C_{60} fullerene[1] could encapsulate a lanthanum atom in its cavity when lanthanum-impregnated graphite was vaporised with a laser.[2] Many endohedral fullerenes containing metals can be made by vaporising the carbon and metal together. For example, scandium endohedral fullerenes ($Sc_2@C_{74}$, $Sc_2@C_{82}$, and $Sc_2@C_{84}$) were first isolated by Shinohara *et al.* and characterised using mass spectrometry and UV-vis spectroscopy.[3] Electron paramagnetic resonance (EPR) can also be used for systems with unpaired electrons, such as $Sc@C_{82}$ and $Sc_3@C_{82}$.[4,5] Experimental and theoretical studies have shown that the metal atom is off-centre and closer to the carbon atoms, indicating a strong metal-cage interaction.[6] Once bulk syntheses of fullerenes[7] and endohedral fullerenes[8] were possible through laser-vaporisation and arc techniques, research groups across the globe carried out extensive studies with vim and vigour.[9–13]

Noble gases (helium and neon)[14] and metal clusters (such as metal carbides, nitrides, oxides and sulfides)[15–18] have also been encapsulated inside fullerenes as well as the nitrogen atom in the fascinating molecule of endohedral N@C_{60}.[19,20] Almeida Murphy *et al.* produced this endohedral fullerene by bombarding a C_{60} substrate with nitrogen ions from a conventional plasma discharge ion source. EPR showed hyperfine splitting due to atomic ^{14}N (dominant triplet from a nuclear spin of I = 1) and ^{15}N (weak doublet from a nuclear spin of I = 1/2) at intensities consistent with the natural abundance of the two N isotopes.

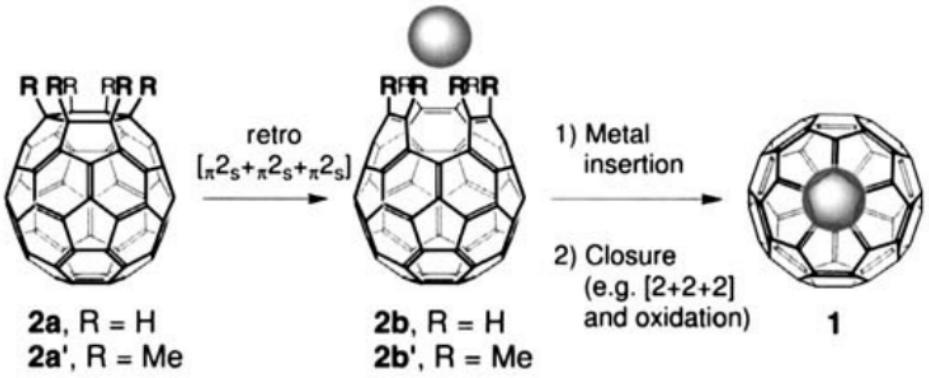

Figure 4.1. Conceptual procedure proposed by Rubin *et al.* for the opening and closing of a C_{60} fullerene to form endohedral metallofullerenes.[21]

Gas-phase synthesis of endohedral fullerenes, either through vaporisation of graphite rods containing metals or ion implantation, generally have yields on the milligram scale and produce complex mixtures of empty fullerenes as well as a range of endohedral fullerenes. These mixtures are typically separated using high-performance liquid chromatography in multiple steps which requires a large volume of organic solvents so alternative approaches in developing synthetic-organic routes have been explored in order to increase yields and purity. Rubin described conceptually two possible ways to insert metals inside a fullerene; either by cracking open the cage or zipping up fullerene precursors.[21] Both have their own challenges but have the potential to give access to a wider variety of endohedral fullerenes than graphite evaporation. Creating a hole in the fullerene cage could be achieved

through a retro $[2+2+2]$ cycloaddition reaction of a hexahydrofullerene $C_{60}H_6$ (Fig. 4.1 **2a**) to give the opened form (Fig. 4.1 **2b**). If this is complexed to a metal atom via three HC=CH π bonds, the hole is then enlarged which allows the metal atom inside the fullerene (Fig. 4.1 **1**). There is a strong thermodynamic driving force for metal insertion because the metal atom binds strongly to the inside of the fullerene surface. Using more sterically demanding groups such as methyls (Fig. 4.1 **2a'**) instead of hydrogens could increase the size of the cavity and therefore lead to easier insertion of metals into fullerenes. Endohedral fullerenes could be formed from these fullerene precursors under conditions such as flash vacuum pyrolysis or solution-phase catalysis.

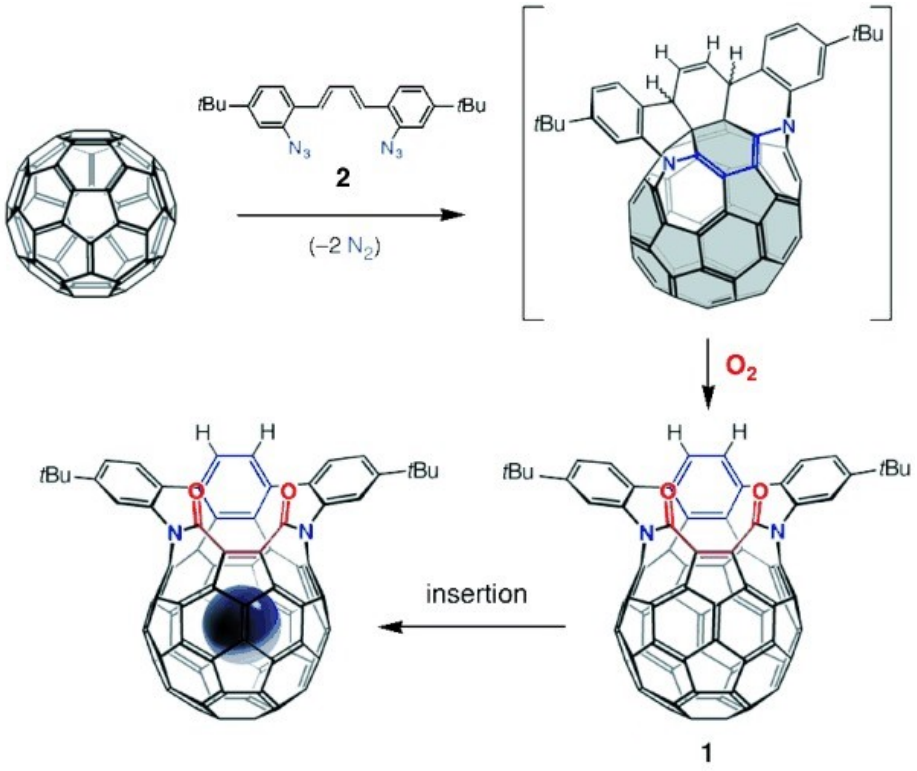

Figure 4.2. Synthesis of the "opened" fullerene bislactam **1** via a reaction with the bisazide **2**. He and H_2 can then be inserted through the hole into the cavity of the C_{60}.[22]

Rubin *et al.* used this "molecular surgery" approach to introduce helium and molecular hydrogen through the hole into the cavity of a fullerene.[22] The C_{60} fullerene was functionalised to give the "opened" bislactam derivative (Fig. 4.2 **1**). Overall insertion of He and H_2 was calculated to be slightly endothermic (0.2-1.4 kcal mol^{-1}) and therefore would require heating and higher pressures to drive insertion.

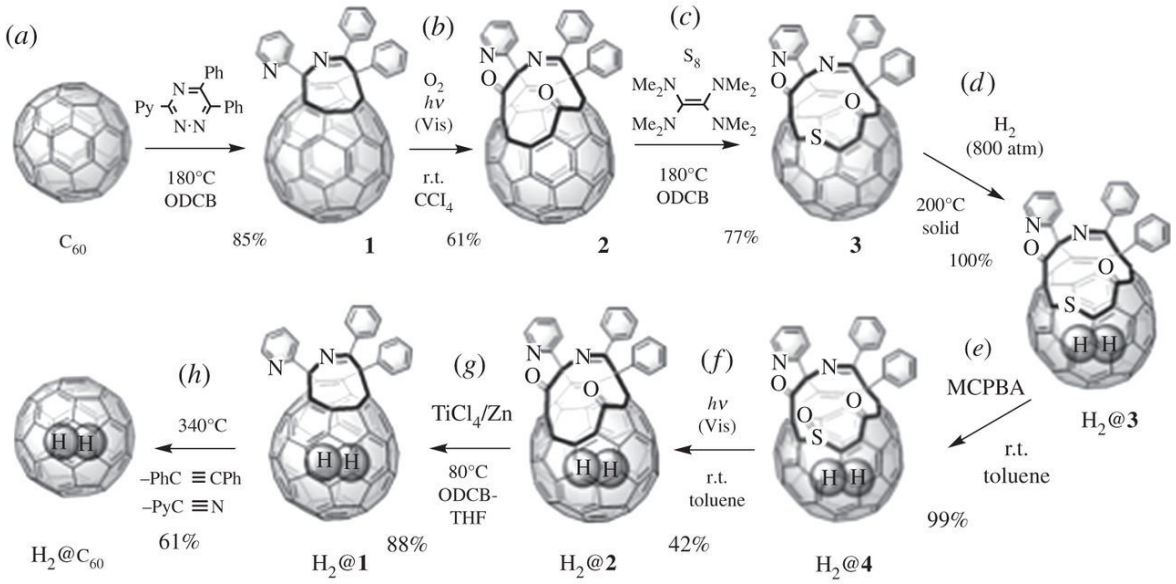

Figure 4.3. Multi-step organic synthesis to produce H_2@C_{60}: a) and b) C_{60} was reacted with a 1,2,4-triazine derivative to give **1** which was oxidised to give the open-cage C_{60} derivative **2** with a 12-membered-ring hole. c) Elemental sulfur was incorporated into the hole in the presence of aπ-electron donor to enlarge the opening into a 13-membered ring derivative **3**. d) Molecular hydrogen was inserted into the open-cage fullerene under high temperature and pressure. e) and f) Sulfur was removed under mild conditions via an oxidation and then a photochemical reaction. g) The 12-membered ring was then shrunk to an 8-membered ring by coupling the two C=O groups. h) Finally, the opening was completely closed using heat to give H_2@C_{60}.[23]

Komatsu *et al.* achieved the incredible synthesis of molecular hydrogen encapsulated in C_{60} using a four-step organic reaction to close the hole of an open-cage endohedral fullerene (Fig. 4.3).[23,24] Using X-ray diffraction, Sawa *et al.* showed that the H_2 molecule is confined to the spherical space at the centre of the cage,[25] unlike metal atoms inside fullerenes. Kurotobi *et al.* developed a multi-step organic reac-

tion to synthesise water encapsulated in C_{60}. The procedure is similarly as creative, requiring careful skill.[26] Study of intrinsic properties of H_2O such as ortho and para conversion would be possible with this endohedral fullerene. Such light-molecule endohedral fullerenes have been studied in great detail spectroscopically by many research groups across a diverse range of scientific fields.[27–29]

Finally, we arrive at the molecule most relevant to this chapter, HF@C_{60} itself. Synthesis of this endohedral fullerene was designed and carried out by Krachmalnicoff *et al.* (Fig. 4.4) where the most challenging part was closing the opened cage while minimising loss of HF. This endohedral fullerene contains a freely rotating electric dipole and could therefore exhibit ferroelectricity through alignment of interacting dipole moments.[30]

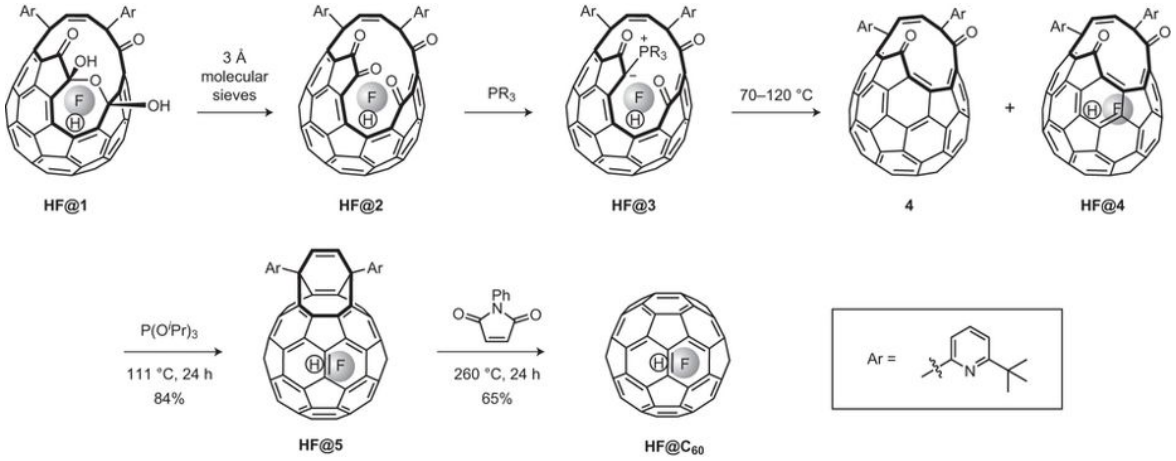

Figure 4.4. Three different phosphines (PR_3) were tried in the intramolecular Wittig reaction to give **HF@4**. With triphenylphosphine, loss of HF from **HF@3** was faster than the elimination of PPh_3O so this gave only the empty open-cage **4**. With tri(2-furyl)phosphine, the formation of **3** required a higher temperature (70-120 ℃ in the above scheme) which resulted in loss of HF again. A successful compromise was found with bis(2-furyl)phenylphosphine, which was reacted with **HF@1** in the presence of molecular sieves at room temperature to give **HF@4**, 30% of which contained HF. The hole of the open-cage was closed via a reduction with triisopropylphosphite ($P(O^iPr)_3$) to give **HF@5**. This was reacted with *N*-phenyl-maleimide to afford the 30% filled **HF@C_{60}**. Filled **HF@C_{60}** was separated from empty C_{60} using HPLC.[30]

Endohedral fullerenes have great potential for use in materials science applications. Most discussions on applications centre around metal-containing endohedral fullerenes. They have particularly interesting electronic properties which are dependent on the nature of the incarcerated entity, the size and symmetry of the fullerene cage, and any exohedral functionalisation. A wide range of HOMO-LUMO band gaps are accessible, for example, which is useful for molecular electronics. Gadolinium endohedral fullerenes have many advantages for use in magnetic resonance imaging. The endohedral fullerenes can be easily functionalised for additional purposes, the cage prevents release of toxic Gd into organisms, and they reduce the spin relaxation time of water protons much better than the currently used Gd^{III} chelates. Gadolinium endohedral fullerenes also appear to have tumour inhibition properties by improving the immune response and scavenging the reactive oxygen species that cause oxidative stress. The endohedral fullerenes did not have any toxic effect *in vivo* and therefore use of these endohedral fullerenes are unlikely to lead to unwanted side effects that are common with existing chemotherapies.[16,31]

The HF@C_{60} endohedral fullerene is interesting to us for an entirely different reason. It is possible for the electron beam of a TEM to initiate transformations of the H−F molecule inside the fullerene which would be completely isolated from any other H−F molecules. We could then probe these individual species using imaging and spectroscopic techniques. HF@C_{60} has been the focus of a collaborative study between the Central Facility for Electron Microscopy at Ulm University, the Nanoscale and Microscale Research Centre (nmRC) at the University of Nottingham, the University of Southampton, the SuperSTEM Laboratory on the SciTech Daresbury Campus, and the University of Leeds.[32]

As with the PCC molecule, HF@C_{60} molecules were encapsulated inside SWNTs to give a one-dimensional material that would allow the observation of each individual endohedral fullerene separated from each other inside the nan-

otube. HF@C_{60} is readily sublimed into SWNTs much like empty C_{60} molecules. Most secondary damage processes such as heating, ionisation, and secondary electrons should be neglibible for (HF@C_{60})@SWNT due to its thin volume and the high heat and charge conductivity of SWNTs. Therefore, the only transfer of energy from the electron beam that can cause permanent structural changes is knock-on damage when an incident electron collides with an atom and transfers some kinetic energy, described by Eq. 1.8 which we introduced back in the first chapter. Some energy is likely transferred via electron-electron interactions to give species such as $H\cdot$ and $F\cdot$ or H^+ and F^-. However, these reactive species will recombine within the fullerene cage.

Equation 1.8 in chapter one shows that at 30 kV, the maximum amount of kinetic energy transferred to an H atom is 67.8 eV. This is an order of magnitude higher than the threshold energy of 7.75 eV (calculated using molecular dynamics) for inducing H–F bond dissociation and subsequent emission of $H\cdot$ from the fullerene through the hexagonal face of the cage (this can be compared to the stationary barrier of 7.63 eV in Fig. 4.5). Once $H\cdot$ is outside of the fullerene, it cannot recombine with $F\cdot$. A homolytic bond dissociation is 11.8 eV lower in energy relative to the heterolytic pathway which would give H^+ and F^- ions. This suggests that, under standard imaging conditions at 30 kV, formation of F^0@C_{60} from ejection of hydrogen is highly energetically favourable. In addition to this, an F atom cannot be emitted through the fullerene cage without breaking carbon-carbon bonds.

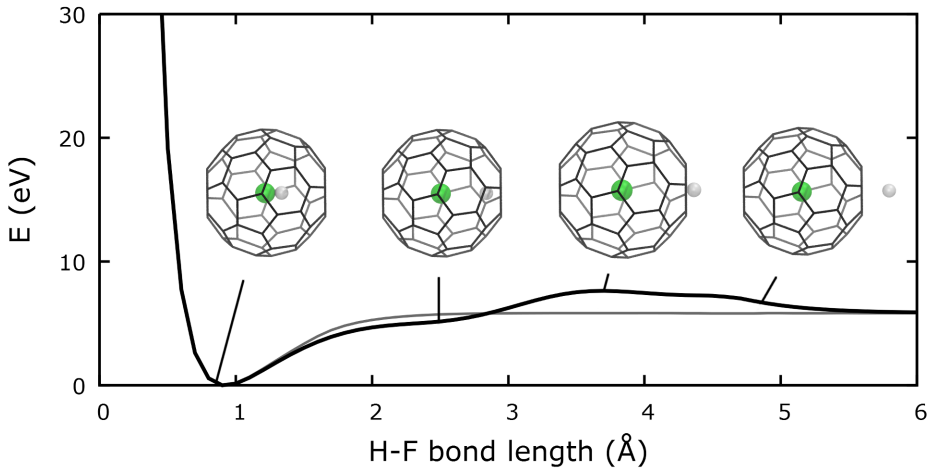

Figure 4.5. Ejection of H from HF@C_{60} through the centre of a hexagonal face of the cage. The grey line shows the ground state energy profile of homolytic HF dissociation. Emission of H$\cdot$ through the cage (black line) introduces a barrier to recombination of H$-$F once H$\cdot$ is outside the cage. This series of single point energy simulations were calculated using density functional theory (DFT) at the ωB97X-D/6-311G* level of theory at the University of Nottingham by S. T. Skowron.

The high resolution TEM images show a dot of contrast corresponding to an F atom in the centre of the fullerene (Fig. 4.6). In order to determine if knock-on damage was the source of permanent structural damage, the total dose required for the first dimerisation of two C_{60} molecules was measured over six image series at 80 kV and four image series at 30 kV. The mean total electron dose for the first dimerisation at 80 kV is 5.27×10^{7} e^{-} nm^{-2} (statistical error of 9.27×10^{6}) while at 30 kV, this value was 5.6 $\times10^{8}$ e^{-} nm^{-2} (statistical error of 7.30×10^{7}). An order of magnitude increase in total electron dose is required to cause any fullerene dimerisations at 30 kV compared to at 80 kV. Since the main change was the kinetic energy of the electrons, this suggests that knock-on damage is the main source of permanent structural damage, which also applies to knocking out H from HF@C_{60}. Indeed, at 30 kV, there should be an increase in damage via radiolysis (e.g. ionization) compared to at 80 kV so if such interactions were causing any irreversible structural changes, one would expect a lower total dose required at 30 kV.

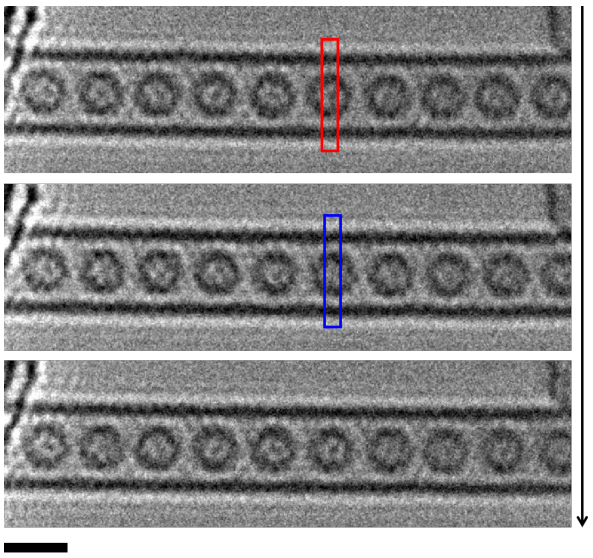

(a)

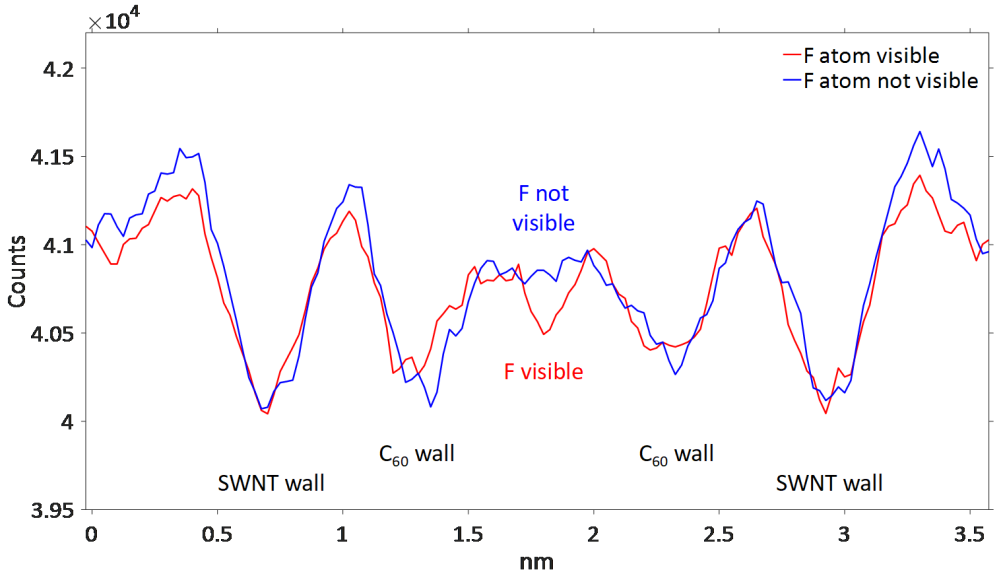

(b)

Figure 4.6. a) HF@C_{60} peapods inside a SWNT where the F atoms seem to disappear and reappear inside the fullerene cage as the sample is imaged (black arrow on the right side indicates forward direction of time). b) Line profiles across the centre of an endohedral fullerene molecule (from the red and blue areas in a) which corresponds to the red and blue plots respectively) show that the dot of contrast does disappear in the second micrograph and reappears in the the third, suggesting that F has not been emitted from the fullerene cage. Scale bar is 1 nm. Aberration-corrected TEM micrographs were recorded at the University of Ulm using the SALVE (sub-Ångström low voltage electron) TEM at 30 kV by J. Biskupek.

4.2 Aims and Objectives

The aim of this chapter is to prove, without a doubt, the existence of F@C_{60}. We will test different approaches, using both local probes and bulk analysis, to develop an experimental method to link together hitherto uncorrelated characterisation techniques.

Electron paramagnetic resonance (EPR) spectroscopy can be used to probe the existence of an F radical inside the C_{60} cage. If the entire HF molecule was ejected from the fullerene, there would be no stable radicals. Emission of an F radical is impossible without breaking the C_{60} cage. If an F radical was emitted from a broken cage, then it would immediately react. Therefore, if an F radical is found, the only location it would be stable in would be inside the C_{60} cage (reminiscent of N@C_{60}). EPR is measured on the bulk scale and therefore we would need to produce enough F@C_{60} for detection by EPR.

We will also use localised probes to study nanoscale quantities of F@C_{60}. High resolution vibrational electron energy loss spectroscopy (vib-EELS) uses the electron beam of a TEM as a probe to induce vibrational transitions in the sample. This technique can be used to follow any changes in the H – F bond before and after irradiation. Energy dispersive X-ray spectroscopy (EDXS) can be carried out on a nanoscale crystal of HF@C_{60} during irradiation to follow the presence of an F signal which, if HF is removed entirely from the fullerenes rather than just emission of H alone, may decrease in intensity over time. Finally, optically detected magnetic resonance (ODMR) is routinely used to study concentrations of radical species orders of magnitudes lower than what EPR can detect. We may be able to use ODMR to study a TEM grid and therefore will need to develop a methodology to prepare and process a sample suitable for both techniques. This chapter describes our diverse experiments on our quest for positive evidence of F@C_{60}.

4.3 Results and Discussion

We began with a technique known as aloof-beam vibrational electron energy loss spectroscopy (vib-EELS) which uses an atom-sized probe to study the vibrational modes of many types of nanostructures. This work was carried out at the SuperSTEM laboratory by Q. M. Ramasse. The probe was positioned a distance *d* away from the sample where *d* can be tens to hundreds of nm. The 'aloof' electron beam can lose energy to delocalised electronic excitations and cause low energy excitations less than an eV which is in the infrared region where vibrational modes occur. Vib-EELS typically has quite low signal-to-background ratios from vibrational modes so to maximise the chance of seeing a H – F vibrational peak, vib-EELS was carried out on a crystal of HF@C_{60} rather than a single nanotube filled with HF@C_{60}.

Several spectra of an organic crystal of HF@C_{60} were recorded in the aloof configuration at 60 kV near the crystal. The first spectrum was on a fresh area i.e. after negligible irradiation; the second after moderate irradiation (total dose of 2.0×10^{6} e^{-} nm^{-2} at a flux of 8.0×10^{3} e^{-} nm^{-2} s^{-1}) on the crystal; the third after high irradiation (total dose of 1.9×10^{7} e^{-} nm^{-2} at a flux of 2.5×10^{5} e^{-} nm^{-2} s^{-1}). The spectra were averaged from larger Spectrum Images (see Fig. 4.7 for the extracted regions for each spectrum).

The dominant feature in vib-EELS experimental data is the zero loss peak (ZLP) which must be removed in order to analyse the vibrational peaks.[33] The ZLP arises due to the electrons that pass through a sample without losing any energy. This peak is, in practice, asymmetric with a tail extending significantly beyond the full-width half-maximum (FWHM) of the ZLP which must be subtracted before any analysis can be carried out (see Fig. 4.8 for the vib-EELS data before background subtraction). The peak position, intensity, and integration can be greatly affected by the model and fitting window chosen for background subtraction.[34]

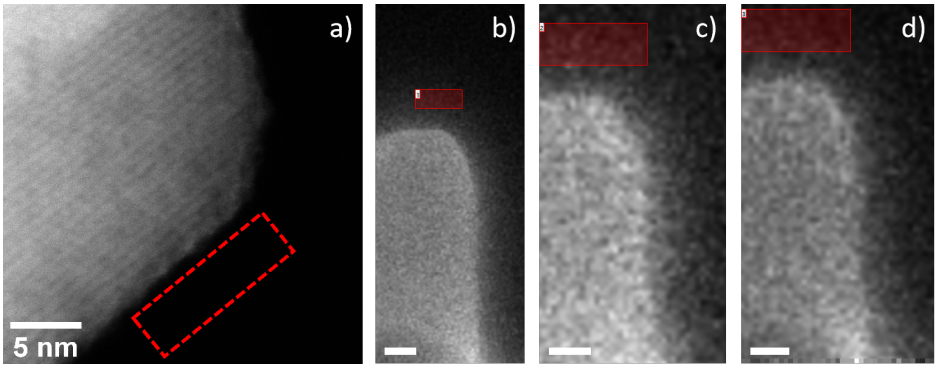

Figure 4.7. a) High-angle annular-dark-field scanning transmission electron microscopy (HAADF-STEM) was carried out on a HF@C_{60} crystal. The red dashed box is a representative region of where the aloof vibrational EEL spectra were recorded. b), c), d) Spectrum Images where EEL spectra were extracted from areas with the same number of pixels and at a similar distance and position from the crystal. Pixel sizes are slightly different for each Spectrum Image so the red boxes are correspondingly different. Since the dose per pixel was the same across all three Spectrum Images, the extracted spectra have been normalised by extracting areas from each Spectrum Image with the same total electron dose. Scale bars for Spectrum Images are 10 nm. HAADF-STEM images were recorded at the SuperSTEM laboratory using the monochromated Nion UltraSTEM 100MC 'Hermes' at 60 kV by Q. M. Ramasse.

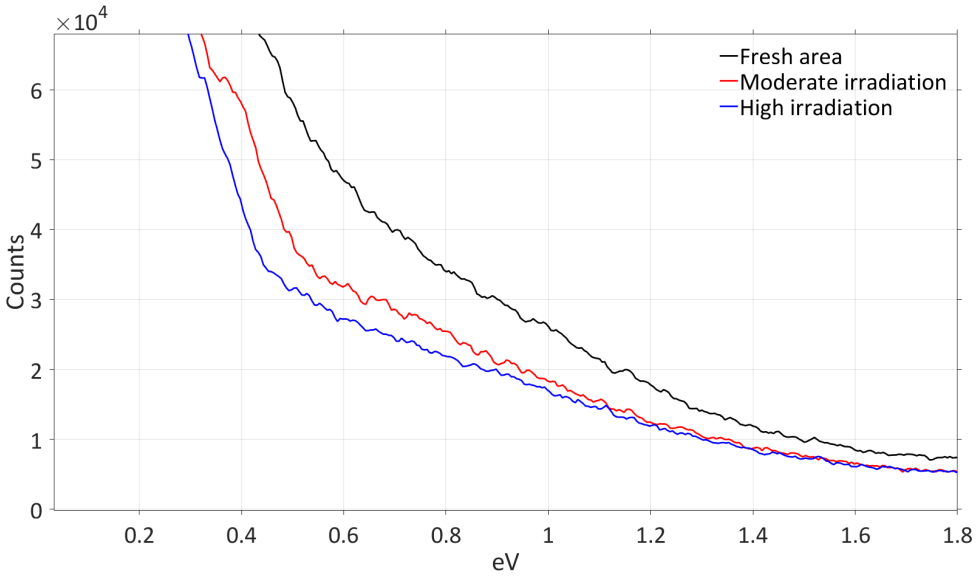

Figure 4.8. Pre-background subtraction Vib-EEL spectra, extracted as described in Fig. 4.7. There is a significant background contribution from the ZLP. The vib-EELS data was collected at the SuperSTEM laboratory using the monochromated Nion UltraSTEM 100MC 'Hermes' at 60 kV by Q. M. Ramasse.

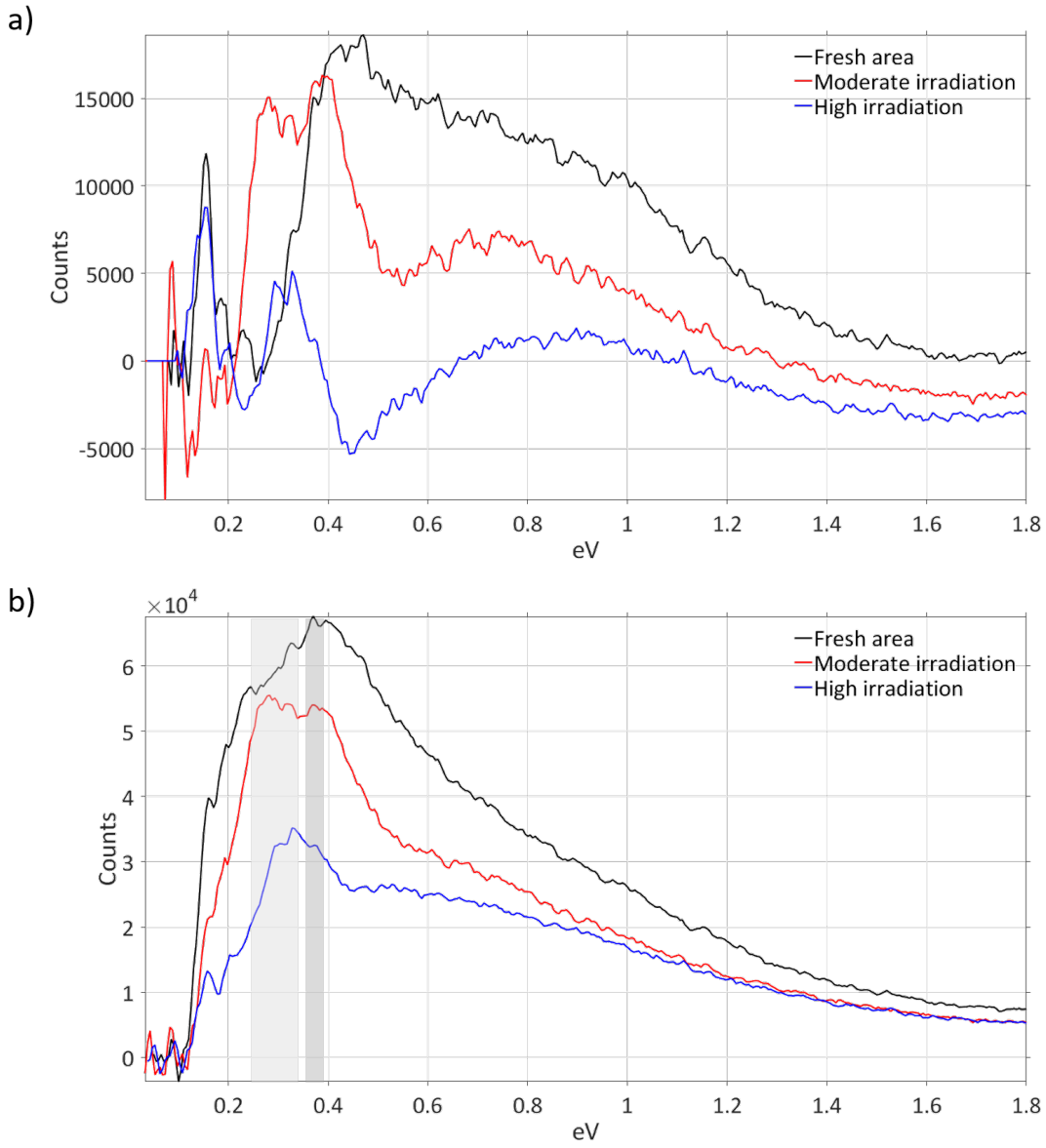

Figure 4.9. a) Vib-EEL spectra extracted as described in Fig. 4.7 were fitted using a one-term power law in GMS 3. Background subtraction was unsuitable and the resulting spectra difficult to interpret. b) The spectra after fitting and background subtraction using a two-term exponential model in MATLAB. The fresh area spectrum shows a F−H stretching vibration mode at 0.38 eV (~3000-3100 cm^{-1}), highlighted by the dark grey region. After moderate irradiation, the major signal is a C−H stretching vibration mode at 0.28 eV (~2200-2300 cm^{-1}). After high irradiation, there is a much weaker band at 0.33 eV (~2600-2700 cm^{-1}) which may be different C−H stretching vibrational mode. Both C-H vibrational modes are highlighted in the light grey region. The vib-EELS data was collected at the SuperSTEM laboratory using the monochromated Nion UltraSTEM 100MC 'Hermes' at 60 kV by Q. M. Ramasse.

Gatan Microscopy Suite (GMS) 3 is the most commonly used software for EELS background fitting, offering users a straightforward non-linear least squares estimation (NLLSE) method to fit the background. However, we found the software unsuitable for background subtraction of vib-EELS data (see Fig. 4.9 a). This is because only one-term power laws are available in GMS 3. Power laws are generally applicable for background subtraction of signals at higher energy losses (> 50 eV) where the largest contribution to the background is from plasmon, and have limited application to ultralow-loss excitations close to the ZLP.[33,34] We wrote custom scripts in MATLAB to circumvent this issue. The primary focus of the scripts is to ensure accuracy in the background subtraction by providing goodness-of-fit information. The three vib-EEL spectra were fitted using a two-term exponential model on data below 0.12 eV, preceding the first observable spectral feature of interest (Fig. 4.9 b).

The F−H stretching vibration mode at 0.38 eV (~3000-3100 cm^{-1}) is the major signal in the spectrum in the pristine area. Gas phase H−F at 120 ℃ exhibits a peak[35] around 3961.64 cm^{-1} which should be red-shifted upon encapsulation so the lower energy stretching vibration mode observed at SuperSTEM is reasonable. After moderate irradiation directly onto the crystal with an estimated total dose of 2.0×10^{6} e^{-} nm^{-2}, the major signal is a band at 0.28 eV (~2200-2300 cm^{-1}) which could be a C−H stretching vibration mode. After high irradiation with a total dose of 1.9×10^{7} e^{-} nm^{-2}, both bands significantly diminished, leaving a much weaker band at 0.33 eV (~2600-2700 cm^{-1}) which may be a different C−H stretching vibrational mode (Fig. 4.9 b). The signal from the H−F molecules has decreased which suggests that HF molecules have been broken apart by the electron beam and emitted from the cage. It is also possible for the fullerenes to have been damaged by the electron beam and the H−F molecules to have escaped entirely, which would lead to the same decrease in the H−F signal.

We then carried out energy dispersive X-ray spectroscopy (EDXS) on a HF@C_{60} crystal at the University of Nottingham Nanoscale and Microscale Research Centre (nmRC) to determine F content before and after irradiation (Fig. 4.10). Six EDX spectra were taken sequentially for a total dose of 2.29×10^{7} e^{-} nm^{-2} at 80 kV using an electron flux of 1.27×10^{4} e^{-} nm^{-2} s^{-1}. The accelerating voltage is different to that previously used because the microscope we used to record vib-EELS data operates at 60 kV while the microscope we used to collect EDXS data operates at either 80 or 200 kV. We decided to compromise with 80 kV since the difference from 60 kV is smaller than at 200 kV. The EDXS data show the continued presence of a virtually unchanged F signal (initial At% of 1.1; final At% of 1.0) after irradiation at total doses similar to that used in the vib-EELS data collection, suggesting that while the H−F bonds break under the electron beam, the F atoms still persist in the crystal. The complementary TEM imaging and Fourier transforms (Fig. 4.10 b-d) show that the overall crystal structure has not been destroyed after high electron beam irradiation. The (1 1 1) diffraction spots are visible before and after irradiation (d-spacings of 8.295 Å and 8.414 Å respectively).[36]

In both spectroscopic studies above, we found that the H−F stretching vibration mode disappeared (in vib-EELS) while for a comparable total dose, we still observed a signal from fluorine (in EDXS). However, this is not conclusive proof that we have formed the radical F@C_{60} because it is possible that H−F emission from the fullerene cage could lead to some sort of fluorine functionalisation of the fullerene exterior without destroying the overall crystal structure. It is possible to use aloof beam EELS to acquire valence as well as vibrational data.[37] However, the electronic transitions of F$\cdot$ [38] overlap with those of C_{60}[39] and it would be difficult to extract information on transitions purely associated with the F$\cdot$. Therefore, we would need to use a different technique to directly detect the F radical.

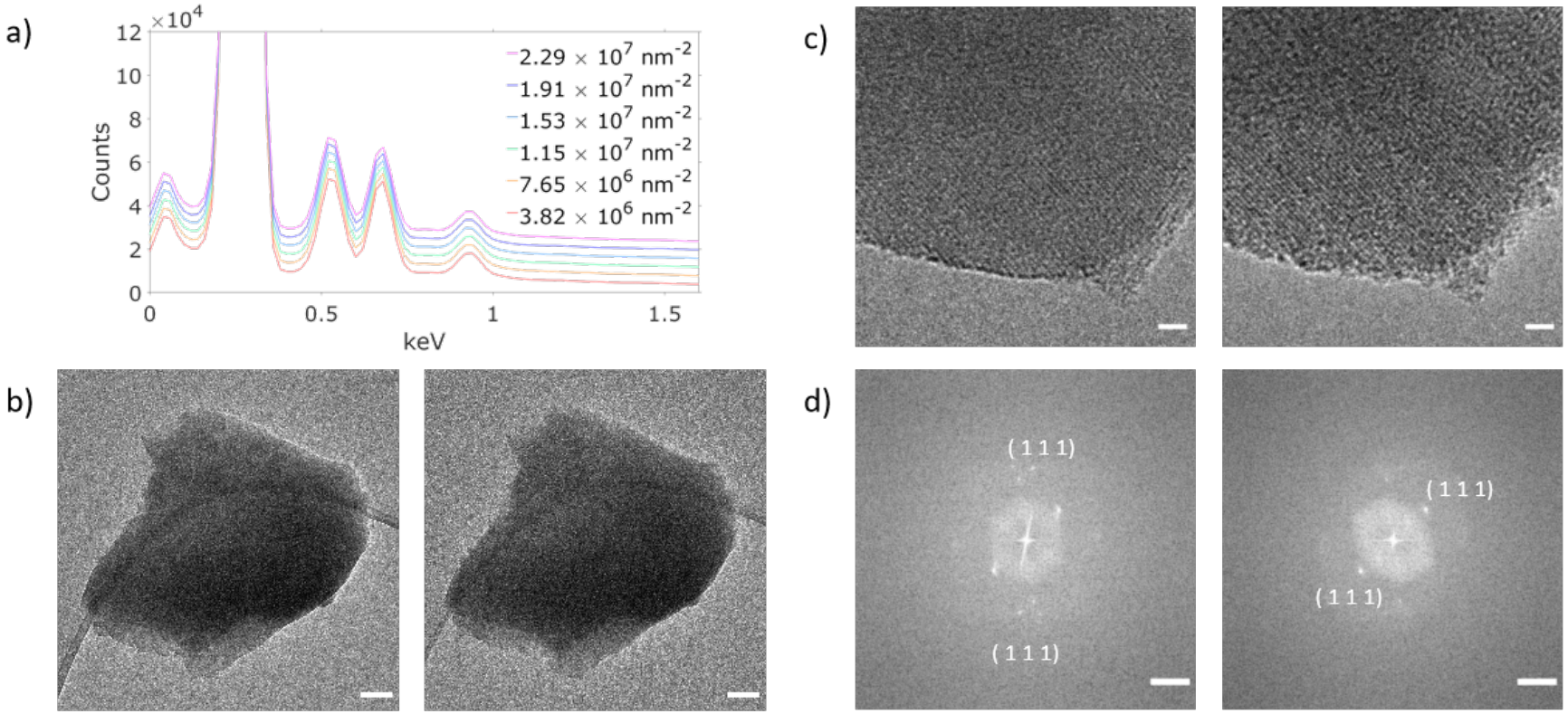

Figure 4.10. a) Six EDX spectra of the HF@C_{60} crystal in b) were taken sequentially for a total dose of 2.29×10^7 e^- nm^{-2} at 80 kV using an electron flux of 1.27×10^4 e^- nm^{-2} s^{-1}. The plot labels indicate the total electron dose after each EDX spectrum had been acquired. Each spectrum is offset from the last by 4000 units in the Y-axis for clarity. The initial F At% is 1.1; the final F At% is 1.0. b) The low magnification micrographs (scale bars are 100 nm) and c) the high magnification micrographs (scale bars are 5 nm) as well as the d) Fourier transforms of the high magnification micrographs (scale bars are 2 1/nm) show that the crystal structure is largely undisturbed after extended electron beam irradiation. The (1 1 1) diffraction spots correspond to d-spacings of 8.295 Å and 8.414 Å respectively.[36] EDXS data was carried out at the Nanoscale and Microscale Research Centre (nmRC) at the University of Nottingham by K. L. Y. Fung.

Electron paramagnetic resonance (EPR) spectroscopy is a technique we could use to probe the F radical directly. An electron has a magnetic moment which can be split into different energies by an external magnetic field; this is known as the Zeeman effect. The magnetic moment m_s aligns itself either antiparallel ($m_s = -\frac{1}{2}$) or parallel ($m_s = +\frac{1}{2}$) to the field. The energy difference ΔE between the lower and upper state is $\Delta E = g_e \mu_B B_0$ for unpaired free electrons where g_e is the electron g-factor, a proportionality constant that relates an electron's observed magnetic moment to its angular momentum quantum number, μ_B is the Bohr magneton, and B_0 is the strength of the external magnetic field in G. This shows that the splitting of energy levels is directly proportional to the magnetic field's strength (Fig. 4.11).

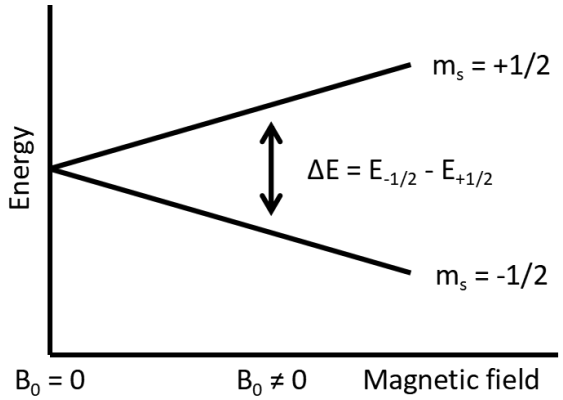

Figure 4.11. Splitting of electron energy states in the presence of an external magnetic field.

An unpaired electron can move between the two energy levels by absorbing or emitting a photon of energy $h\nu$ where $h\nu = \Delta E = g_e \mu_B B_0$. In practice, the paramagnetic centres are exposed to microwaves at a fixed frequency while the external magnetic field is increased. This widens the energy gap between the ($m_s = -\frac{1}{2}$) and ($m_s = +\frac{1}{2}$) energy states until it matches the energy of the microwaves. Unpaired electrons tend to be in the lower state (Eq. 4.1) so at this point, there is absorption of energy which gives rise to an EPR spectrum. The statistical distribution between lower and upper states is dependent upon the temperature so spectra are often recorded at liquid nitrogen temperatures.

$$\frac{n_{upper}}{n_{lower}} = exp(-\frac{h\nu}{kT})$$

Equation 4.1. The Maxwell-Boltzmann distribution where n_{lower} is the number of paramagnetic centres occupying the lower energy state, k is the Boltzmann constant, and T is the thermodynamic temperature.

Conventional EPR at the University of Nottingham (the Bruker EMX X-band EPR spectrometer operated by J. McMaster) is able to detect a minimum concentration on the order of μmol dm^{-3} which is approximately 0.1 nmol of F@C_{60} in 0.1 mL of solvent or 1×10^{13} total spins. We then considered how to generate enough F@C_{60} for EPR detection. S. T. Skowron calculated an approximate isotropic cross-section for hydrogen emission from the fullerene to be 66 barn (10^{-10} nm^2) at 80 kV in order to estimate the total dose required for converting a number of HF@C_{60} into F@C_{60}. The number of HF@C_{60} was determined by approximating the volume of a fullerene particle. The average endohedral fullerene particle was roughly 25 nm in diameter. The crystal structure of C_{60} is face-centred cubic so assuming the fullerene particles to be broadly cubic (i.e. 25 nm $\times$ 25 nm $\times$ 25 nm), the rate of conversion of one monolayer of HF@C_{60} into F@C_{60} (in nm^{-2} s^{-1}) is the electron flux used during irradiation (in e^- nm^{-2} s^{-1}) multiplied by the cross-section for hydrogen emission (in nm^2) multiplied by the concentration of endohedral fullerenes (the areal density in nm^{-2}). We used a typical electron flux of 10^4 e^- nm^{-2} s^{-1}. In order to convert one monolayer of HF@C_{60} into F@C_{60} per irradiation area, we would need to irradiate that area for a minimum of 570 s or a total electron dose of 1×10^7 e^- nm^{-2}. This would give approximately 1000 endohedral fullerenes converted per particle. Each irradiation area contained about 100 particles which corresponds to about 10^5 spins generated per irradiation area. We irradiated eleven similar areas in total, generating on the order of 10^6 spins. In total, we irradiated approximately 9.0 μm^2 of the gold TEM grid (diameter 3 mm) with HF@C_{60} dispersed onto the carbon film. The total electron doses used here were of the same order of magnitude

as the previous irradiation experiments carried out for vib-EELS and EDXS. The irradiation experiments were extremely time-consuming and as a result, we were nowhere near the 1×10^{13} total spins required for EPR detection. Unsurprisingly, there was no EPR signal whatsoever from the endohedral fullerenes (Fig. 4.12).

Another option for generating more spins for EPR is to use a much lower accelerating voltage such as 20 kV. The reasoning behind this is that at 20 kV the cross-section for hydrogen emission is 197 barn, significantly higher than the 66 barn at 80 kV. In addition to increasing the probability of hydrogen emission, use of 20 kV would also lower the T_{max} of carbon, reducing damage to the C_{60} cage. The microscope is aligned at 80 and 200 kV but not at 20 kV. After a lengthy alignment procedure aimed at persuading the electromagnetic lenses to cooperate (recorded in detail in the Experimental Methods), we were able to use the microscope to irradiate HF@C_{60} with 20 keV electrons.

We irradiated 1.6 μm^2 of the TEM grid at 20 kV in a similar manner as at 80 kV for an average total electron dose of 8×10^6 e$^-$ nm^{-2}. The beam intensity at 20 kV is much lower than at 80 kV (average electron flux of 4×10^3 e$^-$ nm^{-2} s^{-1}) so the irradiation times were much longer (1819 s compared to 569 s at 80 kV). Because of this, we chose to irradiate larger endohedral fullerene particles (200 nm in diameter) so that, for every irradiation area (of which we did two), we could potentially generate 10^6 spins. Having said that, it is very likely that the bottom layers of the 200 nm-thick crystals were receiving very little dose so far fewer spins may have been generated. At 20 kV, incidents of radiolysis will increase which could complicate matters and cause damage to the endohedral fullerenes. We did not see an EPR signal from 20 kV irradiation either (Fig. 4.12). In summary, the advantages and disadvantages of using 20 kV to generate enough spins for EPR likely cancelled each other out to give much the same result as at 80 kV. We did not know how many spins we would be able to generate for EPR before we carried out the irradiation experiments. We have

discovered that, in practice, it is rather difficult to use TEM irradiation to generate enough spins for EPR at the University of Nottingham. In principle, much more sensitive EPR facilities could detect this small number of spins. For example, the Israel Institute of Technology have an induction-detection EPR setup that uses an ultra-miniature micrometer-sized microwave resonator under cryogenic conditions to achieve detection of just a few tens of spins.[40,41]

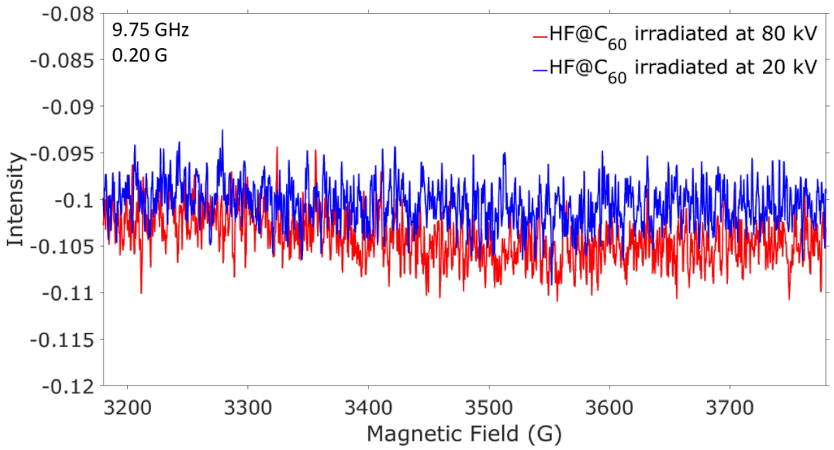

Figure 4.12. Neither of the irradiated HF@C_{60} samples exhibited an EPR signal. This is due to a low number of total spins generated. The microwave frequency used for both spectra was 9.75 GHz; the modulation amplitude 0.20 G. The EPR data was collected at the University of Nottingham using a Bruker EMX X-band EPR spectrometer by J. McMaster.

We subsequently found another possible technique much closer to home for detecting nanoscopic quantities of F radicals: optically detected magnetic resonance (ODMR) of fluorescent nanodiamonds (NDs)[42] carried out by M. L. Mather and V. Radu from the Optics and Photonics Research Group at the University of Nottingham. Like EPR, ODMR uses the Zeeman effect in unpaired electrons. NDs are fluorescent due to their negatively charged nitrogen vacancies (NVs) which are lattice defects typically about 10-20 nm below the diamond surface consisting of a nitrogen atom adjacent to a vacant lattice site. Negatively charged NVs are stable at room temperature and have an electronic structure with six electrons. Two are from the nitrogen atom and three are from the dangling bonds of the three carbon atoms

surrounding the vacancy. The sixth electron is from the lattice, typically a nitrogen donor, making the overall NV negatively charged. Most of the electron density is located on the three carbon atoms and the vacant site. The energy level structure consists of a triplet ground state, a triplet excited state, and two metastable singlet states. The two triplet states are further split into three spin sublevels; two degenerate $m_s = \pm 1$ states and one $m_s = 0$ state that is energetically lower. The energy difference or zero-field splitting between spin sublevels is 2.87 GHz for the ground state and 1.42 GHz for the excited state. The spin-lattice relaxation time T_1, i.e. the transition rate between the excited $m_s = 0$ state and a mixture of the ground triplet states is a few milliseconds at room temperature. Exciting the NV centre with green light results in photoluminescence (PL) emission, with a few percent of photons emitted at 637 nm (the zero phonon line) which is the energy of the excited state to ground state transition. Most luminescence appears in vibrational side bands between 630 and 800 nm. Pumping the NV with microwaves at the resonant frequency of 2.87 GHz raises the NV into the degenerate $m_s = \pm\frac{1}{2}$ ground state which, upon irradiation with green light, excites the NV centre into the degenerate $m_s = \pm\frac{1}{2}$ excited state. There is stronger intersystem crossing into the two metastable singlet states which relaxes back to the ground state via non-radiative decay. Therefore, at that resonant microwave frequency of 2.87 GHz, PL emission is reduced. Applying a magnetic field causes Zeeman splitting and therefore decrease of PL emission at two resonant frequencies given by $h\nu = g_e \mu_B B_0$. This effectively measures the EPR spectrum of NV centres and is known as the ODMR effect (Fig. 4.13). NV centres have been used for nanoscale sensing in applications such as single-spin nuclear magnetic resonance, measurements of cell membrane potentials (NDs have low cytotoxicity), and nanoscale thermometry (the zero-field splitting has a temperature dependence).[42]

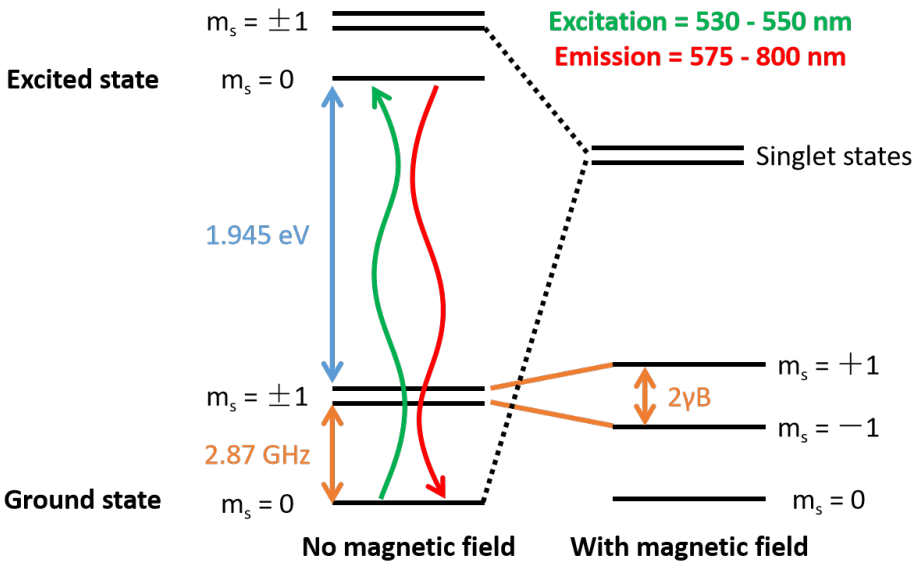

Figure 4.13. Simplified energy level structure of an NV centre.[42]

Interactions between the NVs and nearby paramagnetic species such as F@C$_{60}$ will cause a relaxation from the excited $m_s = 0$ state to a mixture of the three ground triplet states, increasing the NV spin relaxation rate $1/T_1$.[43] Therefore presence of F@C$_{60}$ will reduce PL emission and we could use T_1-based relaxometry to measure the rate at which PL emission decays with respect to control NVs without any paramagnetic species nearby. This would be a direct measurement of the F radical at nanoscale quantities, circumventing the spin generation issue we had with bulk EPR. In order to carry out our ODMR measurements of irradiated HF@C$_{60}$, we would need to make a HF@C$_{60}$/ND sample and irradiate areas where NDs are in contact with HF@C$_{60}$ crystals. Before any ODMR measurements, we must first determine whether or not our electron beam irradiation conditions would damage the NV centres.

Acid-treated nanodiamonds deposited onto a gold TEM finder grid were irradiated at 80 (Fig. 4.14) and 20 kV (Fig. 4.17). We chose to continue using both 80 and 20 kV because of the aforementioned advantages in beam stability with reducing the accelerating voltage. This should also apply to the NV centres. Of course, it could be difficult to navigate the sample and locate suitable irradiation locations at 20 kV due to the lower emission current and image resolution so 80 kV was still a useful accelerating voltage to use for irradiation experiments.

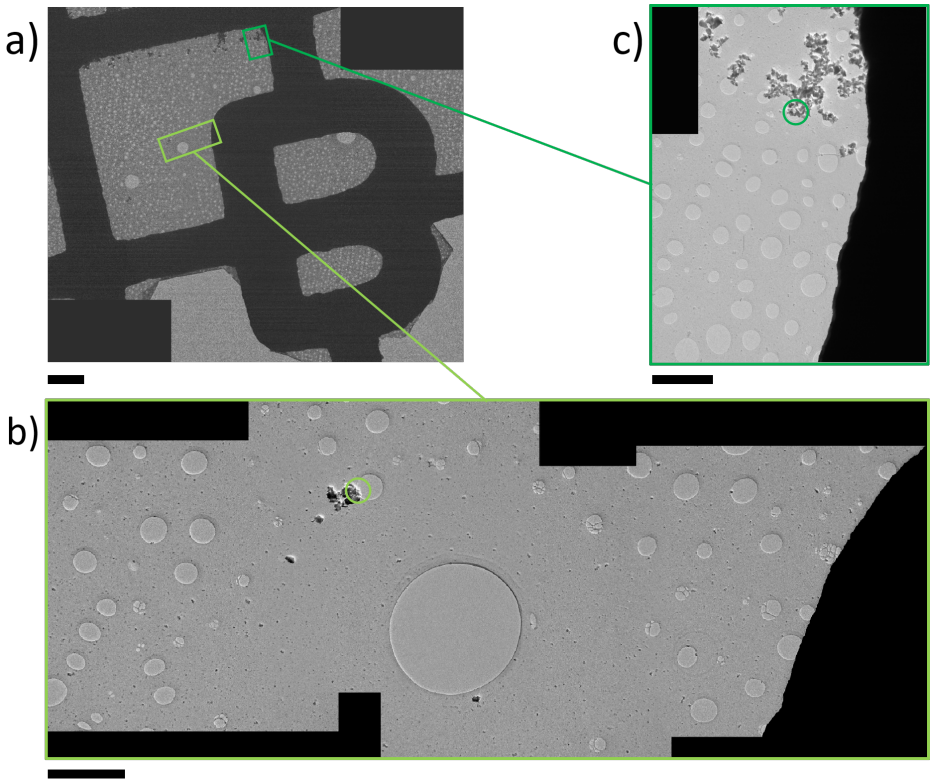

Figure 4.14. a) A low magnification image of the area around the letter 'B', used to locate the nanodiamonds for ODMR after irradiation. The scale bar is 10 µm. The pale green rectangle (expanded in b) was the region irradiated with a high total dose of 1.3×10^{8} e^{-} nm^{-2} and the dark green rectangle (expanded in c) was the region irradiated with a low total dose of 4.2×10^{7} e^{-} nm^{-2}. Irradiation of both regions used a flux of 2×10^{5} e^{-} nm^{-2} s^{-1}. b) The pale green circle indicates where we irradiated with a high total dose. The scale bar is 2 µm. See Fig. 4.15. c) The dark green circle indicates where we irradiated with a low total dose. The scale bar is 2 µm. See Fig. 4.16.

At 80 kV, we irradiated two separate clusters of nanodiamonds near the letter 'B' using a similar electron flux; one with a high total dose (Fig. 4.15) and one with a low total dose (Fig. 4.16). The reason for two different total doses was in case the NV centres happened to be quite beam sensitive. We could be flexible with how much dose we used to give different % conversions of HF@C_{60} to F@C_{60}.

For each irradiated region at 80 kV, we followed the structural integrity of the nanodiamonds using selected area diffraction (SAD) before and after irradiation on the illuminated regions in Fig. 4.15 a-b) and Fig. 4.16 a-b). We have also included high magnification micrographs before and after irradiation without the SA aperture in Fig. 4.15 c-d) and Fig. 4.16 c-d) for comparison. The micrographs and SAD patterns suggest that the overall structure and crystallinity did not change significantly for both high and low dose irradiated nanodiamonds. We were able to identify diffraction spots before and after irradiation with d-spacing similar to the (1 1 1) plane of bulk diamond in Fig. 4.15 e-f) and Fig. 4.16 e-f). Another positive result is that the nanodiamonds did not accumulate any amorphous material on the surface after irradiation. We had some issues with 'coffee stains' during preliminary imaging where rings of amorphous material were deposited on the sample during irradiation. However, this may have been due to contamination of the TEM column since we only had this issue during one irradiation session. While the diamond crystal likely remained intact, this does not necessarily mean the NV centres survived irradiation. We can determine the presence of active NV centres using fluorescence microscopy.

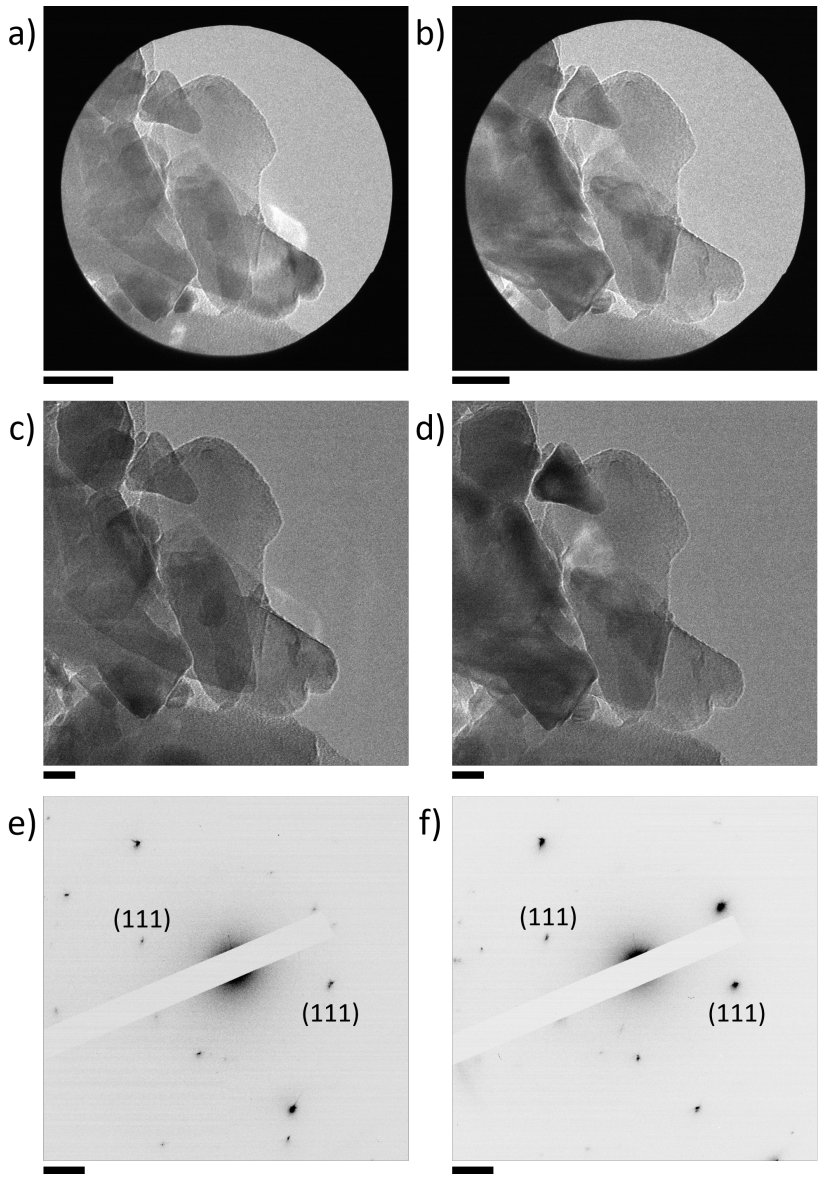

Figure 4.15. Nanodiamonds from the pale green rectangle region a) before and b) after high dose irradiation of 1.3×10^{8} e^{-} nm^{-2} using a flux of 2×10^{5} e^{-} nm^{-2} s^{-1}. The scale bars are 50 nm. Selected area diffraction was carried out on the illuminated regions. High magnification images c) before and d) after irradiation. The scale bars are 20 nm. This would give approximately 57% conversion of HF@C_{60} to F@C_{60}. Selected area diffraction of the nanodiamonds e) before and f) after irradiation. The scale bars are 2 1/nm. This corresponds to a d-spacing of 2.139 Å in e) and 2.114 Å in f) which are similar to the (1 1 1) plane of bulk diamond (d-spacing of 2.059 Å).[44]

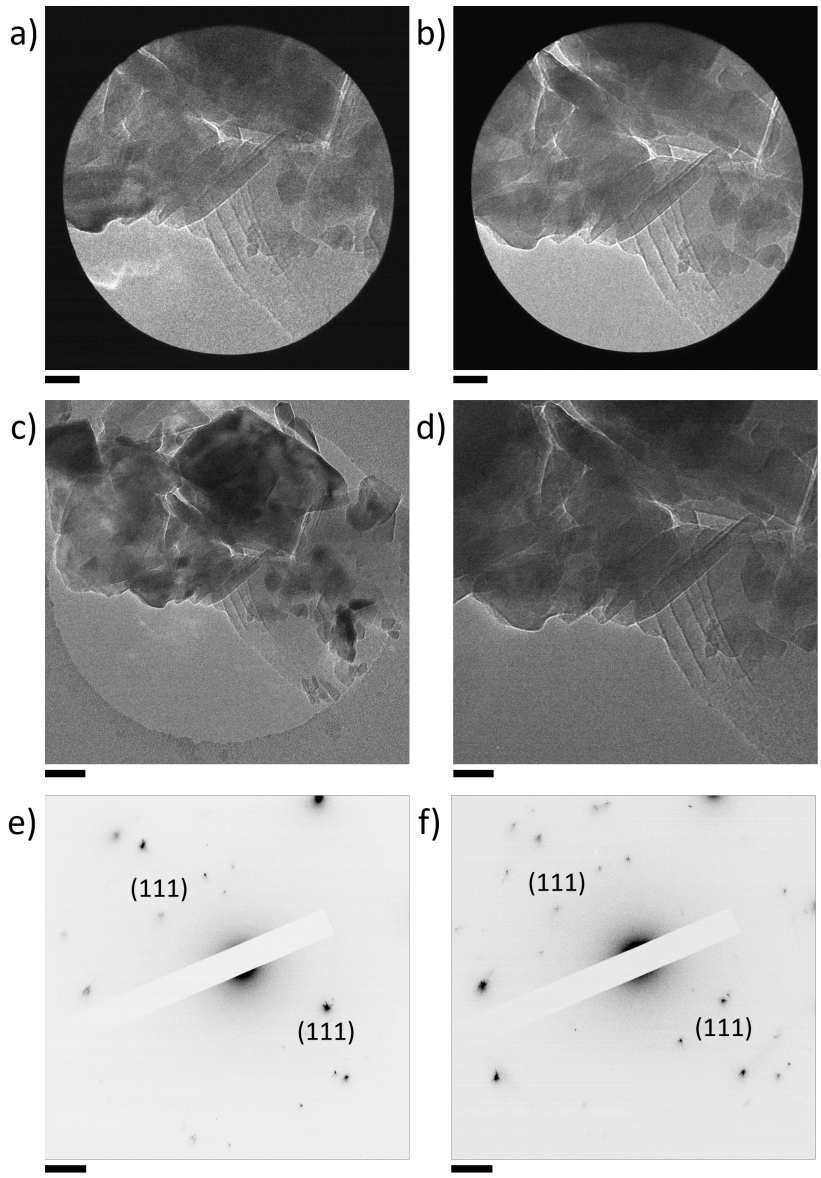

Figure 4.16. Nanodiamonds from the dark green rectangle region a) before and b) after low dose irradiation of 4.2×10^{7} e^{-} nm^{-2} using a flux of 2×10^{5} e^{-} nm^{-2} s^{-1}. The scale bars are 25 nm. Selected area diffraction was carried out on the illuminated regions. High magnification images c) before and d) after irradiation. The scale bars are 50 and 25 nm respectively. This would give approximately 24% conversion of HF@C_{60} to F@C_{60}. Selected area diffraction of the nanodiamonds e) before and f) after irradiation. The scale bars are 2 1/nm. This corresponds to a d-spacing of 2.178 Å in e) and 2.171 Å in f) which are similar to the (1 1 1) plane of bulk diamond (d-spacing of 2.059 Å).[44]

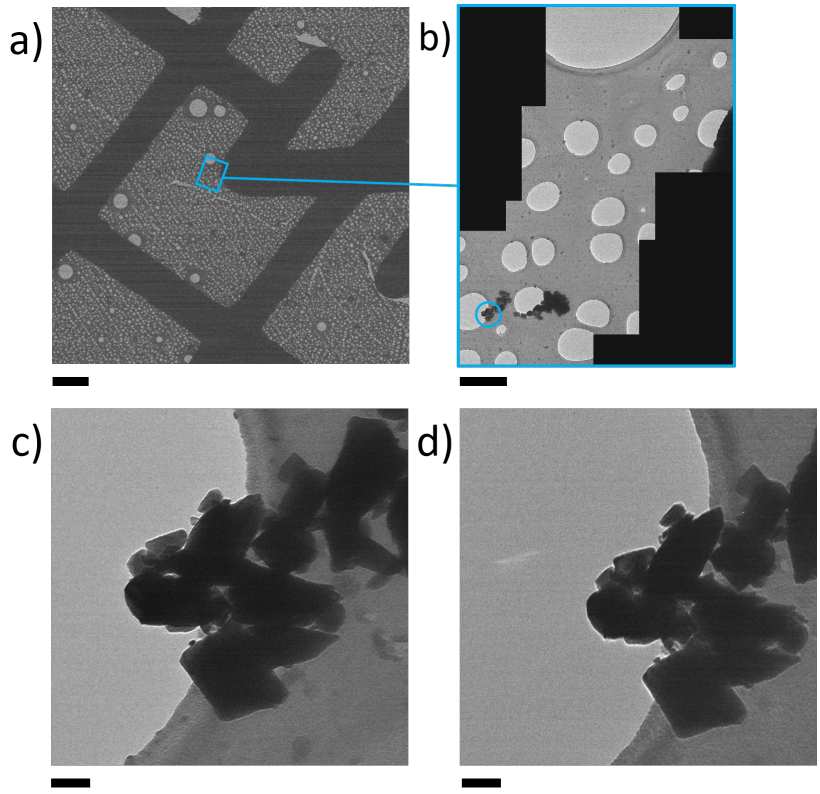

Figure 4.17. a) A low magnification image of the area around the letter 'Z', used to locate the nanodiamonds for ODMR after irradiation. The scale bar is 10 µm. The blue rectangle (expanded in b) was the region irradiated with a low total dose of 1.7×10^{7} e^{-} nm^{-2} using a flux of 1×10^{4} e^{-} nm^{-2} s^{-1}. b) The blue circle indicates the irradiated region. The scale bar is 1 µm. High magnification images c) before and d) after irradiation. The scale bars are 50 nm. This would give approximately 28% conversion of HF@C_{60} to F@C_{60}.

At 20 kV, because emission was low, irradiation consequently took much longer and we irradiated only one cluster of nanodiamonds near the letter 'Z' using a lower electron flux (than at 80 kV) for a lower total dose. At the time of the experiment, not much of the microscope had been calibrated to work at 20 kV so we were unable to carry out SA diffraction on the cluster of nanodiamonds.

Fortunately, electron beam irradiation did not appear to damage the NV centres. PL emission could still be observed for all the irradiated nanodiamond clusters (Fig. 4.19 and Fig. 4.20 for 80 and 20 kV irradiated nanodiamonds respectively). Some irradiated nanodiamond clusters were surrounded by a number of other non-irradiated clusters. The optical microscope was able to resolve the clus-

ters of clusters irradiated at 80 kV but for the nanodiamonds irradiated at 20 kV, only one spot could be distinguished in Fig. 4.20 b). Therefore, the fluorescence signal likely came from both irradiated and non-irradiated clusters (see Fig. 4.20 where there are two regions of nanodiamonds in close proximity). Given that the nanodiamonds were still fluorescent after 80 kV irradiation, it is likely the 20 kV irradiated nanodiamonds also contained active NV centres. However, we should bear in mind the fact that we may not be able to resolve the same clusters in the optical microscope after irradiation. Therefore, we should irradiate isolated regions of HF@C_{60}/nanodiamonds without nearby clusters for the F@C_{60} ODMR measurements. The irradiated HF@C_{60} must also be within 10-20 nm of the nanodiamonds in order to be able to interact with the NV centre.

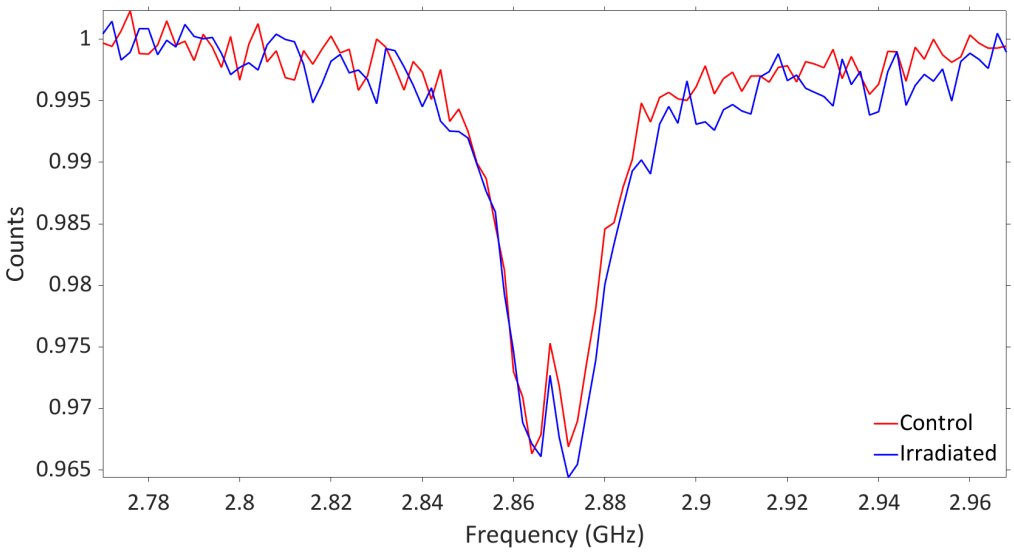

Figure 4.18. Comparison of the ODMR spectra of an irradiated cluster of nanodiamonds and a non-irradiated control cluster. The two spectra are almost identical and have the same midpoint of 2.868 GHz, the resonant frequency of microwaves that raises the NV into the degenerate $m_s = \pm\frac{1}{2}$ state. The ODMR spectra were acquired by V. Radu from the Optics and Photonics Research Group at the University of Nottingham.

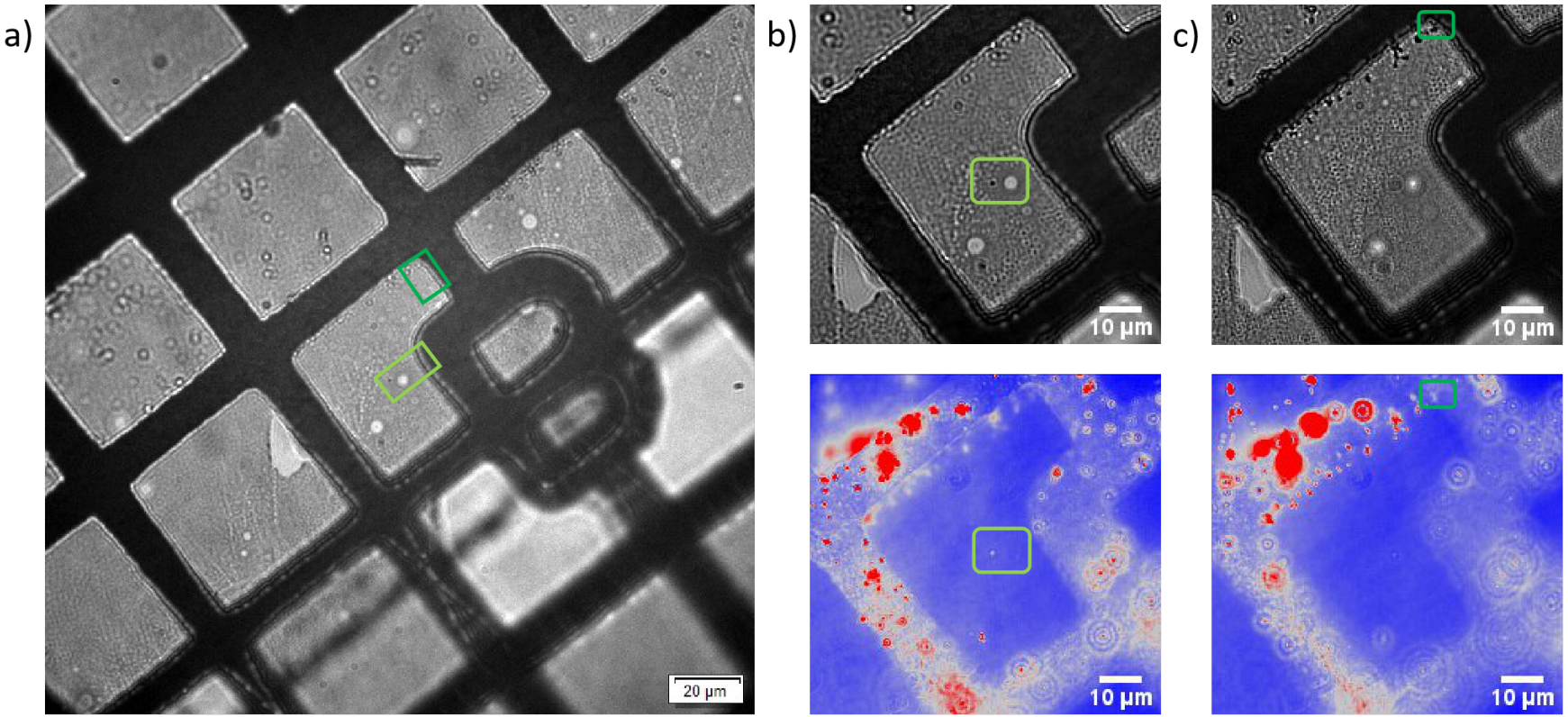

Figure 4.19. a) A low magnification of the same area around the letter 'B'. The regions irradiated with high (pale green) and low (dark green) total doses have been identified. The nanodiamond in the corner (dark green rectangle) appears out of focus as it is in a slightly different focal plane. b) This region was irradiated with a high total dose at 80 kV. The image below shows that the nanodiamond cluster is still fluorescent after irradiation. c) This region was irradiated with a low total dose at 80 kV. The nanodiamond cluster is in a slightly different focal plane and the focus was adjusted to be able to distinguish it from the carbon membrane (bright field image, top; the nanodiamond cluster (high dose region) now appears out of focus). The lower end of the nanodiamond cluster is still fluorescent after irradiation. Fluorescence imaging was carried out by V. Radu from the Optics and Photonics Research Group at the University of Nottingham.

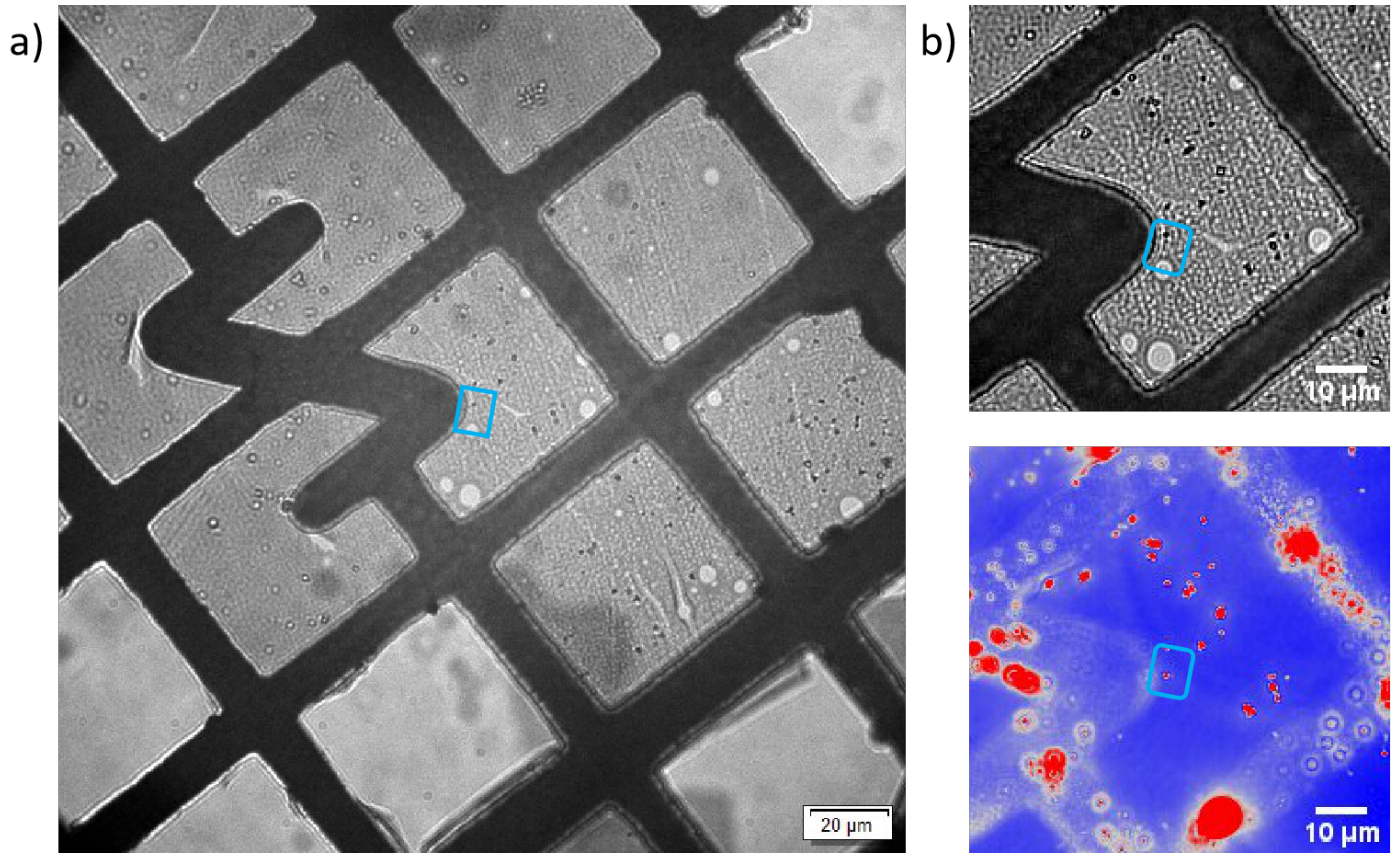

Figure 4.20. a) In the TEM image (Fig. 4.17) there were two clusters in the highlighted blue region. However, only one spot could be distinguished in the optical microscope. b) The nanodiamond cluster is clearly fluorescent after low dose irradiation at 20 kV but it is very likely that the signal might be coming from both those clusters. Based on the photoluminescence of nearby clusters of similar size it seems that at 20 kV the target nanodiamond cluster was slightly brighter than the cluster irradiated at 80 kV. Fluorescence imaging was carried out by V. Radu from the Optics and Photonics Research Group at the University of Nottingham.

An ODMR spectrum was acquired for the cluster irradiated with a high dose at 80 kV since if this cluster is ODMR-active, then the cluster irradiated with a low dose should also be ODMR-active as well. The nanodiamonds irradiated at 20 kV were too close to other non-irradiated clusters for the ODMR spectra to provide meaningful information. A control ODMR spectrum of a non-irradiated cluster of nanodiamonds was also acquired for comparison. The two spectra look more or less identical (Fig. 4.18); the midpoint between the two decreases in PL emission is at 2.868 GHz, the resonant frequency of microwaves that raises the NV into the degenerate $m_s = \pm\frac{1}{2}$ state. Both ODMR spectra were acquired at zero-field i.e. an external magnetic field was not applied.

Having determined with some confidence that the NV centres remained intact after irradiation, we moved on to irradiating a sample of nanodiamonds deposited on top of HF@C_{60} crystals on a gold TEM finder grid. The reasoning behind this orientation of the sample (as opposed to depositing nanodiamonds first and then HF@C_{60} on top) was that in the TEM, the HF@C_{60} ought to be below so that any knocked out H atoms may travel away into vacuum and therefore be less likely to interact with the nanodiamonds, reducing potential damage to the NV centres. We surveyed the TEM grid beforehand with a low electron flux to identify target HF@C_{60}/nanodiamond clusters. Four regions were irradiated at 80 kV (Fig. 4.21) while one was irradiated at 20 kV (Fig. 4.22).

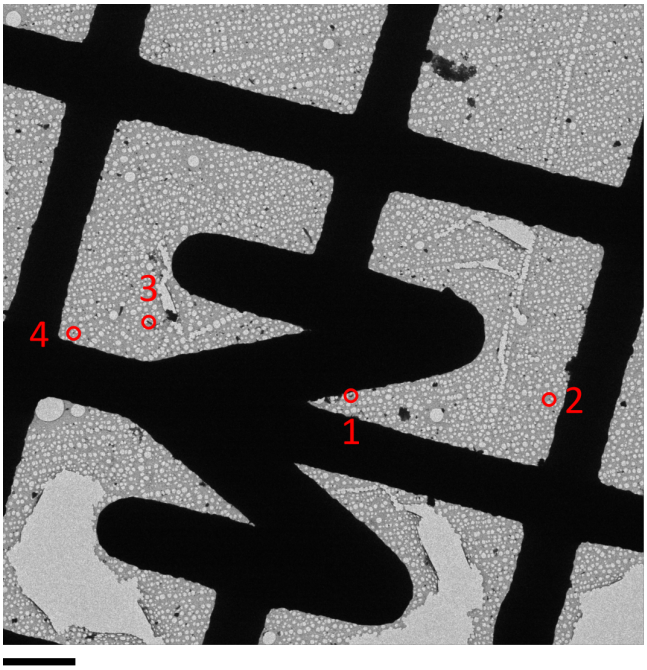

Figure 4.21. A low magnification image of the area around the letter 'M', used to locate the HF@C_{60} crystals and nearby nanodiamonds for ODMR after irradiation at 80 kV. The scale bar is 15 µm. The red circles with numerical labels indicate the regions of irradiation.

At 80 kV, the clusters of HF@C_{60}/nanodiamonds on average were irradiated using a flux of 4.64×10^{5} e^{-} nm^{-2} s^{-1} for a total dose of 1.40×10^{8} e^{-} nm^{-2} over 301 s (Fig. 4.23 and Fig. 4.24). This is comparable to the high dose irradiation experiments we carried out on the purely nanodiamond sample. Because the NV centres appeared to be quite beam stable, we decided to use a high total dose to maximise our chances of generating enough F@C_{60} in close proximity to NV centres for detection. We did not carry out SAD before and after imaging to avoid over-exposure of the sample to the electron beam. Fourier transforms (FTs) of the images at the end of irradiation showed diffraction spots corresponding to various crystallographic planes of C_{60}, confirming that we did not destroy the C_{60} crystal structure during irradiation. There were nanodiamonds near each cluster of HF@C_{60} which were not directly irradiated.

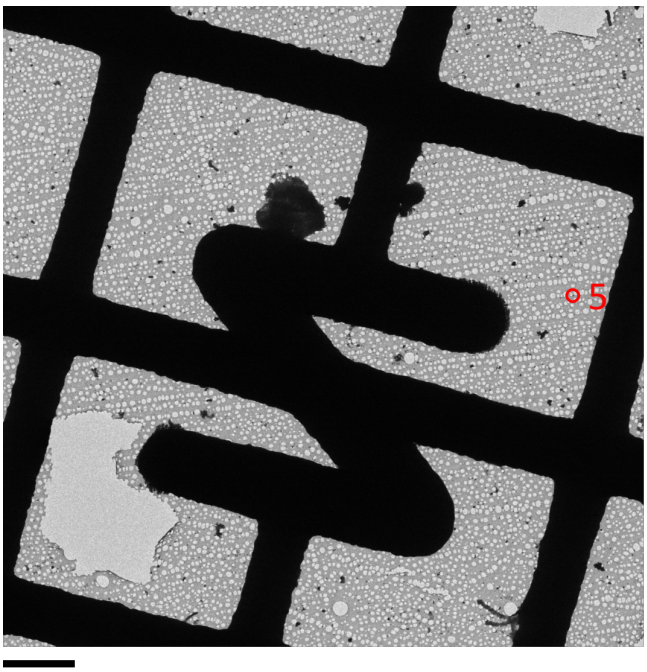

Figure 4.22. A low magnification image of the area around the letter 'N', used to locate the HF@C_{60} crystals and nearby nanodiamonds for ODMR after irradiation at 20 kV. The scale bar is 15 µm. The red circle with a numerical label indicate the region of irradiation.

Similarly at 20 kV, the cluster of HF@C_{60}/nanodiamonds was irradiated using a flux of 6.81×10^4 e^- nm^{-2} s^{-1} for a total dose of 5.00×10^7 e^- nm^{-2} over a period of 367 s (Fig. 4.25). High magnification imaging after irradiation revealed that we were still able to achieve Ångström resolution at 20 kV which was a pleasant surprise (Fig. 4.25 bottom right). FT of that image showed diffraction spots corresponding to the (1 1 1) plane of C_{60}. The scale bars of 20 kV images were based on values from 80 kV and therefore may be slightly incorrect because we had not yet calibrated the scales at 20 kV.

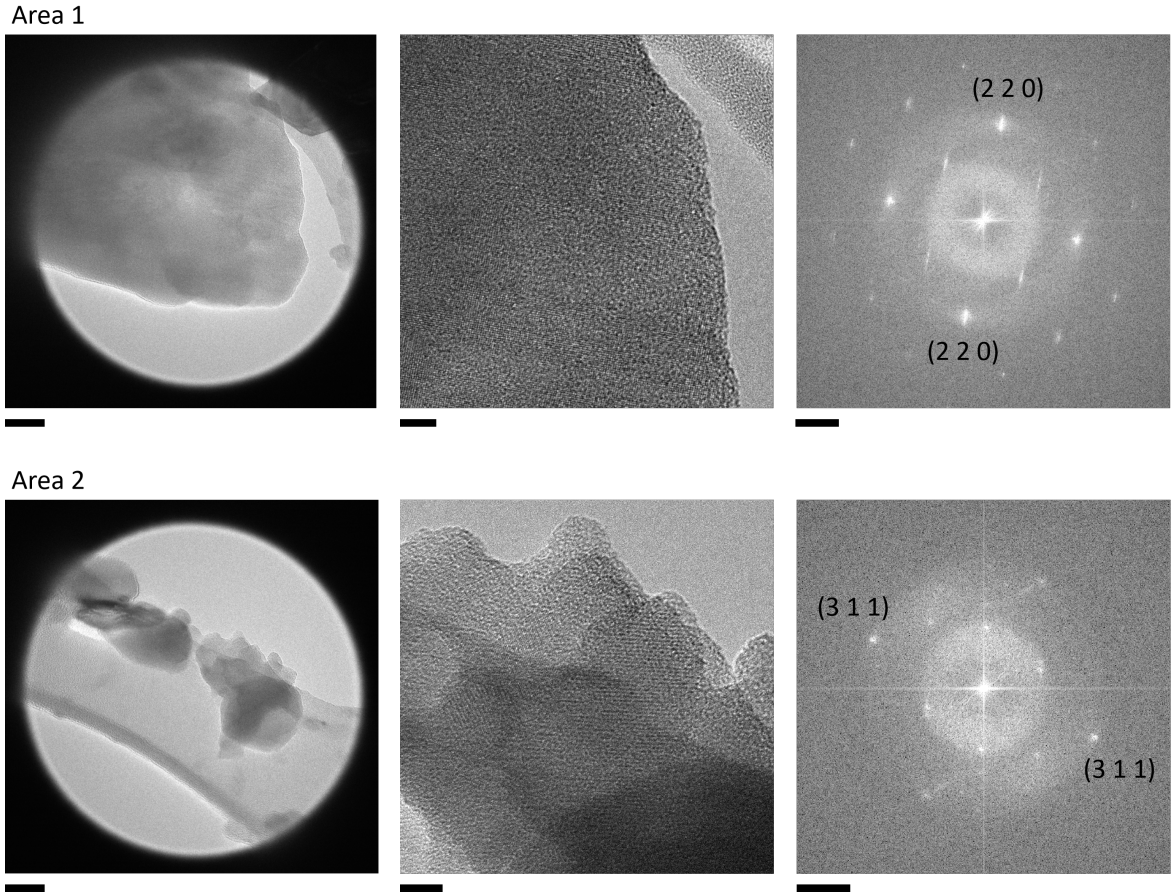

Figure 4.23. Irradiation experiments of the HF@C_{60}/nanodiamonds at 80 kV. All images in the left column have an illuminated area that indicates the region that was irradiated. The average total dose was 1.40×10^{8} e^{-} nm^{-2}. The average flux was 4.64×10^{5} e^{-} nm^{-2} s^{-1}. The average irradiation period was 301 s. The scale bars for those images are 50 nm. All images in the middle column are of high magnification after irradiation. The scale bars for those images are 10 nm. All images in the right column are FTs of the high magnification images in the middle column. The scale bars are 1 1/nm. Area 1. The illuminated region was irradiated at 80 kV with a total dose of 1.39×10^{8} e^{-} nm^{-2} using a flux of 2.32×10^{5} e^{-} nm^{-2} s^{-1} over a period of 300 s. The FT of the high magnification image shows diffraction spots corresponding to the (2 2 0) plane of C_{60}.[36] The d-spacing is 5.106 Å. Area 2. The illuminated region was irradiated at 80 kV with a total dose of 1.37×10^{8} e^{-} nm^{-2} using a flux of 2.28×10^{5} e^{-} nm^{-2} s^{-1} over a period of 302 s. The FT of the high magnification image shows diffraction spots corresponding to the (3 1 1) plane of C_{60}.[36] The d-spacing is 4.368 Å.

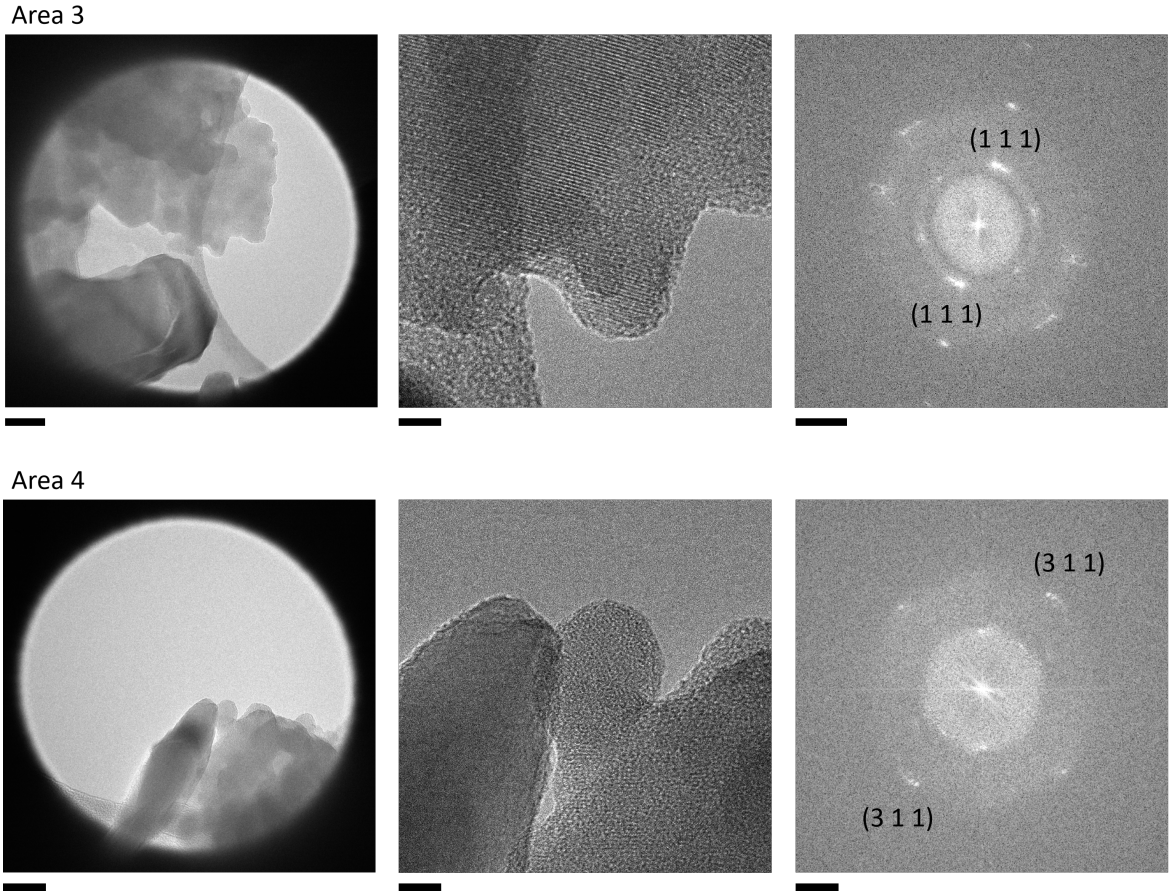

Figure 4.24. Irradiation experiments of the HF@C_{60}/nanodiamonds at 80 kV. All images in the left column have an illuminated area that indicates the region that was irradiated. The average total dose was 1.40×10^{8} e^{-} nm^{-2}. The average flux was 4.64×10^{5} e^{-} nm^{-2} s^{-1}. The average irradiation period was 301 s. The scale bars for those images are 50 nm. All images in the middle column are of high magnification after irradiation. The scale bars for those images are 10 nm. All images in the right column are FTs of the high magnification images in the middle column. The scale bars are 1 1/nm. Area 3. The illuminated region was irradiated at 80 kV with a total dose of 1.37×10^{8} e^{-} nm^{-2} using a flux of 2.26×10^{5} e^{-} nm^{-2} s^{-1} over a period of 303 s. The FT of the high magnification image shows diffraction spots corresponding to the (1 1 1) plane of C_{60}.[36] The d-spacing is 8.337 Å. Area 4. The illuminated region was irradiated at 80 kV with a total dose of 1.46×10^{8} e^{-} nm^{-2} using a flux of 2.43×10^{5} e^{-} nm^{-2} s^{-1} over a period of 300 s. The FT of the high magnification image shows diffraction spots corresponding to the (3 1 1) plane of C_{60}.[36] The d-spacing is 4.417 Å.

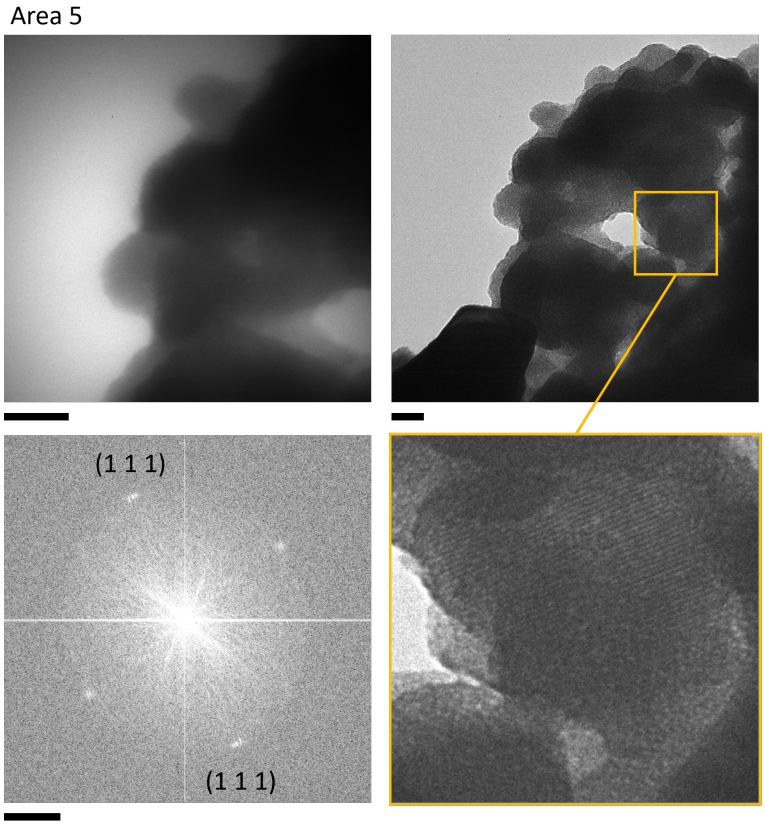

Figure 4.25. Area 5. Top left: the illuminated region was irradiated at 20 kV with a total dose of 5.00×10^{7} e^{-} nm^{-2} using a flux of 6.81×10^{4} e^{-} nm^{-2} s^{-1} over a period of 367 s. The scale bar is 20 nm. Top right: high magnification image after irradiation. The scale bar is 20 nm. An expanded image is shown bottom right with an orange border to show that it is possible to achieve Å resolution at 20 kV. Bottom left: FT of the high magnification image showing the diffraction spots corresponding to the (2 2 0) plane of C_{60}.[36] The d-spacing is 8.418 Å. The scale bar is 0.5 1/nm.

Having completed our irradiation experiments, we then carried out ODMR spectroscopy on each area. We are unable to write a satisfactory end to our quest for the F radical as of yet because fluorescence imaging and T_1-based relaxometry are currently still ongoing. However, initial results looked quite promising and the sample had been taken to another ODMR facility in Melbourne for pulsed experiments where short pulses of microwaves are used in a pump-probe scheme. This is a more sensitive setup where the laser is turned off during the sensing period[42] and should give us the best chance of detecting any F@C_{60}.

4.4 Conclusions

We have developed a general method that combines the use of multiple bulk and local probe analytical techniques. A single sample was analysed using high resolution TEM and STEM, electron diffraction, vibrational EELS, EDXS, EPR spectroscopy, as well as ODMR. There is no reason not to push this further and include techniques such as atomic force microscopy (AFM) or X-ray photoelectron spectroscopy (XPS) to study the surface topology and chemistry, if this is appropriate for the sample. This "lab on a grid" approach correlates data from different laboratories, different machines, to give us a better overall understanding of a sample.

Application of this multi-faceted approach has shown us that after irradiation, the H−F bond is broken (using vib-EELS), that fluorine is still present in the endohedral fullerene crystal (using EDXS), and that the crystallinity has not been excessively damaged (using electron diffraction). It was challenging to generate enough spins for EPR spectroscopy using the irradiation in a TEM so we turned to ODMR for detection of the F radical. Through careful experimentation and control of various parameters such as electron flux, we were able to irradiate the HF@C_{60} and nanodiamond sample without damaging the NV centres. We currently await the ODMR results from Melbourne which may finally provide us with concrete evidence of the existence of F@C_{60}.

During our experimentation with irradiating HF@C_{60}, we have succeeded in aligning and operating the JEOL 2100Plus microscope at 20 kV, a voltage much lower than the typical operating voltages of a Plus. There has been much interest in developing TEMs for operation at very low accelerating voltages, such as the SALVE (Sub-Ångstrom Low-Voltage Electron microscopy) project in Germany,[45] to reduce sample damage as much as possible in order to facilitate the study of particularly electron-beam-sensitive materials. Knock-on damage, where an incident electron transfers kinetic energy to atoms in the sample via ballistic collisions, is

a major source of damage in TEMs. Reducing the voltage is one method of reducing knock-on damage. Another reason for using lower voltages is that elastic and inelastic scattering cross sections increase at lower voltages which increases image contrast. This is an attractive feature for imaging biological and organic samples. However, going to lower voltages increases the likelihood of multiple scattering which reduces resolution so samples for high resolution LV-TEM (below 80 kV) must be incredibly thin; at 20 kV the requirement is less than 10 nm in thickness.[45] Low voltages are also useful for EELS because operating a TEM at low voltages reduces the beam current and therefore the ZLP tail.[46] This reduces the background noise which is useful for studying optical transitions, for example the direct band gap measurement of silicon using 13 keV electrons.[47]

Most TEMs that are designed to operate at low voltages (below 80 kV) are extremely expensive, custom-built, and require a high level of expertise to operate. The Plus, on the other hand, is a commercially available 'work horse' TEM used in many facilities for study of samples ranging from materials to biological specimens. Our JEOL 2100Plus can now be routinely aligned at 20 kV and has the potential for use in characterisation of many different types of samples.

4.5 Future Work

The most exciting "lab on a grid" experiment we have carried out has been the combination of TEM and ODMR because, as far as we know, these are two techniques that have not be correlated with one another before. The ideal TEM-ODMR experiment would involve imaging and detection of thin layers of strongly paramagnetic species such as the metal oxide VO_3 encapsulated within SWNTs. This material is interesting for its potential use in energy storage but has not been fully characterised using TEM or ODMR, and certainly not with both on the same TEM grid. VO_3@SWNTs is quite stable to the electron beam which should allow for atomic resolution TEM without significant beam damage. Other samples that would be interesting for TEM-ODMR are the organic crystals from chapter three. Irradiation of such crystals clearly changes their crystal structure and we suspect that the reactions begin via emission of hydrogen radicals. We already know the critical doses of these molecules and we also know what dose to use in order to not damage the NV centres. ODMR after TEM irradiation of organic crystal/nanodiamond samples may be able to tell us more about the nature of these irradiated crystals.

Aside from future TEM-ODMR experiments, we have also continued pushing the capabilities of the non-aberration-corrected LaB_6 filament JEOL 2100Plus TEM (Plus). We hope to present a method of aligning the Plus at 20 kV and subsequent characterisation of the performance of the Plus at 20 kV such as demonstrating the use of EDXS (Fig. 4.26) and diffraction (Fig. 4.27) and comparing the results to 80 kV.

Alignments of conventional TEMs at very low voltages have been done for similar reasons; such microscopes are more readily available and there is less requirement for extensive funding. Indeed, the TECNAI T20 LaB_6 microscope has been aligned and used as an analytical low-voltage TEM down to beam energies of 10 kV.[47,48]

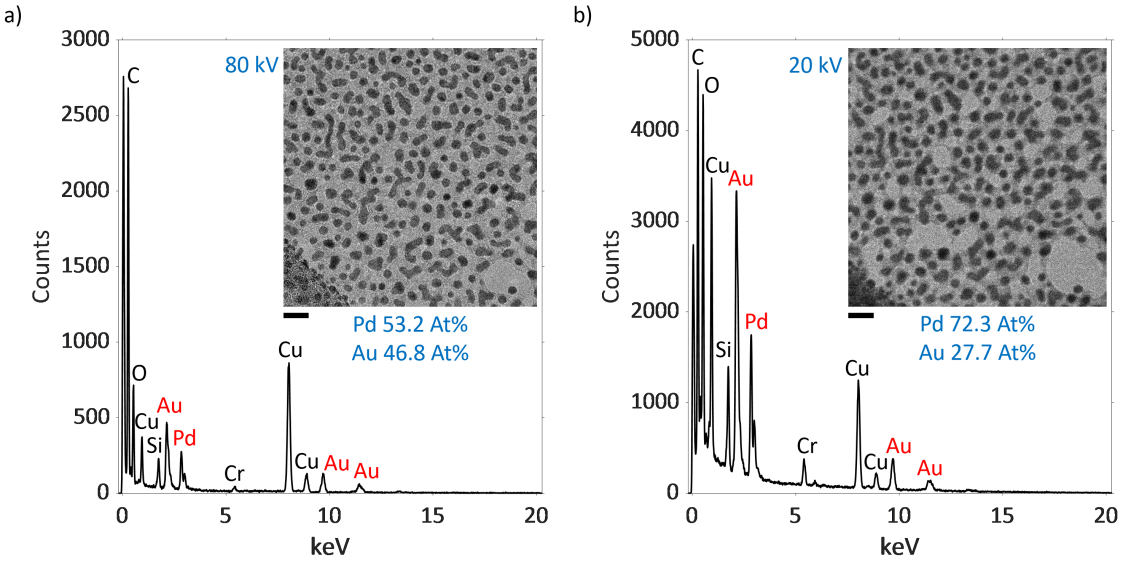

Figure 4.26. a) EDXS at 80 kV of Au and Pd monometallic nanoparticles on graphene oxide film. Inset: Image of a mixture of Au and Pd nanoparticles imaged at 80 kV. b) Energy dispersive X-ray spectroscopy (EDXS) at 20 kV of Au and Pd monometallic nanoparticles on graphene oxide film. Inset: Image of the same area of Au and Pd nanoparticles at 20 kV. The scale bars are 10 nm. There is visible beam damage to the supporting graphene oxide film.

However, most microscopes are used with the factory settings and it is not widely known that conventional microscopes can be aligned at much lower voltages. Showing users that it is possible for them to align their Plus microscope at unconventional voltages may inspire more researchers to explore the use of very low voltages for their investigations.

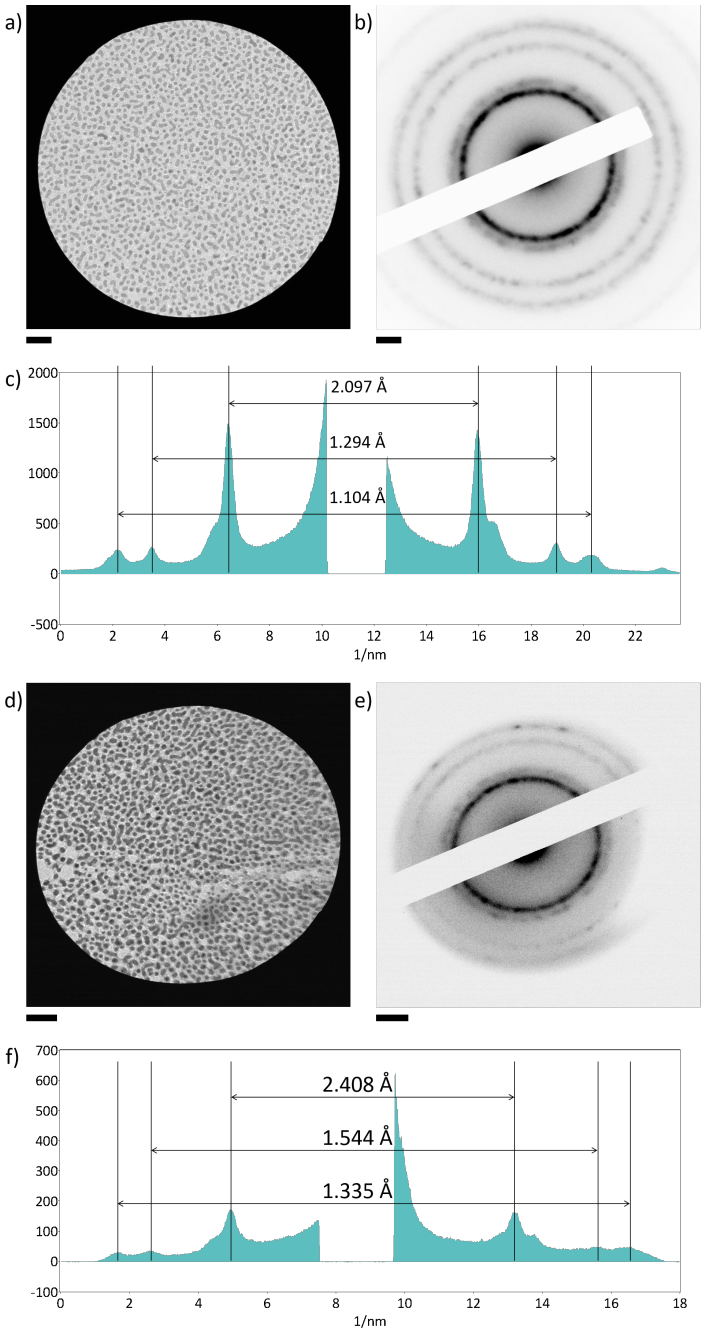

Figure 4.27. Selected area diffractions of similar areas of Au and Pd nanoparticles on graphene oxide film. a) SA diffraction at 80 kV of illuminated region. The scale bar is 20 nm. b) Diffraction pattern at 80 kV of Au and Pd nanoparticles. The scale bar is 2 1/nm. c) Profile of the diffraction pattern. d) SA diffraction at 20 kV of illuminated region. The scale bar is 20 nm. e) Diffraction pattern at 20 kV of Au and Pd nanoparticles. The scale bar is 2 1/nm. f) Profile of the diffraction pattern.

4.6 Experimental Methods

HF@C_{60} (from S. Alom, M. H. Levitt, and R. J. Whitby at the University of Southampton) was synthesised and purified by previously reported methods.[30] Crystals of HF@C_{60} were deposited onto lacey carbon copper TEM grids by drop casting suspensions in isopropanol or methanol.

4.6.1 STEM and vib-EELS data collection

All STEM and vib-EELS data were collected by Q. M. Ramasse at the SuperSTEM laboratory. The energy calibration of vib-EELS data was also carried out by Q. M. Ramasse.

STEM images were carried on a monochromated Nion UltraSTEM 100MC 'Hermes' operated at an accelerating voltage of 60 kV at the SuperSTEM laboratory. This microscope is equipped with a 5th order probe aberration corrector enabling a probe size of approximately 0.09 nm at 60 kV with a convergence semi-angle of 31 mrad in the conditions used for imaging. The monochromator improves the native 350 meV energy resolution of the cold field emitter of this instrument to approximately 15 meV in practical experimental conditions (estimated from the zero loss peak, ZLP, full width half-maximum), with no loss of spatial resolution, enabling the acquisition of molecular vibrational signals. High-angle annular-dark-field images were recorded using a detector with a semi-angular range of 85-195 mrad. EEL spectra were acquired on a Gatan Enfinium ERS spectrometer, modified with high stability electronics for improved resolution. The EELS collection semi-angle was 36 mrad, with spectra acquired in 'dual-EELS' mode whereby two spectra are recorded quasi simultaneously; one with extremely short exposure time (typically 0.001 s) contains the full zero loss and is used for energy calibration, while the other is optimised for higher signal-to-noise ratio with longer acquisition times (0.15

s) with the zero-loss peak shifted off the camera to avoid saturation. Spectra in aloof geometry were averaged from large Spectrum Images (whereby the probe is scanned across a defined region of interest, and the EELS and imaging signal acquired at each probe position).

4.6.2 Background subtraction of vib-EEL spectra

The three spectra were extracted from the same region in the Spectrum Images with the same number of pixels in order to keep the total electron doses comparable. The dose per pixel was the same for all spectra. Background subtraction of the vib-EELS data was carried out using a series of scripts written in MATLAB by K. L. Y. Fung.[49] The backgrounds below 0.12 eV of all three spectra were fitted with a two-term exponential (of the form $f(x) = ae^{bx} + ce^{dx}$ using a non-linear least squares method. The results of the fit are as follows.

Pristine "fresh" area coefficients (with 95% confidence bounds):

$a = 8.313e^5(0.4786e^5, 1.184e^6)$

$b = -42.9(-90.47, 4.667)$

$c = 1.459e^6(8.704e^5, 2.048e^6)$

$d = -13.18(-15.92, -10.45)$

Adjusted R-square value is 0.9999

Area after moderate irradiation (with 95% confidence bounds):

$a = 2.963e^5(5.757e^4, 5.349e^5)$

$b = -55.5(-113.6, 2.639)$

$c = 7.145e^5(5.883e^5, 8.407e^5)$

$d = -12.29(-13.79, -10.79)$

Adjusted R-square value is 0.9994

Area after high irradiation (with 95% confidence bounds):

$a = 4.839e^5(3.861e^5, 5.817e^5)$

$b = -43.53(-64.46, -22.61)$

$c = 5.193e^5(3.98e^5, 6.407e^5)$

$d = -9.075(-10.83, -7.322)$

Adjusted R-square value is 0.9996

4.6.3 EDXS data collection

EDXS and TEM imaging were carried out by K. L. Y. Fung at the nanoscale and microscale research centre (nmRC) at the University of Nottingham.

EDXS as well as the corresponding TEM images and diffraction patterns of a crystal of HF@C_{60} were collected using a JEOL 2100Plus instrument operated at an accelerating voltage of 80 kV. Six EDX spectra were taken sequentially for a total dose of 2.29$\times 10^7$ e^- nm^{-2} using an electron flux of 1.27$\times 10^4$ e^- nm^{-2} s^{-1}.

4.6.4 Aligning the JEOL 2100Plus at 20 kV

Alignment of the JEOL 2100Plus was carried out by K. L. Y. Fung and M. W. Fay at the nanoscale and microscale research centre (nmRC) at the University of Nottingham.

The 20 kV alignment procedure for the JEOL 2100Plus is described in the following paragraphs. We recommend using very low lighting as the beam will not be bright and having two microscopists for the alignment as human eyes will tire easily from staring at the dim beam and incredibly fuzzy images.

The microscope must be fully aligned at 80 kV before atempting alignment at 20 kV. Set the **Condenser Lens aperture** to the largest (150 µm diameter) and remove all other apertures from the beam path. Set the **Spot Size** value to 1 and the **Alpha** value to 3 for ease of alignment. The **Bias** should give a suitably large current increase above dark field and intensity (at 80 kV the beam current value should be

40 $\pm$ 10 % µA). The same **Bias** will be used at 20 kV. Save the alignment. Save a screenshot of the **Lens**/**Def Monitor** (hex values). Turn the **Filament** OFF. Take the voltage down to 20 kV with **HT Scheduling** using a step volt of 0.1 kV with an interval of 1 s for a total time of 10 min. After the voltage has been reduced to 20 kV, turn **HT Wobble** ON for 5 min to improve stability of the beam current. For our microscope at the nmRC, the beam current was 11.3 µA at an emission target of 58% at 20 kV; at 80 kV the beam current was 43.5 µA.

Take the **Magnification** to 10k. Double press **Standard Focus**. The Std Focus is set to the same value as at 80 kV. If the beam is not visible after pressing **Standard Focus**, take **CLA1** (**Shift X**/**Y**) to 8000 (hex value) and vary the **Objective Focus** to find the beam. Once the beam is visible, reduce the **Objective Focus** back to **Standard Focus** while using **Z Up**/**Down** to maintain focus. After this, the beam should be on the large viewing screen and the microscope should be at **Standard Focus**.

Centre the beam with **Gun Align** and **Shift X**/**Y**. Correct any **Condenser Astigmatism**. If the beam is particularly dim, it will be difficult to correct **Gun Align** because the current density may be far too low to be monitored on the small viewing screen. It is possible that **CLA1** is far from being aligned so approximately correct this using **HT Wobble** and **Objective Lens**. Once that has been done, correct **Gun Align** using **Shift X**/**Y**. After this, iteratively correct **CLA2** using **HT Wobble** and **Objective Lens** until **CLA2** is aligned using either the beam centre or a sample feature for correction depending on which is easiest. Do the same for **Tilt Wobble** with **Def X**/**Y** at **Standard Focus** from 80 kV. All alignments may fluctuate significantly and therefore will need frequent correction. Once all of the above has been aligned and fluctuations have minimised, align **Spot Size** 1 with **Gun Align** ON and **Spot Size** 5 with **Gun Align** OFF. Run **Lens Relaxation** to reduce hysteresis and repeat the entire alignment procedure if necessary.

4.6.5 Imaging at 20 kV

Take the **Magnification** up to 50k. Prepare the **Gain Reference** with a beam intensity of 500 counts. Bring the image into focus on the camera using **Z Up/Down**. If the Z limit is reached, use **Objective Focus**. Centre the beam on the camera (the beam will not be bright enough to burn the camera at 20 kV). Find an identifiable feature in the sample (an ideal calibration sample would be heavy metal nanoparticles on graphene oxide). Check **Objective Lens** is aligned by varying **Objective Focus**. The image should blur rather than swing across the screen. Take an image and check for **Objective Lens Astigmatism**. There should be even contrast around the hole. Take the **Magnification** up to 100k or higher, take an image, and check **Objective Lens Astigmatism** again. For example, striping across the image indicates astigmatism. Save the **Lens/Def Monitor** in imaging mode.

4.6.6 Diffraction at 20 kV

We were able to see the beam when we switched to SA diff mode. If 80 kV SA diff mode is well aligned, it should be reasonable at 20 kV as well. Set camera length to 20 or 10 cm. Move the beam to centre using **PLA Def X/Y**. Correct **Shift X/Y** using **Def X/Y** at spread beam (where beam is a spot). Go back to imaging mode and put in 2nd smallest condenser aperture and 3rd smallest SA aperture. Go to SA diff mode again. The **Diff Focus** may need to be changed to reduce the beam to a spot. If the beam is fully spread, the diffraction pattern may be too dim. We selected a reasonable beam intensity and focused the spot using **Diff Focus**. Save the **Lens/Def Monitor** in SA diff mode.

4.6.7 EPR data collection

EPR was carried out by J. McMaster at the University of Nottingham.

HF@C_{60} was dispersed onto gold finder grids with holey carbon film by drop casting from a methanol suspension. One sample was irradiated at 80 kV; one at 20 kV. The irradiated endohedral fullerenes (as well as the holey carbon film) was washed off the TEM grid by sonicating the grid in carbon disulfide (0.1 mL) for 1 hr, after which the carbon disulfide solution was pipetted into a quartz EPR tube and the solvent gradually removed under vacuum. After all solvent had evaporated, the EPR tubes were kept under vacuum for a further 1 min. EPR spectra were collected on a Bruker EMX X-band EPR spectrometer as samples in the solid state at 77K.

4.6.8 Preparation of nanodiamonds for irradiation experiments

Preparation of nanodiamonds for irradiation experiments was carried out by V. Radu from the from the Optics and Photonics Research Group at the University of Nottingham.

The nanodiamonds were refluxed in an acid mixture (sulphuric acid 96% : nitric acid 60% 1:1) for 2 hr. The mixture was then neutralised with sodium hydroxide and the nanodiamonds spun down and resuspended in water (washing repeated five times with deionised water).

4.6.9 Preparation of HF@C_{60}/nanodiamond TEM sample

HF@C_{60} was dispersed onto gold finder grids with holey carbon film by drop casting from a methanol suspension. Afterwards, nanodiamonds were deposited onto the same TEM grid from a suspension of water.

4.6.10 ODMR data collection

ODMR and fluorescence imaging was carried out by V. Radu from the Optics and Photonics Research Group at the University of Nottingham. Experimental details were discussed with both M. L. Mather and V. Radu.

The experimental setup consists of a custom-designed printed circuit board (PCB), an inverted fluorescence microscope (Olympus IX83), a signal generator (Keysight) and a microwave (MW) amplifier (AR). The PCB was designed to have an aperture enabling illumination of the sample via the fluorescence microscope and a fitted 50 Ohm attenuator for the delivery of microwaves (MWs). A straight copper wire (0.125 mm diameter) running across the top of a glass coverslip mounted over the aperture is electrically connected to 50 Ohm tracks on the PCB to deliver MWs from a Keysight N2581B vector signal generator and an AR 20S1G4 MW amplifier. The signal generator power and the MW amplifier gain were 0 dBm and 30%, respectively. NV centres were illuminated with a mercury arc lamp filtered through a narrow bandpass excitation filter centred at 540 nm.The light was subsequently focused on the back focal plane of an oil-immersion 60$\times$ TIRF objective lens (NA = 1.49), providing a power density of 1 W/cm^2 at the sample position. The TEM grid was placed between the copper wire and the glass slide. Emitted photoluminescence (PL) was filtered through a 575 nm long-pass filter and imaged onto a sCMOS camera (Photometrics 95 Prime B) providing a maximum field of view of 200 µm $\times$ 200 µm. Detailed descriptions and schematics of the experimental setup can be found in the following references.[50,51]

Optically detected magnetic resonance (ODMR) spectra were acquired using a continuous wave (CW) measurement regime in which illumination was constant and images of PL were acquired as the MW frequency was swept to probe the ground state (2.77-2.97 GHz) NV-spin transitions. Image acquisition was synchronized with MW sweeps using an Olympus Real-Time Controller (RTC) via the Olym-

pus CellSens software (Tokyo, Japan). The resulting images at each frequency were analysed to extract the PL intensity, determined by summing pixel intensities from fields of view corresponding to individual nanodiamond aggregates. At each frequency, 10 repeats of measurements were performed. ODMR spectra were produced by plotting average PL intensity from all repeats. The spectra were then normalized by dividing all average PL intensities by the maximum averaged intensity within the sweep.

4.7 List of publications

1. K. L. Y. Fung, M. W. Fay, S. M. Collins, D. M. Kepaptsoglou, S. T. Skowron, Q. M. Ramasse and A. N. Khlobystov, "Accurate EELS background subtraction - an adaptable method in MATLAB", *Ultramicroscopy*, 2020, **217**, 113052.

2. J. Biskupek, S. T. Skowron, C. T. Stoppiello, G. A. Rance, S. Alom, K. L. Y. Fung, R. J. Whitby, M. H. Levitt, Q. Ramasse, U. Kaiser, E. Besley and A. N. Khlobystov, "Bond Dissociation and Reactivity of HF and H_2O in a Nano Test Tube", *ACS Nano*, 2020, **14**, 11178-11189.

4.8 References

1. H. W. Kroto, J. R. Heath, S. C. O'Brien, R. F. Curl and R. E. Smalley, *Nature*, 1985, **318**, 162–163.
2. J. R. Heath, S. C. O'Brien, Q. Zhang, Y. Liu, R. F. Curl, H. W. Kroto, F. K. Tittel and R. E. Smalley, *J. Am. Chem. Soc.*, 1985, **107**, 7779–7780.
3. H. Shinohara, H. Yamaguchi, N. Hayashi and H. Sato, *J. Phys. Chem.*, 1993, **97**, 4259–4261.
4. H. Shinohara, H. Sato, M. Ohkohchi, Y. Ando, T. Kodama, T. Shida, T. Kato and Y. Saito, *Nature*, 1992, **357**, 52–54.
5. C. S. Yannoni, M. Hoinkis, M. S. de Vries, D. S. Bethune, J. R. Salem, M. S. Crowder and R. D. Johnson, *Science*, 1992, **256**, 1191–1192.
6. D. S. Bethune, R. D. Johnson, J. R. Salem, M. S. de Vries and C. S. Yannoni, *Nature*, 1993, **366**, 123–128.
7. W. Krätschmer, L. D. Lamb, K. Fostiropoulos and D. R. Huffman, *Nature*, 1990, **347**, 354–358.
8. Y. Chai, T. Guo, C. Jin, R. E. Haufler, L. P. F. Chibante, J. Fure, L. Wang, J. M. Alford and R. E. Smalley, *J. Phys. Chem.*, 1991, **95**, 7564–7568.
9. R. Tenne, *Adv. Mater.*, 1995, **7**, 965–995.
10. S. Nagase, K. Kobayashi and T. Akasaka, *Bull. Chem. Soc. Jpn.*, 1996, **69**, 2131–2142.
11. T. Nakane, Z. Xu, E. Yamamoto, T. Sugai, T. Tomiyama and H. Shinohara, *Fullerene Sci. Technol.*, 1997, **5**, 829–838.
12. H. Shinohara, *Rep. Prog. Phys.*, 2000, **63**, 843–892.
13. H. Shinohara, *Phil. Trans. R. Soc. A*, 2016, **374**, 20150325.
14. M. Saunders, H. A. Jiménez-Vázquez, R. J. Cross and R. J. Poreda, *Science*, 1993, **259**, 1428–1430.
15. L. Dunsch and S. Yang, *Phys. Chem. Chem. Phys.*, 2007, **9**, 3067–3081.
16. M. N. Chaur, F. Melin, A. L. Ortiz and L. Echegoyen, *Angew. Chem. Int. Ed.*, 2009, **48**, 7514–7538.
17. A. Rodríguez-Fortea, A. L. Balch and J. M. Poblet, *Chem. Soc. Rev.*, 2011, **40**, 3551–3563.

18. L. Feng, Y. Hao, A. Liu and Z. Slanina, *Acc. Chem. Res.*, 2019, **52**, 1802–1811.

19. T. A. Murphy, T. Pawlik, A. Weidinger, M. Höhne, R. Alcala and J.-M. Spaeth, *Phys. Rev. Lett.*, 1996, **77**, 1075–1078.

20. A. Weidinger, M. Waiblinger, B. Pietzak and T. A. Murphy, *Appl. Phys. A*, 1998, **66**, 287–292.

21. Y. Rubin, *Chem. Eur. J.*, 1997, **3**, 1009–1016.

22. Y. Rubin, T. Jarrosson, G.-W. Wang, M. D. Bartberger, K. N. Houk, G. Schick, M. Saunders and R. J. Cross, *Angew. Chem. Int. Ed.*, 2001, **40**, 1543–1546.

23. K. Komatsu, *Phil. Trans. R. Soc. A*, 2013, **371**, 20110636.

24. K. Komatsu, M. Murata and Y. Murata, *Science*, 2005, **307**, 238–240.

25. H. Sawa, Y. Wakabayashi, Y. Murata, M. Murata and K. Komatsu, *Angew. Chem. Int. Ed.*, 2005, **44**, 1981–1983.

26. K. Kurotobi and Y. Murata, *Science*, 2011, **333**, 613–616.

27. J. Y.-C. Chen, Y. Li, M. Frunzi, X. Lei, Y. Murata, R. G. Lawler and N. J. Turro, *Phil. Trans. R. Soc. A*, 2013, **371**, 20110628.

28. M. Levitt, *Phil. Trans. R. Soc. A*, 2013, **371**, 20120429.

29. M. Levitt and A. Horsewill, *Phil. Trans. R. Soc. A*, 2013, **371**, 20130124.

30. A. Krachmalnicoff, R. Bounds, S. Mamone, S. Alom, M. Concistré, B. Meier, K. Kouřil, M. E. Light, M. R. Johnson, S. Rols, A. J. Horsewill, A. Shugai, U. Nagel, T. Rõõm, M. Carravetta, M. H. Levitt and R. J. Whitby, *Nature Chem.*, 2016, **8**, 953–957.

31. X. Lu, L. Feng, T. Akasaka and S. Nagase, *Chem. Soc. Rev.*, 2012, **41**, 7723–7760.

32. J. Biskupek, S. T. Skowron, C. T. Stoppiello, G. A. Rance, S. Alom, K. L. Y. Fung, R. J. Whitby, M. H. Levitt, Q. M. Ramasse, U. Kaiser, E. Besley and A. N. Khlobystov, *ACS Nano*, 2020, **14**, 11178–11189.

33. O. L. Krivanek, T. C. Lovejoy, N. Dellby, T. Aoki, R. W. Carpenter, P. Rez, E. Soignard, J. Zhu, P. E. Batson, M. J. Lagos, R. F. Egerton and P. A. Crozier, *Nature*, 2014, **514**, 209–212.

34. J. A. Hachtel, A. R. Lupini and J. C. Idrobo, *Sci. Rep.*, 2018, **8**, 5637.

35. G. A. Kuipers, D. F. Smith and A. H. Nielsen, *J. Chem. Phys.*, 1956, **25**, 275–279.

36. D. L. Dorset and M. P. McCourt, *Acta. Cryst.*, 1993, **50**, 344–351.

37. P. A. Crozier, *Ultramicroscopy*, 2017, **180**, 104–114.

38. C. E. Moore, *NBS Circular*, 1949, **1**, 467.

39. P. L. Hansen and P. J. Fallon, *Chem. Phys. Lett.*, 1991, **181**, 367–372.

40. Y. Artzi, Y. Twig and A. Blank, *Appl. Phys. Lett.*, 2015, **106**, 084104.

41. S. Probst, A. Bienfait, P. Campagne-Ibarcq, J. J. Pla, B. Albanese, J. F. D. S. Barbosa, T. Schenkel, D. Vion, D. Esteve, K. Mølmer, J. J. L. Morton, R. Heeres and P. Bertet, *Appl. Phys. Lett.*, 2017, **111**, 202604.

42. R. Schirhagl, K. Chang, M. Loretz and C. L. Degen, *Annu. Rev. Phys. Chem.*, 2014, **65**, 85–105.

43. D. A. Simpson, R. G. Ryan, L. T. Hall, E. Panchenko, S. C. Drew, S. Petrou, P. S. Donnelly, P. Mulvaney and L. C. L. Hollenberg, *Nature Commun.*, 2017, **8**, 458.

44. R. W. G. Wyckoff, *Crystal Structures - Volume 1*, New York: Interscience Publishers, 2nd edn., 1963.

45. U. Kaiser, J. Biskupek, J. C. Meyer, J. Leschner, L. Lechner, H. Rose, M. Stöger-Pollach, A. N. Khlobystov, P. Hartel, H. Müller, M. Haider, S. Eyhusen and G. Benner, *Ultramicroscopy*, 2011, **111**, 1239–1246.

46. M. Stöger-Pollach, *Micron*, 2010, **41**, 577–584.

47. M. Stöger-Pollach, *Ultramicroscopy*, 2014, **145**, 98–104.

48. M. Stöger-Pollach, *Ultramicroscopy*, 2014, **145**, 94–97.

49. K. L. Y. Fung, M. W. Fay, S. M. Collins, D. M. Kepaptsoglou, S. T. Skowron, Q. M. Ramasse and A. N. Khlobystov, *Ultramicroscopy*, 2020, **217**, 113052.

50. V. Radu, J. C. Price, S. J. Levett, K. K. Narayanasamy, T. D. Bateman-Price, P. B. Wilson and M. L. Mather, *ACS Sens.*, 2019, DOI: 10.1021/acssensors.9b01903.

51. J. C. Price, S. J. Levett, V. Radu, D. A. Simpson, A. M. Barcons, C. F. Adams and M. L. Mather, *Small*, 2019, **15**, 1900455.

CHAPTER 5

Concluding Remarks

"His eyes were eggs of unstable crystal, vibrating with a frequency whose name was rain and the sound of trains, suddenly sprouting a humming forest of hair-fine glass spines." - William Gibson, Neuromancer (1984)

During the three years that culminated in this thesis, we have developed two general kinetic methods to study reactions at the single-molecule level. The kinetic models were based upon chemical kinetics, using familiar forms of rate equations and the Arrhenius equation. Imaging PCC polymerisation reactions can be an arduous task but thanks to the excellent facilities at ePSIC, we were able to collect a vast amount of data for the kinetic studies. We formulated guidelines for ourselves on how to acquire and process the data which will be useful for future studies. The electron beam-induced reaction contained 1425 separate micrographs. The way in which we calculated "concentration" of molecules in SWNTs was to divide the number of molecules by the total area of nanotube (that can be seen in the micrograph). Area was used rather than volume because electrons strike an area per second and every atom in that area (for an extremely thin sample such as molecules in SWNTs) experiences a very similar electron flux. However, counting molecules and calculating the molecules per area of nanotube for all 1425 frames would have been a Sisyphean task. We reduced the number of images by discounting any with blur-

riness, ones that were almost identical to each other, and focused on the images that would tell the story. Where there were significant changes (for example images that contained intermediates), we added the images to the storyboard, as it were. Through this rigorous selection process, we managed to reduce 1425 images to 25 crucial frames, giving the series of images in Fig. 2.18. Using these 25 images, we were able to apply zero order reaction kinetics and calculated the experimental cross section of PCC dimerisation to be 11.3$\pm$0.574 barn. This value is significantly smaller than the calculated upper limit of the cross section of 159 barn which is consistent with direct knock-on damage being the key mechanism for the electron beam-induced polymerisation of PCC.

The purely thermally induced reactions of PCC inside SWNTs were studied at different temperatures on the same heating chip. There were far fewer images for this study owing to the fact that we could not image during heating (to avoid introducing the electron beam as another source of energy). Therefore, we could use all of the single snapshots of the sample for calculating molecules per volume of nanotube (a volume of nanotube experiences a change in temperature). This data was used to approximate the activation energy of the thermally-induced polymerisation of PCC which turned out to be 38.1$\pm$0.0242 kJ mol^{-1}. Given that we heated the same chip to various temperatures, this value is a low estimate. However, we now have the methodology to carry out heating experiments on a sample and apply the Arrhenius equation to calculate the activation energy of a reaction. Together with the beam-induced kinetics study, this method could be applied to any nanoscale system.

We have also considered how to use information gained from experiments in the TEM for bulk procedures. It can be difficult to translate what happens inside a TEM to the real world because of how damaging the electron beam can be. On the other hand, the electron beam is widely used throughout academia and industry for

synthesis in the form of electron beam lithography. Large aromatic molecules are often crosslinked using EBL to form negative resists. We could, of course, have gone straight to an EBL lab, deposited thin crystals of HAT molecules straight onto a silicon chip, and blasted the crystals with some electron flux for some amount of time. However, trial and error with the irradiation procedure would have been time wasting. Instead, we used TEM again to irradiate various HAT crystals in order to find their critical doses. This was defined as the total dose before the tracked diffraction spots faded into noise. We now have the critical dose values of three types of HAT crystals at an accelerating voltage of 80 kV. This may not be directly comparable to the 80 kV microscope used for EBL at the nmRC due to energy transfer from back scattered electrons (off the silicon chips). It is, however, a starting point for the upper limit of the electron fluxes and doses that should be used in future EBL experiments to synthesise crosslinked frameworks from HAT crystals.

Finally, we have also carried out irradiation studies to generate the radical F@C_{60}. However, we cannot detect a radical using *in-situ* TEM techniques. We needed to have a spatially correlated *ex-situ* technique. This became the basis for our "lab on a grid" where the same area of a TEM grid containing HF@C_{60} was studied using different instruments and techniques. F@C_{60} can only be generated through electron beam irradiation (as far as we know). Optically detected magnetic resonance can be used to detect radicals and uses fluorescence microscopy to locate nanodiamonds with nitrogen vacancies (which exhibit ODMR behaviour). Therefore, we located areas on a TEM grid where nanodiamonds were in close enough proximity to crystals of HF@C_{60} so that the nitrogen vacancies could interact with any F$\cdot$ radicals generated after irradiation. We also ensured that the nanodiamonds were not damaged by the irradiation procedure. The initial results from this highly localised probing of nanodiamonds on endohedral fullerene crystals appear promising and we have developed a method for preparing samples so that

they can be studied using TEM in conjunction with ODMR.

TEM was used as the main technique throughout this thesis not because we were ignorant of other methods, but because this was the only technique that could have allowed us to carry out all of this work. The overarching theme has been to use the intense electron beam to induce changes in our materials while simultaneously following these changes using imaging, diffraction, or spectroscopy.

CHAPTER 6

Appendix - TEM Bestiary

"Clever girl..." - Michael Crichton and David Koepp, Jurassic Park (1993)

There comes a point after staring at what amounts to TV static for too long when you begin to see things that are not really there. This appendix is dedicated to those long hours of operating under reduced caffeine levels and lack of sunlight. Someone once said that the perfect microscopist would be a bald orangutan; having no hair means less fluff contaminating the sample holder and longer arms would certainly be useful for reaching up to change and align apertures... Perhaps not speaking a human language would help with communicating with some people. The threat of an angry orangutan might suffice.

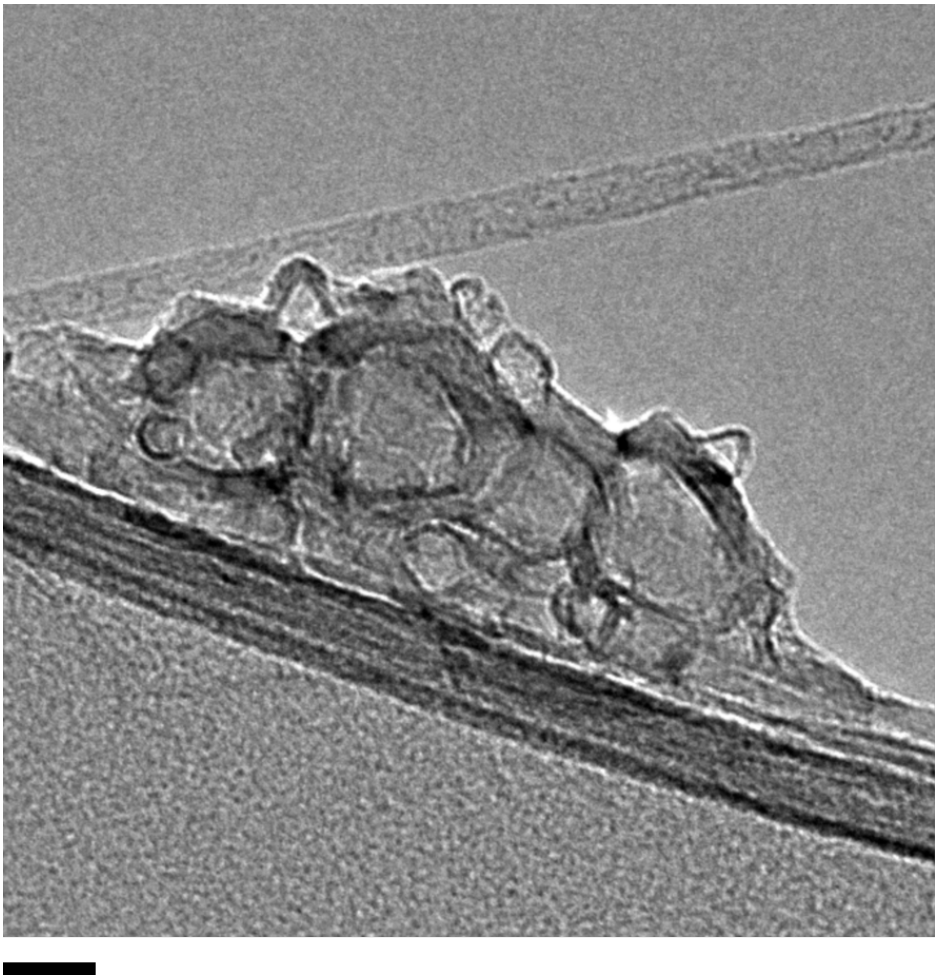

Figure 6.1. This caterpillar was discovered crawling around on the carbon film support. It appeared to exhibit some spiky protrusions from its back which may be for defensive purposes. The caterpillar was quite rotund, suggesting it had been engorging itself on a plentiful supply of food. As of yet, the food source is unknown; given that it was found on carbon film, perhaps it consumes carbon.

A sample of boron nitride nanotubes; the scale bar is 25 nm.

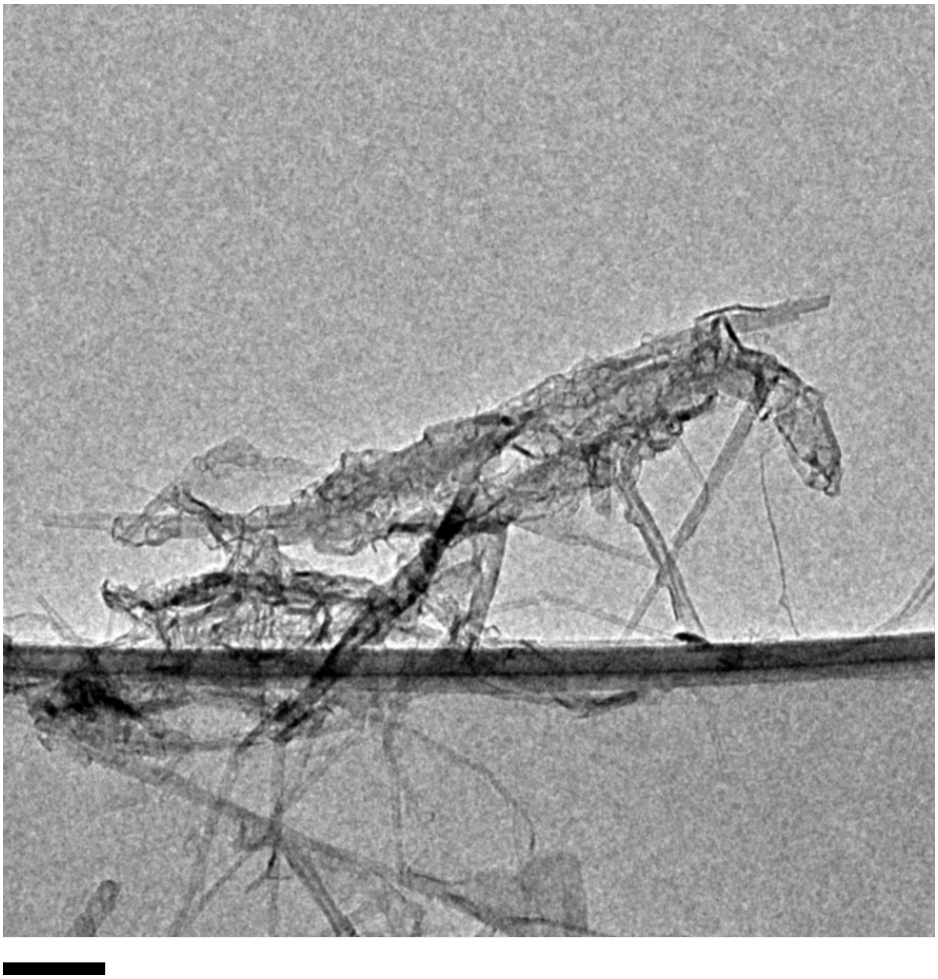

Figure 6.2. This grasshopper was found resting on carbon film. Our observations did not seem to faze the little creature; it maintained unbroken eye contact with the microscope operator as if to say "you wot mate". Most grasshoppers tend to spring away as soon as they are disturbed. This one, whether because of bravery or stupidity, appeared to be standing its ground. Of course, we as observers were only passing by and of no threat whatsoever.

A sample of boron nitride nanotubes; the scale bar is 0.1 µm.

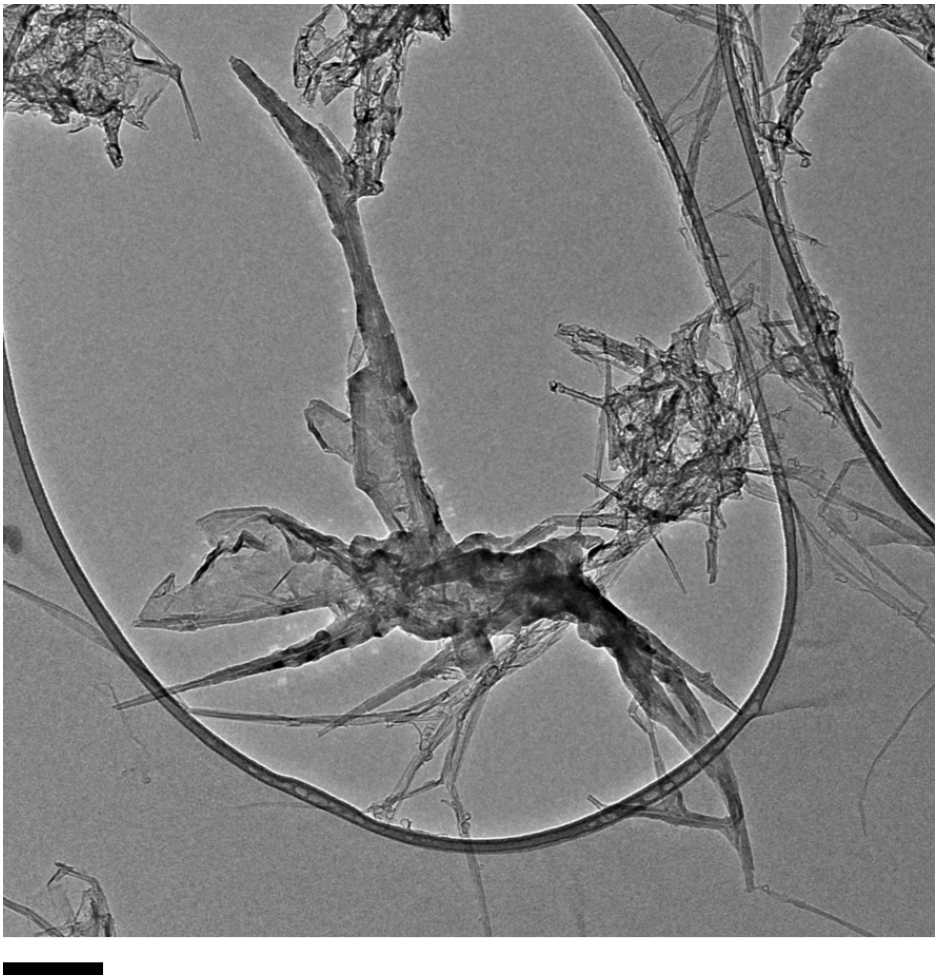

Figure 6.3. The sharp, tapered abdomen of this flying beast indicated its wasp-y nature. Not ones to be trifled with, wasps are like the bad sort of private detectives who shoot first and ask questions later. We quickly moved on from imaging this creature. If we need someone "interrogated", we know who to go to.

A sample of boron nitride nanotubes; the scale bar is 0.2 µm.

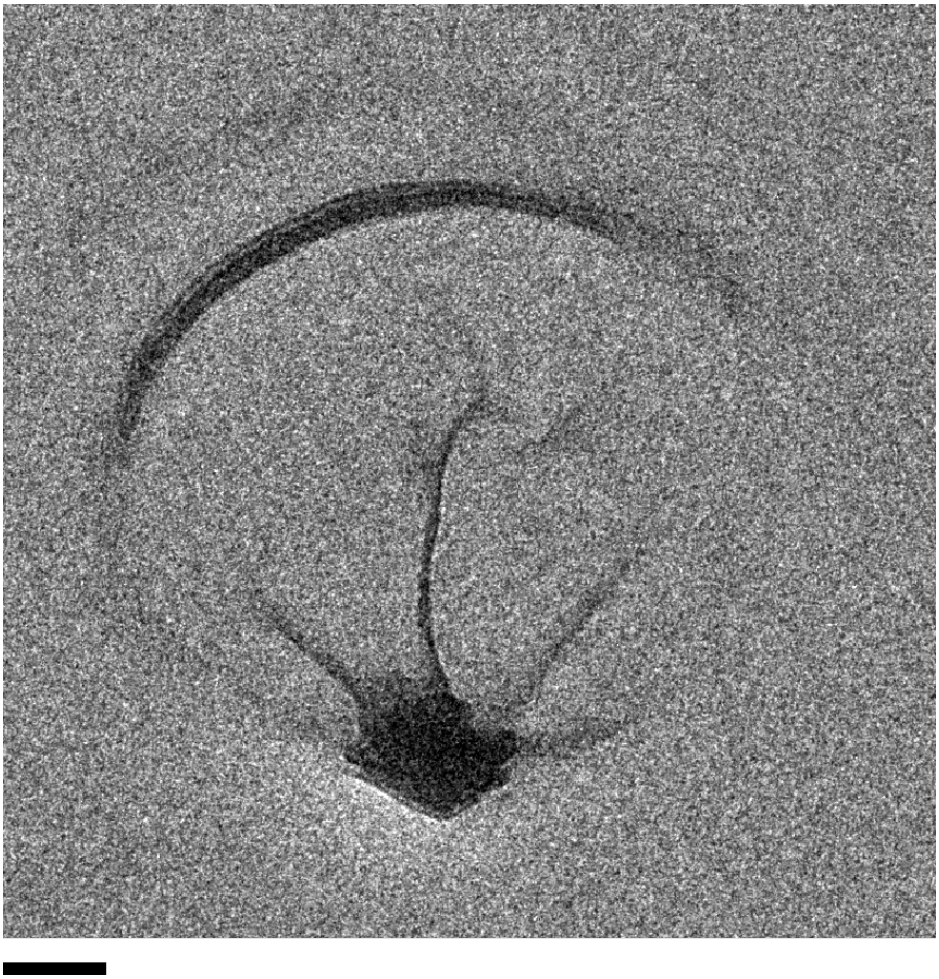

Figure 6.4. We discovered a wrinkle in the fabric of space (on the carbon film). This is the first known sighting of the Interdimensional Jellyfish. From the primordial soup at the beginning of time, this soft (in the sense of not made of matter) creature (in that we have no words to describe this being) was spawned (in as much as something like this can be birthed). A distant cousin of the cephalopod-like cosmic entity Cthulhu, the Interdimensional Jellyfish has no cult following and does not appear in many historical texts. This is, in part, due to its incredibly tiny size. The sparse information we do have on this being suggests that it spends most of its time consuming dark matter and traversing the cosmos in search of supernovas for a good sun tan.

The carbon film support of the TEM grid; the scale bar is 0.1 µm.

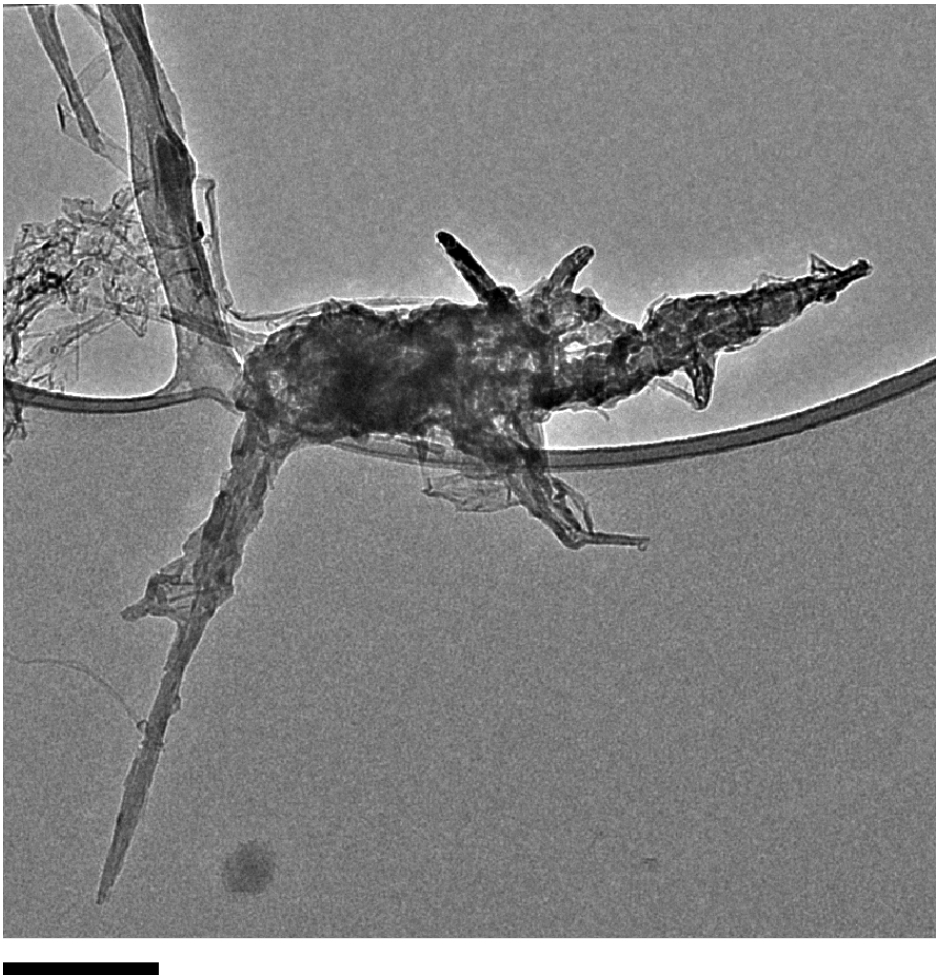

Figure 6.5. This rat held us at gunpoint until we agreed to take its photo and publish it somewhere in order to become internet-famous. It is quite a shame that this photo will only appear in some appendix. Who would believe us when we say that a nanoscopic rat threatened to shoot us if we did not follow its demands?

A sample of boron nitride nanotubes; the scale bar is 0.2 µm.

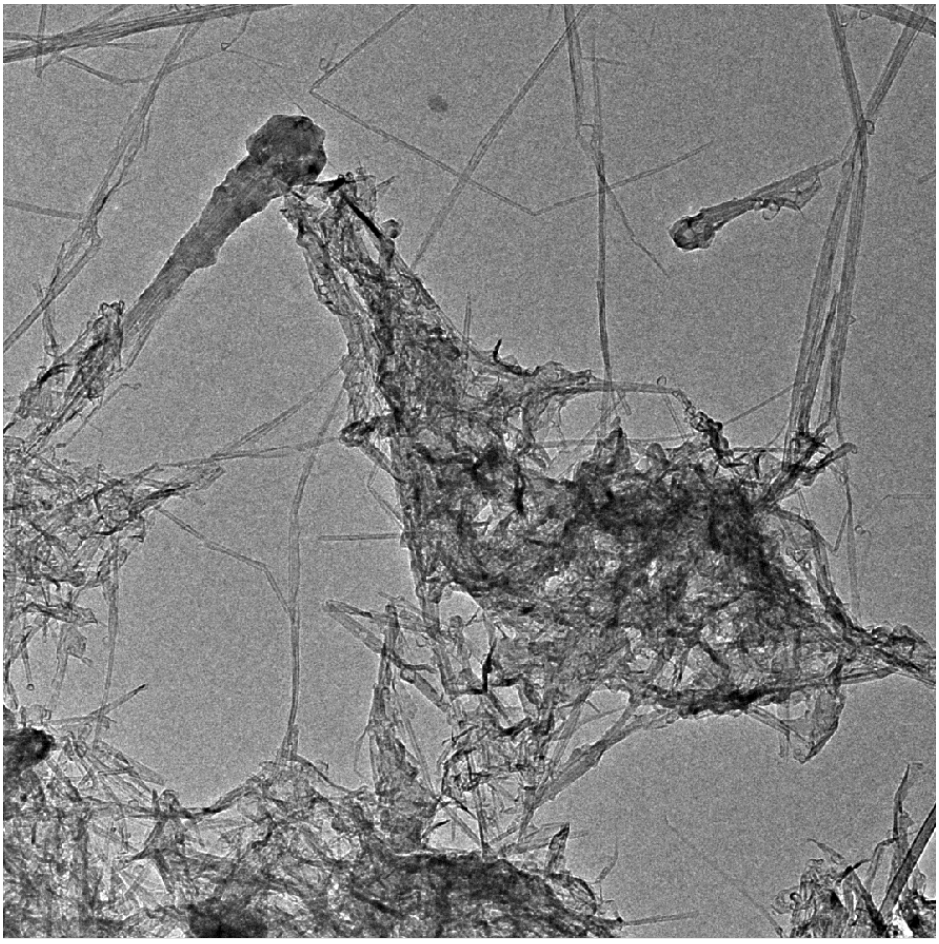

Figure 6.6. The soul of a long-dead emu gazed upon us impassively, its tattered feathers ruffled in the electron wind. It was impossible to understand what it was trying to tell us, although if the emu wars are anything to go upon, it was nothing good for humankind. We can only hope we did not doom our species by accidentally insulting this metaphysical creature.

A sample of boron nitride nanotubes; the scale bar is 0.2 µm.

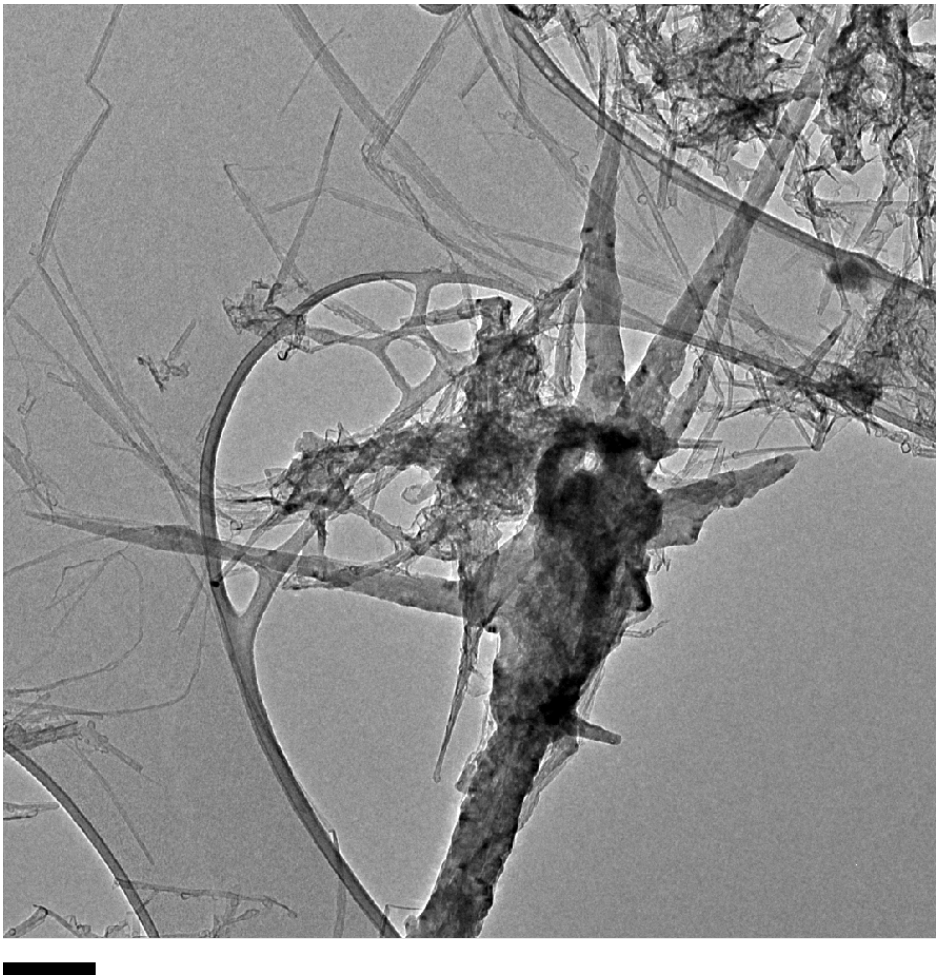

Figure 6.7. With trepidation, we took a photo of this footprint. A claw, outstretched, as though it was grasping at something. We could not find who this appendage belonged to (and now this photo is in the appendix; isn't that ironic).

A sample of boron nitride nanotubes; the scale bar is 0.2 µm.

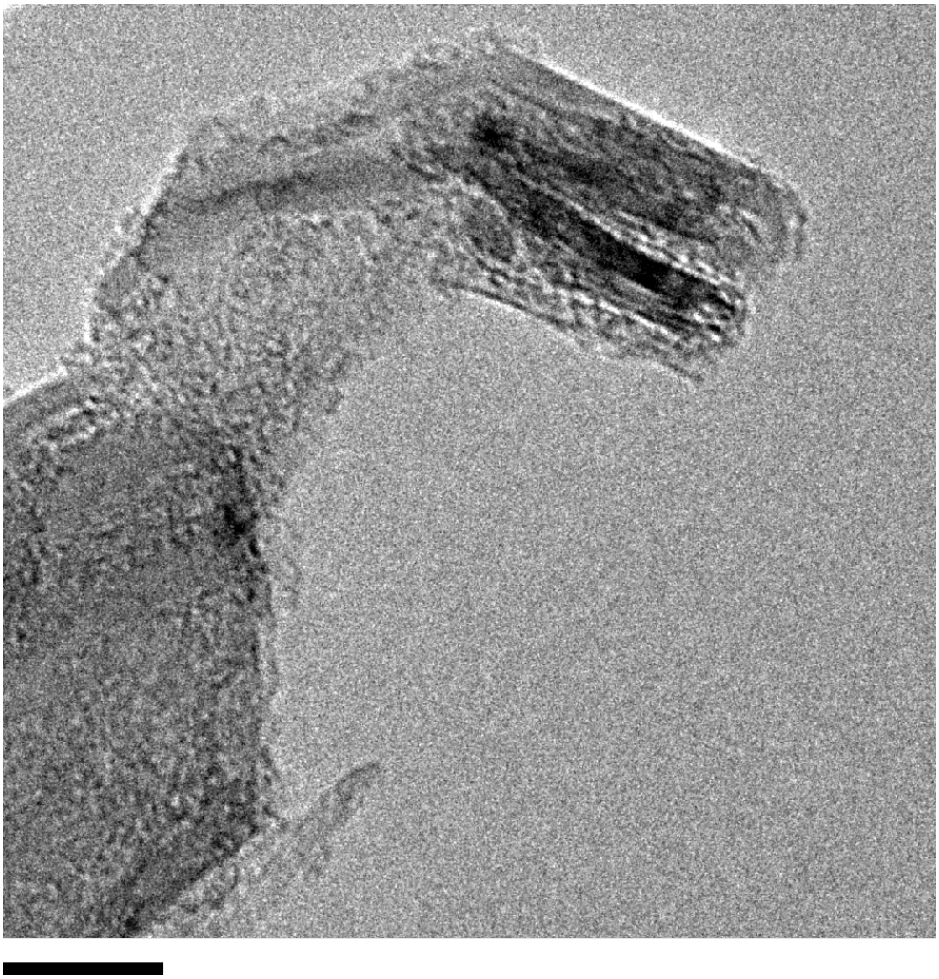

Figure 6.8. We were ambushed by a beast so fearsome, we were lucky it happened to be only a few tens of nanometres in size. As it turned out, this adorably small dinosaur, whom we christened Barney, was extremely curious about us and what we were up to. In between hyperactive running and wanton destruction of the carbon film, we managed to capture this photo of Barney smiling at the camera. You simply cannot remain down in the dumps in the face of such excitement.

A sample of carbon nanotubes; the scale bar is 10 nm.